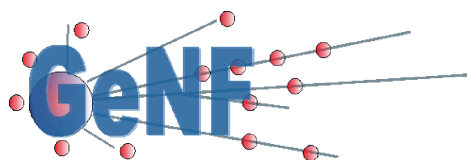


GeNF Experimental Report 2002



Geesthacht Neutron Facility



Editors:

A. Schreyer

J. Vollbrandt

R. Willumeit

GKSS 2003/1

**GeNF
Experimental Report 2002**

Editors:

A. Schreyer

J. Vollbrandt

R. Willumeit

(Institute for Materials Research)

Die Berichte der GKSS werden kostenlos abgegeben.

The delivery of the GKSS reports is free of charge.

Anforderungen/Requests:

GKSS-Forschungszentrum Geesthacht GmbH

Bibliothek/Library

Postfach 11 60

D-21494 Geesthacht

Fax.: (49) 04152/871717

Als Manuskript vervielfältigt.

Für diesen Bericht behalten wir uns alle Rechte vor.

ISSN 0344-9629

GKSS-Forschungszentrum Geesthacht GmbH • Telefon (04152)87-0

Max-Planck-Straße 1 • D-21502 Geesthacht / Postfach 11 60 • D-21494 Geesthacht

GeNF – Experimental Report 2002

Andreas Schreyer, Jürgen Vollbrandt, Regine Willumeit (Editors)

176 pages with 142 figures and 6 tables

Abstract

At the Geesthacht Neutron Facility GeNF about 180 experiments were performed in 2002 by GKSS and by or for external users, partners or contractors. In most cases the measurements were performed and analysed in cooperation by the guests and by the GKSS staff or by the permanent external user group staff. The activities which are based on a proposal procedure and on the in house R&D program are reported in 63 contributions in the annual experimental report for the year 2002. The contributions may contain one or also several combined experiments.

During 2002 the GKSS research reactor FRG-1 achieved an operation time of 219 days for the full 5 MW reactor power providing a neutron flux of ca. $1.4 \cdot 10^{14}$ thermal neutrons/cm² s and for the cold neutron source.

The focus of the in house R&D work at GeNF instruments was the characterisation of metal alloys and metal foams, the analysis of stresses in welds and technical structures at ARES, FSS, DCD and SANS-2, the structural investigation of hydrogen containing substances such as polymers, colloids and biological macromolecules at SANS-1 as well as the characterisation of magnetic thin films at PNR, TOREMA and RÖDI.

Jahresbericht 2002 über die Experimente an GeNF

Zusammenfassung

An der Geesthachter Neutronenforschungseinrichtung GeNF wurden von GKSS und von oder für externe Nutzer, Partner oder Auftraggeber etwa 180 Experimente in 2002 durchgeführt. In den meisten Fällen wurden die Messungen gemeinschaftlich von den Gastwissenschaftlern und GKSS-Personal vorgenommen und ausgewertet. Die Experimente, die über das Vorschlagswesen und über das GKSS-eigene F&E-Programm abgewickelt wurden, sollen in diesem Jahresbericht 2002 in Form von 63 Experimentierberichten dargestellt werden. Dabei können die Berichte einzelne Experimente oder auch mehrere zusammengefasst beschreiben.

Während 2002 erreichte der Forschungsreaktor FRG-1 219 Volllasttage bei 5 MW und bei einem Fluss von $1,4 \cdot 10^{14}$ thermischen Neutronen je cm² und s und **219** Betriebstage für die kalte Neutronenquelle.

Der Schwerpunkt der GKSS-eigenen Forschungsarbeiten lag in 2002 im Bereich der Charakterisierung von Metalllegierungen und Metallschäumen, der Analyse von Eigenspannungen in Schweißverbindungen und technischen Strukturen an ARES, FSS, DCD und SANS-2, im Bereich der Strukturanalyse von wasserstoffhaltigen Substanzen wie Polymere, Kolloide und Biomolekülen an der SANS-1 sowie im Bereich der Charakterisierung magnetisch dünner Filme an PNR, TOREMA und RÖDI.

CONTENTS

Preface

- GeNF Operation
- Operation of FRG-1
- GeNF Instruments (overview)

SANS-1	19
Magnetic structure of the magnetite/oleic acid/benzene ferrofluids by small-angle scattering of polarized neutrons <i>M. V. Avdeev</i>	21
Phase behaviour of the dilute DDAB/C ₁₂ E ₈ /water system <i>E. Feitosa</i>	23
A SANS study of micelles formed by mixtures of a cationic fluorinated surfactant and a cationic hydrocarbon surfactant <i>Mari Kadi</i>	25
Investigation of the three dimensional micro-phase separation and crystallisation of multi block copolymers by means of small-angle neutron scattering <i>H. Kamusewitz</i>	27
Wormlike block copolymer micelles <i>M. Konrad</i>	29
Reversible micelle – vesicle conversion of oleyldimethylamine oxide <i>Hiroshi Maeda</i>	31
Characterisation of hyperbranched polymers with SANS <i>T. Maksimova</i>	33
A SANS Study of micelles formed by pluronic triblock copolymers P84 and P94 in D ₂ O <i>J. S. Pedersen</i>	37
A SANS Study of microemulsion droplets decorated by Brij700 block copolymer as a function of droplet concentration, surfactant to oil ratio and surface coverage <i>J. S. Pedersen</i>	39
A SANS Study of micelles formed by Brij700 block copolymer as a function of concentration and temperature <i>J. S. Pedersen</i>	41
Characterisation of novel ionomer membranes based on poly(ether ether ketone) and layered materials <i>Luis A. S. A. Prado</i>	43
Sol-gel derived hybrid polysaccharide-silica nanocomposites <i>Yurii A. Shchipunov</i>	45
Fractal properties of humic substances revealed from neutron scattering and synchrotron X-ray scattering studies <i>A. Timchenko</i>	47

Structures of block copolymer solutions <i>A. Timmann</i>	49
A SANS study of the concentration and temperature effects on micelles of n-nonyl- β -D-glucoside and n-tetradecyl- β -D-maltoside <i>S. Ulvenlund</i>	51
SANS-2	53
SANS investigation of SiO ₂ nanoclusters in different solutions <i>J. Adam, H. Eckerlebe</i>	55
Continuation of the study of the crystalline quality of large bismuth single crystals <i>L. Dohmen, J. Thelen, B. Alefeld, K. Fischer</i>	57
The study of new magnetic nanocomposites based on mesoporous silica with embedded Fe-particles by SAPNS: technology <i>S. V. Grigoriev, A. I. Okorokov, E. A. Kelberg</i>	59
The study of new magnetic nanocomposites based on mesoporous silica with embedded Fe-particles by SAPNS: magnetic properties <i>S. V. Grigoriev, A. I. Okorokov, E. A. Kelberg</i>	63
SANS investigation of Mg alloys <i>D. Letzig, J. Bohlen, H. Eckerlebe</i>	65
Critical magnetic scattering in an ordered invar Fe ₇₅ Pt ₂₅ alloy <i>A. I. Okorokov, S. V. Grigoriev</i>	67
The study of the spin chirality in MnSi single crystal by means of small angle scattering of polarized neutrons <i>A. I. Okorokov, S. V. Grigoriev, P. Böni, R. Georgii</i>	69
The crystalline quality of large Bismuth single crystals and a Czochralski grown Sapphire single crystal (Al ₂ O ₃) by neutron transmission <i>M. Prager, B. Alefeld</i>	73
Phase separation kinetics in Cu –0.9 at.% Ti <i>S. Prasetyo</i>	75
Test of a new interferometer for cold neutrons built of holographic gratings <i>C. Pruner</i>	77
SANS studies of fossil dinosaur bone <i>A. Pyzalla, M. Stempniewicz</i>	79
Characterization of aging processes of fats by SANS <i>D. W. Schubert</i>	81
Structural parameters of adsorbed detergent on polystyrene latex particles <i>Rongbiao Wang, H. Schmiedel</i>	83

DCD	85
DCD with an additional beam line <i>D. Bellmann</i>	87
Characterization of aging processes of fats by USANS <i>D. W. Schubert</i>	89
TOREMA-2	91
Accurate annealing experiments by time-temperature superposition for polymers close to the glass transition <i>A. Pohlers, M. Stamm, H.-D. Braune</i>	93
Asymmetric interdiffusion between weakly interacting polymers as determined by neutron reflectometry <i>X. Yang, A. Pohlers, D. Jehnichen, M. Stamm</i>	97
Development of asymmetric profile analysis for neutron reflection curves of polymer double layers (progress report) <i>X. Yang, A. Pohlers, D. Jehnichen, M. Stamm</i>	101
Characterization of GaAlAs/GaAs superstructures <i>L. Koenders, V. Wagner</i>	105
PNR	107
Neutron reflectivity from black foam films <i>R. Krastev</i>	109
Neutron reflectivity on Fe/Cr and Fe/Cr/Sn/Cr multilayers <i>D. Lott, D. Solina, M. Almokhtar, K. Mibu, A. Schreyer</i>	111
ARES	113
Residual stress in welded HY-80 steel <i>L. Grünitz</i>	115
Residual stress in IN718 turbine discs <i>W. Marketz</i>	117
Residual stress in friction stir welded AA2024 sheets <i>P. Staron, M. Koçak</i>	119
Residual stress in friction stir welded AA7010 sheets <i>P. Staron, M. Koçak</i>	121
Residual stress in a cold-stretched friction stir welded AA2024 sheet <i>P. Staron, M. Koçak</i>	123
Residual stress in friction stir welded AA2024 thick plates <i>P. Staron, M. Koçak</i>	125

FSS	127
Minimizing residual stresses and distortion of cast iron components <i>W. Stets</i>	129
Neutron TOF diffraction from fiber-reinforced Al-MMC material <i>A. Wanner</i>	131
Stress investigations of Cu-Nb metal-matrix composites <i>Wen Hei Ye, H.-G. Brokmeier</i>	133
TEX-2	135
Modeling of texture evolution of copper under equal channel angular pressing <i>Seung Chul Baik, Y. Estrin, R. J. Hellmig, Hyo-Tae Jeong, Hyoung Seop Kim</i>	137
Texture development during extrusion of magnesium alloy AZ31 <i>J. Bohlen, D. Letzig, K U. Kainer</i>	139
Texture measurements in high Si content Fe alloys <i>R. E. Bolmaro, O. A. Lambri</i>	141
Preferred orientation of phyllosilicates as a control of magnetic fabric, sedimentary rock samples from Rhenohercynian zone of Bohemian Massif <i>M. Chadima</i>	143
Reproduction of historical gypsum plaster <i>S. Follner, A. Wolter, H. Follner</i>	145
Crystallographic preferred orientation of banded iron formations from Singhbhum Craton (Eastern India) <i>M. Mamtani, A. Mukherji, A. Chaudhuri</i>	147
Quartz rich tectonites from Pie de Palo Sierra-Córdoba-Argentina <i>R. Martino, R. E. Bolmaro.</i>	149
Texture of bone mineral in sauropod dinosaur bones <i>A. Pyzalla, M. Stempniewicz</i>	151
Texture investigations of Cu-Nb-rings <i>W. Singer, H.-G. Brokmeier, Wenhai Ye</i>	153
Quantitative texture analysis of R-phase in aged Ni-rich Ti-50.7at.%Ni shape memory alloy using neutron diffraction <i>H. Sitepu</i>	155
Annealing texture of a Cu-Nb composite <i>Wenhai Ye, H.-G. Brokmeier</i>	157
The variation of texture during tensile test of Mg alloy AM20 <i>Sangbong Yi, H.-G. Brokmeier</i>	159
POLDI	161
Magnetic mesostructure of dilute alloy $(\text{Pd}_{0.984}\text{Fe}_{0.016})_{0.95}\text{Mn}_{0.05}$ – Test of simple models of depolarizing inhomogeneities <i>G. Gordeev, L. Axelrod, V. Zabenkin, V. Wagner</i>	163

Developments of electronic mixed field personal dosimeters
M. Luszik-Bhadra 165

Neutron diffraction test of the *Umweganregung* monochromator based
on an elastically bent perfect crystal
P. Mikula 167

Domain structure of Ba-ferrit glass ceramics
V. Wagner, T. Klupsch 169

RÖDI & TOREMA

Internship: X-ray and neutron scattering methods applied to thin films
D. M. Solina, D. Lott, M. Störmer; U. Tietze, A. Schreyer (Co-ordinators) 171

RÖDI INCOATC-Bruker AXS

Characterisation of FeMn-FeNi exchange bias films using X-ray reflection and diffraction
J. Fassbender 173

Proposal Form 175

PREFACE

GeNF Operation

The Geesthacht Neutron Facility (GeNF) is operated as an open facility for external users for about 2/3 of the available beam time and it is used for GKSS in house research within its materials science programme for the remaining 1/3. The external users come either from national and international scientific research institutions, universities and industry, or they own and operate experiments at GeNF as permanent external partners.

The beam time allocations for GeNF instruments are established on the base of a proposal procedure which can react in a flexible and fast way on upcoming proposals. Proposals can be submitted at any time. In 2002 about 180 experiments were performed at GeNF by or for external users, partners or contractors as well as for the in house research programmes. A part of these activities is reported in the present annual experimental report for the year 2002.

Operation of FRG-1

During the routine shut down of the FRG-1 at the start of 2002 the primary reactor cooling loops including their control system have been replaced. Also the pneumatic dispatch system for the short time sample irradiation has been upgraded. These tasks led in 2002 to a slightly reduced an operation time of 219 days at its full 5 MW power providing a neutron flux of ca. $1.4 \cdot 10^{14}$ thermal neutrons/cm² s. The cold neutron source also was available for 219 days.

GeNF Instruments

The current set of instruments at GeNF is shown in Figure A and listed in Table A. The available sample environment is listed in Table B.

In 2002 the installation of a modern hardware and software system based on LabView to control the experiments was finished for SANS-1 and TEX-2. This process is continued next for TOREMA – in parallel with its general upgrading – and planned for all other instruments.

The focus of the research at GeNF is the investigation of metal alloys and metal foams, the analysis of stresses in welds and technical structures at ARES, FSS, DCD and SANS-2, the structural investigation of hydrogen containing substances such as polymers, colloids and biological macromolecules at SANS-1 as well as the characterisation of magnetic and polymer thin films at PNR, TOREMA and RÖDI. Regarding instrument improvements, TOREMA is currently refitted with a complete new sample goniometer and a 2-dimensional position sensitive ³He-detector. The DCD has been enhanced by a second beam line operating at an alternative wavelength doubling the detectable size range.

Geesthacht Neutron Facility (GeNF)

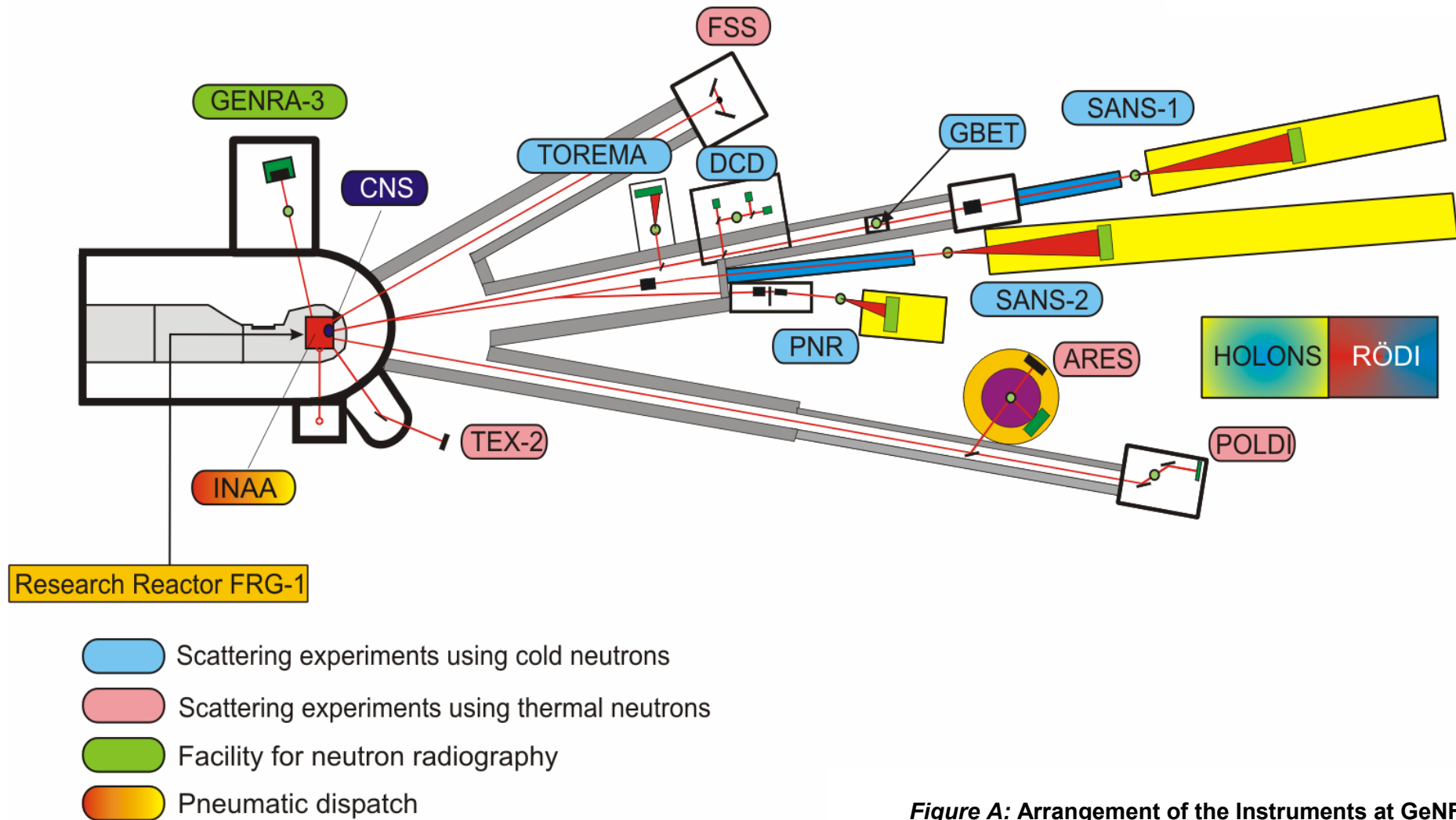


Figure A: Arrangement of the Instruments at GeNF.

Table A: List of GeNF Instruments.

Instrument	Short Instrument Description /Main Tasks	Characteristic Data	Operator / Local Contact
SANS-1	<u>S</u> mall <u>A</u> nge <u>N</u> eutron <u>S</u> cattering using cold non-polarised/polarised neutrons primarily to investigate molecular biology, colloids and polymers	$\Phi_{\max} = 6 \cdot 10^5 \text{ cm}^{-2} \text{ s}^{-1}$ (coll.2 m, $\lambda=0.8\text{nm}$) $\Delta\lambda/\lambda = 0.1$ ($\lambda = 0.85 \text{ nm}$) Particle sizes: 2 - 80 nm 2-D position-sens. ^3He - detector	GKSS / Regine Willumeit
SANS-2	<u>S</u> mall <u>A</u> nge <u>N</u> eutron <u>S</u> cattering using cold non-polarised/polarised neutrons to characterise precipitates, clusters, interfaces, grain sizes, magnetic structures etc. in materials (metals, polymers, colloids a.o.)	$\Phi_{\max} = 2 \cdot 10^7 \text{ cm}^{-2} \text{ s}^{-1}$ (coll.1 m, $\lambda=0.5\text{nm}$) $\Delta\lambda/\lambda = 0.1$ Particle sizes: 1 - 100 nm 2-D position-sens. ^3He - detector	GKSS / Helmut Eckerlebe P. Klaus Pranzas
DCD	<u>D</u> ouble <u>C</u> rystal <u>D</u> iffractometer for ultra small angle neutron scattering (USANS) using non-polarised cold neutrons to characterise large creep pores, fatigue and sintering cavities, precipitates, voids, bubbles, etc. in materials	$\Phi \approx 0.5 \cdot 10^3 \text{ cm}^{-2} \text{ s}^{-1}$ $\Delta\lambda/\lambda = 1 \cdot 10^{-5}$ ($\lambda = 0.443 \text{ nm}$) Particle sizes: 30 nm - 24 μm 3 x ^3He - detectors	GKSS / Dieter Bellmann
ARES	Diffractionmeter for the <u>A</u> nalysis of <u>R</u> esidual <u>S</u> tresses in specimens with technical sizes (up to 100 kg) using thermal non-polarised neutrons	$\Phi \approx 3 \cdot 10^5 \text{ cm}^{-2} \text{ s}^{-1}$ (perfect Si-Monochr.) $\Delta d/d \approx 4 \cdot 10^{-3}$ take-off angle: 57° - 120° 2-D position-sens. ^3He - detector	GKSS / Peter Staron
FSS	Time of flight <u>F</u> ourier <u>S</u> train <u>S</u> pectrometer to investigate residual stresses in specimens with technical sizes using thermal neutrons	$\Phi = 5.5 \cdot 10^6 \text{ cm}^{-2} \text{ s}^{-1}$ timing res. ca. $4 \cdot 10^{-3}$ ($\lambda = 0.1 - 0.4 \text{ nm}$) Analyser: 2 x 3072 TOF channels 2 detector banks (90° & 270°)	CAU - Universität Kiel / Hans-Georg Priesmeyer
TOREMA-2	<u>T</u> otal <u>R</u> eflection <u>M</u> Achine, reflectometer to study surfaces, thin films and membranes with cold non-polarised neutrons with high resolution	$\Phi = 5 \cdot 10^4 \text{ cm}^{-2} \text{ s}^{-1}$ (standard collimation) $\Delta\lambda/\lambda = 0.02$ ($\lambda = 0.435 \text{ nm}$) 2-D position-sens. ^3He - detector	GKSS / Dieter Lott
PNR	<u>P</u> olarised <u>N</u> eutron <u>R</u> eflectometer to study magnetic and other surfaces, layers, thin films and membranes using cold non-polarised/polarised neutrons at high fluxes	$\Phi_{\text{nonpol}} = 1 \cdot 10^5 \text{ cm}^{-2} \text{ s}^{-1}$ $\Phi_{\text{nonpol}} / \Phi_{\text{pol}} = 3 / 1$ $\Delta\lambda/\lambda = 0.05$ ($\lambda \geq 0.635 \text{ nm}$) 2-D position-sens. ^3He - detector	GKSS / Danica Solina

Table A: List of GeNF Instruments (continued).


Instrument	Short Instrument Description /Main Tasks	Characteristic Data	Operator / Local Contact
RÖDI	X-ray (<u>R</u> öntgen) <u>D</u> iffractometer to investigate residual stresses, textures and thin films	Seifert XRD 3003 PTS Heavy load goniometer	GKSS / Peter Staron
TEX-2	Four circle neutron <u>T</u> EXture diffractometer to characterise textures in metallic, ceramic and geologic materials using thermal non-polarised neutrons	$\Phi = 0.3 - 2 \cdot 10^6 \text{ cm}^{-2} \text{ s}^{-1}$ take-off angle: $17^\circ - 57^\circ$ (in 10° -steps) λ -range: 0.08 – 0.27 nm ^3He -single detect., 38° JULIOS-PSD	TUC – Technische Universität Clausthal / Heinz-Günter Brokmeier
POLDI	<u>P</u> OLARISED <u>D</u> iffractometer; 3-D depolarisation analysis is used to investigate magnetic properties and correlations in magnetic materials; additional time of flight option in non-polarised mode	$\Phi_{\text{max}} = 0.8 \cdot 10^5 \text{ cm}^{-2} \text{ s}^{-1}$ (polarized) take-off angle: $10^\circ < 2 \Theta_M < 65^\circ$ λ -range: 0.1 nm - 0.36 nm ^3He -single detector	PTB – Physikalisch Technische Bundesanstalt / Volker Wagner
HOLONS	<u>H</u> OLOgraphy and <u>N</u> eutron <u>S</u> cattering to investigate the properties in functional materials of photonics (e.g. photopolymers and photorefractive crystals) and to study light-induced changes simultaneously by light and neutron diffraction	holographic setup in SANS-2: angular resol. $\leq 0.01^\circ$; angul. setting acc = 0.001° lasers (excitation & diffract.): Ar^+ -laser (single&multi line mode: 25 W /visible, 5.5 W / UV), HeNe-lasers (green, red)	Universities of Vienna and Osnabrück / Romano Rupp
GENRA-3	<u>G</u> Eesthacht <u>N</u> eutron <u>R</u> Adiography facility for non-destructive analysis of materials by static and dynamic imaging	$\Phi_{\text{therm}} / \Phi_{\text{epi}} = 1.4 \cdot 10^6 / 8 \cdot 10^3 [\text{cm}^{-2} \text{ s}^{-1}]$ image: 15 x 15 to 45 x 45 cm^2 max. size of specimen: 100 x 200 cm^2	GKSS / Jürgen Vollbrandt
GBET	<u>G</u> eesthachter <u>B</u> oron- capture (<u>E</u> infang) <u>T</u> herapy originally designed to study cell cultures in tumours with enriched boron; now available as a cold neutron irradiation facility	$\Phi = 1.6 \cdot 10^8 \text{ cm}^{-2} \text{ s}^{-1}$ ($\lambda_m = 0.6 \text{ nm}$) irrad. area : 30 x 40 mm^2 $E_m = 2.3 \text{ meV}$	GKSS / Hans-Ulrich Ruhnau
ICI	<u>I</u> n <u>C</u> ore <u>I</u> rradiation - service for industry and others, different core positions, pneumatic dispatch system available	$\Phi_{\text{therm}} = 2 \text{ to } 8 \cdot 10^{13} \text{ cm}^{-2} \text{ s}^{-1}$ $\Phi_{\text{fast}} = 0.02 \text{ to } 0.06 \Phi_{\text{therm}}$ max. sample size: 40 mm \varnothing x 100 mm	GKSS / Wolfgang Knop
NAA	<u>N</u> eutron <u>A</u> ctivation <u>A</u> nalysis used as qualitative and quantitative multielement analysis of major, minor and trace elements	> 50 chem. elements can be determined sample mass: $10^{-3} - 1 \text{ g}$ LOD - range: $10^{-5} \text{ to } 10^{-12} \text{ g}$	GKSS / Rainer Niedergesäss

Table B: GeNF Sample Environment.

Instrument	Cryostat	Magnets	Temp. Conditioning	Other Devices
SANS-1	³ He / ⁴ He – Cryostat: horizontal dilution-refrigerator with NMR sample coil and microwave source: T-range: 120 mK - RT; NMR: 106 and 16 MHz; Microwave: tunable: 68 to 74 GHz sample dimension: 2,8 x 17 x 19 mm ³ (optimum design for NMR coil), NMR is made for ¹ H and ² H resonance in 2.5 Tesla continuous wave mode;	2.5 Tesla magnet	heater up to 80 °C	
SANS-2	refrigerator cryostat Model Leybold RGD 210, temp.-range: 12–475 K flexible operation in various instruments	<ul style="list-style-type: none"> • B-E 25: up to 2 Tesla with closed cycle refrigerator (T: 8–300 K) • B-E 15: up to 1.5 Tesla with closed cycle refrigerator (T: 8–300 K) • B-E 10: up to 1 Tesla with closed cycle refrigerator (T: 8–300 K), alternative furnace (T: 300–900 K), usable for polarised neutrons 	heater (electric) / cooler (thermostat liquid circuit): T-range: -30–400 °C vacuum or inert gas atmosphere	<ul style="list-style-type: none"> – sample container for big samples – lasers;
DCD	refrigerator cryostat Model Leybold RGD 210, temp.-range: 12–475 K flexible operation in various instruments			
ARES	refrigerator cryostat Model Leybold RGD 210, temp.-range: 12–475 K flexible operation in various instruments			
FSS	refrigerator cryostat Model Leybold RGD 210, temp.-range: 12–475 K flexible operation in various instruments		heater (up to 1000 °C)	– stress rig max. force: 30 t

Table B: GeNF Sample Environment (continued).

Instrument	Cryostat	Magnets	Temp. Conditioning	Other Devices
PNR	refrigerator cryostat Model Leybold RGD 210, temp.-range: 12–475 K flexible operation in various instruments	• superconducting magnet: up to 5 Tesla with closed cycle refrigerator (T: 8–300 K) usable for polarised neutrons		
TOREMA-2	refrigerator cryostat Model Leybold RGD 210, temp.-range: 12–475 K flexible operation in various instruments		2 x vacuum furnaces: T-range: RT - 200 °C - one especially. for annealing purposes under PC control	
TEX-2			mirror furnace up to 2000 °C	– loading device: tension up to 1.5 t, compression up to 2.0 t – sophisticated set of sample holders
POLDI	– refrigerator T > 10 K – Orange cryostat T > 1.5 K	DC magnetic field < 160 A/cm pulsed field < 6.5 kA/cm		

	EXPERIMENTAL REPORT	GeNF SANS-1
Small-angle scattering instrument SANS-1		

Short Instrument Description:

The small angle neutron scattering instrument SANS-1 using cold non-polarised/polarised neutrons serves primarily to investigate molecular biology, colloids and polymers.

Local Contact:

Dr. Regine Willumeit

Phone/Fax : +49 (0)4152 87 – 1291 / +49 (0)4152 87–1356

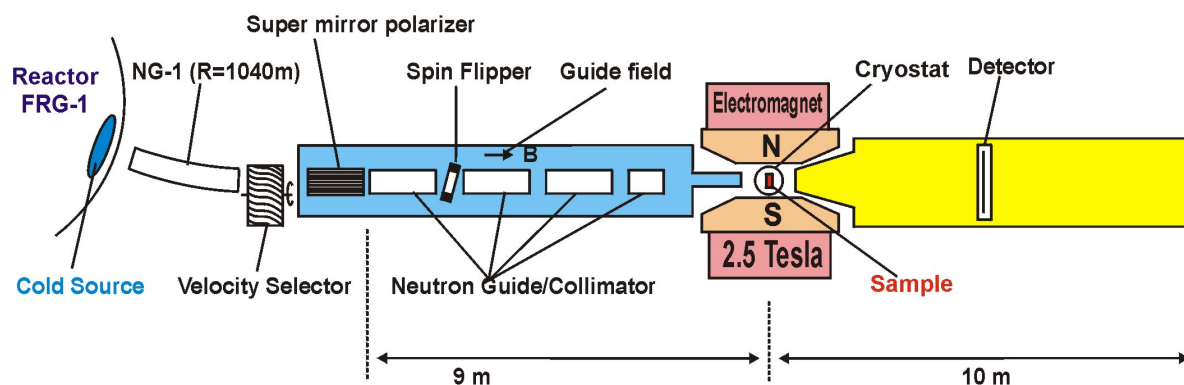
e-mail: regine.willumeit@gkss.de

Dr. Vasyli Haramus

Phone/Fax : +49 (0)4152 87 – 1290 / +49 (0)4152 87 – 1356

e-mail: vasyl.haramus@gkss.de

Schematic View of SANS-1:



Instrument Details:


<u>Beamline:</u>	Beamline 8 – NG-1, radius of curvature R = 1040 m, cross section 3 x 4 cm ² , cold neutrons
Monochromator	helical slot selector
Wavelength range behind polariser and selector:	≥ 0.45 nm;
Wavelength resolution	$\Delta\lambda / \lambda = 0.1$ ($\lambda = 0.85$ nm)
Length L of collimation:	1 m, 3 m, 5 m, 7 m, 9 m
Flux at specimen:	$\Phi = 0.04\text{--}6 \cdot 10^5$ cm ⁻² s ⁻¹ see table

Instrument Details (continued):

Range of momentum transfer:	$0.05 \leq Q \leq 3 \text{ nm}^{-1}$
Distance sample to detector:	$0.7 \text{ m} \leq d \leq 9\text{m}$
<u>Detector:</u> active area: effective pixel size: background:	2-dim position-sensitive ^3He -counter $55 \times 55 \text{ cm}^2$ $0.7 \times 0.7 \text{ cm}^2$ 1 cps
<u>Polarized target station:</u>	dilution refrigerator (120 mK) 2.5 T C-shaped electro-magnet microwave emitter (68–74 GHz) NMR circuit for protons and deuterons selective nuclear spin depolarisation
<u>Other sample environment</u>	thermostat ($5 \text{ }^\circ\text{C}$ to $+200 \text{ }^\circ\text{C}$) automatic sample change

Flux of polarized cold neutrons at the sample position:

length of collimator [m]	1	3	5	7	9
$\Phi [10^3 \text{ n cm}^{-2} \text{ s}^{-1}]$ ($\lambda = 0.85 \text{ nm}$)	600	360	120	72	40

	EXPERIMENTAL REPORT	GeNF SANS-1
Magnetic structure of the magnetite/oleic acid/benzene ferrofluids by small-angle scattering of polarized neutrons		
Principal Proposer:	M. V. Avdeev ¹ ¹ Frank Laboratory of Neutron Physics, JINR, Dubna, Russia	
Experimental Team:	V. Haramus ² , M. Balasoiu ¹ , V. L. Aksenov ¹ , L. Vekas ³ , D. Bica ³ ² GKSS Research Centre	
	³ Center of Fundamental and Advanced Technical Research, Timisoara Branch of RAS, Timisoara-1900, Romania	
Date(s) of Experiment:	May 2002	

Specific properties in a magnetic field of ferrofluids (colloidal solutions of magnetic materials stabilized by adding surfactants) determine their wide use in different industrial applications [1]. In our recent experiments [2–4] the magnetite/oleic acid/d-benzene ferrofluids were investigated by means of the scattering of non-polarized neutrons. It was shown that the nuclear scattering of these fluids is described well by the spherical core-shell model (magnetite core plus surfactant shell), and no significant effects of aggregation and interparticle interaction were observed up to the magnetite concentration of 10 vol.%. Along with it the magnetic scattering does not fit the expected spherical model and reveals more complex structure. The aim of the presented experiments was to clarify the magnetic structure of these fluids using the polarized neutron beam.

Experiments with the ferrofluids based on h- and d-benzene (magnetite concentration $c_m=7$ vol.%) were performed at room temperature in a q-range $0.04\div 2.7$ nm⁻¹. The magnetic field of 2.5 T, which corresponds to the magnetization saturation in the studied fluids, was applied to the samples perpendicular to the neutron beam. Separation of the nuclear and magnetic scattering was made using anisotropy in respect to the radial angle φ in the scattering patterns corresponding to two polarization states of incident neutrons, parallel (-) and antiparallel (+) to the direction of the magnetic field [5]:

$$I^+(q, \varphi) = F_n^2(q) + \{F_m^2(q) - 2PF_n(q)F_m(q)\} \sin^2 \varphi, \quad (1a)$$

$$I^-(q, \varphi) = F_n^2(q) + (F_m^2(q) + 2P\varepsilon F_n(q)F_m(q)) \sin^2 \varphi, \quad (1b)$$

where P is the polarization of the neutron beam (≈ 1), and ε (0.9) is the efficiency of the spin-flipper. In data treatment the lognormal particle size distribution ($\langle R \rangle = 4.2$ nm, $\sigma_R = 1.3$ nm, $R = 2.5\div 9.0$ nm) obtained [6] from electron microscopy images was taken into account.

Averaged scattering curves for different states of neutron polarization are presented in Fig. 1. One can see that the effect of magnetic scattering in the h-benzene-based ferrofluid is negligible, and experimental curves fits well the core-shell model comprising the size distribution mentioned above. The separation of the nuclear and magnetic scattering in accordance to Eqs.1 is demonstrated in Fig. 2. The nuclear-magnetic cross term in Eqs.1 is liner in respect to the magnetic scattering amplitude, which allows one to determine more precisely, in comparison to the scattering of non-polarized neutrons, the magnetic contribution. The curve corresponding to the nuclear scattering fits well the core-shell model, and the resulting parameters are in good agreement with those found previously [4]. At the same time, the magnetic scattering curve does not confirm the general view on the magnetic

structure of ferrofluids revealing some peculiarities at the scale of $R \approx 10$ nm in the absence of large aggregation, which would be seen in the nuclear scattering. This radius is about two times more that the nuclear one. Indications of this fact were also found in full polarization and depolarization analysis of the scattering from non-magnetized magnetite/oleic acid/kerosene ferrofluids [7]. The treatment of the cross term (Fig. 2) to determine directly the magnetic scattering length density profile is in progress. Despite the fact that the studied particles are isotropic the polydispersity has much effect and complicate the treatment.

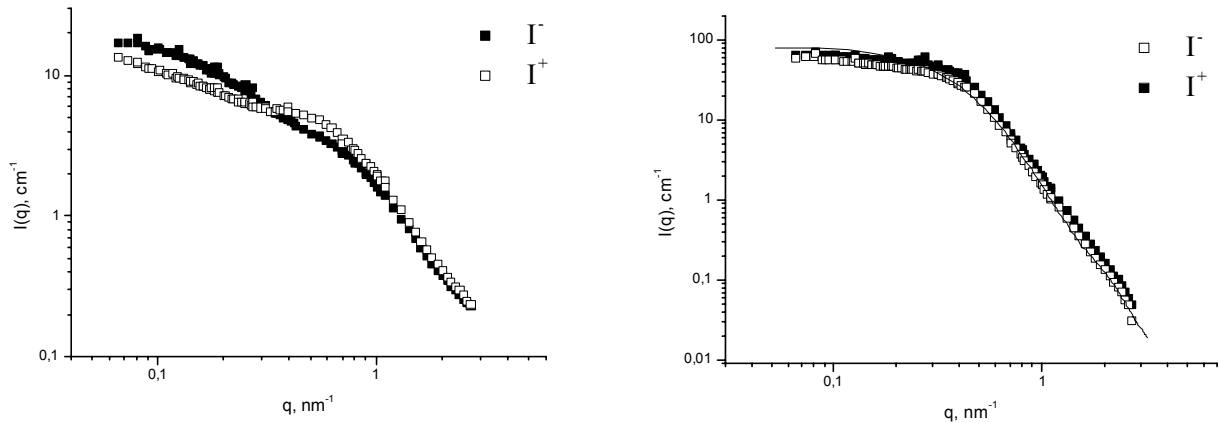


Figure 1: Averaged SANS curves for two polarization states in the case of d-benzene- (Left) and h-benzene- (Right) based ferrofluids; solid line at the right graph corresponds to the modelling curve according to the core-shell model.

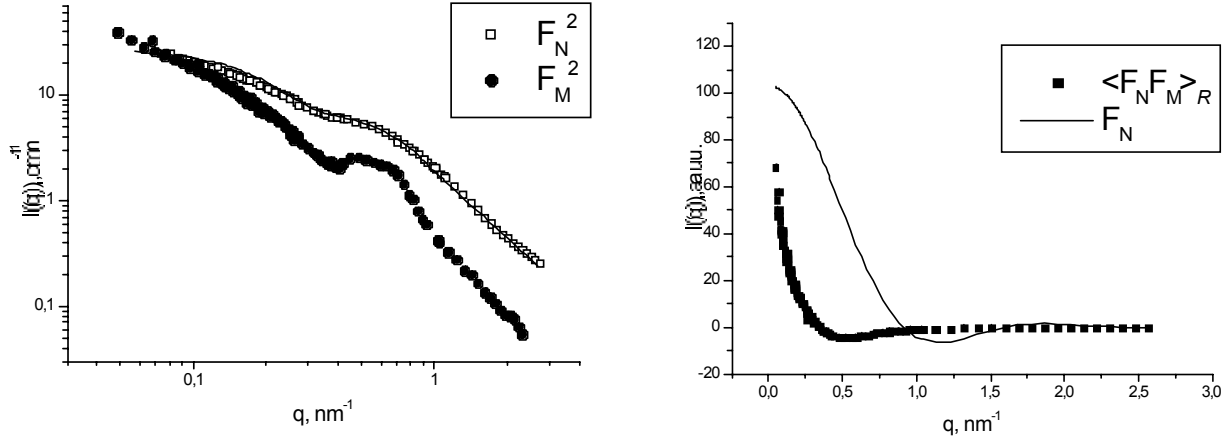



Figure 2. Left: separated nuclear and magnetic scattering; solid line corresponds to the model curve calculated by core-shell model. Right: nuclear-magnetic cross term and nuclear scattering amplitude according to the core-shell model (monodisperse case, $R = 4.2$ nm).

References

- [1] Proc. of the 8th International Conference on Magnetic Fluids, J. Magn. Magn. Mater. 201 (1999).
- [2] M.V. Avdeev, M. Balasoiu, D. Bica, L. Rosta, Gy.Torok, L.Vekas, Materials Science Forum, 373-376, 457 (2001)
- [3] M.V. Avdeev, M. Balasoiu, D. Bica, L. Rosta, Gy. Torok, V.L.A ksenov, L.Vekas, J. Mag. Mag. Materials, 252, 86 (2002)
- [4] V.L. Aksenov, M.V. Avdeev, M. Balasoiu, L. Rosta, Gy. Torok, L. Vekas, D. Bica, V.M. Garamus, J.Kohlbrecher, Applied Physics A, 74/7-8 (2002), to appear.
- [5] A. Wiedenmann, J. Appl. Cryst., 33, 428 (2000)
- [6] D. Bica, Rom. Repts. in Phys., 47, 265 (1995)
- [7] L.A. Akselrod, G.P. Gordeev, G.M. Drabkin, I.M. Lazebnik, V.T. Lebedev, JETP, 91, 531 (1986)

	EXPERIMENTAL REPORT	GeNF SANS-1
Phase behaviour of the dilute DDAB/C₁₂E₈/water system		
Principal Proposer:	E. Feitosa, ^{1,*} ¹ Physical Chemistry 1, Center of Chemistry and Chemical Engineering, University of Lund, Lund, Sweden; [*] Permanent address: IBILCE/UNESP, São José do Rio Preto, SP, Brazil	
Experimental Team:	A. Khan, ¹ V. Haramus, ² B. Lindman ¹ ² GKSS Research Centre	
Date(s) of Experiment:	November 2002	

Summary

We have investigated the phase behavior of didodecyldimethylammonium bromide/octa-ethyleneglycol mono n-dodecyl ether/water (DDAB/ C₁₂E₈/water) up to 97 wt.% water and 3 wt.% total surfactant concentration by small angle neutron scattering (SANS), crossed polaroids (CP) and differential scanning calorimetry (DSC) The addition of DDAB to C₁₂E₈/water stabilizes the micellar phase up to ca 50 % of each surfactant (C₁₂E₈/DDAB = 1), ie., half the ternary phase diagram consists of isotropic micellar solution (Region I). At higher DDAB (smaller C₁₂E₈) concentrations, within C₁₂E₈/DDAB ≈ 0.3 and 1, vesicles are formed and phase separates, with the bottom phase being bluish indicating the presence of unilamellar vesicles, whereas the top phase is milky containing probably multilamellar vesicle structures (Region II). Between C₁₂E₈/DDAB ≈ 0–0.3, lamellar structures dominate and the solutions are birefringent (Region III).

Experimental

Didodecyldimethylammonium bromide, DDAB (Tokyo Kasei Kogyo Co. Ltd., Tokyo, Japan), and octa-ethyleneglycol mono n-dodecyl ether, C₁₂E₈ (Nikko Chemicals Co. Ltd., Tokyo, Japan) were used as received. All samples were prepared by simply weighing the compounds in cylindrical glass flasks at the right amount and kept continuously mixing in a mechanical mixer for around one week. All samples were prepared using heavy water for the SANS measurements.

Results

The ternary phase diagram for the DDAB/C₁₂E₈/D₂O for surfactant composition up to 3.0 wt. indicates three regions I, II and III, respectively for micelle, vesicle and lamellar phases. In Region III, at very low surfactant concentrations, however, vesicle structures dominate the phase area. Micellar region I occupies half the phase diagram. Straight lines from the water corner to C₁₂E₈/DDAB = 0.5 and 0.3 give the borders of these phases. Figure 1 shows typical SANS curves for DDAB/C₁₂E₈/D₂O in Regions I and III, characteristic of micelle solution and vesicle dispersions, respectively, indicating that the structure of the association colloids in solution is clearly a function of surfactant composition. The SANS curves for samples in the

two-phase region (Region II) are similar to those in Region III (not shown). A more detailed analyses of the SANS data will take into account strong electrostatic interaction between aggregates in the case of vesicle dispersions and charged micelles.

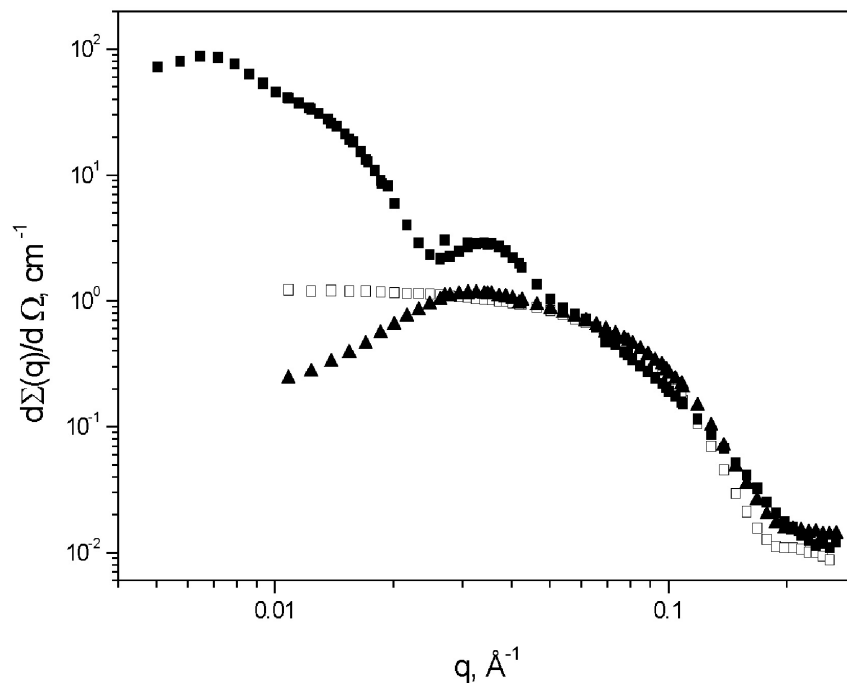



Figure 1: Scattering intensities from different region of phase diagram: Region III – vesicle dispersions (filled squares), Region I – non-charged micelles solution (empty squares) and charged micelles solution (triangles). Total surfactant concentration is 0.5 wt.% (25 °C).

	EXPERIMENTAL REPORT	GeNF SANS-1
A SANS study of micelles formed by mixtures of a cationic fluorinated surfactant and a cationic hydrocarbon surfactant		
Principal Proposer:	M. Kadi ¹ ¹ Department of Physical Chemistry, Uppsala University, Uppsala, Sweden	
Experimental Team:	M. Bergström ² , V. Haramus ³ , P. Hansson ⁴ , M. Almgren ¹ ² Department of Chemistry, Surface Chemistry, Royal Institute of Technology, Stockholm, Sweden and YKI, Institute for Surface Chemistry, Stockholm, Sweden, ³ GKSS Research Centre, ⁴ Department of Pharmacy, Uppsala Biomedical Center, Uppsala, Sweden	
Date(s) of Experiment:	November 2002	

We have investigated mixtures of the cationic fluorocarbon surfactant HFDePC (N-(1,1,2,2-tetrahydroperfluorodecanyl)pyridinium chloride) with the cationic hydrocarbon surfactant CTAC (cetyltrimethylammonium chloride) at different concentrations and compositions in the presence of 100 mM NaCl using small-angle neutron scattering. We have earlier investigated this mixture by a number of different techniques including NMR diffusion measurements and time resolved fluorescence quenching. These earlier results indicated, which has also been observed for other fluorocarbon-hydrocarbon surfactant mixtures, that the two surfactants form two different kinds of micelles, hydrocarbon rich and fluorocarbon rich. In the present study we used refractive index matching to make one of the two surfactants invisible for the beam. If two different micelle-types coexist in the solution, we should be able to observe them separately.

The mixtures have been investigated at different molar compositions at three different total surfactant concentrations: 0.5 wt.%, 2 wt.% and 12 wt.%. The D₂O/H₂O ratios used were $X(D_2O) = 1$, where both surfactants are visible, $X(D_2O) = 0.67$ where only the hydrocarbon surfactants can be observed and at $X(D_2O) = 0.05$ where the fluorinated surfactant is visible. The scattering intensity as a function of the scattering vector for three different samples at a total surfactant concentration of 2 wt.% are shown in Fig. 1.

It seems clear that at the highest surfactant concentration investigated here, 12 wt.%, separate micelles are formed by the two surfactants, large micelles rich in fluorinated surfactant and smaller micelles richer in hydrocarbon surfactants. At this concentration there is a better maximum at intermediate q -range for $X(D_2O)=1$ than for $X(D_2O)=0.67$ and there is also an increased scattering at lower q -values with $X(D_2O)=0.67$.

The results at lower total surfactant concentrations are not easily interpreted without a more detailed analysis of the data. They can be interpreted either as a coexistence of two different populations of micelles or as mixed micelles with some shell or layer structure.

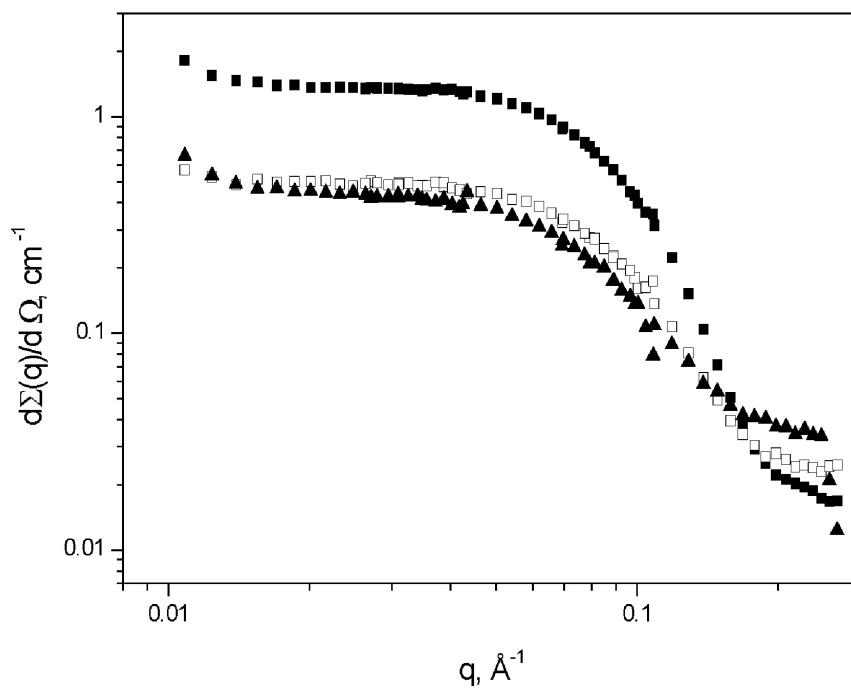



Figure 1: Scattering intensities as a function of scattering vector q for samples with a total surfactant concentration of 2 wt.% and a molar ratio of CTAC of 0.5 at $X(\text{D}_2\text{O}) = 1$ (filled squares), 0.67 (empty squares) and 0.05 (filled triangles). All samples contained 100 mM NaCl.

	EXPERIMENTAL REPORT	GeNF SANS-1
Investigation of the three dimensional micro-phase separation and crystallisation of multi block copolymers by means of small-angle neutron scattering		
Principal Proposer: H. Kamusewitz ¹ ¹ GKSS Research Centre Experimental Team: R. Willumeit ¹ , V. Haramus ¹ Date(s) of Experiment: September – December 2002		

Recently, characterisation and fabrication of nano-structures have attracted much attention in various fields of polymer application. Memory shaped polymers use the spontaneous phase separation between chain sequences of different chemical nature and the specific crystallisation in ordered micro-domain morphologies at different temperatures. The multi block copolymer Poly(p-dioxanon)-Poly(ϵ -caprolacton) segregates into the dioxanon- and the caprolacton-phase with different molecular order. The temperature dependence of the crystallisation properties of the caprolacton-phase becomes important because it controls the shape memory behaviour. Responsible for the switching process is the melting temperature region around 42 °C and important for the programming procedure is the temperature rearrangement of the caprolacton-crystals and -spherulites around 20 °C measured by differential scanning calorimetry (DSC; NETZSCH). In addition the first and the second heating process show different melting behaviour.

SANS-experiments should help to examine the crystal morphologies of the whole polymeric system especially the crystallisation behaviour of the caprolacton-phase as function of temperature.

Results

The scattering data were collected for different temperatures from 25 to 60 °C by heating and cooling. Two such heating-cooling cycles were performed.

Typical scattering curve (Fig. 1) of multi block copolymer Poly(p-dioxanon)-Poly(ϵ -caprolacton) exhibits two power-law regions $d\Sigma(q)/d\Omega \sim q^{-\alpha}$: $\alpha \sim 2.5$ for low $q < 0.01 \text{ \AA}^{-1}$ and $\alpha \sim 3.5$ for high $q > 0.05 \text{ \AA}^{-1}$; and a crossover region with almost Guinier behaviour $d\Sigma(q)/d\Omega \sim \exp(-q^2 R_g^2/3)$ for $0.01 < q < 0.05$. It points on the presence of aggregates with different scale lengths and morphology.

As temperature increases (Fig. 1), the main changes are observed at the crossover region, i.e., scattering shifts to larger q values. We have applied Indirect Fourier Transformation method to high q ($q > 0.02 \text{ \AA}^{-1}$) part of scattering curves. Obtained radius of gyration (R_g) is $69 \pm 1 \text{ \AA}$ (25 °C) and is $62 \pm 1 \text{ \AA}$ (60 °C), that could be connected with partial melting of smaller aggregates. Hysteresis of structural changes varying temperature has been observed for 1st heating-cooling cycle, however for 2nd one – not.

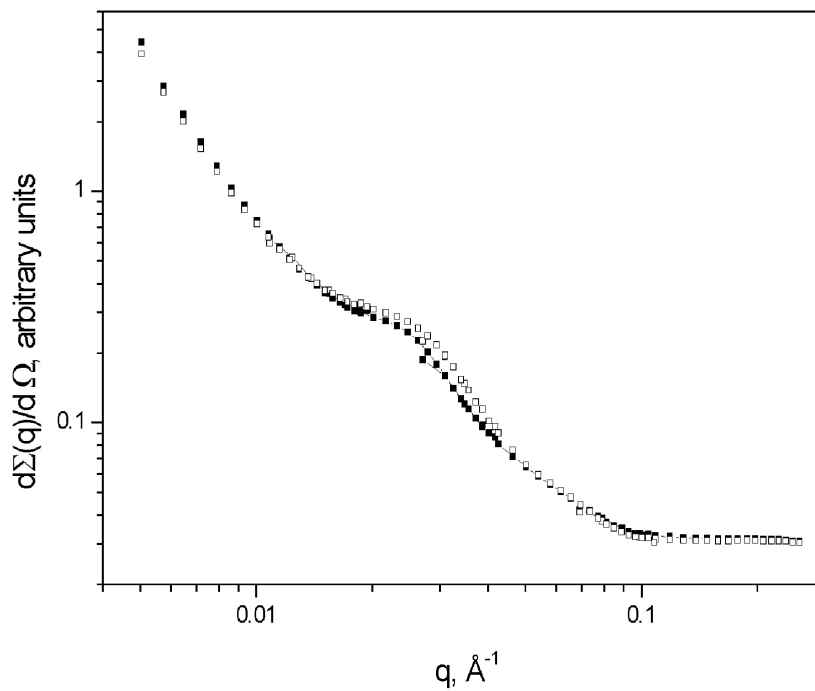



Figure 1: Scattering data for multi block copolymer Poly(p-dioxanon)-Poly(ϵ -caprolacton) sample with varying temperature (filled symbols 25 °C and empty ones 60 °C).

	EXPERIMENTAL REPORT	GeNF SANS-1
Wormlike block copolymer micelles		
Principal Proposer:	M. Konrad ¹ University of Hamburg, Institute for Physical Chemistry, Hamburg, Germany	
Experimental Team:	V. Haramus, ² S. Förster ¹ ² GKSS Research Centre	
Date(s) of Experiment:	November – December 2002	

Dispersions containing wormlike surfactant aggregates exhibit interesting properties which can be compared to the behaviour of polymer solutions [1]. Most known examples of surfactants forming wormlike micelles are of the ionic type. In such systems structural parameters like the persistence and contour length are strongly dependent on the type and nature of the counter ion and excess salt. Nevertheless, there are also nonionic surfactants of the alkyl poly(ethylene oxide) ether type capable of forming cylindrical micelles in water [2]. As such systems contain no other added substances and electrostatical effects can be neglected, these dispersions are excellent model systems for the statics and dynamics of wormlike micelles. Poly(ethylene oxide) containing block copolymers [3] are structurally related, e.g. poly(butadiene-*b*-ethylene oxide). Among them there are also examples which form wormlike micelles with a core shell structure of the cross section. Here the core is built by the hydrophobic blocks of the aggregating polymers and the shell consists of the poly(ethylene oxide) blocks.

In our case we investigated three different butadiene ethylene oxide block copolymers (PB₂₇-PEO₅₁, PB₄₃-PEO₆₀, PB₁₄₇-PEO₂₀₅) and one polymer with poly(ethyl ethylene) as the hydrophobic block (PEE₃₉-PEO₁₀₂) in water. All polymers have polydispersities below 1.1. We tried to take a look at the behaviour at different temperatures and we were also interested in the semi concentrated regime (about 10 wt.%) as an addition to rheo-SANS experiments made at ILL/Grenoble [4].

We tested two different temperatures (10 °C and 25 °C) on polymer solutions of 1wt.%. The results for one of the polymers (PB₂₇-PEO₅₁) are shown in Fig. 1. The scattering curves of the different temperatures exhibit only slight differences in the high *q* range. This may be attributed to increased thermal fluctuations at higher temperatures. Both curves have a characteristic -1 slope in the low *q* range, which is expected for cylindrical objects. There is no change of the slope to zero in the experimentally accessible low *q* range. So the length of the micelles must be rather high, as can also be shown with transmission electron microscopy. Analysis in the middle region including the oscillation provides values for the core and total radius of the wormlike micelles (6.0 and 11.0 nm respectively in the case of PB₂₇-PEO₅₁).

There is strong evidence that the wormlike micelles form a lyotropic nematic phase at concentrations of about 10 wt.% (Fig. 2). These liquid crystal like nematic structures show a lack of long range order (as would be the case for typical lyotropic mesophases) but are determined by a short range order caused by parallel alignment of cylinders or worms; actually the 2D scattering patterns of our samples have a pronounced anisotropy indicating parallel alignment in a preferred orientation over a wide area. In order to analyse the isotropic scattering curves of the nematic phases (yielded after averaging), we tried a Percus-Yevick type structure factor which describes the short-range interaction of particles caused by the increased concentration. In the strict sense, the model is only valid for spherical objects.

Nevertheless the agreement with the experimental data of our wormlike systems is quite satisfactory. The inter particle effect causes a suppression of the intensity at low q values and thus a marked deviation from the slope of dilute dispersions.

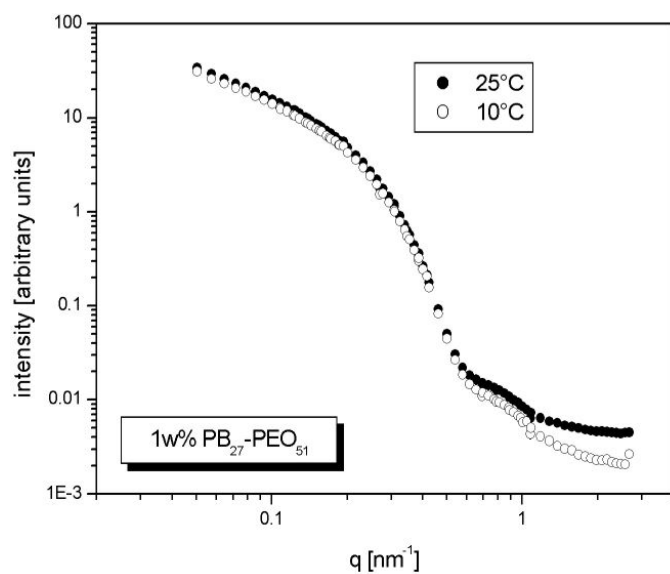


Figure 1:

1 wt.% solution of worm-like block copolymer micelles at different temperatures.

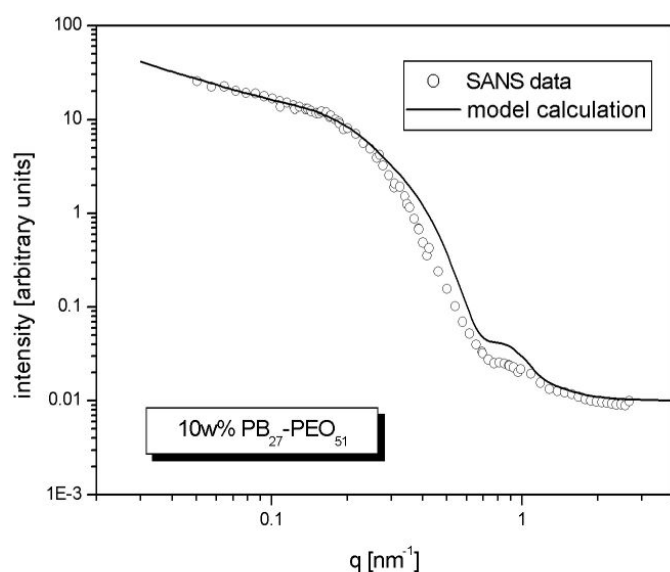



Figure 2:

10 wt.% solution. Experimental data and model calculation.

References

- [1] M. E. Cates, S. J. Candau, *J. Phys. Condens. Matter* 1990, 2, 6869–6892
- [2] D. J. Mitchell, G. J. T. Tiddy, L. Waring, T. Bostok, M. P. McDonald, *J. chem. Soc. Faraday Trans. I* 1983 79, 975–1000
- [3] K. Mortensen, *Colloids and Surfaces A* 2001, 277–292
- [4] S. Förster, M. Konrad, P. Lindner, *to be published*.

	EXPERIMENTAL REPORT	GeNF SANS-1
Reversible micelle – vesicle conversion of oleyldimethylamine oxide		
Principal Proposer:	Hiroshi Maeda ¹ ¹ Department of Chemistry, Faculty of Science, Kyushu University, Fukuoka, Japan	
Experimental Team:	Hideya Kawasaki ¹ , Mats Almgren ² ² Department of Physical Chemistry, Uppsala University, Uppsala, Sweden	
Date(s) of Experiment:	July 2002	

Surfactants can form various self-assemblies in dilute aqueous solutions including micelles, vesicles and bilayers and various liquid crystalline phases in the concentrated regime. Among them, vesicles are important mainly because of their wide application in biology and medicine as model cell membranes as well as their potential as drug carriers and other encapsulating agents of industrial relevance. In recent years, various systems including single-chain amphiphiles have been reported to form vesicles and these results are summarized in review articles [1–4]. From the standpoint of the application as carriers of various substances, it will be important and also interesting to control the formation/destruction of vesicles by a physical perturbation in reversible manner.

Recently, the first report on the reversible micelle – vesicle conversion by changing pH has appeared [5]. Oleyldimethylamine oxide (OleylDMAO) in water at 25 °C forms micelles at low degrees of ionization (α) (pH > 6), while it forms vesicles in the range of α around 0.5 (pH ~ 5). The conversion was confirmed by viscoelastic measurements and cryoTEM observations. The correlation between the viscoelastic properties and the cryoTEM observations was good. The viscoelastic changes were confirmed to be reversible with respect to a pH change. The time intervals required for the solutions to recover the vesicle behavior at $\alpha = 0.5$ after the addition of HCl to the solutions of $\alpha = 0$ were about twenty-five hours at 0.05 mol (kg water)⁻¹ and 14 days at 0.15 mol (kg water)⁻¹. It was suggested from the viscoelastic properties that the long threadlike micelles grew further with α at $\alpha = 0.2$. Micelles and vesicles were found to coexist at $\alpha = 0.5$. On increasing the concentration at $\alpha = 0.5$, the vesicles became perforated, probably due to the increased counterion concentration. Many other vesicles become perforated on dilution due probably to enhanced undulation motion.

A characteristic and also interesting aspect of the vesicle formation of OleylDMAO resides in the effect of electric charges on the structure change. Generally, introduction of charges makes the mean curvature of the structure greater due to electric repulsion. In the case of OleylDMAO, however, the introduction of charge induces a change from micelles to vesicles, a decrease of the mean curvature by charging up the aggregates. This is quite unusual. The ionization of OleylDMAO is coupled with the protonation of amine oxide group. A short-range attractive interaction should be introduced between the head groups of OleylDMAO in couple with this protonation process in order to make the packing parameter greater. A hydrogen bond between the nonprotonated and protonated head groups has been suggested for this short-range attraction. Recent infrared spectroscopic results support the suggested hydrogen bond [6]. The structure of the formed vesicles has been characterized only by TEM observations and the viscoelastic properties. Further study by means of the scattering technique (SANS) to elucidate the vesicle structure is highly demanded.

Two sets of experiments were performed: a) varying the concentration of OleyDMAO($\alpha = 0$) from 1.6 to 15.5 mg/mL and b) OleyDMAO($\alpha = 0.5$) from 1.7 to 49.7 mg/mL. OleyDMAO ($\alpha = 0$) exhibits the characteristic scattering of non-charged polymer-like micelles (Figure 1). Indirect Fourier Transformation analysis of high q -range of scattering curves gives the radius gyration of cross section of polymer-like micelles as $15.0 \pm 0.2 \text{ \AA}$.

OleyDMAO($\alpha = 0.5$) shows more complicate scattering with significant interaction among aggregates (Figure 1). Analysis of position of interference maximum points on the transition in the system from spherical micelles to rod-like or vesicles aggregates. Further analysis will be performed with taking into account electrostatic interaction among aggregates and different aggregate shapes.

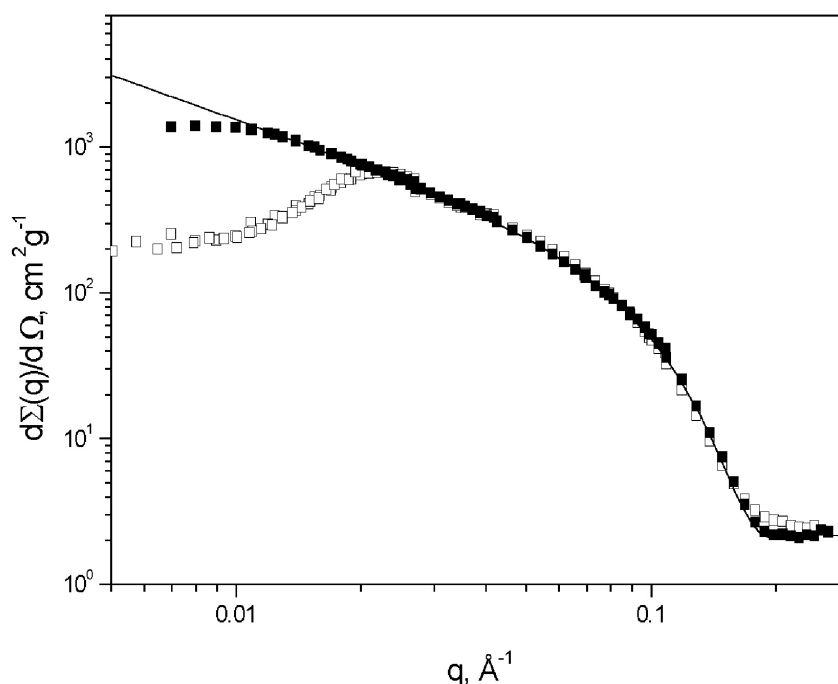



Figure 1: SANS data 6.6 mg/mL of OleyDMAO($\alpha = 0$) – solid symbols, 6.8 mg/mL of OleyDMAO($\alpha = 0.5$) – empty symbols and Indirect Fourier Transformation analysis fit – solid line. Solvent heavy water and $T= 25 \text{ }^\circ\text{C}$.

References

- [1] Engberts, J.; B.F.N, Kevelam, J. *Current Opinion Colloid Interface Sci.*, 1996, 1, 779
- [2] Khan, A.; Marques, E. F. *Current Opinion Colloid Interface Sci.*, 2000, 4, 402
- [3] Lasic, D. D. et al., *Adv. Colloid Interface Sci.*, 2001, 89-90, 337–349
- [4] Tondre, C.; Caillet, C., *Adv. Colloid Interface Sci.*, 2001, 93, 115–134
- [5] Kawasaki, H., Souda, M., Tanaka, S., Nemoto, N., Karlsson, G., Almgren M., Maeda, H., *J. Phys. Chem. B.* 2002, 106, 1524–1527
- [6] Kawasaki, H., and Maeda, H., *Langmuir*, 2001, 17, 2278–2281

	EXPERIMENTAL REPORT	GeNF SANS-1
Characterisation of hyperbranched polymers with SANS		
Principal Proposer:	T. Maksimova ¹ ¹ University of Kiel, Institute of Physical Chemistry, Kiel, Germany	
Experimental Team:	W. Richtering ¹ , S. Mecking ² , U. Schlitterbeck ² , L. Antonietti ² ² Institute for Makromolekular Chemistry, Albert-Ludvigs-University Freiburg, Germany	
Date(s) of Experiment:	May – December 2002	

Hyperbranched polymers are a relatively new type of highly branched materials, which – in contrast to dendrimers – often are prepared via a one-step synthesis [1]. Their molecular architecture is not as well-defined as for dendrimers and their molecular mass distribution is not monodisperse, giving rise to different properties. Controlling the molecular architecture of dendrimers is crucial for their intended use in applications such as drug delivery, biocides, gene transfer, catalyst supports and processing aids. [1–3] The molecular conformation in solution, which controls efficiency in such applications, has been the subject of theory and experiment. [2]. In order to analyze the correlation between the nanostructure of hyperbranched polymer and its function as a scaffold for further syntheses we performed neutron scattering experiments.

We investigated Polyethylene Imines different with a systematically varied molecular weight and degree of esterification with/without silver nanoparticles. The samples were synthesized in Institute for Makromolekular Chemistry, Albert-Ludvigs-University Freiburg. As solvent we used C₆D₆. The concentration of solutions was from 0.5 wt.% to 4 wt.%. The neutron wavelength was 8.1 Å with 10 % of wave length resolution. The range of scattering vectors ($0.005 < q < 0.25 \text{ \AA}^{-1}$) was obtained using four sample-to-detector distances (0.7–9.7 m). The samples were measured at 25 °C in quartz cuvettes with a path length of 1–2 mm.

Figure 1 shows the q dependence of measured neutron scattering intensity divided by concentration of hyperbranched polyethylene imines and core in C₆D₆ for polyethylene imines, CDCl₃ for core solutions by different concentration. At all curves there are at low q a typical Guinier behavior originating from the overall size of polymers. The radius of gyration (R_G) of polymers were obtained from the Guinier approximation eq. 1.

$$I(q) = I_0 \exp(-q^2 R_G^2 / 3), \quad (1),$$

where $I(q)$ is the scatter intensity, q – the wavevector, defined as $q = (4\pi/\lambda)\sin(\theta/2)$, with λ the wave length of the incident beam (the neutrons) and θ the scattering angle; $\langle s^2 \rangle$ is average size of particles (polymer).

The calculated R_G via eq. 1 for hyperbranched polyethylene imines with different degree of esterification (45 % and 90 %) in C₆D₆ are given in Table 1. As can be directly seen, R_G doesn't depend on the degree of esterification but decrease by increase in concentration of solution.

In Table 2 shows the calculated R_G via eq.1 for hyperbranched polyethylene with $AgNO_3$ and silver nanoparticles in C_6D_6 . If compare R_G for polymer without metal and R_G for their with their can be seen that R_G weren't practically changed.

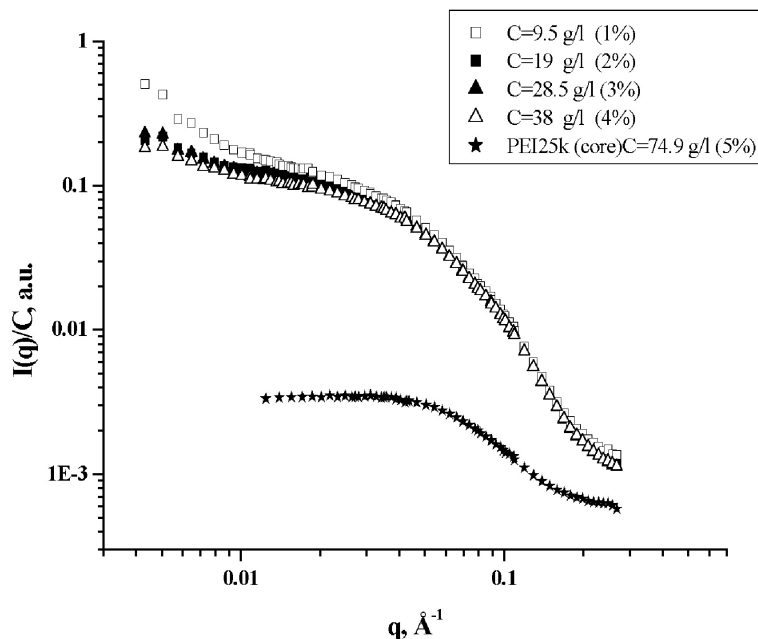
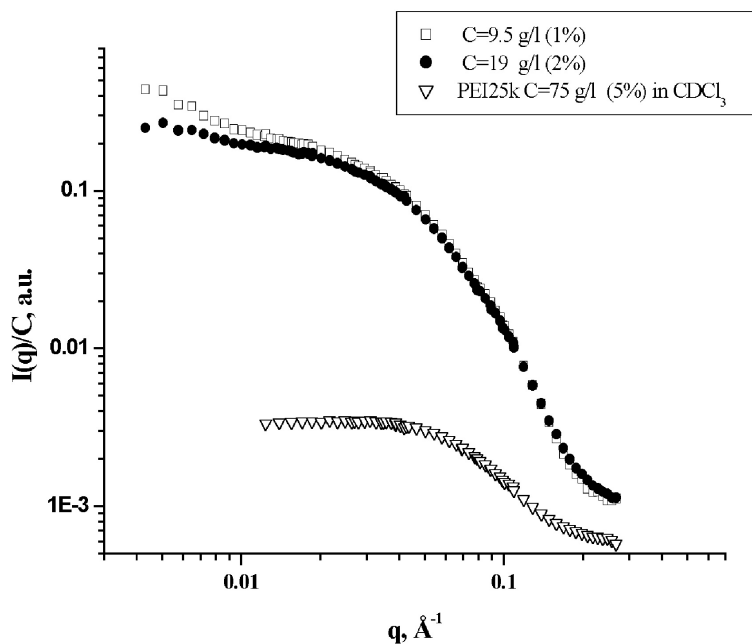


Figure 1:

Scattering curves of hyperbranched PEI25k/Am^{lin}C16 45 % for different concentration in C_6D_6 and $CDCl_3$ for core;



Scattering curves of hyperbranched PEI25k/Am^{lin}C16 90 % for different concentration in C_6D_6 and $CDCl_3$ for core, $T=25\pm 1 \text{ }^\circ\text{C}$.

Table 1: The Radius of Gyration for the Polyethylene Imines obtained by application of the Guinier's approximation.


<i>Sample</i>	<i>Degree of derivatisation</i>	<i>Kind of derivatisation</i>	<i>Solvent</i>	<i>C, g/l</i>	<i>R_G (Guinier)</i>
PEI25k/Am ^{lin} C16	45 %	C16	C ₆ D ₆	9.5	5.2±0.3 nm
PEI25k/Am ^{lin} C16	45 %	C16	C ₆ D ₆	19	5.0±0.3 nm
PEI25k/Am ^{lin} C16	45 %	C16	C ₆ D ₆	28.5	4.7±0.2 nm
PEI25k/Am ^{lin} C16	45 %	C16	C ₆ D ₆	38	4.6±0.2 nm
PEI25k/Am ^{lin} C16	90 %	C16	C ₆ D ₆	9.5	5.1±0.2 nm
PEI25k/Am ^{lin} C16	90 %	C16	C ₆ D ₆	19	4.6±0.2 nm
PEI25k	-	core	CDCl ₃	74.9	1.1±0.2 nm

Table 2: The Radius of Gyration for the Polyethylene Imines with/without metals obtained by application of the Guinier's approximation.

<i>Sample</i>	<i>Degree of derivatisation</i>	<i>Kind of Derivatisation</i>	<i>Solvent</i>	<i>R_G (Guinier)</i>
PEI5k/Am ^{lin} C16	45 %	C16	C ₆ D ₆	3.0 ± 0.2 nm
PEI5k/Am ^{lin} C16 + AgNO ₃	45 %	C16	C ₆ D ₆	3.2 ± 0.1 nm
PEI25k/Am ^{lin} C16 + Ag nanoparticles	45 %	C16	C ₆ D ₆	3.1 ± 0.2 nm

References

- [1] Frechet, J. M. J.; Hawker, C. J.; Gitsov, I.; Leon, J. W. *Pure Appl. Chem.* 1996. A33, 1399
- [2] Tande, B. M.; Wagner, N. J.; Mackay, M. E.; Hawker, C. J.; Jeong, M. *Macromolecules* 2001, 34, 8550
- [3] Schild, H. G.; *Prog. Polym. Sci.*, 1992, Vol. 17, p. 163

	EXPERIMENTAL REPORT	GeNF SANS-1
A SANS study of micelles formed by Pluronic triblock copolymers P84 and P94 in D₂O		
Principal Proposer:	J. S. Pedersen ¹ ¹ Department of Chemistry, University of Aarhus, Denmark	
Experimental Team:	C. Sommer ¹ , V. Haramus ² ² GKSS Research Centre	
Date(s) of Experiment:	October 2002	

The micelles of the Pluronic triblock copolymer P85 in water are probably the polymeric micelles, which have been most extensively studied by the small-angle scattering techniques [1]. P85 is like the P94 block copolymer a poly(ethylene oxide)-poly(propylene oxide)-poly(ethylene oxide) (PEO-PPO-PEO) polymer. The compositions of P85 and P94 are EO₂₅PO₄₀EO₂₅ and EO₁₇PO₄₂EO₁₇, respectively. The solvent quality of water for the PPO changes markedly as the temperature is increased and water becomes a poor solvent at around 25 °C. The solvent quality of water for the PEO changes also with temperature, however, the theta temperature is only reached at around 110 °C. The temperature dependence of the solvent quality leads to the formation of spherical micelles at around 20-25 °C, which coexist with individually dissolved molecules up to around 35-40 °C; above this temperature only micelles are present. The PPO constitutes the micellar cores, whereas the PEO chains make up a solvated corona around the cores. Due to the change in solvent quality of the PEO chains, the spontaneous curvature of the PPO-PEO interface changes upon increasing the temperature further and this leads to a change in the shape of the micelles, so that they gradually becomes cylindrical.

We are currently in several studies of micellar systems combining SAXS and SANS experiments in order to increase the available information content in the scattering data so that a higher resolution structure can be determined with confidence. The analysis of the data is usually done using an advanced model, based on Monte Carlo simulations [2], where the scattering of both the core and corona is taken into account. The chain-chain interaction in the corona is described by the random phase approximation, and the radial profile of the corona is modelled using a set of three partial cubic b spline functions. The model allows the extraction of extensive quantitative information on the structure of the micelles. Due to the well-characterized general behaviour of P85 and P94, the micelles of these block copolymers are good candidates for testing the modelling approach and it is of course also highly interesting to have reliable structural information on the micelles for these systems, where theoretical calculations have been performed [3]. The systems have already been studied by both SANS and SAXS, however, consistent data sets on the same batch of polymers from both techniques are not available. We have therefore decided to perform such measurements.

For both SANS and SAXS the polymer is dissolved in D₂O. This gives a homogenous contrast for SANS, where the scattering length density of both PEO and PPO have the same

sign. For SAXS the contrast is provided by the excess electron densities with respect to water, which turns out to be negative for PPO and positive for PEO. Therefore a core-shell type contrast is obtained in which there is a sign change at the PPO-PEO interface, so that this interface is easily located. The interpretation and modelling of the SAXS data is very sensitive to the actual values of the electron densities (or equivalently, the partial specific densities) and it is therefore necessary to know these accurately. In our first attempts to model the scattering data we have used values derived from data published in the literature, however, this did not provide good fits to the SAXS data for models that already fitted previously recorded SANS data [1]. The values we have from the literature for the PEO partial specific densities do not agree with our own measurements on similar systems and we will therefore remeasure the partial specific densities before we continue the modelling work.

Two examples of scattering data for 5 wt.% solutions are shown in the Figure 1.

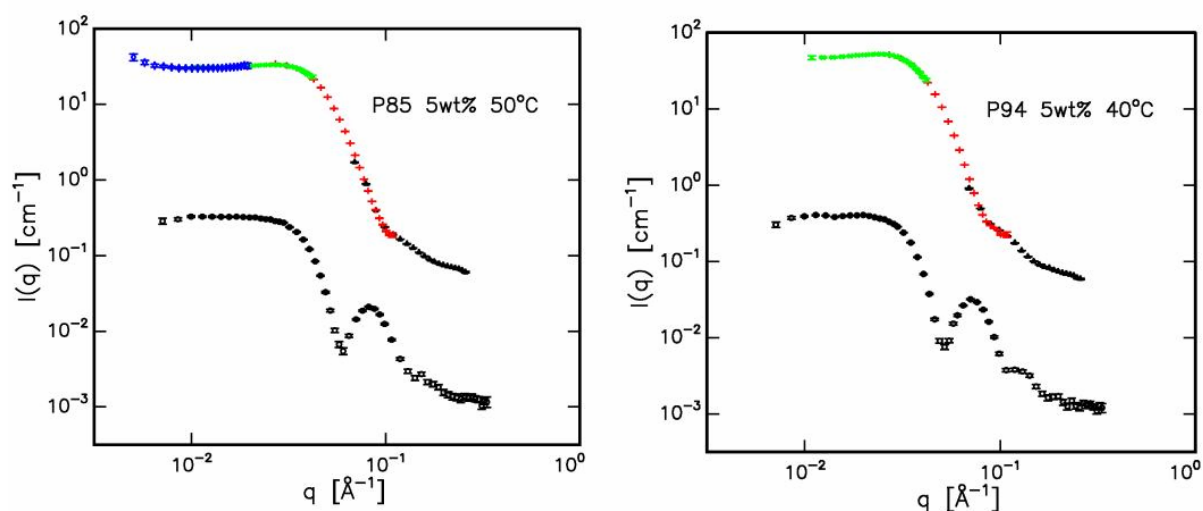



Figure 1: The P85 data (left) have been taken at 50 °C, whereas the data for P94, (right) has been taken at 40 °C, so that both samples are expected to have spherical micelles. The different contrast conditions for PEO and PPO for SANS (upper data sets) and SAXS (lower data sets) lead to markedly different scattering curves. Note that the scattering cross section is two orders of magnitude smaller for SAXS than for SANS.

References

- [1] Jan Skov Pedersen and Michael C. Gerstenberg, *Colloids and Surfaces A*, 2003 (in press) and references therein
- [2] Carsten Svaneborg and Jan Skov Pedersen, *Macromolecules* 2002, 35, 1028
- [3] Jaan Noolandi, An-Chang Shi, and Per Linse, *Macromolecules* 1996, 29, 5907

	EXPERIMENTAL REPORT	GeNF SANS-1
A SANS study of microemulsion droplets decorated by Brij700 block copolymer as a function of droplet concentration, surfactant to oil ratio and surface coverage		
Principal Proposer:	J. S. Pedersen ¹ ¹ Department of Chemistry, University of Aarhus, Denmark	
Experimental Team:	C. Sommer ¹ , V. Haramus ² ² GKSS Research Centre	
Date(s) of Experiment:	June – July 2002	

We have investigated the structure of a microemulsion system composed of four different components: Brij700 block copolymer ($C_{18}E_{100}$), surfactant ($C_{12}E_5$), oil (decane), and water (D_2O). The microemulsion forms droplets with cores of oil surrounded by surfactant and 'decorated' by the long poly(ethylene oxide) (PEO) chains of the Brij molecules. The expected structure of droplets has a corona of dissolved PEO chains attached to the surface of spherical droplets. The system is studied both with SAXS and SANS by varying parameters such as the droplet concentration, the oil-to-surfactant ratio and the coverage density of the droplets with Brij700. The SANS technique allows us to perform contrast variation measurements by using either deuterated (shell contrast) or hydrogenated decane (core contrast) in the core of the particles.

From a theoretical point of view, this system represents an ideal model system for studying interactions in tethered chain systems due to the many parameters that can be varied. Small-angle scattering measurements allow us to extract detailed information on the droplet structure, the corona shape of the E_{100} chains and the interaction between the droplets. The system may also be of practical interest in various industrial products ranging from cosmetic products to pharmaceutical formulations.

The analysis of the data is done using an advanced model, based on Monte Carlo simulations [1], where the scattering of both the core and corona is taken into account. The chain-chain interaction in the corona is modelled using the random phase approximation, and the inter-particle interactions are taken into account by using the structure factor of hard spheres. The radial profile of the corona is modelled using a set of three partial cubic b spline functions. The model allows us to obtain extensive quantitative information on the structure. The main results are the radial density profiles, the strength of the chain-chain interactions, the effective structure factors, and the related parameters.

Qualitative results can rapidly be obtained after evaluation of the SANS curves (Fig. 1). As an example, we show here the sphere-to-rod transition that can be observed when Brij700 is added to the droplets at a surfactant-to-oil ratio of 2. The transition is a result of a change in the spontaneous curvature of the Brij-surfactant film.

A large range of conditions has been investigated both with SAXS and SANS experiments, and the preliminary fits of SAXS data are very encouraging. The simultaneous fitting of SANS and SAXS data is expected to bring quantitative and detailed information on the microstructure and interaction effects under a change of one or several factors.

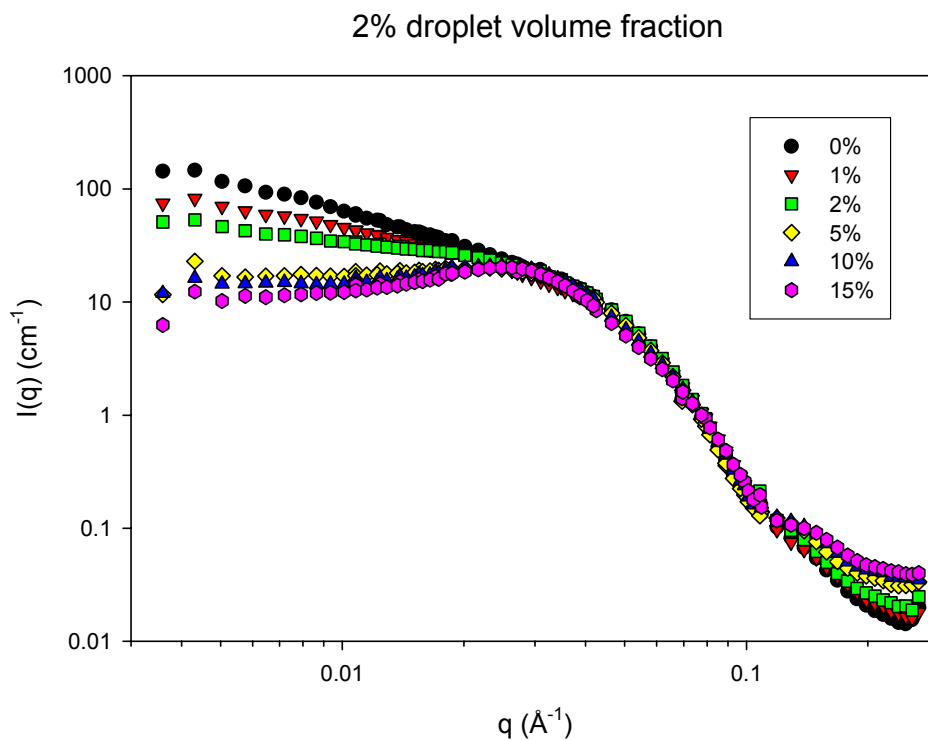



Figure 1: The plot shows curves at a fixed droplet concentration of 2 % and increasing Brij700 amounts, corresponding to 0 to 15 % Brij molecules in the Brij-surfactant film. The black curve is a typical scattering curve for rod-shaped objects, whereas there is clear evidence of a transition to a spherical structure under addition of Brij700 molecules.

Reference

[1] Carsten Svaneborg and Jan Skov Pedersen, *Macromolecules* 35 (2002), 1028

	EXPERIMENTAL REPORT	GeNF SANS-1
A SANS study of micelles formed by Brij700 block copolymer as a function of concentration and temperature		
Principal Proposer:	J. S. Pedersen ¹ ¹ Department of Chemistry, University of Aarhus, Denmark	
Experimental Team:	C. Sommer ¹ , V. Haramus ² ² GKSS Research Centre	
Date(s) of Experiment:	October – November 2002	

The diblock copolymer Brij700 (C₁₈EO₁₀₀), which forms micelles in water, was studied. The micelles are spherical and consist of a hydrophobic core and a corona of poly(ethylene oxide) (PEO) chains in contact with water. SAXS and SANS experiments are combined in order to obtain micro-structural information as a function of concentration and temperature. The change of temperature gives a variation of the solvent quality of water for the PEO chains.

The project is of particular interest from a theoretical point of view: It allows us to study the structure of the micelles, and thus the radial profile of the corona, the interactions between the particles and the related structure factor effects. The system may also be of practical interest since the results could be potentially useful for various industrial products ranging from cosmetic products to pharmaceutical formulations.

The polymer concentration may influence the micellar structure, the size and form of the corona, the typical minimum distance between micelles and the chain-chain interactions. The temperature effect is also highly interesting since the associated change in solvent quality results in changes in the inter-micellar interactions as well as in the chain-chain interactions within the corona.

The analysis of the data is done using an advanced model, based on Monte Carlo simulations [1], where the scattering of both the core and corona is taken into account. The chain-chain interaction in the corona is modelled using the random phase approximation, and the inter-particle interactions are taken into account using the structure factor of hard spheres. The radial profile of the corona is modelled using a set of three partial cubic b spline functions. An important feature of the model is that at high concentration, where coronas from different micelles overlap, a fraction of the PEO chains has to be considered as belonging to the solvent. This has the effect that the solvent scattering length density is modified, which is particularly important when fitting SAXS data from the same system. The model allows us to obtain extensive quantitative information on the structure of the micelles.

The SANS measurements are combined with SAXS experiments on the same samples, and we have recently succeeded in simultaneously fitting both data sets for the Brij700 system at different concentrations and temperature. A plot with a fit is shown in the following Figure 1.

5% Brij700 in D₂O at T=30°C : SANS and SAXS data with fits

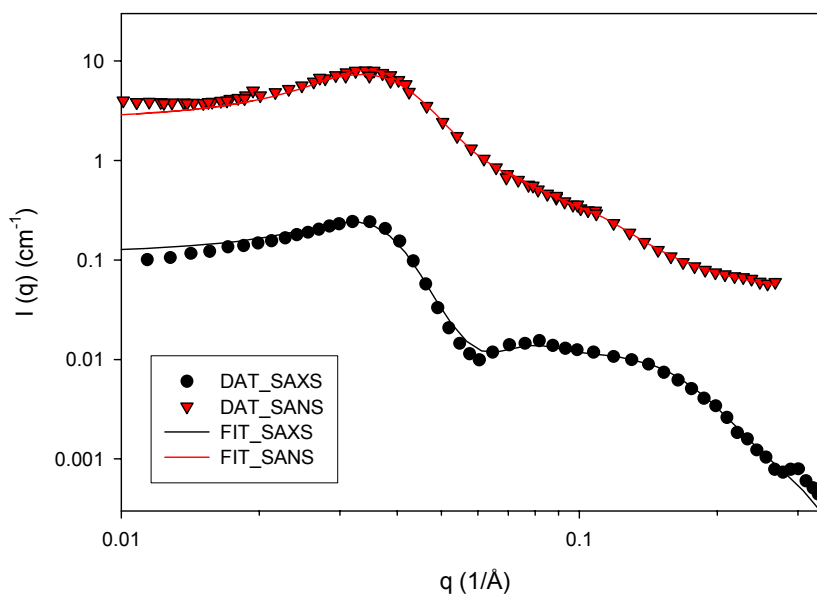


Figure 1: The plot shows a typical set of data with the corresponding fits.


From the fits, we derive radial profiles of the core and corona, as well as effective structure factors $S(q)$ for both SAXS and SANS. The obtained fit results for the parameters of the model can then be plotted as a function of concentration and temperature. The most interesting conclusions so far are the following:

- The width of the corona smoothly decreases when either the concentration or the temperature are increased.
- The hard-sphere volume fraction and radius decreases significantly with increasing temperature as a result of the change of quality of the solvent
- The effective form factor of the chains decreases with increasing concentration but increases with temperature as we come closer and closer to the theta point of the PEO chains.
- The fraction of PEO chain that can be regarded as being part of the solvent becomes non-negligible at concentrations as low as 2 %, and this parameter decreases, as can be expected, when the temperature increases.

These results show the strong effect of concentration and temperature on the chain interactions in the corona and therefore on its structure.

Reference

- [1] Carsten Svaneborg and Jan Skov Pedersen, *Macromolecules* 35 (2002), 1028

	EXPERIMENTAL REPORT	GeNF SANS-1
Characterisation of novel ionomer membranes based on poly(ether ether ketone) and layered materials		
Principal Proposer:	Luis A. S. A. Prado ¹ ¹ Polymer Composites, TUHH, Denickerstrasse 15, D-21073 Hamburg-Harburg, Germany	
Experimental Team:	V. Haramus ² , C. S. Karthikeyan ² , B. Ruffmann ² , S. P. Nunes ² , R. Willumeit ² , K. Schulte ¹ ² GKSS Research Centre	
Date(s) of Experiment:	August 2002	

Sulphonated poly(ether ether ketone), SPEEK, is a good example of hydrocarbon-based polymer having potential applications in fuel-cells [1]. However, multi-component materials based on SPEEK have been found to yield better properties, namely proton conductivity and methanol permeability, when compared to the plain polymer [2]. Layered materials have already proved to decrease the methanol crossover, without decreasing the proton-conductivity [3]. In this work composite membranes based on SPEEK were prepared by the casting process. Layered alpha-zirconium hydrogeno-phosphate, layered silicates, and amorphous zirconium oxide were used as additives in order to obtain desirable properties for fuel-cell applications. The composition of the membranes and some characteristics of the additives are reported in the Table 1.

Table 1: Composition of the membranes investigated (weight percent).

Sample	% polymer	% Additive	Nature of the additive
SPEEK1-ZrO ₂	90	10	Amorphous oxide
SPEEK1-Zr(HPO ₄) ₂	86.5	13.5	Layered Phosphate
SPEEK2-CDI-MG-AS	90	10	Layered Silicate (synthetic)
SPEEK2-MM784	95	5	Layered Silicate (commercial)

SPEEK 1 and SPEEK2 have 40 and 67 % sulphonation degree, respectively. CDI: carbo-diimidazole, MG: magadiite, AS: 3-aminopropyltrimethoxysilane and MM784: organoclay provided by Süd Chemie.

The samples containing zirconium displayed a significant scattering. The reason could be due to the high contrast between the polymeric matrix and inorganic filler. The plot for SPEEK1-ZrO₂ shows a correlation peak with a maximum at $q = 0.036 \text{ \AA}^{-1}$ (which corresponds to the correlation distance of 174 Å) (see figure 1). The size of the zirconium oxide particles, which was found to be 45 Å, was calculated from the partial volume of the oxide in the membrane. Taking into account that the zirconium oxide particles cannot penetrate each other, one can assume a distribution of oxide particles in the size range of 45–87 Å. This value was about 10 times higher than found by ASAXS measurements of the same membrane. Since, ASAXS is much more selective and no peak was observed in the ASAXS curve of this sample at $q = 0.036 \text{ \AA}^{-1}$, one can assume that this peak comes from some organisation of the polymer chain in order to accommodate the oxide particles. This can explain the decrease in the conductivity of the membranes, if excess of zirconium oxide particles is generated in the polymer matrix.

On the other hand, the SPEEK1-Zr(HPO₄)₂ does not show a correlation peak, but a well-defined upturn. Data were modelled by Indirect Fourier transformation (IFT) method. The value of the radius of gyration determined was 125 Å. A similar value was found using the Guinier approximation. At this point, we acknowledge the possibility of higher aggregates that cannot be identified in the q -range of our measurements. For instance, in the SPEEK1-Zr(HPO₄)₂ membrane, we know from our own experience that the particle size should be bigger than 125 Å. The fact that both Guinier's approximation and IFT method gave similar values indicating that these values may describe the reality. Probably, these values reflect small or primary particles of the phosphate.

The membranes based on SPEEK2 and layered silicates did not exhibit good scattering patterns. The curves of the SPEEK2-CDI-MG-AS and SPEEK2-MM784 membranes were analysed in the same manner as SPEEK1-Zr(HPO₄)₂ and the values of the radius of gyration are 130.8 and 132.5 Å, respectively. This indicates a good dispersion of the silicate sheets in the polymeric matrix. In the case of SPEEK2-CDI-MG-AS, CDI, was added to the polymer solution in order to promote partial cross-linking in the polymer matrix. Moreover, 3-aminopropyltrimethoxysilane, AS, was used to improve the compatibility between the magadiite and the SPEEK2. By this approach, an organically modified silicate was obtained *in situ* by a reaction between the silane and the ≡SiOH groups of the silicate. Such modification did not bring much difference in comparison to a commercial silicate.

It is important to mention that the composite SPEEK membranes did not show the so-called "ionomer peak". Moreover, the neutron scattering could not be detected for the plain SPEEK membrane. These differences in the morphology may contribute to the relatively low conductivity of SPEEK-membranes.

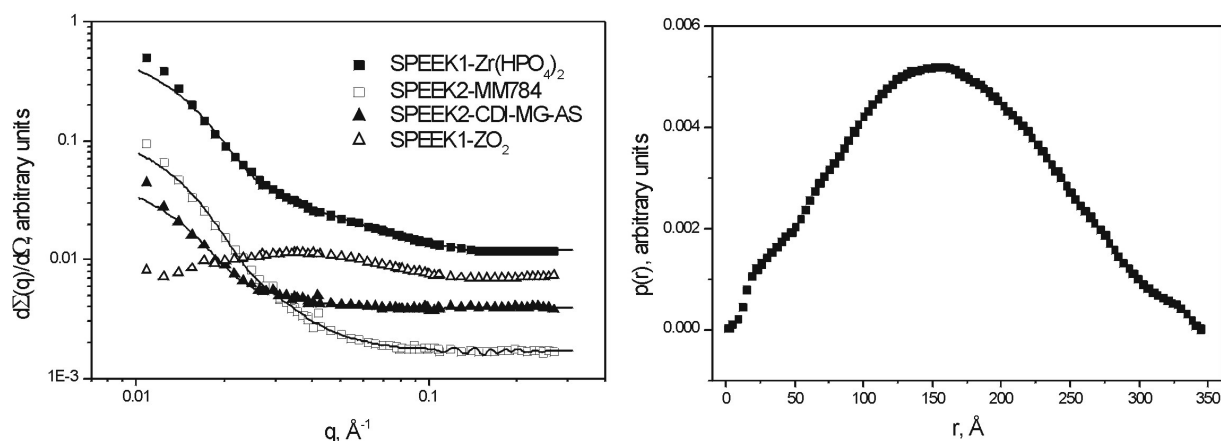



Figure 1: (left) SANS plots for the SPEEK based membranes and model fits – solid lines; (right) the shape of the pair distribution functions of SPEEK2-Zr(HPO₄)₂ membrane, obtained by inverse Fourier-transform of the SANS plot.

References

- [1] Alberti G, Casciola M, Massinelli L, Bauer B J. *Memb. Sci.* 185 (1), 73-81 (2001)
- [2] Nunes, S. P., Ruffmann, B., Rikowski, E., Vetter, S. and Richau, K. J. *Memb. Sci.*, 203, 215 (2002)
- [3] Karthikeyan, C. S., Schossig, M., Ruffmann, B., Schulte, K. and Nunes, S. P., "Novel Ionomeric membranes with layered silicates", *Proceedings in International Conference on Solid State Protonic Conductors, Univeristy of Surrey, Guildford, UK, August, 2002*

	EXPERIMENTAL REPORT	GeNF SANS-1
Sol-gel derived hybrid polysaccharide-silica nanocomposites		
Principal Proposer:	Yurii A. Shchipunov Institute of Chemistry, Far East Department, Russian Academy of Sciences, 690022 Vladivostok, Russia	
Date(s) of Experiment:	December 2002	

Scientific Objective

Nanocomposites produced by the sol-gel techniques are considered as a promising approach for the synthesis of a variety of materials suitable for diversified applications including glasses, ceramics, aerogels, biocomposites, biocatalysts, etc. [1] Biopolymers are introduced to influence the structure of silica nanocomposites and mimicking biomineralization processes. A new route has been developed in Institute of Chemistry (Vladivostok) for preparing hybrid materials by using natural polysaccharides [2].

The approach is based on the hydrolyses of a tetraalkoxysilane (precursor). It happens after its dissolution in an aqueous solution of biopolymer. A produced silicic acid is involved into the following polycondensation reactions that leads first to the formation of colloidal particles (sol) of nano-size dimension and then to their cross-linking into a three-dimensional network in the bulk solution. This is accompanied by a jellification of the system that provides the sol-gel transition. We found out that the silica synthesis can be controlled by polysaccharides. They play a role of a template for inorganic compound generated *in situ*. It was also established that polysaccharides can provide an about ten-fold reduction of the critical concentration at which the silica gel starts forming a monolith.

The aim of this study was to examine the structural features of diluted hybrid polysaccharide-silica nanocomposites with the help of the small-angle neutron scattering (SANS) technique.

Experimental Technique

Alginate was obtained from Fluka AG. It was used as received. A precursor of silica was prepared as suggested in [3]. Hybrid materials were synthesised in accordance with the following procedure. Weighted amount of polysaccharide was dissolved in deuterated water and left for an equilibration for 1 day. The precursor was added in the solution of polysaccharide, stirred to have a homogeneous mixture and then left at the ambient temperature. The gel settled within 10–180 min that depended on the concentrations of both polysaccharide and precursor.

Small-angle neutron scattering experiments were performed with the SANS-1 instrument at the FRG-1 research reactor of GKSS Research Centre. The neutron wavelength was 8.5 Å. The range of scattering vectors ($0.008 < q < 0.25 \text{ \AA}^{-1}$) was obtained using four sample-to-detector distances (0.7–7 m). The wavelength resolution was 10 % (fwhm). The samples were kept at $25 \pm 1 \text{ }^\circ\text{C}$ in quartz cells with a path length of 2 mm.

Results

A set of hybrid materials with various polysaccharides have been prepared for examination. It was found that the biopolymers occur a notable effect on their properties and structural organization. The silica generated *in situ* stabilized the polymer structure in solution, increasing the contrast. As a result, a notable grow in the neutron scattering was observed that made the poorly detected polysaccharides convenient for studying by the SANS technique.

SANS data are presented in Figure 1. Silica was prepared in solution with 0.2 wt.% of alginate. The concentration of precursor was 2 wt.%. SANS data were analysed by Indirect Fourier Transformation (model independent approach). The obtained radius of gyration is $120 \pm 3 \text{ \AA}$.

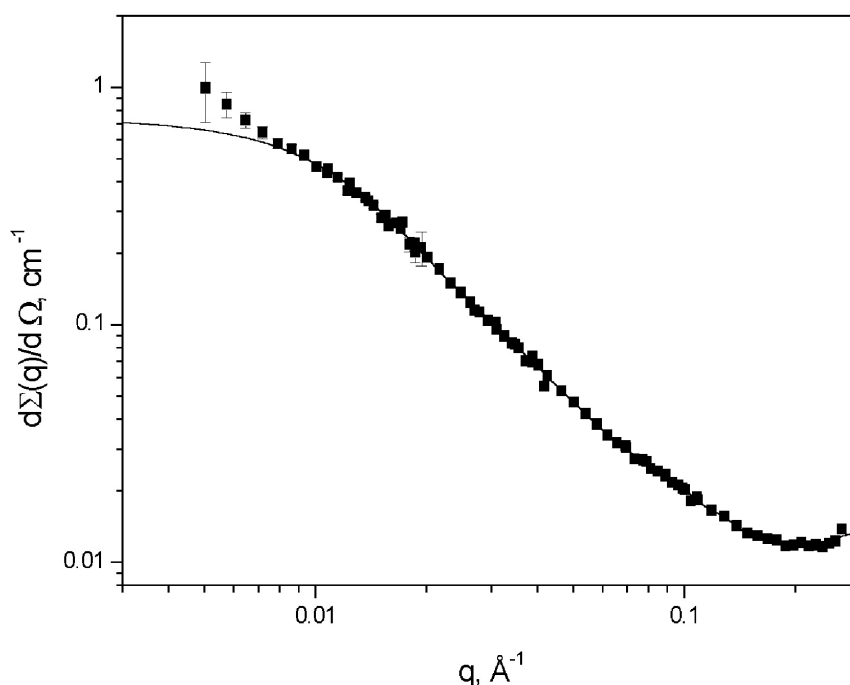



Figure 1: SANS pattern from a solution containing 0.2 wt.% of polysaccharide and 2 wt.% of hydrolysed silica precursor and fit curve obtained by Indirect Fourier Transformation method (solid line).

References

- [1] Pierre AC: Introduction to sol-gel processing. Boston: Kluwer; 1998
- [2] Shchipunov YuA, Karpenko TYu. Hybrid silica-polysaccharide materials prepared by the sol-gel processing. Ed. by Maestro P, Roux D. 72. 2002. Bristol, University of Bristol. In: In: Proc. The 2nd Intern. Rhodia Conf. "Physical Chemistry of polymeric systems". 2002
- [3] Meyer M, Fischer A, Hoffmann H. J. Phys. Chem.B. 2002, 106: 1528–1533

	EXPERIMENTAL REPORT	GeNF SANS-1
Fractal properties of humic substances revealed from neutron scattering and synchrotron X-ray scattering studies		
Principal Proposer:	A. Timchenko ¹ ¹ Institute of Protein Research, Pushchino, Moscow Region, Russia	
Experimental Team:	I. N. Serdyuk ¹ , R. Willumeit ² , V. Haramus ² , H. Kihara ³ , R. Oberthur ⁴ ² GKSS Research Centre; ³ Physics Laboratory, Kansai Medical University Uyamahigashi, Hirakata Osaka 593, Japan ⁴ Labor Dr. Oberthur, Bawinkel, Germany	
Date(s) of Experiment:	June – July 2002	

Introduction

It is generally accepted that humic substances play a crucial role in aquatic and terrestrial environments and have a great influence on crop production. At the same time it is known that appreciable amounts of humic substances are accumulated in various environments, e.g. in lignite (brown coal) which was formed 20 to 60 million years ago, in peat, formed about 5 to 10 thousand years ago, in some natural soils like the chernozem of the steppes of Ukraine or in some man made soils, fertilized with organic matter, formed at least since medieval time, like the plaggenesch in Northern Germany and bordering areas of the Netherlands or, more recently in composted organic matter, where the humic acids (HA) are formed within less than a month.

Despite the fact that the study of HA has more than 200 years of history until now the structure of humic acids is not known in detail. The main reasons are the following:

- 1) HA are physically and chemically heterogeneous mixtures whose typically characteristics are the absence of a repeating structural organization and an intrinsic lack of order at the molecular level
- 2) HA have amphipatic character, they bind both hydrophilic and hydrophobic compounds, including metal ions, organic compounds.
- 3) These substances are characterized by a wide interval of size and shapes which depends on the procedure of isolation of HA.

The main goal of our study was the systematic comparison of physico-chemical properties of humic substances prepared from these different sources using small angle scattering methods. Here the results for HA from budetorf are represented.

Experimental

The samples are obtained by extraction of the organic material from the original source with 0.2 M ammonium hydroxide, subsequent microfiltration to remove large particles (>500 nm) and dialysis to remove low molecular weight compounds (<10 000 dalton) and eventually freeze or spray drying of the thus obtained solutions. The samples were analysed in 0.1 M NaOH dissolved in light and heavy water at concentrations not exceeding 1 % where the humic substances are well dissolved. Neutron scattering experiments were performed using

the SANS-1 instrument of the GKSS Research Centre as described earlier [1]. Synchrotron X-ray measurements were done on a small-angle camera BL-15A (Photon Factory, Tsukuba) [2]. Data treatment of neutron scattering experiments were made by our modified version of RI program with cut off for low statistics. Analogous data treatment for X-ray data were carried out by SAXSTIM program.

Results

To characterise such irregular systems as HA the methods of fractal geometry [3] have been used. In application to scattering data they are based on the study of asymptotic behaviour of scattering patterns at large scattering angles. The log-log dependence of scattered intensity on the scattering vector module has a long linear part whose slope is connected to the fractal dimension of the object. Fig.1 (left) represents such plot for neutron scattering data. The slope here is 2.64. Fig.1 (right) presents X-ray scattering data for the same object in heavy water. Here the slope is 1.65 (approximately such incline is also observed for the sample in light water). Thus, the neutron and X-ray scattering patterns give different fractal dimension. Moreover, the behaviour of scattering patterns at large scattering angles ($Q > 0.1 \text{ \AA}^{-1}$, where $Q = (4\pi/\lambda)\sin(\theta/2)$, λ - the wavelength, θ - scattering angle) for neutron and X-ray scattering is also different: concave for neutrons and convex for X-ray scattering. The latter observation can be partly explained by the availability of incoherent background. Such background can be easily calculated from the sample content. In our case we evaluated this background for aminoacids and corresponding scattering curve is presented in Fig.1. It was concluded that for dry substances with known content the sample should be dissolved in heavy water without dialysis and then incoherent background can be easily taken into account. The former observation is most likely due to nonuniform H-D exchange, thus, scattering pattern reflects not only conformational fractal nature but the fractal nature of H-D distribution. It gives additional information for HA conformation. We are going to study this phenomenon more detailed. Authors express their gratitude to W. Müller for technical assistance.

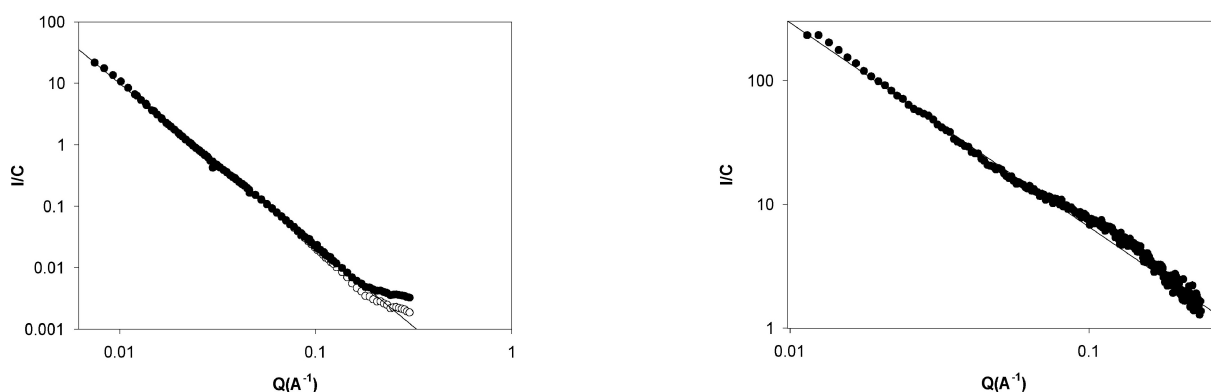



Figure 1: (Left) Log-log dependence of neutron scattering pattern for TB1a (budetorf) sample of HA (full circles) in 0.1M NaOD. Slope is 2.64. Empty circles for the scattering pattern with incoherent background subtraction. (Right) Log-log dependence of X-ray scattering pattern for TB1a (budetorf) sample of HA in 0.1M NaOD. Slope is 1.65.

References

- [1]. Zhao, J. & Stuhrmann, H.B. (1993), *J. de Physique*, 3, 233–236.
- [2]. Amemiya Y. et al. (1983) *Nucl. Instr. Methods*, 208, 471–477.
- [3]. Rice J.A. & Lin J.-S. (1993) *Environ. Sci. Technol.*, 27, 413–414.

	EXPERIMENTAL REPORT	GeNF SANS-1
Structures of block copolymer solutions		
Principal Proposer:	A. Timmann, ^{1,*} ¹ University of Hamburg, Institute for Physical Chemistry, Hamburg, Germany	
Experimental Team:	V. Haramus, ² S. Förster ¹ ² GKSS Research Centre	
Date(s) of Experiment:	October, December 2002	

In aqueous solutions, amphiphilic block copolymers consisting of a hydrophobic and a hydrophilic polymer block form vesicles with a bilayer of block copolymers similar to cell membranes. They also form spherical or cylindrical micelles with a hydrophobic micellar core and a water-swollen micellar shell. These structures are not only interesting in their own right, but are used in materials science for pharmaceutical applications and for the preparation of nanostructured materials such as semiconductors, noble metals, and mesoporous ceramics [1].

Our aim is to find out the structure that is formed in aqueous solution. Structural information can be obtained from the slope of the scattering curve at low q . If there is a q^{-n} -law, then the "n" is the dimension of the structure. For $n = 1$ there is a linear structure e.g. cylindrical micelles. For $n = 2$ there is a planar geometry e.g. the bilayer of a vesicle.

We investigated two amphiphilic poly(isoprene-*b*-ethyleneoxide) (PI-PEO) block copolymers with the degree of polymerisation PI88-PEO81 (PI-PEO-a) for the first polymer and PI100-PEO200 for the second block copolymer (PI-PEO-b).

SANS experiments were carried out at the SANS1 instrument at the FRG1 research reactor of GKSS. The range of scattering vectors ($0.005 < q < 0.25 \text{ \AA}^{-1}$) was covered by four combinations of and sample-to-detector distances (0.7–9.0 m) The neutron wavelength was $\lambda = 8.1 \text{ \AA}$ with a resolution of 10 % (fwhm).

Solutions of block copolymers in D_2O at a concentration of 1 wt.% (PI-PEO-a) and 0.5 % (PI-PEO-b) were kept in quartz cells with a path length of 1 and 2 mm. The raw spectra were corrected for backgrounds from the solvent, sample cell, and other sources by conventional procedures. The two-dimensional isotropic scattering spectra were azimuthally averaged and corrected for detector efficiency. The results are shown in Fig. 1 for the two different block copolymers.

We have found that the PI-PEO-a shows clearly a slope of q^{-2} characteristic for a planar geometry. We were able to approve by light microscopy that this polymer forms vesicles. The oscillation at $q = 0.05 \text{ \AA}^{-1}$ corresponds to a thickness of the bilayer of 62 \AA . For the PI-PEO-b there appears to be a gradient of q^{-1} which would be an indicator for cylindrical micelles with a radius of 160 \AA . Further measurements to resolve the exact structure are in progress. These micelles and vesicles are investigated with aspect to take up and release of hydrophobic drugs.

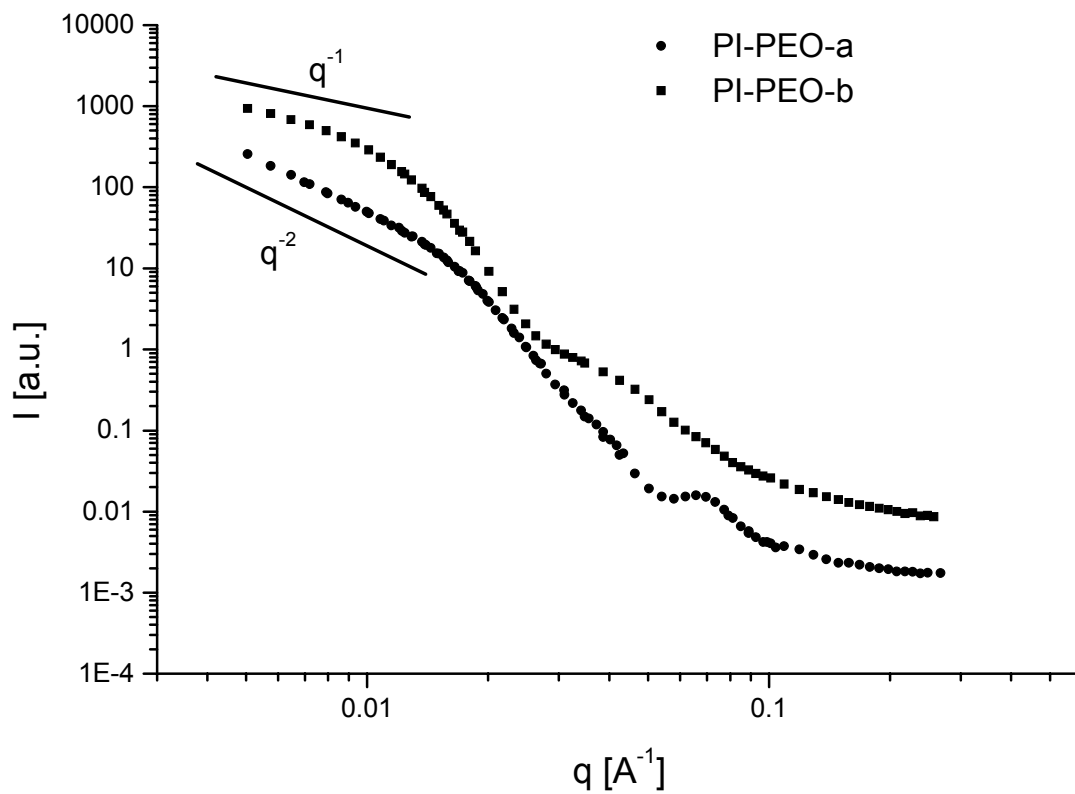



Figure 1: SANS-Data of the two block copolymers.

Reference

[1] S. Förster, T. Plantenberg, *Angew. Chem. Int. Ed.* 41. 688 (2002)

	EXPERIMENTAL REPORT	GeNF SANS-1
A SANS study of the concentration and temperature effects on micelles of n-nonyl-β-D-glucoside and n-tetradecyl-β-D-maltoside		
Principal Proposer:	S. Ulvenlund AstraZeneca R&D, Lund, Sweden	
Experimental Team:	C. Ericsson Department of Physical Chemistry 1, Lund University, Sweden	
Date(s) of Experiment:	August–September 2002	

The purpose of this study was to investigate how the micellar structure of alkylglycosides in aqueous solution is affected by temperature and concentration. We have focused on n-nonyl- β -D-glucoside (β -C₉G₁) and n-tetradecyl- β -D-maltoside (β -C₁₄G₂). According to previous dynamic light scattering (DLS) measurements, the hydrodynamic diameter of β -C₉G₁ decreases with temperature between 10 °C and 70 °C, while it increases for β -C₁₄G₂. For the latter surfactant, the micelle size seems to reach a maximum around 70°C. In interpreting the data, it should be borne in mind that the Krafft temperature for β -C₁₄G₂ is 31.8 °C (as determined by differential scanning calorimetry, DSC) and, consequently, that solutions below that temperature are not thermodynamically stable. The deuterium isotope effect on the micellar size has also been investigated with DLS and it was observed that a substitution of D₂O for H₂O causes a large increase in micelle size for both surfactants.

The DLS data reveals how the hydrodynamic diameter is affected by temperature but not how the actual micelle morphology changes. The SANS study was performed to confirm the DLS results and to extract data on micelle morphology and the mechanism of micelle growth. It seems that the cross section diameter is unaffected by temperature for 10 mg/ml β -C₉G₁. Furthermore, the micelles decrease in length when the temperature is increasing from 20 °C to 50 °C (Fig. 1). This is in accordance with the DLS measurements and clearly suggests a formation of threadlike micelles that grow one-dimensionally.

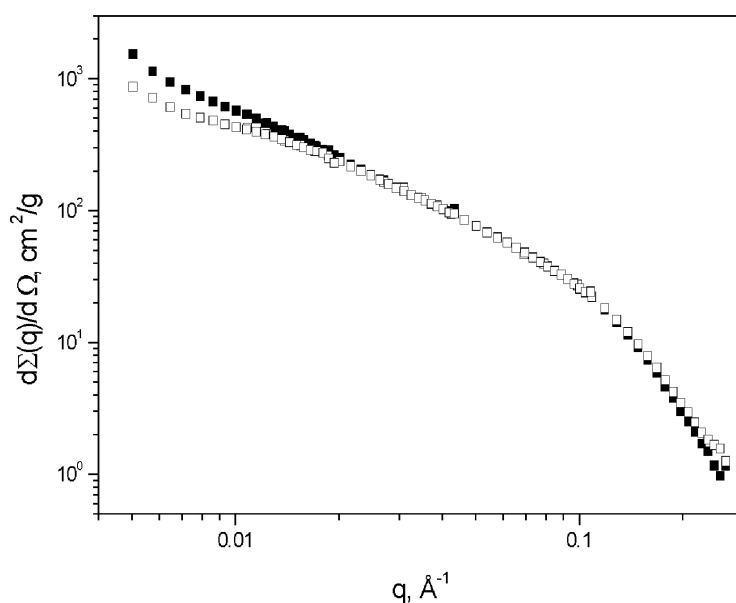



Figure 1: Normalised scattering intensity (cm^2/g) as a function of scattering vector q (\AA^{-1}) for 10 mg/ml β -C₉G₁ at 20 °C (filled symbols) and 50 °C (empty symbols). The scattering data were concentration normalised by dividing the intensity by (c-CMC).

According to DLS and turbidity measurements, there is a pronounced increase in micelle size with temperature for β -C₁₄G₂, but this effect is not observed with SANS. A possible explanation is that the accessible q range is insufficient to determine the overall size of the micelles. If the temperature only affects the length of very long and/or branched micelles this effect would not be possible to detect in the present SANS data.

In the SANS data no concentration dependence was observed between 10 mg/ml and 50 mg/ml for either of the surfactants. In contrast, the DLS measurements reveal an increase in size with concentration for both the surfactants. The same argument could be used to rationalise the lack of concentration dependence as for the lack of temperature effect on β -C₁₄G₂. The further data analysis will be done by polymer-like micelle approach [1].

Reference

- [1] Jerke, G.; Pedersen, J.S.; Egelhaaf, S. U.; Schurtenberger, P. *Phys. Rev. E.* 1997, 56, 5772.

	EXPERIMENTAL REPORT	GeNF SANS-2
Small-angle scattering instrument SANS-2		

Short Instrument Description:

Small angle neutron scattering using cold non-polarised/polarised neutrons is a powerful tool for investigating the structure of matter in the range between 1 and 100 nm. It is a non destructive method for a wide range of application in:

- Metal physics (precipitates, clusters, interfaces, grain boundaries,...)
- Materials science (defects, porosity,...)
- Nanocrystalline materials (grain size, magnetic structures,...)
- Polymers and polymer systems (blends, mixtures, structure and morphology,...)
- Biology (viruses, proteins,...)
- Complex liquids (microemulsions, colloids, liquid crystals,...)

Local Contacts:

Helmut Eckerlebe

Phone/Fax : +49 (0)4152 87-1202 / +49 (0)4152 87-1338

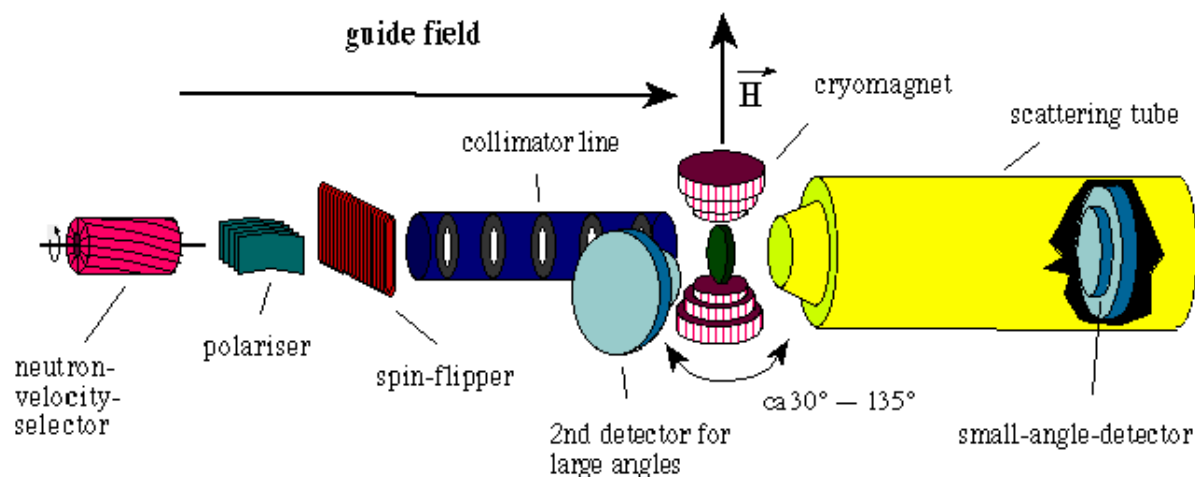
e-mail: helmut.eckerlebe@gkss.de

Dr. P. Klaus Pranzas

Phone/Fax : +49 (0)4152 87-1326 / +49 (0)4152 87-1338


e-mail: pranzas@gkss.de

Schematic View of SANS-2:



Instrument Details:

Beamline:	beamline 8 – cold neutron guide NG-2, radius of curvature $R = 900$ m, cross section 3×4 cm ²
Monochromator:	helical slot velocity selector (Dornier)
Wavelength range at sample position:	0.3 to 2.0 nm
Wavelength resolution:	$\Delta\lambda/\lambda = 0.1$ (2 additional velocity selectors with $\Delta\lambda/\lambda = 0.05$ and 0.2 available)
Length of collimation:	max. 16 m (2 m elements)
Flux at sample position:	$\Phi_{\max} = 2 \cdot 10^7$ cm ⁻² s ⁻¹ (1 m collimation, $\lambda = 0.5$ nm)
Range of momentum transfer:	$0.01 \leq q \leq 3$ nm ⁻¹ (small-angle scattering) $q \leq 25$ nm ⁻¹ (wide-angle scattering with 2. detector)
Distance sample to detector:	1.0 m $\leq d \leq 22$ m optional 2. detector for wide angles: $d = 1$ m
Detector:	2-dim position-sensitive ³ He-counter
active area:	55 x 55 cm ²
resolution:	0.7 x 0.7 cm ²
background:	4 cps
Supplementary equipment:	<ul style="list-style-type: none"> – several electro-magnets up to 2.0 T (horizontal and vertical fields) – superconducting magnet up to 5.0 T – cryostats (2–300 K) – furnace (-30 °C to +400 °C, atmospheric condition, inert gas and vacuum) – linear translation, rotary and lift tables (freely programmable sample position) – “HOLONS”: holographic combined with SANS setup (see table A)
Special features:	<ul style="list-style-type: none"> – Sample environment space is variable from a few mm up to 2500 mm – User-friendly software for data reduction and evaluation running on PC (SANDRA a. o.)

	EXPERIMENTAL REPORT	GeNF SANS-2
SANS investigation of SiO₂ nanoclusters in different solutions		
Principal Proposer:	J. Adam ¹ , H. Eckerlebe ² ¹ HANSE CHEMIE GmbH, Geesthacht, ² GKSS Research Centre	
Experimental Team:	H. Eckerlebe ²	
Date(s) of Experiment:	April 2002	

Scientific Objective

Nanoscaled particles play an important role in various fields, e. g. as pigments and filler material in paints, coatings, castings, pottery or insulating materials. Using nanoscaled inorganic fillers new products can be developed and product properties can be optimized. In addition to particle size, the degree of agglomeration has an important influence on the properties of new materials. Small-angle neutron scattering has been applied for the analysis of size and shape of nanoscaled SiO₂ particles in different organic solvents.

Experiment

Four samples with 5 % SiO₂ referred to as H1,H3,H5,H7 in different organic solutions and one sample with 40 % SiO₂ in water (H8) filled in quartz cells (Suprasil from Hellma, 1 mm flight path) were measured at the SANS-2 facility. The mean neutron wavelength was $\lambda = 0.57$ nm ($\Delta\lambda/\lambda=0.2$). The range of the scattering vector ($0,01 \text{ nm}^{-1} < q < 2,5 \text{ nm}^{-1}$) was covered by 4 detector-sample distances (1 m, 3 m, 9 m, 21 m) with appropriate collimations. The scattered neutrons were detected by a position sensitive detector with 128x128 pixels. Measured intensities were corrected for sample transmissions, background and detector efficiency. The absolute cross section was calculated by comparison with the incoherent scattering of vanadium.

Results

To obtain the scattering pattern of the SiO₂ particles, the differences of the scattering spectra of the samples and the corresponding solvents were calculated. The scattering behaviour of the samples is compared in Fig. 1. All scattering spectra show an isotropic scattering pattern, thus the data were averaged over azimuthal scattering angle. Sample H8 shows an interference peak due to the high concentration of SiO₂ particles. At large scattering angles ($q > 0.5 \text{ nm}^{-1}$) the scattering curves of all samples decrease with q^{-4} . This is an indication for the existence of homogeneous particles with sharp boundaries. The cluster size distribution and the distribution of the volume fraction resp. is shown in Figures 2 and 3. The best fit for these calculations was obtained by assuming spherical particles. The broad particle size distribution of the samples H5 and H7 reveals the agglomeration of SiO₂ particles. Especially in sample H7 about 50 % of the total quantity of SiO₂ formed agglomerates of sizes > 15 nm (Fig. 3). In contrast to this, the size distribution of the sample H1 and H8 are narrow, almost

no SiO₂ particles agglomerated. The mean radius of a SiO₂ particle in the samples H1, H3 and H5 is approx. 8 nm, whereas in the samples H7 and H8 it is about 4 nm and 12 nm respectively.

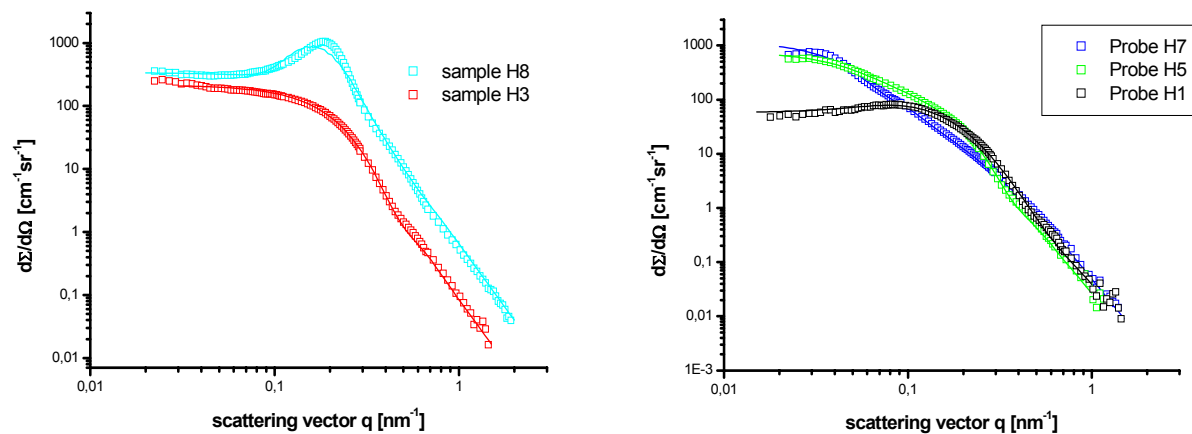


Figure 1a+b: Scattering curves of the samples H3, H8 and H1, H5, H7 (measurements: open squares, calculated fit: solid).

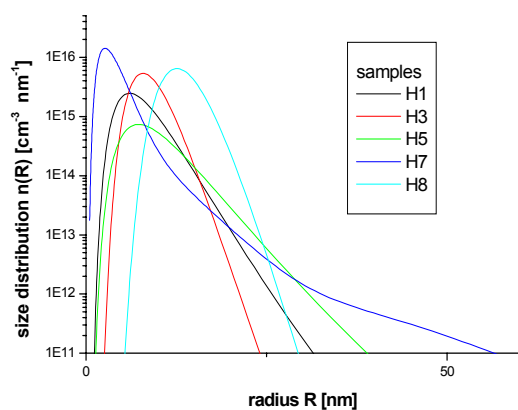


Figure 2: Particle size distributions assuming spherical SiO₂ particles.

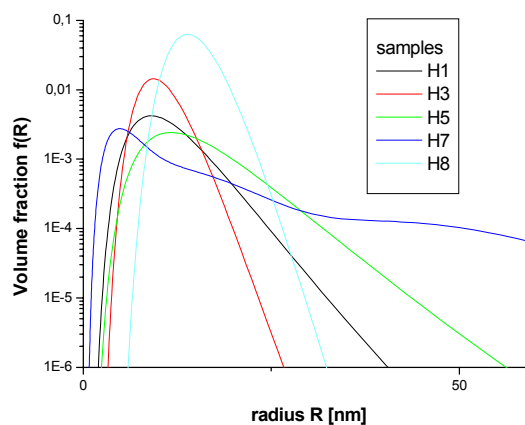


Figure 3: Distributions of the volume fraction f .

	EXPERIMENTAL REPORT	GeNF SANS-2
Continuation of the study of the crystalline quality of large bismuth single crystals		
Principal Proposer:	L. Dohmen, J. Thelen, B. Alefeld, K. Fischer ¹ ¹ Forschungszentrum Jülich GmbH	
Experimental Team:	H. Eckerlebe, J. Vollbrandt, G. Kozik ² ² GKSS Research Centre	
Date(s) of Experiment:	29.10.–01.11.2002	

Scientific Objective

The scientific objective of this work is partly the same as that of measurements in June of this year at the same instrument at the GKSS, where the crystalline quality of large Bi-single crystals was studied. The crystals, grown by K.Fischer in Jülich, showed quite different transmission spectra and reflectivities [1]. This time, the homogeneity of large crystals ($\approx 10 \times 10 \times 10 \text{ cm}^3$) was studied by measuring the transmission spectra for the same orientation at different positions of the crystal. In addition the influence of the azimuthal orientation of two crystals on the transmitted intensity was studied. With other words, if two crystals are oriented with the (111)-planes perpendicular to the neutron beam, there remains a degree of freedom about the direction of the neutron beam. This angle is called azimuthal angle. The axis perpendicular to the (111)-planes has threefold symmetry. If a dependence of the transmitted intensity on this angle exists, a threefold intensity pattern should be observed.

Homogeneity of bismuth single crystals

A bismuth single crystal was oriented on the sample table of the SANS-II instrument in the same orientation relative to the neutron beam as will be done later in the neutron filter. The orientation is performed with the observed dip produced by the (111)-reflex. Since this dip is due to a plane perpendicular to the n-beam, the accurate orientation can easily be found by turning the crystal about the two perpendicular axes to the neutron-beam. An accuracy of ± 0.5 degrees can easily be obtained. With two translation-tables moving perpendicular to the neutron beam, the whole crystal could be scanned. Quite different spectra were observed at different spots of the crystal. Two examples are shown in Fig. 1 and Fig. 2, which were measured on one side of the crystal near the edges, in a distance of about 8 cm. We observed a big difference of the transmission below a wavelength of $\approx 4 \text{ \AA}$ and at the 8 \AA dip, leading to the conclusion that this crystal is rather inhomogeneous.

Intensity dependence of the transmission spectrum on the azimuthal angle of two bismuth single crystals

In our n-filter about five single crystals, each with a thickness of about 10 cm, giving a total thickness of about 50 cm, will be used. Here we studied the intensity dependence on the azimuthal angle of two crystals. A device was built, in which one crystal was oriented and fixed and a second crystal was also oriented as the first crystal but could be rotated about the n-axis. The transmitted intensity of both crystals was measured in dependence of the azimuthal angle. Because the rotation axis is perpendicular to the (111)-plane it has threefold symmetry. The same symmetry is expected for the intensity pattern. The intensity

[1] Report in this issue

of the transmission spectrum from 2 Å to 4 Å was integrated, because in this region a dependence on the azimuthal angle was expected. Fig. 3 shows the intensity in dependence on the azimuthal angle. Within a statistical error below 1 % no modulation could be observed. From this result it can be concluded that the individual azimuthal orientation of the single crystals within the filter is not necessary.

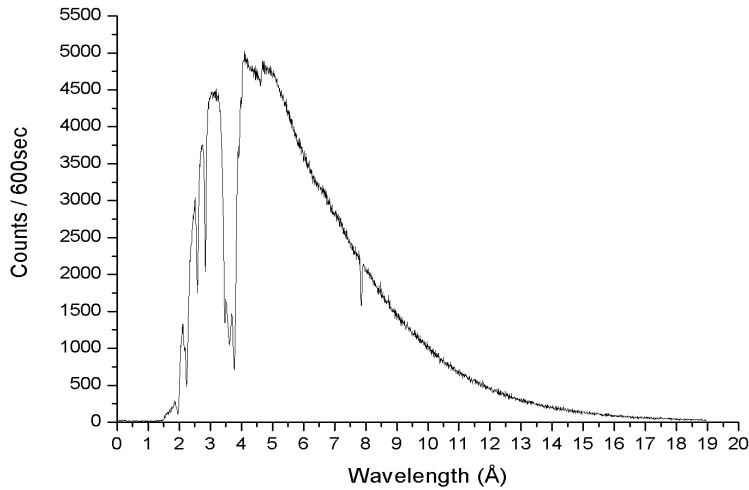


Figure 1:
Crystal 1 measured on the top left.

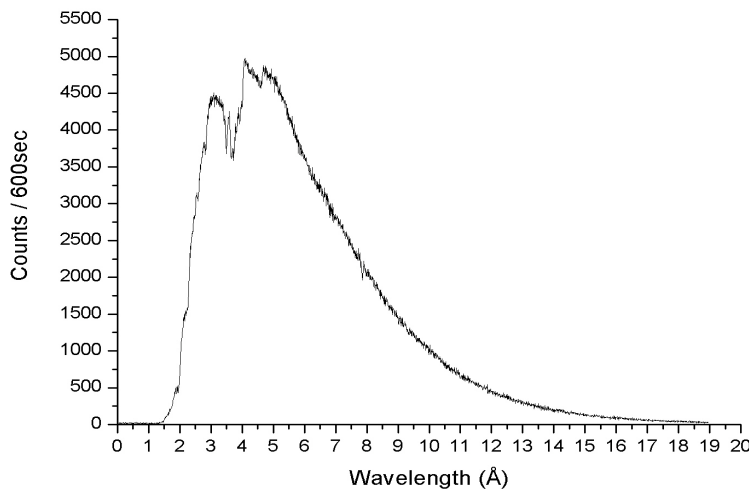


Figure 2:
Crystal 1 measured on the top right.

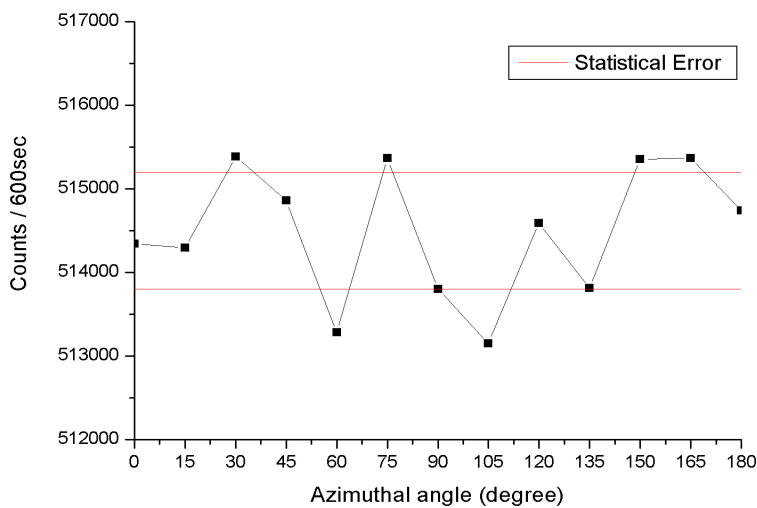



Figure 3:
Intensity dependence on the azimuthal angle.

	EXPERIMENTAL REPORT	GeNF SANS-2
The study of new magnetic nanocomposites based on mesoporous silica with embedded Fe-particles by SAPNS: technology		
Principal Proposer:	S. V. Grigoriev ² , A. I. Okorokov ² , E. A. Kelberg ² ² Petersburg Nuclear Physics Institute, Russia	
Experimental Team:	H. Eckerlebe ¹ , P. K. Pranzas ¹ , A. I. Okorokov ² , S. V. Grigoriev ² ¹ GKSS Research Centre	
Date(s) of Experiment:	June 2002	

Scientific Objective

The proposal aimed to investigate magnetic and structural features of a new class of nanocomposites based on silica matrix with embedded iron particles. Mesoporous silica is a promising potential matrix for the preparation of nanocomposites. One could expect that size and shape of nanoparticles incorporated into the mesoporous silica would be consistent with the dimensions of the porous framework. A hydrophobic metal complex $\text{Fe}(\text{acac})_3$ or $\text{Fe}(\text{CO})_5$ was introduced into the hydrophobic part of the as-prepared meso- SiO_2 /surfactant composite. Decomposition of $\text{Fe}(\text{CO})_5$ was carried out by UV-irradiation in vacuum for 10 hours. To provide better crystallinity of iron nanowires we performed additional annealing in hydrogen flow at temperatures of 260, 300, 350, 375 and 400 °C for 3 hours. The samples obtained were denoted as FeSiO_2 -260, FeSiO_2 -300, FeSiO_2 -350, FeSiO_2 -375 and FeSiO_2 -400, respectively. The magnetic nanocomposites had been studied by Small Angle Polarized Neutron Scattering (SAPNS) in order to reveal the effect of annealing on their properties.

Experimental Technique

The SAPNS experiments were carried out at the SANS-2 scattering facility of FRG-1 research reactor in Geesthacht (Germany). A polarized beam of neutrons with an initial polarization of $P_0=0.94$, the neutron wavelength $\lambda=5.8 \text{ \AA}$ ($\Delta\lambda/\lambda=0.1$) and a divergence of 1.5 mrad was used. The scattered neutrons were detected by a position sensitive detector with 128x128 pixels. The scattering intensity was measured at room temperature. An external magnetic field of 0.25 T was applied in the horizontal plane and perpendicularly to the incident beam in order to reveal nuclear magnetic cross-correlator of the system. We determine the total (nuclear and magnetic) scattering as: $I(q) = I^+(q) + I^-(q)$. The polarization dependent part of the scattering is determined as the difference ($\Delta I(q) = I^+(q) - I^-(q)$) of the intensities for neutrons polarized parallel (+) and anti-parallel (-) to the magnetic field.

Results

A typical 3-dimensional picture of the neutron scattering for mesoporous silica samples is presented in Fig. 1. The ring of scattering intensity corresponds to the scattering of the regular two-dimensional structure of nanotubes in the randomly oriented single particles. The period of the structure d is obtained from the Bragg law $\lambda = 2d \sin(\theta/2)$, or, $d = 2\pi/q_c \cong 3.6 \text{ nm}$. The q -dependence of the neutron intensity $I(q)$ for the pure SiO_2 matrix and for the sample FeSiO_2 -375 is shown in Fig. 2. The data were fitted with the expression $I(q) = A_1/q^4 + A_2/((q-q_c)^2 + \omega^2)$. The first term describes scattering from the particles and their surfaces while the second term describes the diffraction peak centered at q_c with a width of ω .

Figure 1:

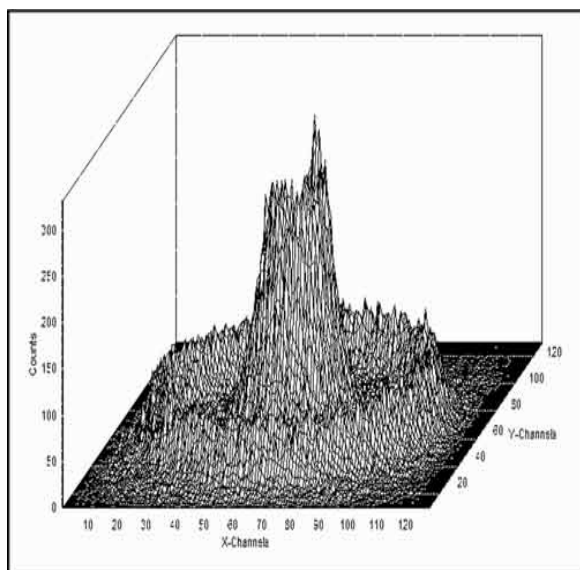


Figure 2:

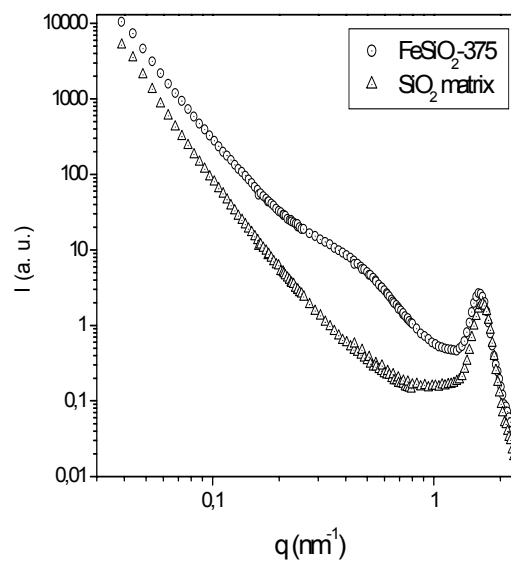


Figure 3:

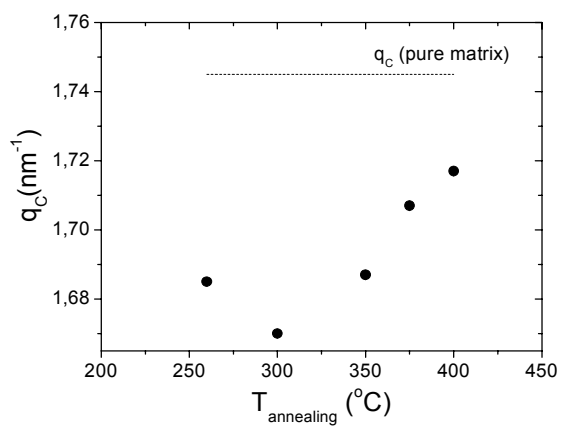


Figure 4:

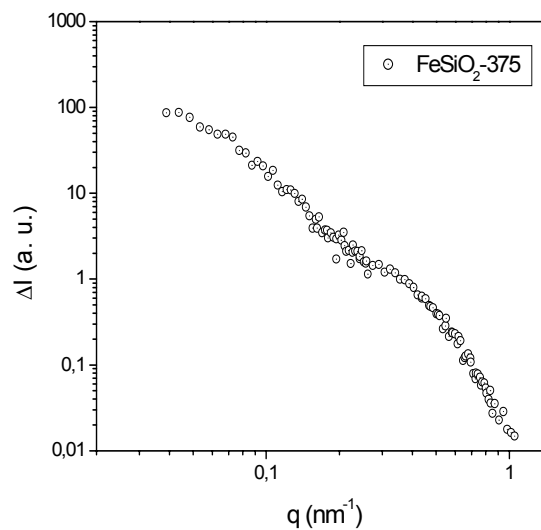


Figure 5.

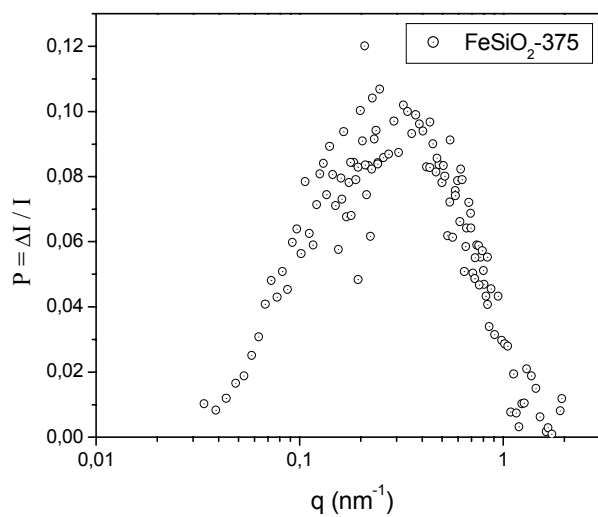



Fig. 3 shows the dependence of q_c on the annealing temperature. The intercalation of iron into the matrix leads to a shift of q_c toward smaller q , because the expanding by filling up the pore space by iron increases the structure period d . It is well seen in Fig. 2 that SANS intensity increases at $q < 1 \text{ nm}^{-1}$ for the samples with iron what implies the formation of clusters. The polarization analysis clarified the location of the intercalated iron in the matrix. The interference scattering $\Delta I(q)$ was observed in the small q -range but not at the peak position (Fig. 4). Fig. 5 shows the value of the polarization $P(q) = \Delta I(q)/I(q)$. The polarization has a maximum at $q \cong 0.3 \text{ nm}^{-1}$. The interference correlation length may be estimated as $R_{\text{int}} \sim 2\pi/q = 20 \text{ nm}$. This means that most of the magnetic nanowires are correlated with the distance, which is 5–6 times larger than the distance d .

Conclusion

The intercalation of iron into the matrix SiO_2 and annealing at different temperatures don't destroy the matrix but form a system of nanowires of iron. The magnetic contribution of the scattering increases with an increase of crystallinity of the wires (temperature of the annealing) and is maximal for the samples $\text{FeSiO}_2\text{-375}$ and $\text{FeSiO}_2\text{-400}$. We suppose that the iron nanowires consist of partially crystalline and partially amorphous pieces, which are randomly distributed along the SiO_2 -tubes. The crystalline pieces are ferromagnetic ones with high density. The amorphous iron pieces are superparamagnetic with low density. Thus, they form the nuclear magnetic correlated network that provides the appearance of the interference in the scattering.

	EXPERIMENTAL REPORT	GeNF SANS-2
The study of new magnetic nanocomposites based on mesoporous silica with embedded Fe-particles by SAPNS: magnetic properties		
Principal Proposer:	S. V. Grigoriev ² , A. I. Okorokov ² , E. A. Kelberg ² ² Petersburg Nuclear Physics Institute, Russia	
Experimental Team:	H. Eckerlebe ¹ , P. K. Pranzas ¹ , E. A. Kelberg ² , S. V. Grigoriev ² ¹ GKSS Research Centre, ² Petersburg Nuclear Physics Institute, Russia	
Date(s) of Experiment:	November 2002	

Scientific Objective

The proposal was aimed to study the magnetic behaviour of the nanocomposites based on mesoporous silica SiO₂ with embedded iron particles. In the previous experiments by Small Angle Polarized Neutron Scattering (SAPNS) [1] a diffraction peak at $q_c \sim 1.7 \text{ nm}^{-1}$ was observed, which corresponds to a hexagonal structure of nanotubes and/or nanowires with periodicity $d \sim 3.6 \text{ nm}$. The nuclear-magnetic interference in scattering of polarized neutrons was studied. The interference revealed the absence of the periodical magnetic structure at room temperature which would be consistent with the hexagonal structure of nanotubes in pure matrix. Instead of that we observed a remarkable interference scattering at $q < q_c$. In a course of the present experiment we studied the interference term as a function of the temperature in a range from 10 to 300 K using a magnetic field of up to 0.35 T.

Experimental Technique

The experiments were carried out at the SANS-2 scattering facility under the same condition as in [1]. Theoretically, the interference term can be written as: $\sigma_{\text{int}}(q, P_0) = 2 \langle P_0 m_{\perp} \rangle A_n A_m \text{Re}(F_{nm}(q))$, where A_n , A_m are the nuclear and magnetic contrasts, $m_{\perp} = m - (me)e$, m is the magnetization and $e = q/q_c$. The polarization dependent part of the scattering is determined as the difference $\Delta I(q) = I^+(q) - I^-(q)$ of the intensities for neutrons polarized parallel (+) and anti-parallel (-) to the magnetic field.

Sample

The same powder as in [1] consisting of small particles of mesoporous silica was used. Iron nanowires in the SiO₂ matrix were synthesized by a standard method [2]. To provide better crystallinity of iron nanowires, the sample was annealed in hydrogen flow at different temperatures. The optimal annealing temperature was found to be equal to 375 °C.

Results

In this experiment the nuclear scattering cross-section dominates the magnetic one, the magnetic scattering is only a few percents of the nuclear one. Nevertheless, the nuclear-magnetic interference term exceeds 10–20 % of the total scattering. The q -dependence of the neutron intensity difference $\Delta I(q)$ at $H = 100 \text{ mT}$ and $T = 293 \text{ K}$ is shown in Fig.1. It is obvious that the scattering intensity has several humps shown by arrows which implies the presence of the magnetic structures correlated with the nuclear one with periodicity $2d$, $3d$, $4d$, $5d$, and $10d$ while the magnetic structure with periodicity d is absent. We may interpret the data in two margin limits: the diffraction one and the SANS one. The diffraction limit implies the regular periodical structure and therefore the scattering on it reproduces as the diffraction peak. The SANS limit represents the scattering on a single wire or a single tube which is uncorrelated with other similar objects. In the case of the object under study we have the intermediate case when the magnetic iron wires are correlated with distances larger

than d . As a result we have the contributions from the regular structures with periodicity of $N d$, where $N = 2,3,4,5,6,7,8,9$ up to the SANS limit with $N d$ where $N \gg 1$. The interpretation is not finished yet.

We summarized the interference term over the detector area and plotted the integral intensity ΔI_{int} as a function of the magnetic field for temperatures $T = 8 \text{ K}$ and $T = 293 \text{ K}$. Fig. 2 reveals the magnetic hysteresis at $T = 8 \text{ K}$. It should be noticed that it is not observed at $T = 300 \text{ K}$. The temperature dependence of the integral intensity ΔI_{int} was also measured for Field Heating after Zero Field Cooling (FH after ZFC) and for Field Cooling (FC) regimes. The results of the measurements are presented in Fig. 3 and in Fig. 4 for the magnetic fields 100 Oe and 300 Oe, respectively. The temperature hysteresis is observed in the range from 8 to 300 K for both magnetic fields. The observed hysteresis at low temperatures is interpreted as a formation of a complicated magnetic structure composed of magnetic nanowires. The system is ruled by the competition of the magnetic field, dipole-dipole and thermal interactions.

Figure 1:

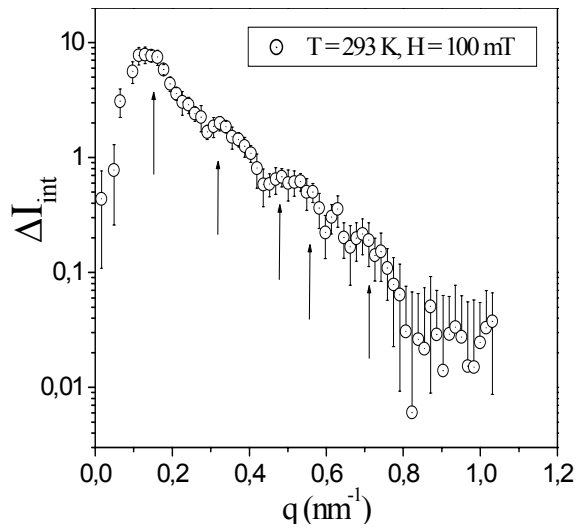


Figure 2:

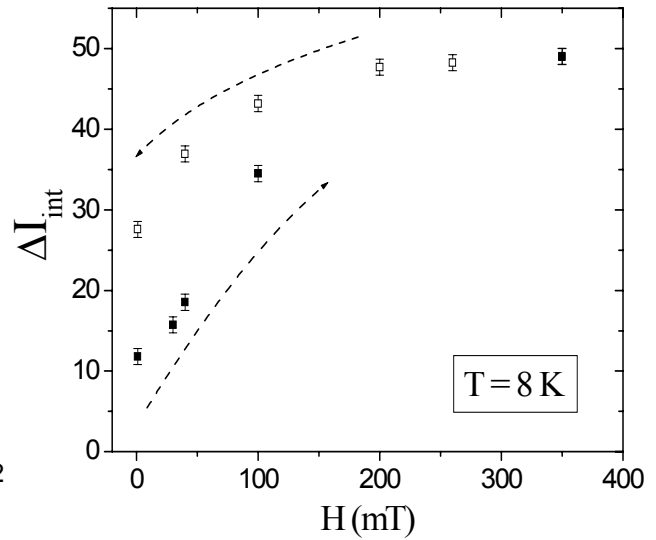


Figure 3:

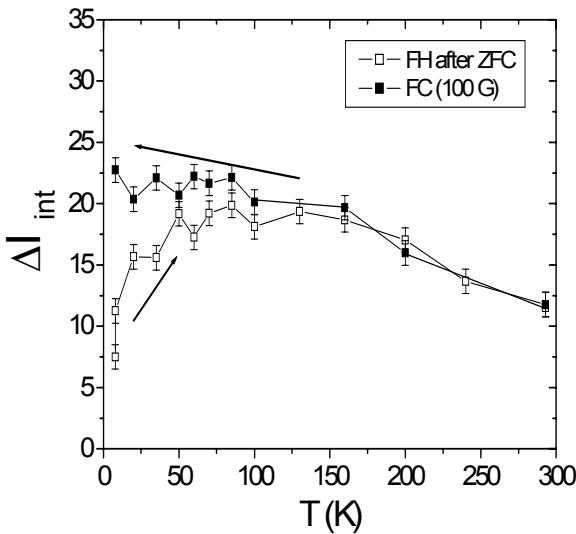
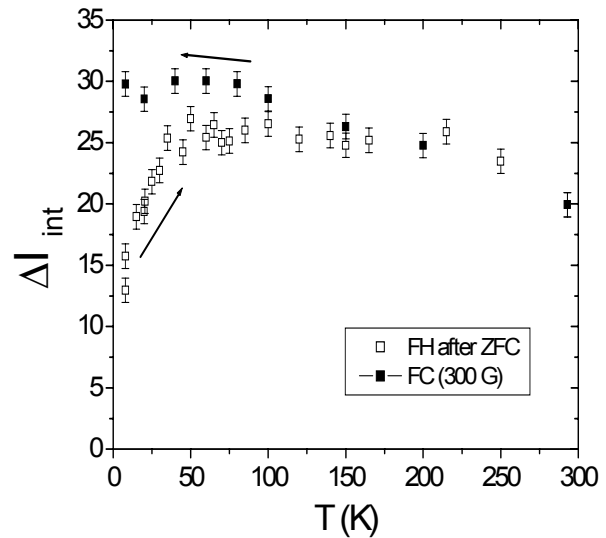



Figure 4:



References

[1] E. A. Kelberg, S. V. Grigoriev, A. I. Okorokov, H. Eckerlebe, N. A. Grigorieva, "SANS study of new magnetic nanocomposites embedded into the mesoporous silica", Physica B (2002) is accepted; see also the present GeNF Experimental Report 2002.
 [2] A. A. Eliseev, A. V. Lukashin, A. A. Vertegel, K. S. Napolskii, to be published

	EXPERIMENTAL REPORT	GeNF SANS-2
SANS investigation of Mg alloys		
Principal Proposer:	D. Letzig, J. Bohlen, H. Eckerlebe GKSS Research Centre	
Experimental Team:	H. Eckerlebe GKSS Research Centre	
Date(s) of Experiment:	June 2002	

Scientific Objective

The feedstock quality has an important influence on the processing like rolling or extrusion and with that on the semi-finished product. In the case of magnesium alloys the content of impurities, pores and/or intermetallic phases (like e.g. $Mg_{17}Al_{12}$ in AZ31) has to be determined. For this purpose the small-angle neutron scattering technique has been applied.

Experiment

Three different samples were measured: commercial AZ31 sheet, commercial AZ31 cast and a Mg cast of commercial purity. The SANS experiments were carried out at the SANS-2 scattering facility. The measurements were performed at a neutron wavelength $\lambda=5.8 \text{ \AA}$ ($\Delta\lambda/\lambda=0.1$). The range of the scattering vector $0.01 \text{ nm}^{-1} < q < 2,5 \text{ nm}^{-1}$ was covered by 4 detector-sample distances (1 m, 3 m, 9 m, 21 m) with appropriate collimations. The scattered neutrons were detected by a position sensitive detector with 128x128 pixels. Measured intensity was corrected for sample transmissions, background and detector efficiency. The scattering data were averaged over azimuthal scattering angle and absolute cross sections were calculated by comparison with the incoherent scattering from vanadium.

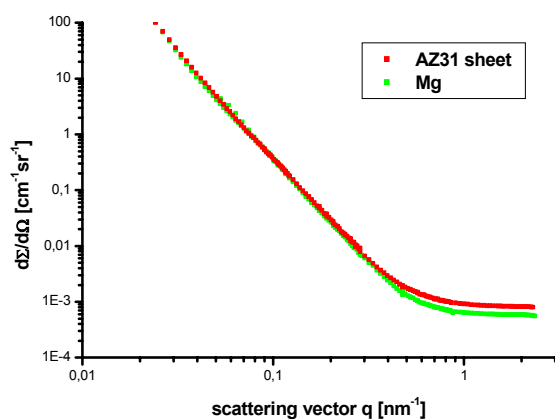


Figure 1: Scattering curves of samples Mg and AZ-31 sheet.

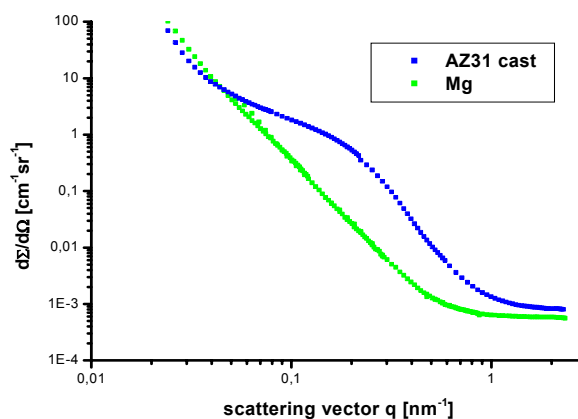


Figure 2: Scattering curves of samples Mg and AZ-31 cast.

Results

As it can be seen from Fig. 1, there are no precipitates in the sample AZ31 sheet. The identical coherent scattering of both samples at small angles $q < 0,3 \text{ nm}^{-1}$ may be related to inclusions in the bulk and to grain boundaries. At large scattering angles $q > 1 \text{ nm}^{-1}$ the sample AZ31 sheet shows both the contribution of the incoherent scattering from the alloying constituent Al, Zn and the contribution of the Laue monotonic scattering in addition to the incoherent scattering of pure Mg. In contrast to AZ31 sheet, precipitates are existing in the sample AZ31 cast (Fig. 2).

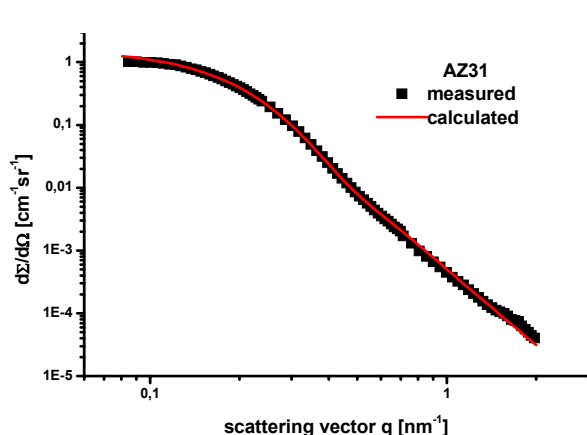


Figure 3: Differential cross section of precipitations in AZ 31 cast.

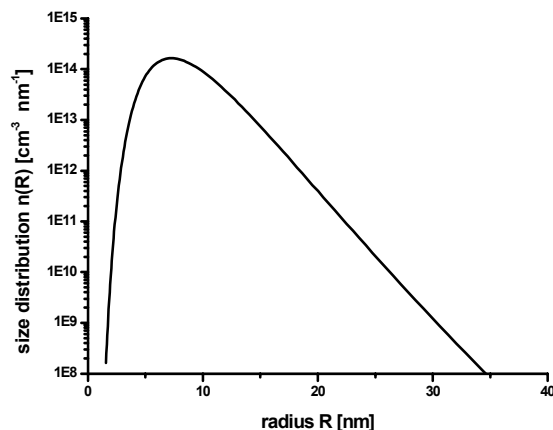



Figure 4: Particle size distribution corresponding to the SANS curve in Figure 3 assuming spherical $\text{Mg}_{17}\text{Al}_{12}$ particles.

Fig. 3 shows the remaining scattering pattern of the precipitates after subtracting the differential cross section of pure Mg from AZ31 cast. At large scattering angles ($q > 0,5 \text{ nm}^{-1}$) the scattering curve decreases with q^{-4} , this is an indication for the existing of homogeneous particles with sharp boundaries. From the phase diagram it is known that the precipitates are mainly $\text{Mg}_{17}\text{Al}_{12}$ [1]. Assuming spherical particles the corresponding cluster size distribution is shown in Fig. 4. The fit for this calculation is the red line in Fig. 3. The mean radius of the particles is approximately 10 nm. The volume fraction of 0,0028 is significantly smaller than the maximum possible amount of 0,02. This is in agreement with almost the same scattering intensities of both samples AZ31 cast and AZ31 sheet at large scattering vectors $q > 1 \text{ nm}^{-1}$. Further SANS measurement at very small angle (USANS) at the DCD instrument are planned, to obtain information about pores, voids and cavities in the range from 100 nm to about 20 μm .

Reference

[1] Magnesium Taschenbuch, Aluminium Verlag Düsseldorf (2000), 1. edition

	EXPERIMENTAL REPORT	GeNF SANS-2
Critical magnetic scattering in an ordered invar Fe₇₅Pt₂₅ alloy		
Principal Proposer:	A. I. Okorokov, S. V. Grigoriev ¹ ¹ Petersburg Nuclear Physics Institute (PNPI), Russia	
Experimental Team:	H. Eckerlebe ² , P. K. Pranzas ² , A.I. Okorokov ¹ , S. V. Grigoriev ¹ ² GKSS Research Centre	
Date(s) of Experiment:	June 2002	

Scientific Objective

This experiment was aimed to investigate the spin dynamics of an ordered invar alloy Fe₇₅Pt₂₅ near the magnetic phase transition by means of small angle polarized neutron scattering (SAPNS). SAPNS experiments were performed using a special "inclined" magnetic field geometry. Two contributions to the critical magnetic scattering were studied in the temperature range around T_C = 400 K. One of them comes from the pair spin correlations. Another contribution caused by the three-spin chiral fluctuations. It is separated from other contributions as the asymmetric part of the polarization dependent scattering [1–4].

Experimental Techniques

The SAPNS experiments were carried out at the SANS-2 scattering facility of FRG-1 research reactor in Geesthacht (Germany). A polarized beam of neutrons with an initial polarization of P₀=0.9, the neutron wavelength λ=5.8 Å (Δλ/λ=0.1) and a divergence of 1.0 mrad was used. The scattered neutrons were detected by a position sensitive detector with 128x128 pixels. The scattering intensity was measured in the temperature range from T = 370 K to T = 470 K, i.e. from far below to far above T_C = 400 K. The external magnetic field H from 1 to 230 mT was applied at the angle φ = 45°, with respect to the incident beam k, providing, so-called, "inclined" geometry. This geometry allows observing the left-right asymmetry in SAPNS pattern that originate from the interaction of the neutron spin with the chiral dynamic excitations. According to Ref. [2] in a magnetized sample the magnetic cross section has the form:

$$\sigma(q, \omega) = \sigma_0(q, \omega) + (q, P_0)(q, H)\sigma_{ch}(q, \omega)/q^2,$$

where the second term is determined by chiral dynamic spin fluctuations and P₀ and H are the neutron polarization and the magnetic field, respectively. In the case of small-angle scattering ω integrated chiral contribution to the cross section changes sign with θ and may be easily extracted from the total scattering intensity. Following Refs.[1–4] we investigated experimentally the quantity P_A(θ) = Δ I_A(θ)/I(θ), where

I(θ) = [I₊(θ)+I₊(-θ)+I₋(θ)+I₋(-θ)] and ΔI(θ) = [I₊(θ)+I₋(-θ)-I₊(-θ)-I₋(θ)] and I₊(θ) and I₋(θ) are ω integrated intensities with polarization directed along and opposite to the field.

Results

The measured SAPNS intensity is well described by the Ornstein-Zernike expression: I(q) = A/(q² + κ²), where A and κ are the scattering amplitude and the inverse correlation length, respectively. As shown in Fig. 1, the correlation radius R_C = κ⁻¹ increases while temperature decreases to T_C = 400 K and saturates with further lowering of T. The value of A demonstrates a similar behavior. The effect of the magnetic field on the inverse correlation length R_C at T = 402 K is shown as an inset of Fig. 1. The value of R_C linearly decreases with increasing field. It is interesting to note that the amplitude A does not depend on H. This behavior of R_C is a result of a crossover to the strong field regime, which is determined by the condition T_C(κ_Ca₀)^Z = gμ H, where Z = 5/2 and a₀ is a constant in the order of 1Å (see for example [5]). The points lay in line on a log-log scale. The fit gives value of the parameter 1/Z = 0.30± 0.02, that is somewhat different from the theoretical value of 1/Z = 2/5 for classical ferromagnets.

Figure 2 provides typical examples of the polarization $P_A(k\theta)$ as a function of q at the magnetic field of $H = 80, 170$ and 230 mT and at $T = 402$ K. P_A is q -independent for $k\theta > \kappa$ within the error bars. We have averaged the value of P_A over all these points and studied $\langle P_A \rangle$ as a function of temperature and magnetic field. It appears that $\langle P_A \rangle$ is temperature independent in a broad temperature range near T_C (Fig.3) what may indicate that the applied magnetic field is relatively large. Inside this temperature range $\langle P_A \rangle$ changes linearly with the magnetic field (see the inset of Fig.3) in agreement with the theoretical prediction [3]: $\langle P_A \rangle = ((g \mu H)/E)(k/\kappa)$.

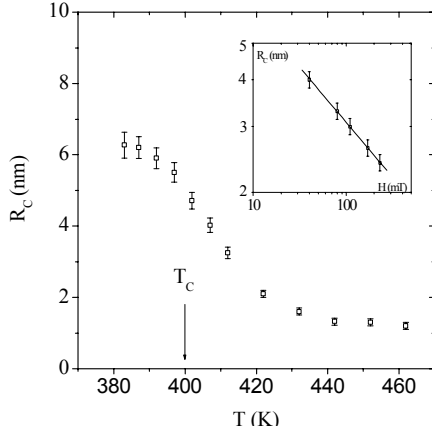


Figure 1.

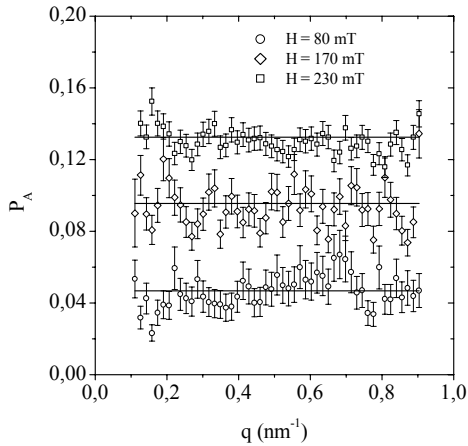


Figure 2.

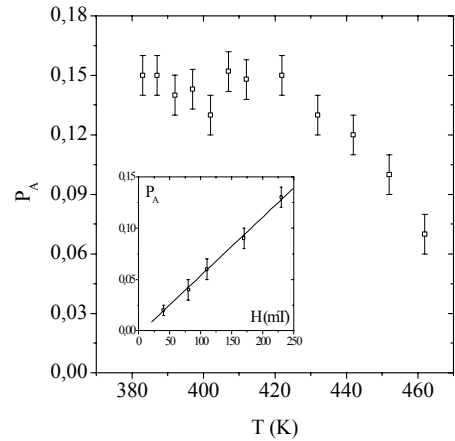



Figure 3.

Conclusion

The experimental data confirm the principle of the critical factorization [5], which is known as Polyakov-Kadanoff-Wilson operator algebra.

References

- [1] A.I. Okorokov, A.G. Gukasov, V.V. Runov, M. Roth, Sol.St.Comm. 38 (1981), 583
- [2] A.V. Lazuta, S.V. Maleyev, B.P. Toperverg, Sol.St.Comm. 38 (1981), 589
- [3] A.I. Okorokov, V.V. Runov, B.P. Toperverg, A.D. Tret'yakov, E.I. Mal'tsev, I.M. Puzerii, V.E. Mikhailova, JETP Lett. 43 (1986), 503
- [4] V. Deriglazov, A. Okorokov, V. Runov, B. Toperverg, R. Kampmann, H. Eckerlebe, W. Schmidt, W. Lobner, Physica B 181-182 (1992), 262
- [5] S.V. Maleyev, in Physics Review, edited by I.M. Khalatnikov (Harwood Academic, Chur, 1987) Vol. 8, p. 323.

	EXPERIMENTAL REPORT	GeNF SANS-2
The study of the spin chirality in MnSi single crystal by means of small angle scattering of polarized neutrons		
Principal Proposer:	A. I. Okorokov ¹ , S. V. Grigoriev ¹ , P. Böni ² , R. Georgii ² ¹ Petersburg Nuclear Physics Institute (PNPI), Russia ² Technical University Munich	
Experimental Team:	H. Eckerlebe ³ , P. K. Pranzas ³ , A. I. Okorokov ¹ , S. V. Grigoriev ¹ ³ GKSS Research Centre	
Date(s) of Experiment:	November 2002	

Scientific Objective

The proposal was aimed to investigate the spin chirality in a single crystal MnSi in the critical range near $T_C = 29$ K and below T_C by means of small angle polarized neutron scattering (SAPNS). The theoretical and experimental studies had shown the single handed helicity of the spin density wave in the crystal of MnSi [1,2]. The magnetic structure is a helical spin density wave below 29 K with a propagation vector $2\xi/a(\xi, \xi, \xi)$ with $\xi = 0.017$. The helicity is realized by an antisymmetric exchange interaction often called the Dzyaloshinski-Moria interaction. Dzyaloshinskii-Moria (DM) vector is an axial vector and therefore the presence of DM interaction leads to appearance of the polarization dependent contribution into the neutron scattering cross-section. This interaction fixes the direction of the magnetic spirals below T_C and it results in the polarization-dependent contribution into the paramagnetic scattering at high temperatures. [1-3]

Experimental Technique

The SAPNS experiments were carried out at the SANS-2 scattering facility of FRG-1 research reactor in Geesthacht (Germany). A polarized beam of neutrons with an initial polarization of $P_0=0.94$, the neutron wavelength $\lambda=5.8 \text{ \AA}$ ($\Delta\lambda/\lambda=0.1$) and a divergence of 2.5 mrad was used. The scattered neutrons were detected by a position sensitive detector with 128x128 pixels. The scattering intensity was measured in the temperature range from $T = 10$ K to $T = 40$ K. The external magnetic field H from 1 to 350 mT was applied perpendicularly to the incident beam and the polarization followed the direction of the magnetic field. According to Ref. [4] the elastic chiral magnetic cross section has the form:

$$\sigma_{el}(q) = [r S F(q)/2]^2 \{ (1+(qm)^2 + 2(q, P_0)(q, m))\Delta_{q+Q} + (1+(qm)^2 - 2(q, P_0)(q, m))\Delta_{q-Q} \} \quad (1)$$

where $r = 0.54 \times 10^{-12}$ cm, $m = [S_1 \times S_2]/S^2$ is a direction of the magnetic spiral, q is a momentum transfer and $\Delta_{q\pm Q} = [(2\pi)^3/V] \delta(q \pm Q)$. We study the diffraction pattern at $q=\pm Q$ in a range of small-angle range scattering. The cross section depends on the mutual orientation of the P_0 and m (Eq.1). When $P_0 \parallel m$, the scattering is fully polarized at $q=\pm Q$. When $P_0 \perp m$, the scattering is fully depolarized at $q = \pm Q$. We investigate experimentally the quantity $P_A(q) = \Delta I_A(q)/I(q)$, where $I(q) = [I(q, P_0) + I(q, -P_0)]$ and $\Delta I(q) = [I(q, P_0) - I(q, -P_0)]$. $I(q, P_0)$ and $I(q, -P_0)$ are intensities with the polarization directed along and opposite to the field. The single crystal was oriented in such a way that two axes [111] were set in a plane perpendicular to the incident beam. According to the geometry of the crystal, these two axes are inclined at about 71° with respect to each other. The direction of the magnetic spirals, or the chiral vectors m are expected to be parallel to these two axes. The polarization vector P_0 was set as perpendicularly to one of the axes [111] and therefore it was inclined at about 19° with respect to another axis [11-1]. This geometry allows one to observe the polarization effect on the scattering for one of the axes that originates from the interaction of the neutron spin with the chiral static spin wave.

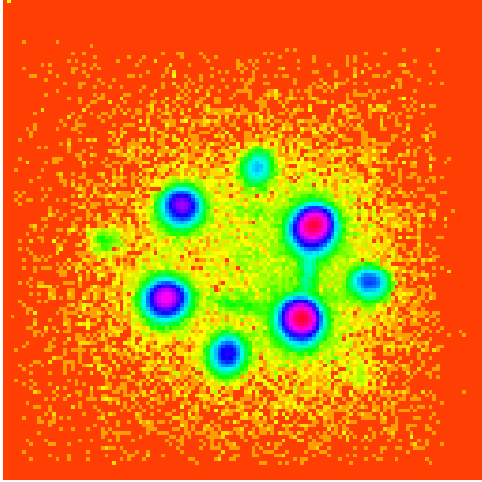


Figure 1.

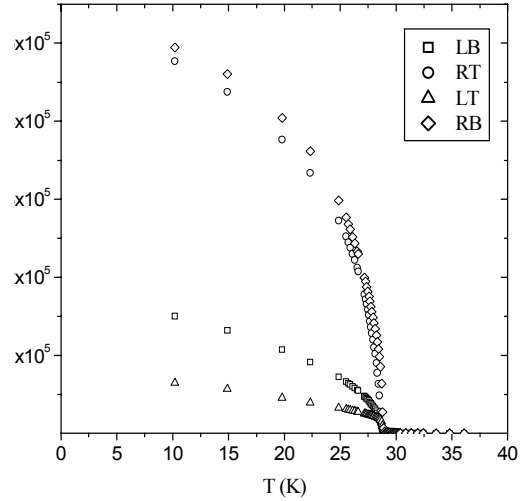


Figure 2.

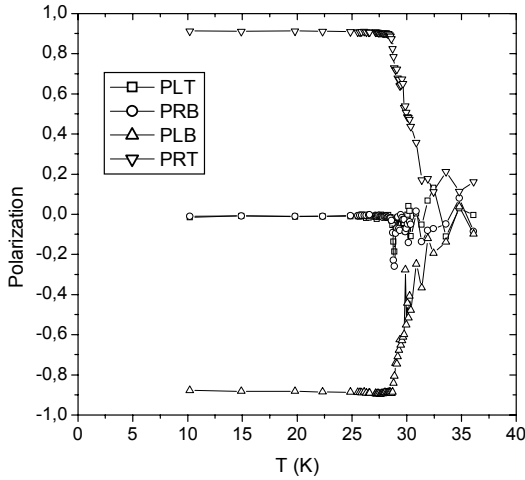


Figure 3.

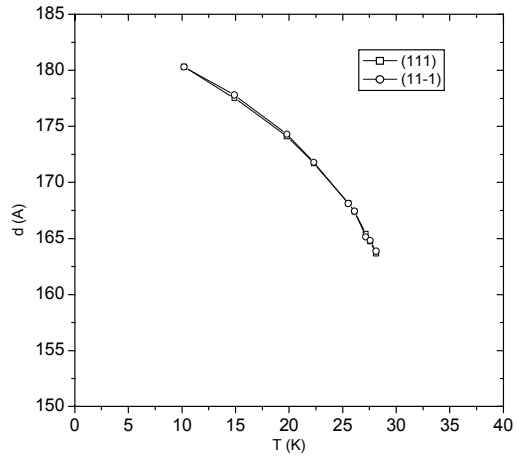


Figure 4.

Results: part 1

The contour map of the diffraction peaks in a logarithmic scale at $T = 10$ K is presented in Fig. 1. Four major peaks (closest to the center) are reflections of two different axes $[111]$ which were visible for this geometry of the experiment. Therefore two chiral vectors $m_{1,2}$ are collinear to these axes. We denote these four peaks as Left-Top (LT), Left-Bottom (LB), Right-Top (RT) and Right-Bottom (RB) ones. Additional small peaks at $q = q_{LB} + q_{RB}$, $q = q_{RB} + q_{RT}$ and $q = q_{RT} + q_{LB}$ appear as a result of a double scattering process. The integral intensity for LT, LB, RT and RB peaks is shown in Fig. 2 as a function of the temperature. The polarization of the peaks is presented in Fig. 3. The polarization is constant for the temperature range below T_C . It is equal to 0.9 for LB peak, -0.88 for RT peak and it is equal to 0 for both LT and RB peaks. The peaks LT and RB are depolarized due to the fact that P_0 is perpendicular to q_{LT} and q_{RB} (see also Eq.(1)). The peaks RT and LB are polarized with the theoretical value $P = P_0 \cos(\angle(q_{RT, LB} P_0)) = 0.94 * 0.946 = \pm 0.89$. Thus we observed the single handed helicity of the spin density wave in the crystal of MnSi. The period of spin density wave d is readily obtained from the Bragg law $\lambda = 2d \sin(\theta/2)$, or, $d = 2\pi/Q$, where Q is calculated for two different axes as: $|q_{[111]}| = |q_{LT} - q_{RB}|/2$ and $|q_{[1\bar{1}\bar{1}]}| = |q_{RT} - q_{LB}|/2$. The temperature dependences of the period d coincide for both axes coincide and are shown in Fig.4. The period decreases with increasing temperature which can be interpreted as interplay between Dzialoshinskii-Moria interaction and the temperature.

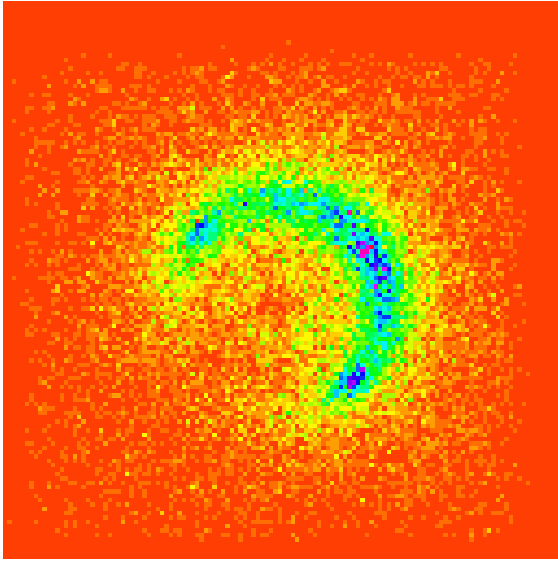


Figure 5.

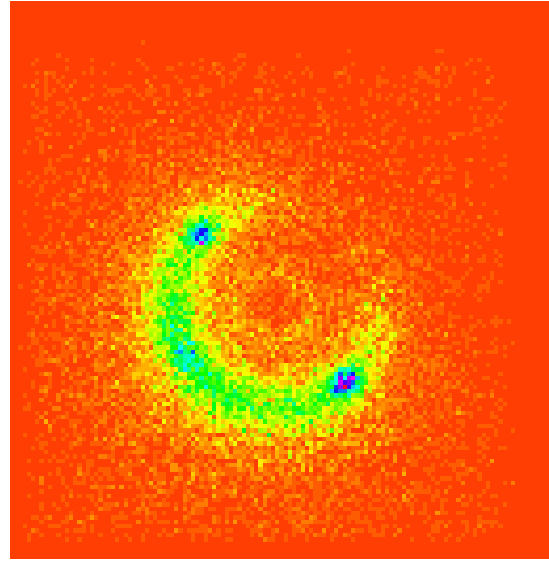


Figure 6.

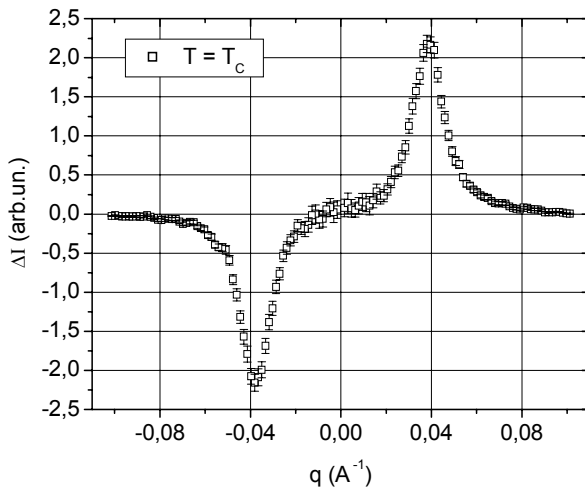


Figure 7.

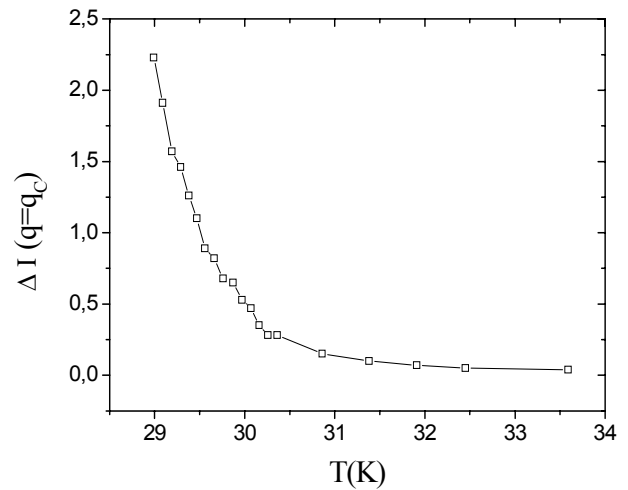


Figure 8.

Results: part 2

The typical pattern of the scattering in the critical range is shown in Fig. 5 and Fig. 6 for the incident polarization $\pm P_0$ directed along the diagonal of the detector (from LB corner to RT corners). The scattering is concentrated within the narrow band near $|q| = q_C = 2\pi/d$. The scattering is isotropic although it is polarized along the direction of the incident polarization P_0 . Thus we conclude that the fluctuations of the spin spirals appear in all possible directions, having, nevertheless, the same periodicity and the only handedness of the helicity. The difference $\Delta I(q)$ at $T = 29.0$ K in the direction along the polarization is shown in Fig. 7. It is purely antisymmetric. We plot the maximal intensity $I(q=q_C)$ as a function of the temperature in Fig. 8. The data will be interpreted in accordance with the theoretical predictions [5].

References

- [1] G. Shirane, R. Cowley, C. Majkrzak, J. B. Sokoloff, B. Pagonis, C. H. Perry, Y. Ishikawa, Phys. Rev. B, 28 (1983) 6251.
- [2] M. Ishida et al., J. Phys. Soc. Jpn. 54 (1985) 2975.
- [3] B. Roessli, P. Boni, W. E. Fisher, Y. Endoh, Phys. Rev. Lett. 88 (2002) 237204
- [4] S. V. Maleyev, V. G. Bar'jakhtar, R. A. Suris, Fiz. Tv. Tela 4 (1962) 3461; M. Blume, Phys. Rev. 130 (1963) 1670
- [5] S.V. Maleyev, Phys. Rev. Lett., 75 (1995) 4682; D.N. Aristov, S.V. Maleyev, Phys. Rev. B, 62 (2000) R751

	EXPERIMENTAL REPORT	GeNF SANS-2
The crystalline quality of large Bismuth single crystals and a Czochralski grown Sapphire single crystal (Al₂O₃) by neutron transmission		
Principal Proposer:	M. Prager ¹ , B. Alefeld ¹ ¹ Forschungszentrum Jülich GmbH	
Experimental Team:	L. Dohmen ¹ , A. Christ ¹ , H. Eckerlebe ² , J. Vollbrandt ² , G. Kozik ² ² GKSS Research Centre	
Date(s) of Experiment:	09, 10, 12 / 2002	

Scientific Objective

The cold neutron beam used in the external neutron laboratory at the FRJ-2 (research reactor in Jülich), emerges from the cold neutron source, which is located very near to the reactor core. Because of the large beam cross section of $7 \times 10 \text{ cm}^2$ and the unbent neutron guides it is necessary to shield the X-rays and fast neutrons, which are coming from the reactor core. This shielding is achieved with a 50 cm long, composed Bi-single crystal. The transmission of the cold beam depends on the crystalline quality and the orientation of the single crystals, the higher the quality (low mosaic spread), the better the transmission. The built-in crystals at the FRJ-2 are of poor quality.

Results for Bismuth

At the FZ-Jülich, K. Fischer has grown large Bi-single crystals, cut oriented of a size of $12 \times 12 \times 12 \text{ cm}^3$, whose quality was tested at the SANS-2 instrument at the GKSS. There are two reasons to test the crystals at this instrument. Firstly the beam is very clean, with only weak Bragg edges of the polycrystalline Aluminium windows in the beam at the wavelengths of $\lambda = 4.665 \text{ \AA}$ for the (111)-reflex and at 4.040 \AA for the (200) reflex. Secondly there exists a built-in time of flight chopper, which immediately can be used. The crystals were aligned with the (111)-planes perpendicular to the beam. In this case the area of the (111)-dip at 7.89 \AA is a measure of the quality of the crystal. In Fig.1a an empty measurement is shown. In Fig.1b a measurement of crystal-1, the best crystal, is shown. A value of $\Delta\lambda/\lambda \approx 0.0003$ is estimated. In Fig.1c a measurement of crystal-3 is shown with an estimated value $\Delta\lambda/\lambda \approx 0.0012$. This value is by a factor of 4 worse than that of crystal-1. It is also clearly observed, that between 1.5 \AA and 4 \AA the transmission of crystal-1 is much better than that of crystal-3.

Results for Al₂O₃

Sapphire single crystals, Al₂O₃, are used as filters for thermal neutrons. Al₂O₃ is especially liked as a filter material because it does not require cooling. Because of its hardness the filter properties at room temperature are almost as good as at liquid nitrogen temperature. The so far used so-called HEMEX quality is extremely expensive (46 USD/cm³). Therefore we decided to test a Czochralski grown single crystal (6 USD/cm³) which, according to the producer, shows the same optical quality like the HEMEX material. The experiment on the sapphire filter has shown, that the Czochralski grown material has exactly the same good filter properties for thermal neutrons as the expensive HEMEX one. The 10 cm long filter crystal tested shows a maximum transmission of 0.82 around a neutron wavelength $\lambda = 2.8 \text{ \AA}$, Fig.1d. At the shortest wavelength evaluated, $\lambda = 1.9 \text{ \AA}$, the transmission has slightly reduced to 0.78. At long wavelengths this value is obtained around $\lambda = 4.5 \text{ \AA}$.

Conclusion

Sapphire crystals grown using the Czochralski-method show the same good filter properties for thermal neutrons as the much more expensive HEMEX quality.

The results obtained for the crystal-1 of Bismuth are very encouraging. It is expected that a Bi-filter, composed of several independent single crystals, should be very carefully aligned with the (111) planes parallel to each other and what is very important, also with the same azimuth orientation. This should be tested in a forthcoming experiment.

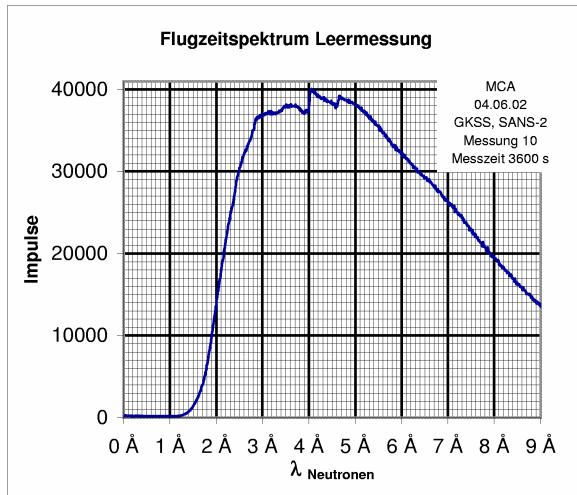


Fig.1a

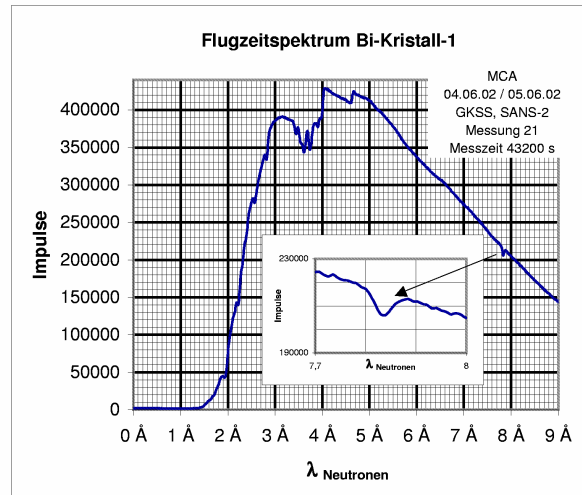


Fig.1b

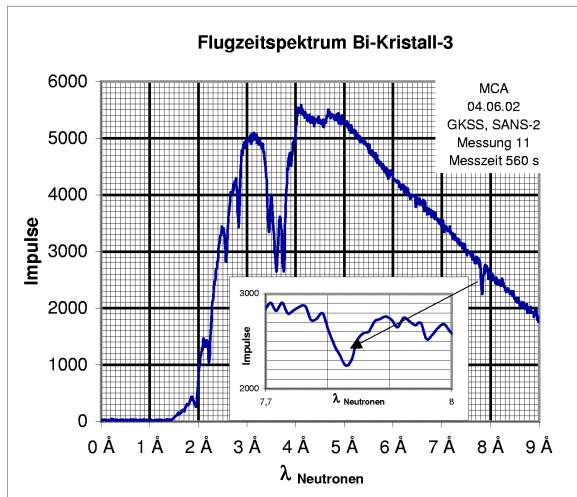


Fig.1c

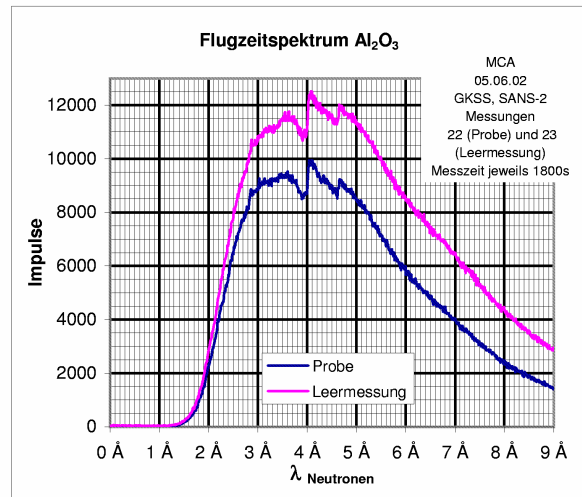



Fig.1d

	EXPERIMENTAL REPORT	GeNF SANS-2
Phase Separation Kinetics in Cu –0.9 at.% Ti		
Principal Proposer:	S. Prasetyo GKSS Research Centre	
Experimental Team:	S. Prasetyo, H. Eckerlebe GKSS Research Centre	
Date(s) of Experiment:	09, 10, 12 / 2002	

Scientific Objectives

A fine scale dispersion of second phase within a metallic matrix in a copper-titanium alloy can lead to significant strengthening. The most important methods of introducing a second phase within a metallic matrix are through precipitation hardening or age hardening. This commonly results from the decomposition of the solid solution during cooling. For reasons of entropy, the single phase state α of a solid solution with certain composition is thermodynamically stable only at elevated temperature. At lower temperatures the free energy of the system is lowered through phase separation or decomposition of the α phase into two phases α' and β .

The diffusion mechanism of the atomic species is involved in the decomposition reactions, and the thermodynamic equilibration of the precipitate microstructure vary as a function of both time and temperature. Therefore, the strength of the alloy can be determined by the precipitate microstructure as a result of the kinetics of precipitation hardening.

Small Angle Neutron Scattering (SANS) is used in this work because of its ability to provide access to structural analysis of unmixing alloy, in both, the early stages where the composition fluctuation can be small in spatial extension and in amplitude, and in the later stages of decomposition. By using SANS the quantity of the precipitates can also be determined.

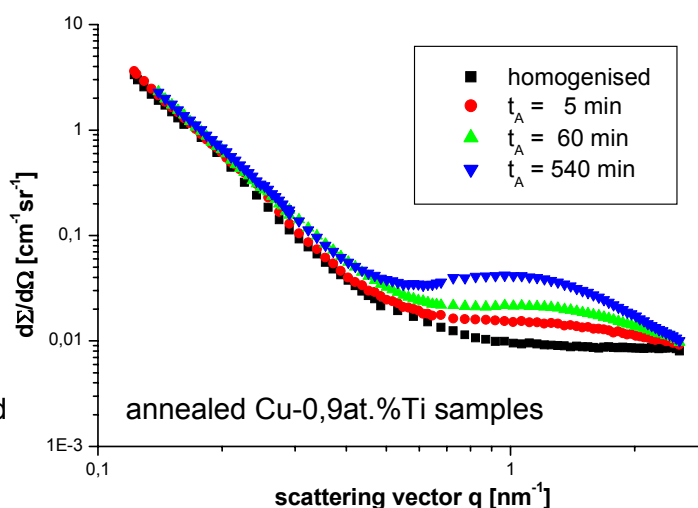


Figure 1:
Scattering curves of homogenised and for 5, 60 and 540 minutes annealing time.

Experimental Technique

Four Cu-0,9at.%Ti single crystals were solution annealed at four different homogenisation temperatures of 650 °C, 700 °C, 750 °C, and 800 °C respectively. These specimens were aged at 300 °C for 5, 20, 60, 180, and 540 minutes.

The neutron scattering measurements were carried out using the small angle scattering instrument SANS-2 at GKSS. The neutron wavelength was 0.57 nm. Distances from the 2-dimensional detector to the sample of 1 m, 3 m, 9 m, and 21 m were used.

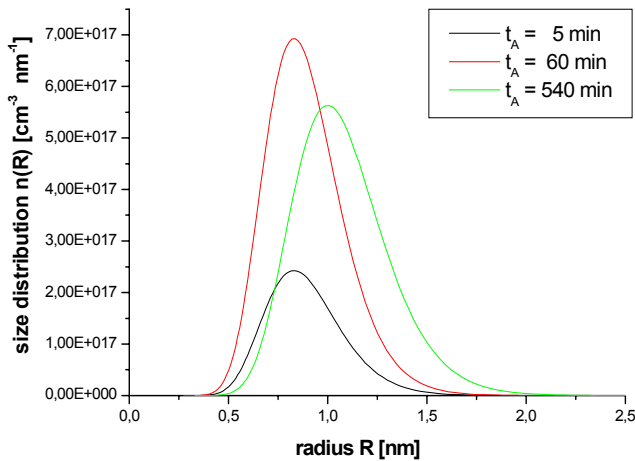
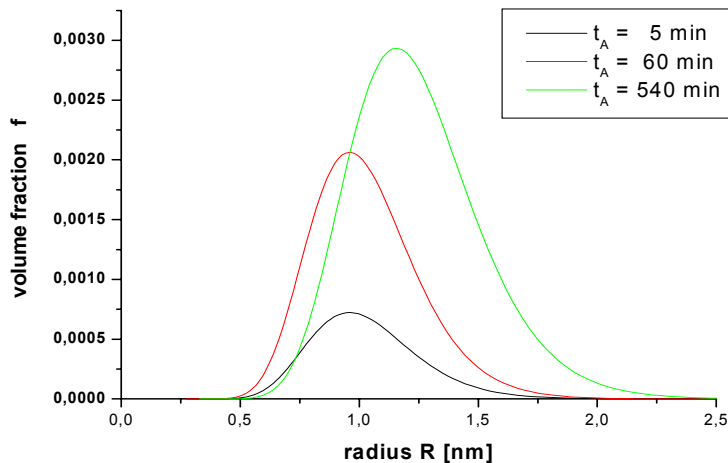


Figure 2:
a: Particle size distributions and




b: Volume fractions of precipitations assuming spherical particles.

Results

No precipitation had been formed in the sample during quenching (Fig. 1). After annealing for $t_A = 5$ minutes only, the effect of phase separation can clearly be seen. With increasing aging time (until $t_A = 60$ min), the volume fraction and the number density of the formed particles grow rapidly, but the radius remains nearly constant. This indicates, that the nucleation process is in progress during the first 60 min. Up to $t_A = 540$ min the mean radius increases, hence the nucleation process had already finished and the coarsening process had become dominant.

Reference

- [1] Wagner, R. and Kampmann, R., 1991, Homogeneous Second Phase Precipitation in Materials Science and Technology, Ed. Cahn, R.W., Haasen, P., and Kramer, E.J. Vol. 5, Chapt.4, Verlag Chemie GmbH, Weinheim.

	EXPERIMENTAL REPORT	GeNF SANS-2
Test of a new Interferometer for cold Neutrons built of Holographic Gratings		
Principal Proposer:	C. Pruner University of Vienna, Institute of Experimental Physics, Strudlhofgasse 4, A-1090 Vienna	
Experimental Team:	C. Pruner, M. Fally University of Vienna, Institute of Experimental Physics	
Date(s) of Experiment:	April 2002	

Scientific Objective

A novel type of interferometer for cold neutrons was employed to record interference fringes by rotating an auxiliary phase-flag through both beam paths. The observed decay of the interferogram directly yields the complete function $\Gamma^{-1}(x-x',t-t')$. Our interferometer consists of three holographically recorded neutronrefractive-index gratings (spacing: $\lambda = 385$ nm) made from deuterated (polymethyl)methacrylat, d-PMMA, which are arranged in the so-called symmetric LLL-geometry (Fig. 1). The overall length of the interferometer is $L = 300$ mm. To fulfill the high demands on stability the gratings are fixed on a rigid chassis made from Super-Invar. The advantage of this type of interferometer is that the gratings were adjusted once for ever during the optical recording. The recording parameters are optimized for a diffraction efficiency $\eta_{1,2,3}$ of about 50 % for each of the three gratings for a neutron wavelength of $\lambda = 2$ nm. The latter had been carried out in our laboratory in Vienna about four month before the measurement at the neutron beamline SANS-2.

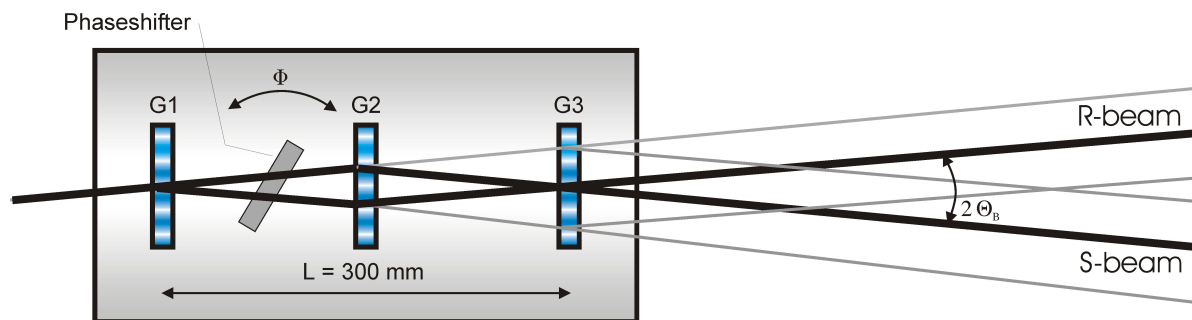


Figure 1: Sketch of the interferometer for cold neutrons based on holographically created density gratings in d-PMMA. By rotating a phase-flag through both beam paths a relative phase-difference occurs between the R- and the S-beam.

Experimental Techniques

To record an interferogram the interferometer was adjusted to the exact Bragg angle where maximum overall diffraction efficiency is observed. A phase-flag of Sapphire was inserted in both beam-paths between the first and the second grating. A rotation of the Sapphire generates phase-differences between the two beams which result in correlated intensity modulations behind the third grating. Those intensity changes are monitored on the detector matrix. The neutron-optical path-difference Δx as a function of the relative angle Φ of the phase-flag is given by

$$\Delta x = \lambda^2 \frac{\bar{b}_c}{2\pi} D_0 \left[\frac{1}{\cos(\Theta_B - \Phi)} - \frac{1}{\cos(\Theta_B + \Phi)} \right] \quad (1)$$

Here, D_0 is the thickness of the phase-flag, \bar{b}_c the coherent scattering-length density, and Θ_B the Bragg angle. The interference fringes and their decay with increasing phase-difference give direct experimental access to the absolute value of the normalized coherence function $\Gamma^{-1}(x-x',t-t')$ via the visibility, and as a by-product to the coherence length l_c (Fig. 2). The visibility v is defined as

$$v = \frac{I_{\max} - I_{\min}}{I_{\max} + I_{\min}} = m \left| \Gamma^{-1}(\Delta x - x_0) \right| \quad (2)$$

Main Results

If a Gaussian coherence function is assumed, the expected interference pattern can be described by

$$I_{R,S} = A_{R,S} + m \exp\left(-\left[\frac{\Delta x - x_0}{\sigma}\right]^2\right) \cos(\bar{b}_c \lambda (\Delta x - x_0)) \quad (3)$$

where σ is the width of the coherence function which is directly related to the coherence length l_c . Here, x_0 is the internal phase of the empty interferometer, the parameters $A_{R,S}$ and m are functions of the diffraction efficiencies $\eta_{1,2,3}$. From these considerations we obtained a coherence length of $l_c = 7 \pm 2$ nm and a maximum visibility of $v_{\max} = 1.75$ %. As a byproduct we estimated a value of $\bar{b}_c = 5.8 \pm 0.1 \cdot 10^{-14} \text{ m}^{-2}$ (theoretical value $\bar{b}_c = 5.715 \cdot 10^{-14} \text{ m}^{-2}$) for the coherent scattering-length density of Sapphire.

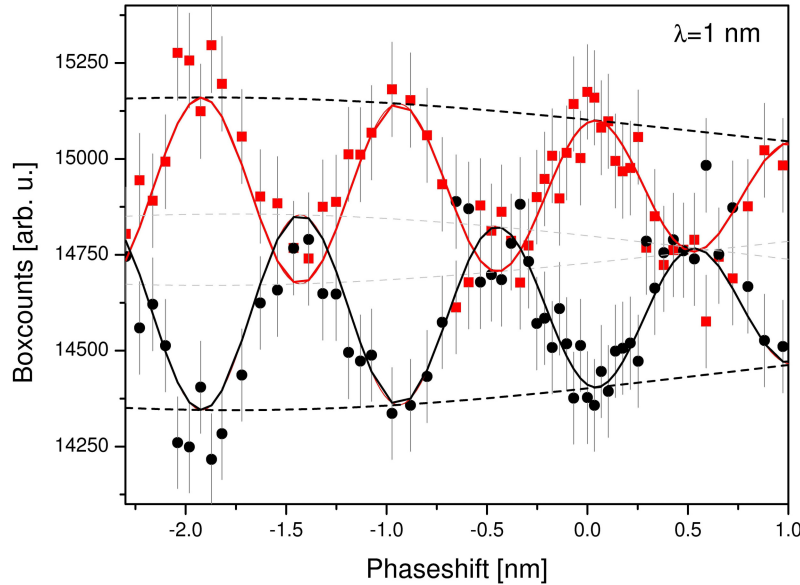



Figure 2: Interferogram obtained by rotating a $D_0 = 4.1$ mm thick phase-flag from Sapphire around an axis perpendicular to the plane of incidence. The measurement was performed at a neutron wavelength $\lambda = 1$ nm with a wavelength distribution $\Delta\lambda/\lambda = 10$ % and a detector counting rate of about 110/s. The collimation parameters are: Distance neutron-guide – interferometer 15.3 m, distance interferometer – detector 21.6 m, diaphragm neutron guide 10 mm x 40 mm, diaphragm interferometer 1 mm x 14 mm. The solid lines obtained from fitting eq. (3) to the data. The dashed lines represent the Gaussian envelope function which describes the decay of the visibility.

Relevance to other Applications or to other Techniques

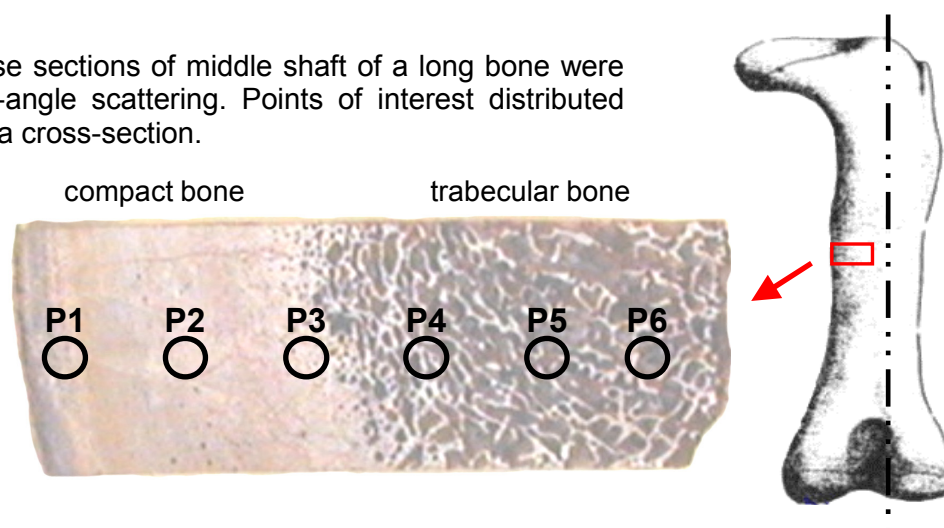
This new interferometer opens up the possibility of direct investigations about coherence properties of several cold neutron beamlines. A near future perspective will be the introduction of neutron interferometric techniques into material science by combining standard small angle measurements with interferometric techniques which will allow to determine the phase of small angle scattering signals.

	EXPERIMENTAL REPORT	GeNF SANS-2
SANS studies of fossil dinosaur bone		
Principal Proposer:	A. Pyzalla ¹ , M. Stempniewicz ¹ ¹ Institute for Materials Science and Technology, TU Berlin	
Experimental Team:	M. Stempniewicz ¹ , P. K. Pranzas ² , G. Kozik ² ² GKSS-Research Centre	
Date(s) of Experiment:	October 2002	

Scientific Objective

The growing interest in biologically formed high strength materials gave the motivation for experiments on sauropod bones. Sauropod dinosaurs were one of the largest terrestrial creatures (estimated body mass up to 80 tonnes) that lived for over 10 million years during the Jurassic period, 150 million years ago. Due to the body mass their bones were mechanically loaded more than any contemporary bone. Thus, features resulting from mechanical adaptation are expected to be found. Unfortunately, the information inscribed in the fossils has been altered in the perthotaxic and taphic processes (pre-burial removal and post-burial modifications). Thus, bone tissue is mineralized but organic. It is the interaction between organic phase, chiefly collagen, and mineral phase, apatite, that produces the mechanical properties. Obviously, these properties cannot be investigated directly since the half-life period of collagen is not longer than 30 thousand years. Therefore, this small-angle neutron scattering investigation is a preliminary study of the structures present in fossil bone that might be useful in future explanation of mechanical behaviour of the giant animals skeletons.

Figure 1: Transverse sections of middle shaft of a long bone were subjected to small-angle scattering. Points of interest distributed along the radius of a cross-section.



Experimental Techniques

The middle shaft of a long bone was chosen for the investigation for two reasons. First, ontogenetically it is the oldest part of bone, containing information on the biological development of an individual. Second, it is build mainly by compact bone structure, which is highly mineralised, thus, more resistant to taphonomic processes. Cylinders of 15 mm diameter were drilled out of long bones of *Barosaurus africanus* and *Brachiosaurus brancai* (museum pieces collected by German Tendaguru Expedition 1909–1913 in Tanzania, East Africa; presently stored in Natural Science Museum of the Humboldt University in Berlin). The cylinders were subsequently cut along the cylinder axis to uncover the transverse projection of compact bone structure.

Small-angle neutron scattering measurements were carried out with the SANS-2 instrument on sections thinned to approx. 3.5 mm. Selector monochromated neutrons with a mean wavelength of $\lambda = 0.57$ nm and a wavelength spread of $\Delta\lambda/\lambda = 10\%$ were used. The scattered beam was recorded by means of an area detector. Since the samples showed the transverse projection of the compact bone structure no anisotropy was observed, therefore the intensity was azimuthally averaged. Macroscopic differential scattering cross sections were obtained by calibration against a Vanadium standard. Sample to detector distance was adjusted to cover the range of scattering vector: $2.1 \cdot 10^{-3} - 2.7 \cdot 10^{-1} \text{ \AA}^{-1}$.

Main Results

Fig. 2 shows a typical set of scattering curves collected for femur of *Barosaurus africanus*. Subsequent curves correspond to the points distributed along the radius of the cross-section. All the curves are corrected for the sensitivity of the detector and background. In contemporary bone the scattering contrast is due to mineral particles suspended in collagen pattern. The fossil bone contains no collagen due to the decay of organic matter in the process of fossilization. The space left by the collagen is then taken by recrystallizing bone mineral. Thus, the scattering observed is most likely due to porosity of the recrystallized mineral, which is confirmed by the high value of scattering cross section. The tendency observed in all samples is that the scattering cross section increases for points located closer to the marrow canal.

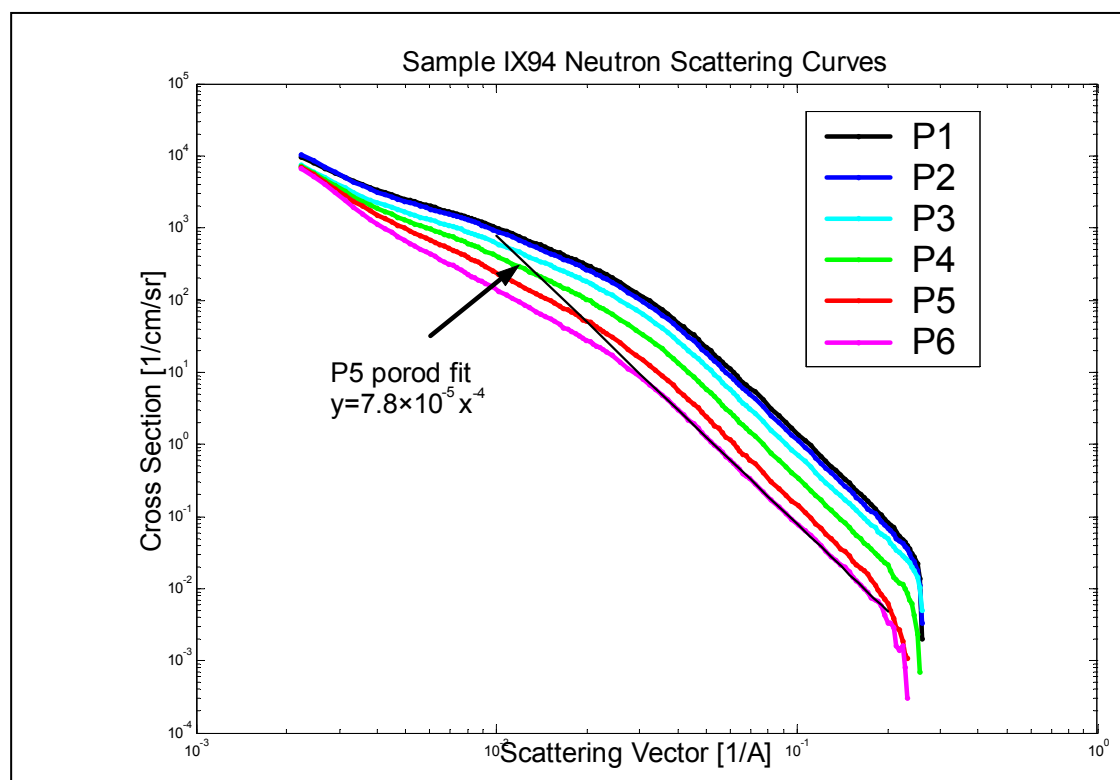



Figure 2: A typical set of scattering curves collected for femur of *Barosaurus africanus*. Subsequent curves correspond to the points distributed along the radius of the cross-section (see Fig. 1).

References

- [1] Thomas R.D.K., Olson E.C. *A Cold Look at the Warm-Blooded Dinosaurs* Westview Press 1980;
- [2] Turner C.H., Burr D.B. *Bone* 14: 595–608, 1993
- [3] Heinrich W-D. *Mitt. Mus. Nat. kd. Berl. Geowiss.* 2:25–61, 1999
- [4] Bacon G.E. *et al. Journal of Applied Crystallography*, Vol. 12, 1979
- [5] Weiner *et al. Journal of Structural Biology*, Vol. 126, 1999, pp. 241–255

	EXPERIMENTAL REPORT	GeNF SANS-2
Characterization of aging processes of fats by SANS		
Principal Proposer:	D. W. Schubert Freudenberg Forschungsdienste KG, Weinheim, Germany	
Experimental Team:	P. K. Pranzas, G. Kozik GKSS Research Centre	
Date(s) of Experiment:	April 2002	

Scientific Objective

Fats or triglycerides are glycerol esters with saturated aliphatic carboxylic acids with long carbon chains (fatty acids) [1, 2]. They are used for nutrition and in technical applications, e. g. as lubricants. Our aim is to study structural changes in fats due to aging processes with the help of small angle neutron scattering (SANS) and to correlate the results with rheological properties.

Experimental Technique

Two fats – a new and an aged sample which is approx. 2 years older – were measured at the SANS-2 instrument at room temperature in quartz cuvettes with a sample thickness of 1 mm. A wavelength of 0.58 nm with a resolution of $\Delta\lambda/\lambda = 0.1$ and distances between sample and detector of 80, 380, 780, 1380 and 2080 cm were used to cover the range of scattering vector q from 0.018 to 2.28 nm^{-1} .

Results

In figure 1 the scattering incoherent scattering curves of the two samples are shown after subtraction for empty cuvette and ring.

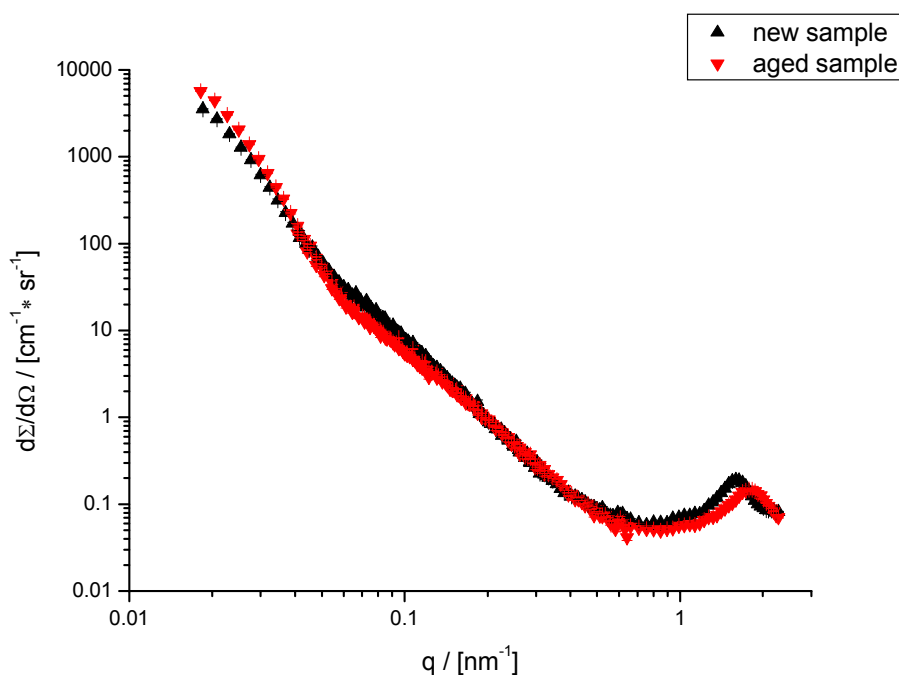



Figure 1: SANS curves of two fat samples of different age.

Both curves have a maximum at high q -values which corresponds to an ordered structure having a size between 3 and 4 nm. At medium q -range a significant difference between the two curves is visible. In this q -range the scattering of the aged sample is lower than the scattering of the new sample. From the mean q -value we calculated a structural dimension of approx. 80 nm. In the range of low q -values where large particles are scattering it is reverse: Here the scattering of the older sample is higher than that of the new sample.

The described changes in the scattering curves from new to aged sample demonstrate that an aggregation of large particles (> 100 nm) has taken place during the aging process. A reduction of structures with sizes of approx. 80 nm was observed due to aging. This indicates that particles which have sizes of about 80 nm form preferentially the large agglomerates. First measurements with the DCD instrument could not confirm the formation of large particles due to small scattering power, high absorption and incoherent scattering (see DCD report).

References

- [1] Fat. Sci. Technol. (1987) 89, 99
- [2] Seifen, Öle, Fette, Wachse (1987) 113, 455

	EXPERIMENTAL REPORT	GeNF SANS-2
Structural parameters of adsorbed detergent on polystyrene latex particles		
Principal Proposer:	Rongbiao Wang, H. Schmiedel Institute for Experimental Physics I, University Leipzig, Germany	
Experimental Team:	P. K. Pranzas, Rongbiao Wang GKSS Research Centre	
Dates of Experiment:	29.07.–05.08. and 07.10.–13.10.2002	

Scientific Objective

We have demonstrated a novel method of evaluating SANS curves which allows determining in a straightforward manner simultaneously the internal geometry and hydration of single bilayers in unilamellar vesicles at high water excess [1] and the multilamellar vesicle portions in extruded POPC dispersions [2].

The main objective of this experiment is to apply the method to anionic polystyrene latex particles coated with cationic detergent cetyltrimethylammonium bromide (CTAB). From the results of our Isotherm Titration Calorimeter (ITC) experiment, the latex particles adsorb an amount of CTAB after the ionization of its surface by NaOH. In this SANS experiment, we plan to determine the thickness of the adsorbed detergent layers and to explain the coating mechanism in terms of a scattering density profile. Further more we need to confirm the contrast matching point of these small commercially available latex particles (91 and 61 nm diameter) in D₂O/H₂O mixtures.

Experimental Techniques

In order to maintain the physical properties of latex dispersion in light water, we carried out all coating experiments in H₂O/D₂O mixtures with a mole ratio for D₂O (X_D) of 0.9, a latex concentration of 2.61 mg/ml for PSCOOH 91 and 2.51 mg/ml for PSCOOH 61 for every dispersion. After adding NaOH and CTAB to latex dispersion ultra sonic treatment for at least 30 minutes at 50 °C ensures that all samples are homogeneous. Samples without CTAB were measured as background.

For contrast variation measurements 7 samples were prepared with increasing concentrations of D₂O. To avoid multiple scattering we used a 1 mm cuvette for low D₂O concentrations and a 2 mm cuvette for higher D₂O concentrations. The measurement times were chosen such that we obtained approximately the same ratio for all samples.

Main Results

Our latex nanoparticles exhibit characteristic oscillations in the SANS curves for small q values (up to 0.3 nm⁻¹, Figure 1). The concentration of CTAB below the critical micelle concentration (cmc) 0.33 mg/ml (= 0.9 mM) does not influence the scattering curve significantly. The scattering intensity increases with the concentration of CTAB. Our fitting program [1] can detect the multi layers of detergent on latex particles in terms of the scattering length density. However, further calculations have to be performed, to obtain reliable scattering length densities. The Gift program (available from Prof. Dr. Otto Glatter,

University of Graz, Austria) shows clearly that the latex beads increase their size by 2.3 nm in radius after the addition of 0.8 mg/ml (=2.25 mM) CTAB. Polystyrene latex particles modified with carboxylic group adsorb the cationic surfactant CTAB through electrostatic attraction. The adsorption isotherms of DTAB (cmc 14 mM) on latex particles of low negative charge and modified with aromatic amino groups have been already studied [3, 4] by a surface tension technique. These studies by Zhao *et. al.* by means of dynamic light scattering (DLS) support the postulate that the surface roughness (“hairness”) of the latex particle causes low particle mobility. Instead of adding the salt NaBr which enhances the hydrophobic interaction between polymer chains and the alkyl tails of surfactant and also between the alkyl tails themselves, we applied NaOH for latex surface ionization. The ITC experiment demonstrates the effective adsorption of CTAB (Figure 3). With increasing NaOH concentrations the amount of adsorbed CTAB also increases.

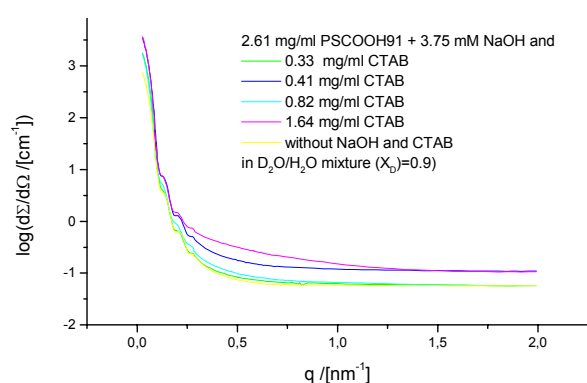


Figure 1: Scattering curve of 2.61 mg/ml PSCOOH 91 in $X_D=0.9$ with different concentration of CTAB.

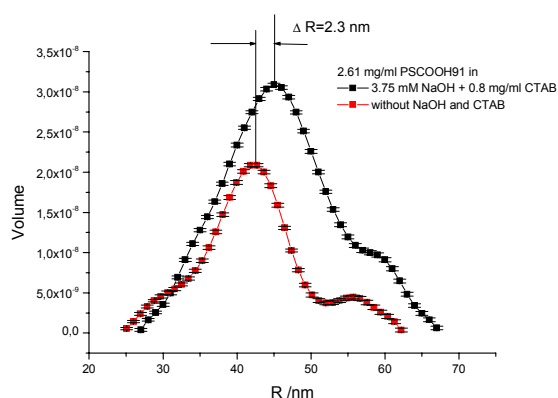


Figure 2: Calculation of GIFT Program for scattering curve after subtraction of incoherent scattering. The latex particles became in this case 2.3 nm larger in radius.

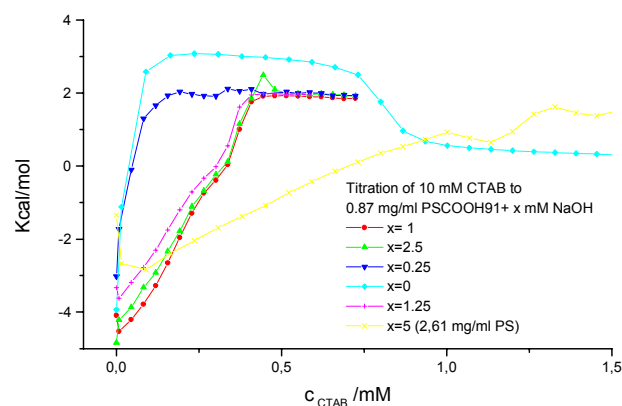



Figure 3: ITC (Isotherm Titration Calorimeter) experiment depends on NaOH concentration.

References

- [1] H. Schmiedel, P. Jörchel, M. Kiselev, G. Klose: Determination of Structural Parameters and Hydration of Unilamellar POPC/ $C_{12}E_4$ Vesicles at High Water Excess from Neutron Scattering Curves Using a Novel Method of Evaluation, *J. Phys. Chem. B*, 105, 2001, 111–11.
- [2] H. Schmiedel, R. Wang, A. Islamov, G. Klose: Determination of multilamellar vesicle portions and structural parameters in extruded POPC dispersions by SANS, *J. Phys. Chem. B, in preparation*
- [3] J. Zhao and W. Brown, *Langmuir*, 12, 1996, 1141–1148
- [4] J. Zhao and W. Brown, *Langmuir*, 12, 1995, 2944–2950

	EXPERIMENTAL REPORT	GeNF DCD
Double crystal diffractometer DCD		

Short Instrument Description:

The double crystal diffractometer for ultra small angle neutron scattering (USANS) uses non-polarised cold neutrons to characterise in materials large creep pores, fatigue and sintering cavities, precipitates, voids, bubbles, etc. with particle sizes with about 100 nm to 40 µm in diameter.

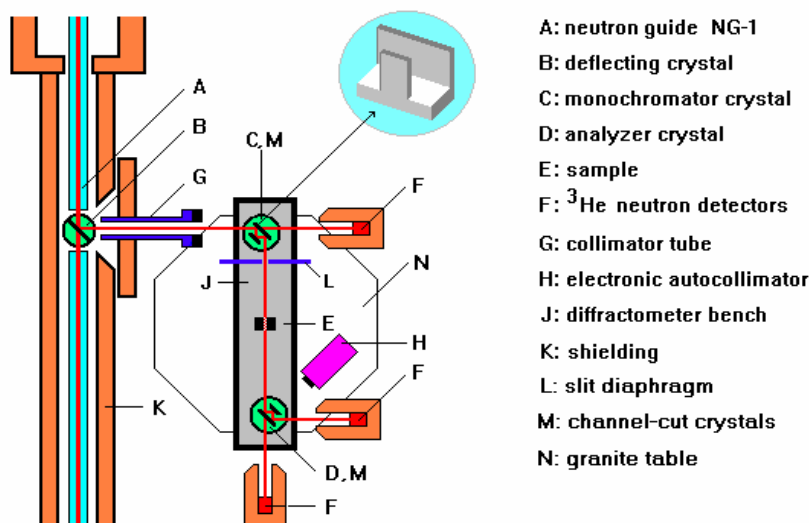
Local Contact:

Dieter Bellmann

Phone/Fax : +49 (0)4152 87-2803 / +49 (0)4152 87-2840


e-mail: dieter.bellmann@gkss.de

Schematic View of DCD:



Instrument Details:

Beamline:	beamline 8 – cold neutron guide NG-1, max. beam cross section 30 x 40 mm ²
Deflecting crystal:	Si(111), Si(311), mosaic spread 0.1 mrad
Monochromator / analyser:	channel-cut perfect Si crystals
Wavelength resolution	$\Delta\lambda/\lambda = 1 \cdot 10^{-5}$ ($\lambda = 0.443$ nm)
Max. flux at deflecting crystal	$\Phi = 2.3 \times 10^8$ cm ⁻² s ⁻¹
Flux at sample position:	$\Phi \approx 500$ cm ⁻² s ⁻¹ (Si(111), $\lambda = 0.443$ nm) $\Phi \approx 180$ cm ⁻² s ⁻¹ (Si(311), $\lambda = 0.232$ nm)
Range of momentum transfer:	$1 \cdot 10^{-5}$ nm ⁻¹ $\leq Q \leq 5 \cdot 10^{-2}$ nm ⁻¹
Detectors:	three ³ He-detectors
Control of crystal alignment:	electronic autocollimator, angular resolution < 0.05 µrad

	EXPERIMENTAL REPORT	GeNF DCD
DCD with an additional beam line		
Principal Proposer:	D. Bellmann GKSS Research Centre	
Experimental Team:	D. Bellmann GKSS Research Centre	
Dates of Experiment:	July – Sept. 2002	

Experimental Technique

Ultra small-angle neutron scattering (USANS) experiments combined with the conventional SANS instrument is a useful technique for detecting particles in a wide size range from nanometres to about 20 μm . Up to the present DCD was operating at a wavelength of 0.443 nm. USANS investigations of early stages of metal foam formation have shown [1] that structures greater than 20 microns have to be taken into account for the detection of much greater pores in the samples. Therefore DCD was equipped with a second beam line using triple-bounce channel-cut perfect Si(311) crystals at a neutron wavelength of 0.232 nm. Thus the detectable size range was extended to more than 40 microns. By changing the deflecting crystal automatically in the gap of the cold neutron guide NG-1 neutrons with a wavelength of 0.443 nm and 0.232 nm are now available for scattering experiments with DCD.

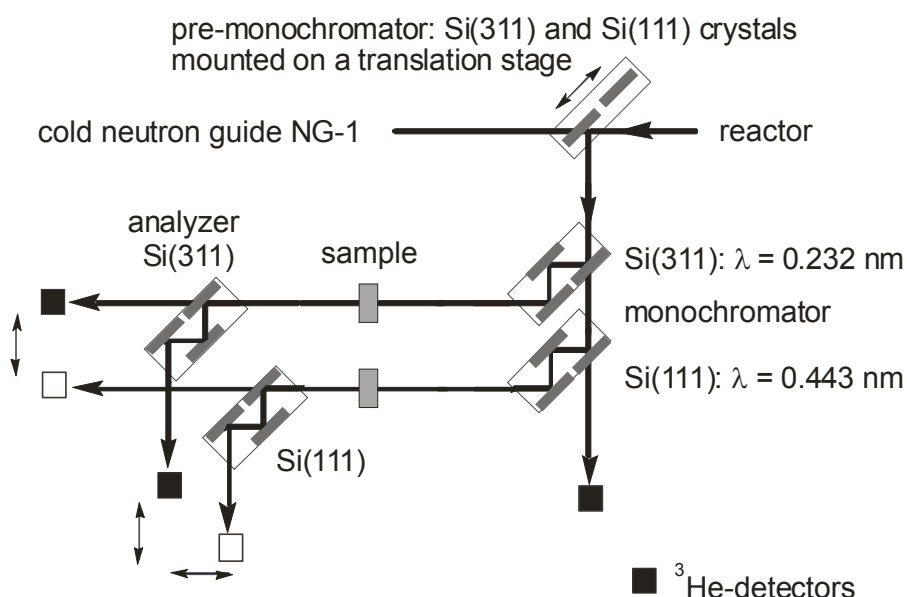


Figure 1: The layout of DCD at GeNF with triple-bounce channel-cut perfect silicon crystals.

In figure 2 the “rocking curves” (without a sample in the beam) at both neutron wavelengths are shown. The FWHM of these distributions decreases from 18.3 μrad to 5.4 μrad . Therefore the maximum detectable pore sizes increases from about 24 μm to 43 μm .

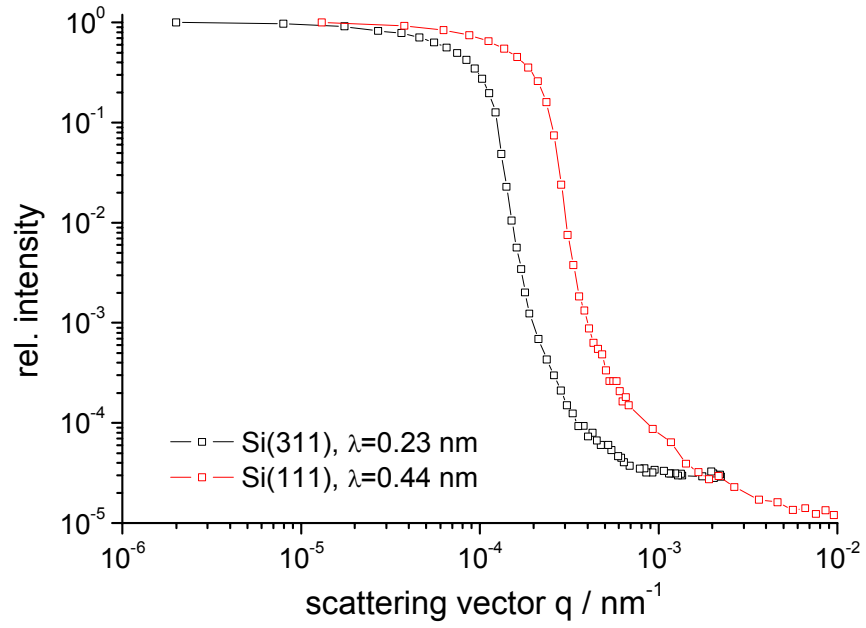



Figure 2: Resolution function of DCD for triple-bounce channel-cut perfect Si(311) and Si (111) crystals.

Reference

- [1] Banhart, J.; Bellmann, D.; Clemens, H.: Investigation of metal foam formation by microscopy and ultra small-angle neutron scattering, Acta Mater. 49 (2001) 3909–3420

	EXPERIMENTAL REPORT	GeNF DCD
Characterization of aging processes of fats by USANS		
Principal Proposer:	D. W. Schubert Freudenberg Forschungsdienste KG, Weinheim, Germany	
Experimental Team:	D. Bellmann GKSS Research Centre	
Dates of Experiment:	April 2002	

Scientific Objective

Fats or triglycerides are glycerol esters with saturated aliphatic carboxylic acids with long carbon chains (fatty acids) [1]. They are used for nutrition and in technical applications, e. g. as lubricants. Our aim is to study structural changes in fats due to aging processes with the help of ultra small angle neutron scattering (USANS).

Experimental Technique

Two fats – a new and an aged sample, approx. 2 years old, were measured with the double crystal diffractometer (DCD) at room temperature in quartz cuvettes, sample thickness of 1 mm. DCD measurements were carried out at a wavelength of 0.44 nm to detect “particles” in the range from about 500 nm to 10 μm .

Results

The aim of this experiment was to get information about structures greater than 500 nm which may be a result of an aging process in these samples.

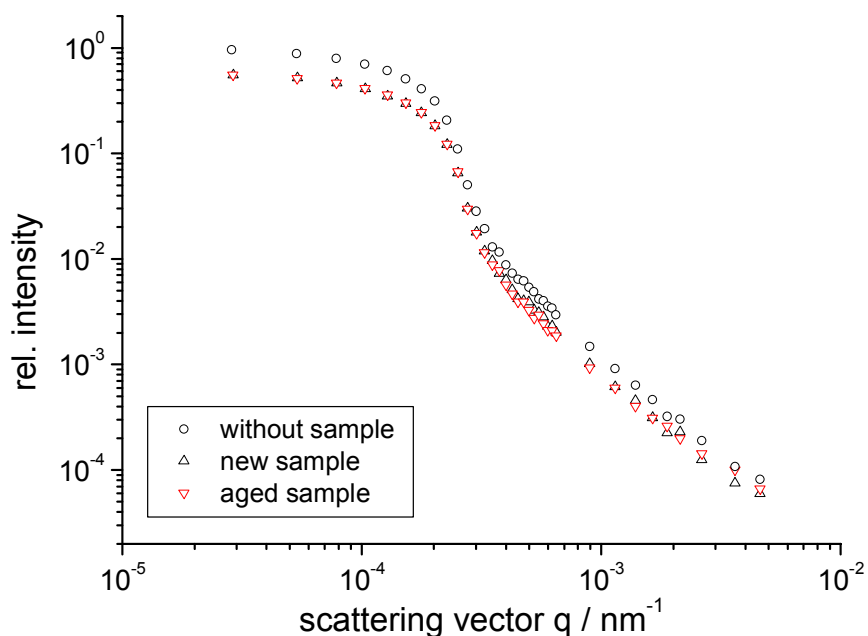



Figure 1: USANS curves of two fat samples of different age.

In figure 1 the scattering curves of the two samples without correction of absorption and incoherent scattering are shown together with the so called "rocking curve" of the empty beam without a sample.

By reason of the very small scattering power of the new and the aged sample, which are nearly equal in the measured scattering vector range, and a transmission of only about 60% as a result of absorption and incoherent scattering, an analysis of these scattering data is very uncertain. In order to get reliable results measurements have to be done with a much higher precision. The structure of possible agglomerates is not really known and it seems that an essential scattering length density difference does not exist between such structures and the matrix.

Reference

- [1] Seifen, Öle, Fette, Wachse 113 (1987), 455

	EXPERIMENTAL REPORT	GeNF TOREMA-2
Neutron reflectometer TOREMA-2		

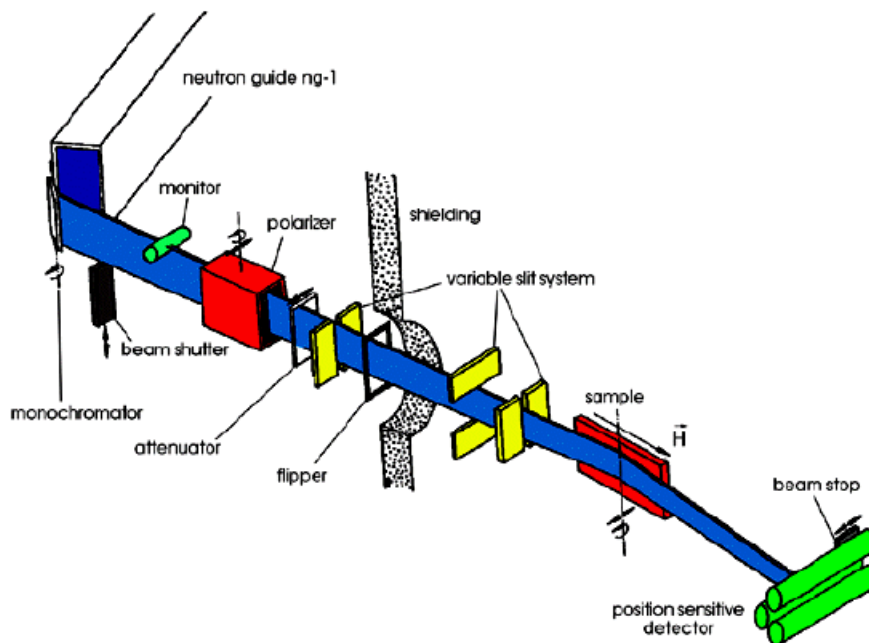
Short Instrument Description:

The total reflection machine TOREMA is a reflectometer to study surfaces, thin films and membranes with cold non-polarised neutrons with high resolution. In 2003 TOREMA will be modernised in order to provide an environment for polarised neutrons, to improve the sample environment and to apply a new detector.

Local Contact:


Dr. Dieter Lott
 Phone/Fax : +49 (0)4152 87-2806 / +49 (0)4152 87-2840
 e-mail: dieter.lott@gkss.de

Schematic View of TOREMA-2:



Instrument Details:

Beamline:	beamline 8 (NG-1)
Wavelength:	$\lambda = 0.435 \text{ nm}$
Wavelength resolution	$\Delta\lambda/\lambda = 0.02$
Collimation:	$1.745 \times 10^{-4} \text{ to } 8.73 \times 10^{-4} \text{ rad}$
Angular range:	$0 \leq \theta \leq 2.5^\circ$ (in preparation: $0 \leq \theta \leq 10^\circ$)
Flux at sample position:	$\Phi = 5 \cdot 10^4 \text{ cm}^{-2} \text{ s}^{-1}$
Detector:	2-dim position-sensitive ^3He -counter ^3He pencil counter
Ancillary equipment:	refrigerator cryostat; temp.-range: 12-475 K

	EXPERIMENTAL REPORT	GeNF TOREMA-2
Accurate annealing experiments by time-temperature superposition for polymers close to the glass transition		
Principal Proposer:	A. Pohlers ¹ , M. Stamm ¹ , H.-D. Braune ²	
Experimental Team:	A. Pohlers ¹ , H.-D. Braune ² , U. Tietze ²	
	¹ Institute of Polymer Research Dresden, Germany	
	² GKSS Research Centre	
Dates of Experiment:	December 2001 / April – June 2002	

The interdiffusion at polymer-polymer interfaces in the region of the glass temperature depends both on time t and temperature T of the annealing process. With increasing temperature as well as with increasing time the interdiffusion proceeds further, and both parameters are therefore equivalent to some extent. To achieve a certain amount of interdiffusion one can wait a long time at low temperature close to the glass transition temperature T_g or one can receive the same result by waiting a shorter time at a higher temperature. This equivalence is expressed by the time-temperature superposition principle. One can define an effective annealing time

$$\tau = \int_{t=0}^{t_E} \frac{dt}{\alpha(T,t)} \approx \sum_{t \leq t_E} \frac{\Delta t}{\alpha(T,t)} \quad (1)$$

with the shift factor $\alpha(T,t)$ described by the semi-empirical Williams-Landell-Ferry (WLF) equation [1]:

$$\lg \alpha(T,t) = \frac{-c_1(T_{Ref.}) \cdot (T(t) - T_{Ref.})}{c_2(T_{Ref.}) + T(t) - T_{Ref.}} \quad (2)$$

The material coefficients c_1 and c_2 must be specified separately for the interested polymer material as well as the used reference temperature $T_{Ref.}$. For polystyrene and $T_{Ref.} = 120$ °C it was found [2,3]:

$$c_1 = -9,06 \text{ and } c_2 = 69,8 \text{ } ^\circ\text{C}. \quad (3)$$

Using a short integration time of $\Delta t \approx 1$ s, it is possible to register all annealing contributions over the general annealing run including heating and cooling processes accurately and the effective annealing time τ can be determined [4..6].

Fig. 1 shows the PC-controlled offline-annealing equipment with a vacuum drying oven HERAEUS VT 6060P ($T_{max} = 300$ °C). The oven has a special mushroom-like sample table with a cooling option for the heating plate. To measure the temperature, a thermocouple with a small thermal capacity is installed directly onto the sample surface. After evacuation, the oven is heated up to the reference temperature. During the annealing experiment the temperature is measured in short time intervals and the effective annealing time is calculated by WLF-equation. When the effective annealing time was reached, the heating is stopped and the nitrogen cooling gas is inserted. One part of the nitrogen gas cools the sample surface directly, another part flows through the sample table to both the separated heating

plate and the surface of the sample table. For a faster cooling process the cooling gas is pumped through. The effective annealing time is accumulated over heating as well as cooling process. Fig. 2 and 3 show an annealing experiment at a PS(D)/PS(H) double layer sample for neutron reflectivity experiments. It should be noted that the parts of the effective annealing time are neglected where the temperature drops significantly below T_g , i.e. at 90..95 °C.

Acknowledgment

We thank Dr. T. Kuhlmann, Fraunhofer Institute for Applied Optics and Precision Engineering Jena for helpful discussions and a software example of data handling. We thank GKSS Research Centre Geesthacht GmbH for the financing support and BMBF for a research grant.

References

- [1] J. D. Ferry: Viscoelastic Properties of Polymers, Wiley, New York (1981), Cap. 11
- [2] P. F. Green, J. Kramer: J. Mater. Res., 1 (1) (1986) 202–204
- [3] J. F. Tassin, L. Monnerie: Macromolecules, 21 (1988) 1846–1854
- [4] J. F. Tassin, L. Monnerie, L.J.Fetters: Macromolecules, 21 (1988) 2404–2412
- [5] T. Kuhlmann: Diss., J. G. - Universität Mainz, Mainz (1999), 70–73
- [6] A. Pohlers, H.-D. Braune, U. Tietze: Accurate annealing experiments by time-temperature superposition principle on polymer interfaces, ESS European Conf., Bonn, 14.–17.05.2002

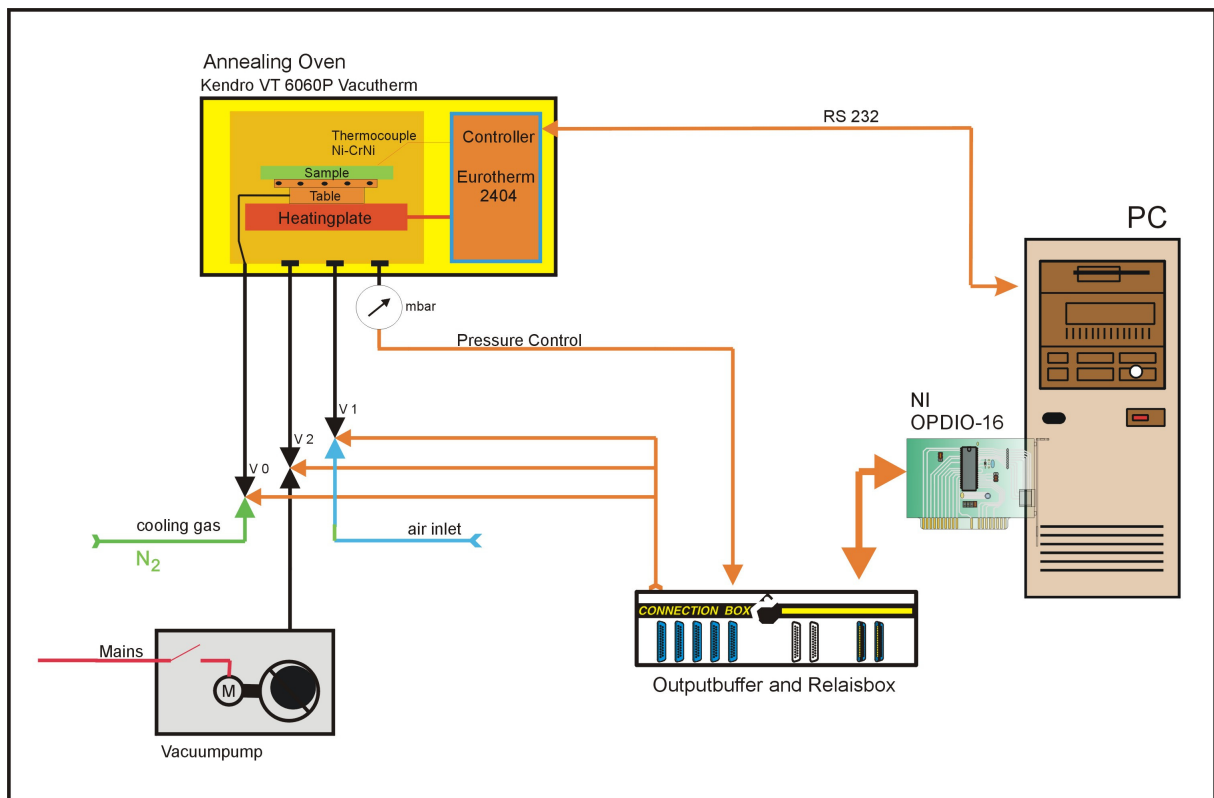


Figure 1: Block diagram of the annealing experiment.

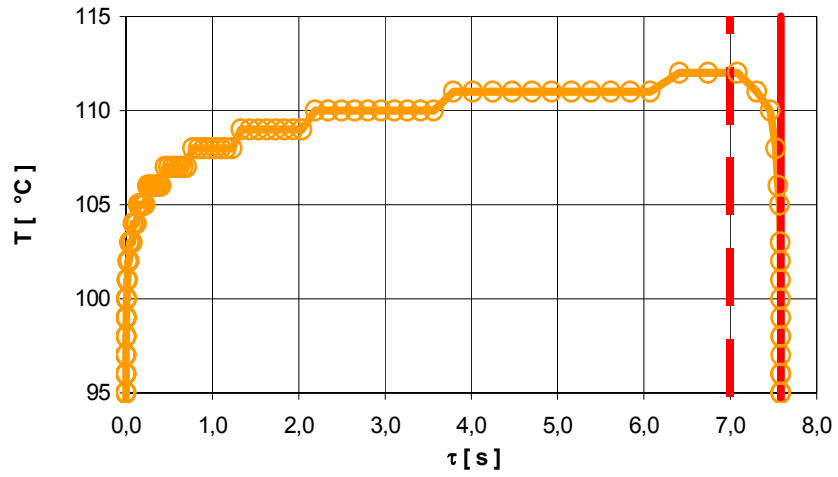


Figure 2: $T - \tau$ diagram (heating stop --- , cooling stop —).

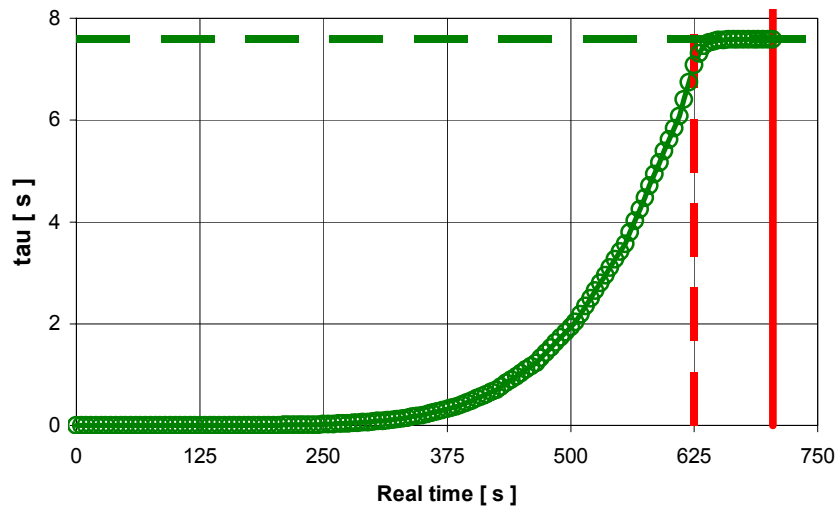
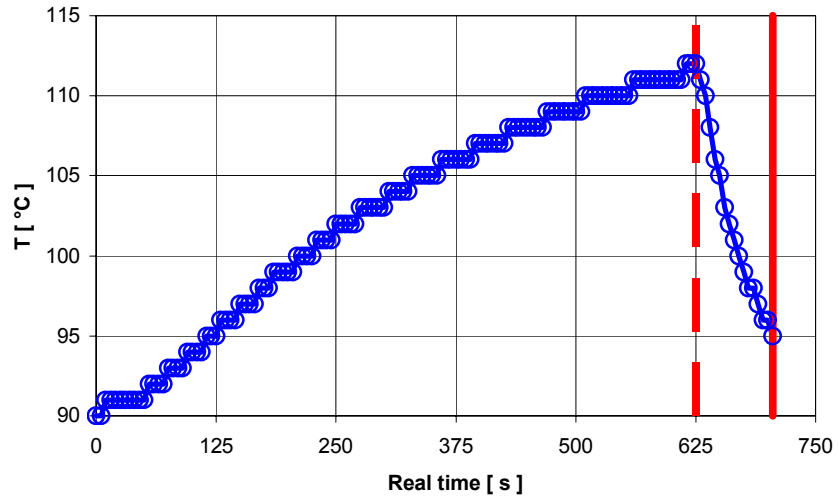



Figure 3: Real annealing time diagram (heating stop --- , cooling stop —).

	EXPERIMENTAL REPORT	GeNF TOREMA-2
Asymmetric interdiffusion between weakly interacting polymers as determined by neutron reflectometry		
Principal Proposer:	X. Yang ² , A. Pohlers ¹ , D. Jehnichen ¹ , M. Stamm ¹	
Experimental Team:	X. Yang ² , A. Pohlers ¹ , U. Tietze ³	
	¹ Institute of Polymer Research Dresden, Germany	
	² Dutch Polymer Institute and Applied Physics Department, Eindhoven University of Technology, The Netherlands	
	³ GKSS Research Centre	
Date(s) of Experiment:	April – June 2002	

It is of great importance to understand the basics of polymer interdiffusion and adhesion for many practical applications. The interdigitation of the chains at the polymer-polymer interfaces plays a decisive role. Studies of the thermally initiated interfacial diffusion connected with the formation of interface thickness and profile are of particular interest in this respect.

A suitable experiment is the study of neutron reflection (NR) on a polymer-polymer sample system consisting of deuterated and protonated layers generating a scattering contrast at the interface. In our experiments we use partially compatible layers of deuterated polystyrene PS(D) and brominated polystyrenes PBr_x(H) with a variable degree of bromination x. PS(D) and PS(H) (i.e. PBr_xS at x = 0) are at investigated molecular weights fully compatible, while brominated polystyrene (PBr_xS with x = 1) is strongly incompatible with polystyrene [1]. Interfacial diffusive mixing begins when two polymer surfaces are brought into contact and when at least one polymer is in the molten state [2]. Extent and rate of interdiffusion depend on the mobility and interactions between the two polymers [3]. Generally, polymer diffusion in the melt can be described within the framework of the reptation model proposed by Edwards [4] and De Gennes [5]. For a rigorous application of the reptation model, however, equal molecular weights, zero effective interaction and equal mobility of components has to be assumed. Those quantities are not equal in present experiments and interaction is not negligible. For the analysis of the experiments we assume a model which can be justified by the reptation model.

The characteristic parameters of used sample materials are given in Tab. 1. The double layers were prepared on polished silicon wafers (diameter 4") after cleaning with isopropanol, acetone and toluene by using spin coating and floatation techniques. Each layer has a thickness of about 500 nm. After preparation the samples were dried in vacuum at 60 °C/ 24 h to remove residual solvent and water.

Table 1: Characteristic parameters of sample materials.

Parameter	Bottom layer	Top layer of sample			
		A	B	C	D
Material	PS(D)	PS(H)	PBr _{0.037} S (H)	PBr _{0.076} S (H)	PBr _{0.11} (H)
M _n (kg/mol)	113.0	113.5	123.4	127.8	180
M _w / M _n	1.03	1.03	1.04	1.03	1.05
T _g (°C)	103	102	107	109	110

All samples were examined on the neutron reflectometer TOREMA II over some decades in a logarithmic scale of annealing time. The neutron wavelength was $\lambda = 0.435$ nm with a resolution $\Delta\lambda/\lambda \leq 1.5$ % and the incident angle $\alpha \leq 2.2^\circ$. The offline annealing experiments were carried out in a special furnace [6,7]. According to suitable reduction of experimental data by the software PANORAMA [8], the measured reflection curves were approximated with an asymmetric fitting model [9..11]. Starting conditions of the fit model assume homogeneous sample layers with an estimated film thickness as well as estimated scattering length densities.

Bromination does not only change the compatibility with PS(D), but also increases the glass transition temperature T_g (see table 1). This causes an asymmetrical interdiffusion between both sublayers and, consequently, at a critical degree of bromination the molecular interaction and interdiffusion will be disordered significantly by repulsive forces. Above the critical degree of bromination the interdiffusion slows down more and more. The comparison of concentration profiles for PS(D)/PS(H) and PS(D)/PBr_{0.11}S(H) samples in figure 1 shows clearly these effect during increasing annealing time. It should be noted that the degree of bromination $x = 0.11$ is close to the critical one.

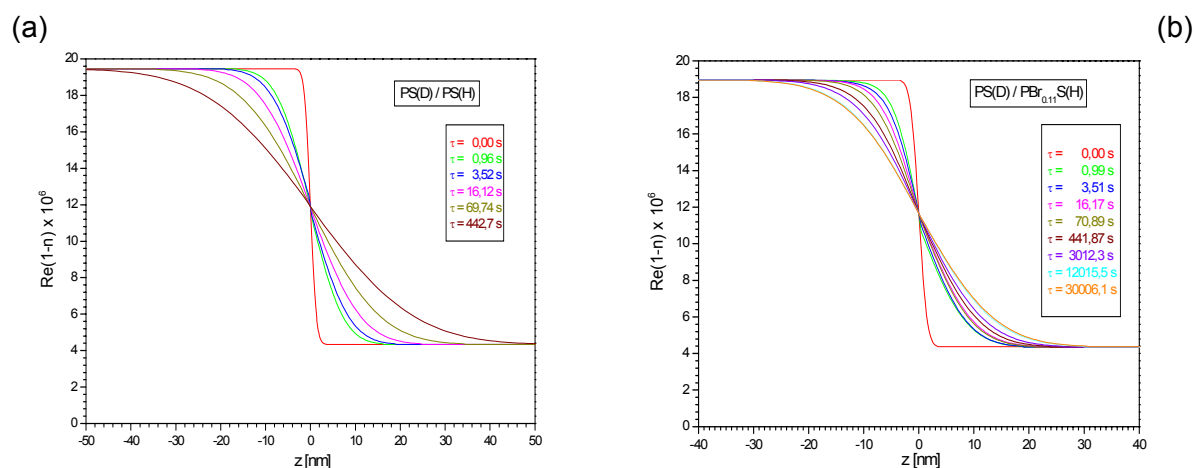


Figure 1: Comparison of concentration profiles vs. real annealing time for the samples: (a) PS(D)/PS(H), (b) PS(D)/PBr_{0.11}S(H).

Figure 2 shows measured and calculated reflectivity curves of the PS(D)/ PBr_{0.11}S(H) double layers for increasing annealing times. The fringes are more and more damped and the interpretation and fitting becomes increasingly difficult, especially for the last two annealing times. Therefore, conclusions close to the interaction balance and at the end of the interdiffusion processes are limited. The effect of changing T_g of both sublayers also should be kept in mind.

We get more detailed analysis of concentration profiles with moment plots versus the real annealing time [11]. The first moment of the concentration profile reflects the form of interface during interdiffusion (figure 3) and permits a determination of time-dependent movement of both sublayers. The results for the PS(D)/PS(H) sample show a symmetrical interdiffusion during the annealing process, but all samples with a brominated component indicate asymmetrical interdiffusion at the beginning of annealing and symmetrical interdiffusion profile later. In comparison with the other brominated samples the PS(D)/PBr_{0.11}S(H) double layer shows slower interdiffusion from the beginning, which is another argument for the proximity to the critical degree of bromination, where critical slowing down is expected.

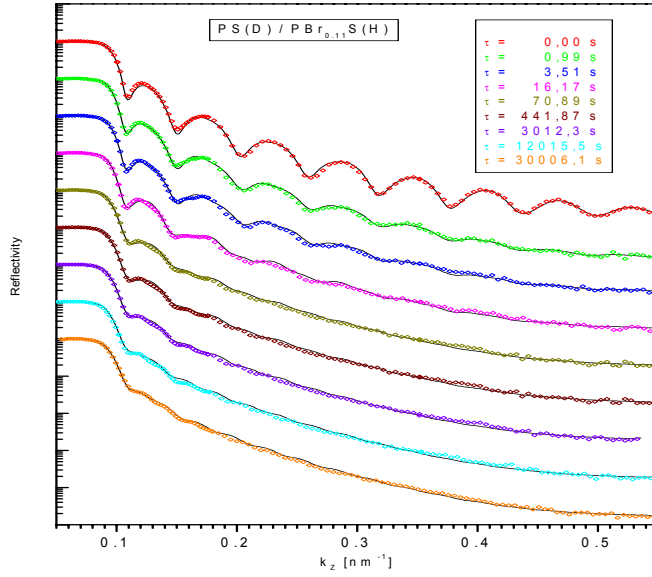


Figure 2: Measured (dots) and calculated (lines) NR curves of the PS(D)/PBr_{0.11}S(H) sample.

The second moment of the time dependent concentration profiles reflecting the interface thickness of the samples is shown in fig. 4. Except for the first point of annealing the interface thickness hardly increases during the initial annealing process. The interdiffusion seems to be frozen in for some time and thereafter starts to increase. This could be a relaxation effect or a contact problem between sublayers. In the reptation model the second moment should follow the scaling law at later times:

$$M^{(2)} \equiv \langle z^2 \rangle^{1/2} \sim t^{2\alpha}$$

For all samples with a degree of bromination $x < 0.11$ we found an exponent $\alpha = 0.19 \dots 0.22$ approximately corresponding to the prediction of the reptation model for real annealing times between entanglement time τ_e and Rouse time τ_r . On the other hand, for the PS(D)/PBr_{0.11}S(H) sample we found an exponent $\alpha = 0.072 \pm 0.003$, which is far below. Bromination thus has a pronounced effect on the interdiffusion and the application of the simple reptation picture is not possible.

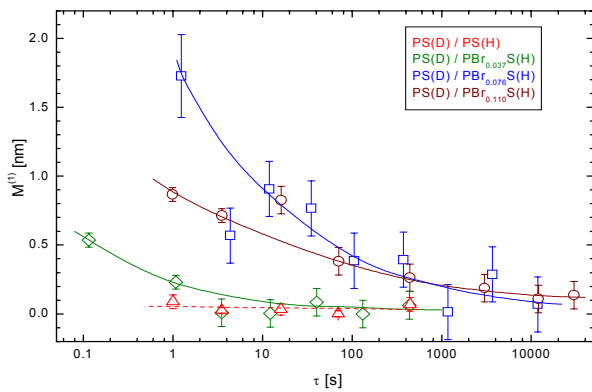


Figure 3: The first moment of concentration profile for all samples vs. real annealing time.

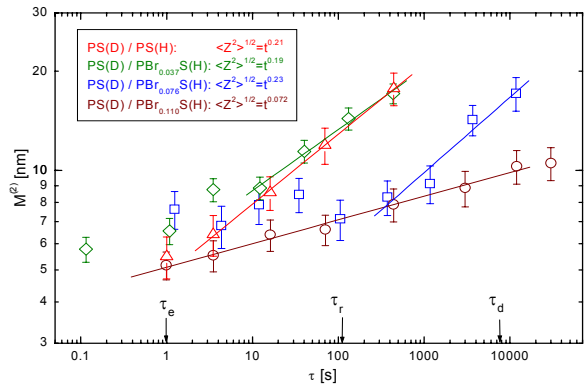


Figure 4: The second moment of concentration profile for all samples vs. real annealing time.


It should be noted, that the PS(D)/PBr_{0.11}S(H) double layer shows the same time behavior of the interface thickness at all annealing times. One reason could be the large T_g difference between both sublayers, which also causes a slowing down of interdiffusion. Chain movement in the brominated polymer is very slow and thus mainly PS(D) participates in the diffusion process which is limited by the layer thickness of brominated polymer.

Acknowledgement

The technical assistance of Mr. H.-D. Braune and Mr. P. Biemann from the GKSS is gratefully acknowledged. This work was supported by BMBF (research grant number 03ST5MP1/6).

References

- [1] Hüttenbach, S.; Stamm, M.; Reiter, G., Foster, M.: *Langmuir*, 7 (1991) 2438
- [2] Voyutskii, S. S.: *J. Adhes.*, 3 (1971) 69
- [3] De Gennes, P. -G.: *Acad. Sci. Paris, Ser. II*, 292 (1981) 1505
- [4] Edwards, S. F.: *Proc. Phys. Soc.*, 92 (1967) 9
- [5] De Gennes, P. G.: *J. Chem. Phys.*, 55 (1971) 572
- [6] Pohlers, A.; Braune, H.-D.; Tietze, U.; Stamm, M.: Accurate annealing experiments by time-temperature superposition principle on polystyrene - polystyrene interfaces, In: Schreyer, A.; Vollbrandt, J.; Willumeit, R. (Eds.): *GeNF – Experimental Report 2002*, GKSS Research Centre, Geesthacht, 2003. Report No.: GKSS 2003/1.
- [7] Pohlers, A.; Braune, H.-D.; Tietze, U.: Accurate annealing experiments by time-temperature superposition principle on polymer interfaces, *ESS European Conference*, Bonn, 14. - 17.05.2002
Abstract in: *Abstract Book*, Jülich (2002) 46
- [8] Biemann, P.; Pohlers, A.; Tietze, U.; Schubert D.W.: *PANORAMA – a new WINDOWS program for neutron reflection data reduction on FRG-1*, Poster of *ESS European Conference*, Bonn, 14. - 17.05.2002, Abstract in: *Abstract Book*, Jülich (2002) 47
- [9] Lekner, L.: *Theory of Reflection*, Martinus Nijhoff Publishers: Amsterdam, 1987
- [10] Kunz, K.; Reiter, J.; Götzelmann, A.; Stamm, M.: Model-free analysis of neutron reflectivity data from polymer thin films with the simulated annealing technique, *Macromolecules*, 26 (1993) 4316-4323
- [11] Yang, X., Pohlers, A.; Jehnichen, D.; Tietze, U.; Stamm, M.: The use of an asymmetric fit model on neutron reflection curves of double layers consisting of polystyrene and low brominated polystyrene (progress report), In: Schreyer, A.; Vollbrandt, J.; Willumeit, R. (Eds.): *GeNF – Experimental Report 2002*, GKSS Research Centre, Geesthacht, 2003. Report No.: GKSS 2003/1.

	EXPERIMENTAL REPORT	GeNF TOREMA-2
Development of asymmetric profile analysis for neutron reflection curves of polymer double layers (progress report)		
Principal Proposer:	X. Yang ² , A. Pohlers ¹ , D. Jehnichen ¹ , M. Stamm ¹	
Experimental Team:	X. Yang ² , A. Pohlers ¹ , U. Tietze ³	
	¹ Institute of Polymer Research Dresden, Germany	
	² Dutch Polymer Institute and Applied Physics Department, Eindhoven	
	University of Technology, The Netherlands	
	³ GKSS Research Centre	
Date(s) of Experiment:	April – June 2002	

Neutron reflectivity (NR) is a powerful method for the investigation of thermally initiated diffusion between polymer layers of suitable scattering contrast. One of the big advantages of neutrons over x-rays is in this application that this contrast can very favourably be generated for many polymer systems by deuteration of one component. Then nanoscopic resolution is achieved and accurate information about interface thickness and interfacial concentration profile is obtained. For a precise interpretation of reflection curves during annealing processes it is necessary to use a suitable fit model [1..3]. Former examinations on a test sample show that the interfacial diffusion between partially compatible layers consisting of deuterated polystyrene PS(D) and brominated polystyrene PBr_{0.076}S(H) cannot be described with a symmetric fit model [4].

The diffusion speed and, consequently, the interface width is dependent on the compatibility of both sublayers. However, if there is a mismatch in the mobility of polymers in the sublayers, the interface thickness and the concentration profile will be distorted due to the different diffusion speeds of polymer segments on both sides of the interface and the interface profile will not longer be a symmetrical one. It is known that the mobility of a particular polymer chain is dependent on its molecular weight (which determines its gyration radius in the bulk), temperature and surrounding matrix. One may use the difference between the annealing temperature and the glass transition temperature T_g to estimate the effect of entropic driving forces on the diffusion speed of polymer chains. For our test sample [4], the glass transition temperature of the PBr_{0.076}S(H) sublayer is 109 °C and, consequently, 6 K higher than for the PS(D) sublayer.

Mathematically, this interdiffusion can be described with a superposition of two asymmetrical error functions for the refractive index n depending on a coordinate z in direction perpendicular to the polymer-polymer interface [2, 3]:

$$n(z) = n_i + (n_{i+1} - n_i) \cdot \left((1 - P') \left(1 - \frac{1}{2} \operatorname{erfc}\left(\frac{z}{\sqrt{2}\sigma}\right) \right) + P' \left(1 - \frac{1}{2} \operatorname{erfc}\left(\frac{z}{\sqrt{2}\sigma'}\right) \right) \right) \quad (z < 0), \quad (1a)$$

$$n(z) = n_i + (n_{i+1} - n_i) \cdot \left((1 - P'') \left(1 - \frac{1}{2} \operatorname{erfc}\left(\frac{z}{\sqrt{2}\sigma}\right) \right) + P'' \left(1 - \frac{1}{2} \operatorname{erfc}\left(\frac{z}{\sqrt{2}\sigma''}\right) \right) \right) \quad (z > 0), \quad (1b)$$

with

- σ the width parameter of the primary error function,
- σ', σ'' the both asymmetrical width parameters,
- P', P'' the weight proportions ($0 \leq P^i \leq 1$).

Via $\sigma', \sigma'', P', P'' \rightarrow 0$ the formalism characterize the symmetrical interdiffusion, but for $\sigma', \sigma'' \gg \sigma$ it becomes strong asymmetrically. Finally, there is a linear relation between

refractive index and concentration profile. The examination of the n-th moments of concentration profile $M^{(n)}$ yields further information, e.g.:

$M^{(1)}$: tests of concentration profile symmetric:

$$M^{(1)} \equiv \langle z^n \rangle = \int_{-\infty}^{+\infty} z \frac{d\phi(z)}{dz} dz / \int_{-\infty}^{+\infty} \frac{d\phi(z)}{dz} dz \quad (2)$$

$M^{(2)}$: tests of interface width modification:

$$M^{(2)} \equiv \langle z^n \rangle^{1/2} = \left(\int_{-\infty}^{+\infty} z^2 \frac{d\phi(z)}{dz} dz / \int_{-\infty}^{+\infty} \frac{d\phi(z)}{dz} dz \right)^{1/2} \quad (3)$$

Thereby, the concentration profile $\Phi(z)$ corresponds with the single error functions in eq. (1a/b).[2,3].

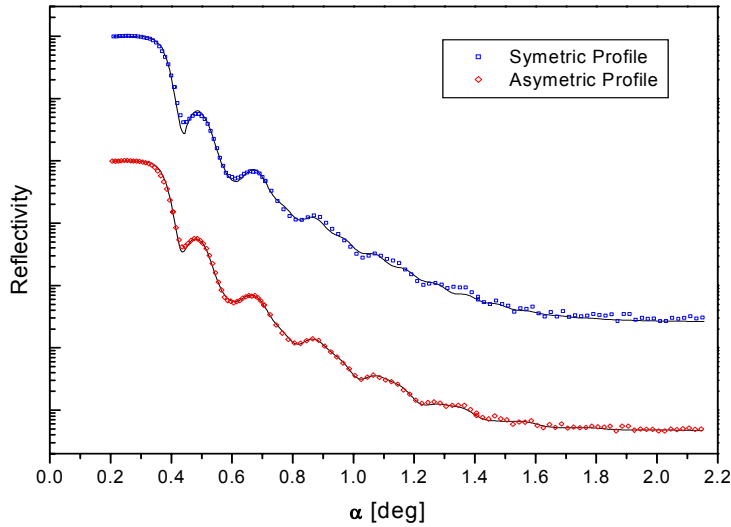


Figure 1: Comparison of symmetric and asymmetric model fits on the NR curve of the sample PS(D) / PBr_{0.076}S(H) given in [4].

Fig. 1 displays the fitting results by using a single error function with $\sigma = 5.5$ nm and superposition of two error functions with different interface widths. Obviously, the interface profile described by such a model is more successful as a conventional error function and shows an excellent agreement with the measured reflectivity data. The profiles used for reconstruction of the reflectivity are shown in Fig. 2.

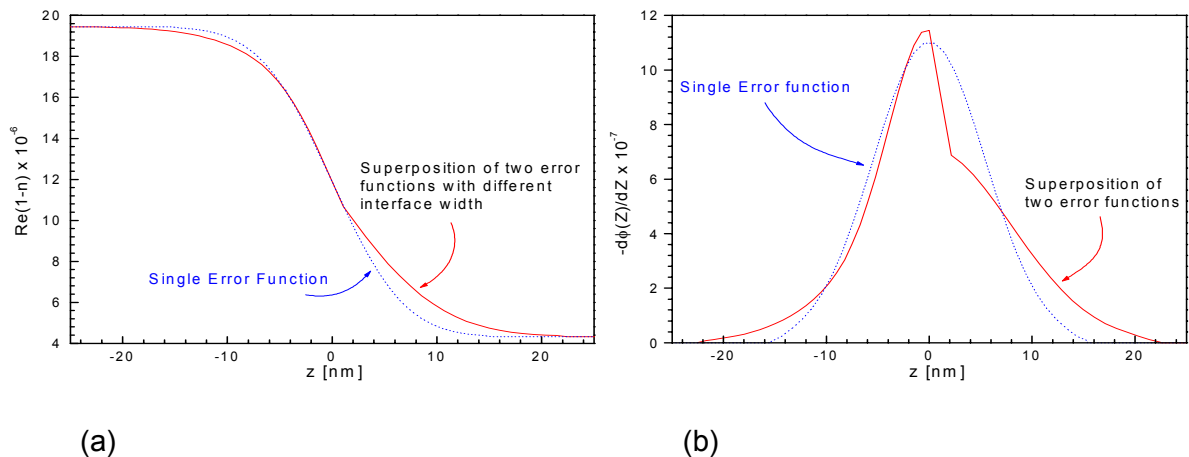


Figure 2: The real space profile (a) and the derivative of the concentration profiles (b) for the sample given in Fig. 1.

The neutron beam is highly sensitive to the interface concentration profile and the subtle difference of two profiles contributes to the significantly different model fitting quality. By using the model described by the superposition of two error functions, the measured reflectivity curves were fitted. During model fits, the following refractive indices (calculated for $\lambda = 0.435$ nm) were used for all measurements:

$$\begin{aligned} n_{\text{PS(D)}} &= 1 - 19.45 \times 10^{-6} \\ n_{\text{PBr}_{0.076}\text{S(H)}} &= 1 - 4.32 \times 10^{-6} \\ n_{\text{Si-wafer}} &= 1 - 6.5 \times 10^{-6} \end{aligned}$$

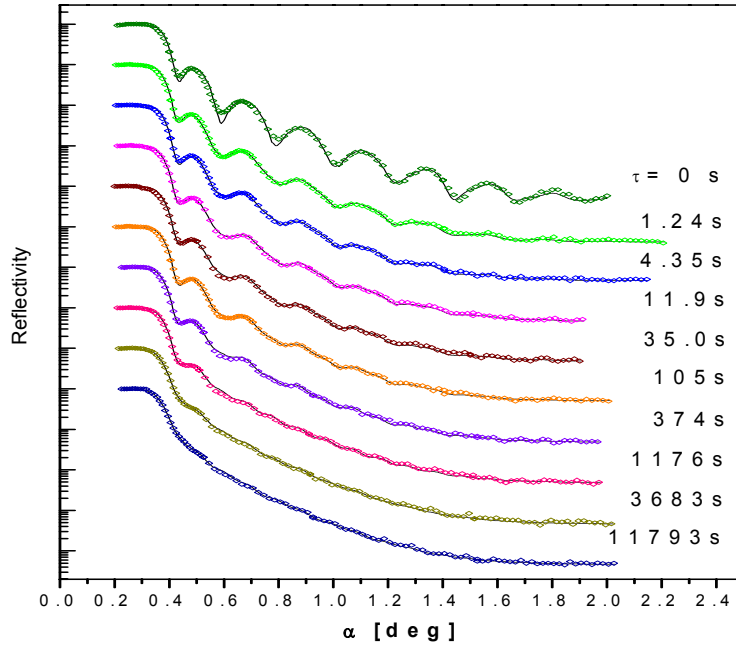


Figure 3: Measured (dots) and calculated (lines) NR curves according to the polymer-polymer interface profiles shown in Fig. 4.

In good approximation, the air-polymer interface could be described by a simple error function with $\sigma = 2.1$ nm (variation ± 0.1 nm) and this value did not change during the overall fitting process. The results of optimization are shown in Fig. 3 as a comparison of experimental and calculated reflectivity curves depending on annealing time. The corresponding interface profiles are given in Fig. 4.

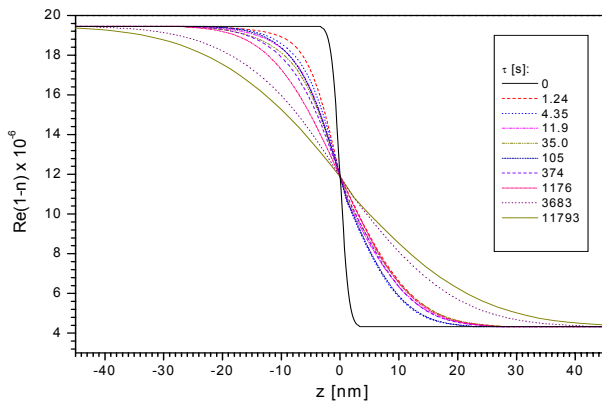


Figure 4: The interface profile of sample PS(D)/PBr_{0.076}S(H) to different annealing times.

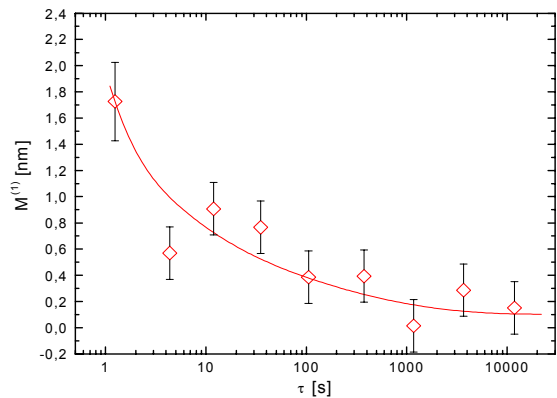


Figure 5: Plot of the first moment of concentration profiles vs. annealing time.


The first moment of interfacial concentration profile is shown in Fig. 5 as a function of annealing time. One can easily notice that within the short annealing times those values contribute to large deviations from zero. With increasing annealing time, the first moment decreases rapidly and approaches zero after long annealing times. As mentioned before, the net mass flow took place at the early stages due to the different glass transition temperatures of the two layers, which results from the different mobilities of polymer segments. Due to the very short annealing time after conversion to the reference temperature for the first point, the highest temperature to which the sample was exposed was 107°C exceeding the glass transition temperature of PS(D). But obviously, it is still slightly lower than T_g of PBr_{0.076}S(H). Initially, only PS(D) can penetrate into PBr_{0.076}S(H), thus softening this material, where movement at higher PS(D) concentration will become possible. At the second point, the temperature exerted by the double layer sample has reached exactly T_g of PBr_{0.076}S(H), where now movement of both components takes place. When PS(D) molecules have penetrated into the PBr_{0.076}S(H) component the T_g difference will be narrowed. With increasing interdiffusion both sides increasingly intermix and in this way become more equal. Interdiffusion then finally will stop, while also differences between both sides disappear. The interfacial profile therefore is initially quite asymmetric, while it becomes symmetric at later stages.

Acknowledgement

The technical assistance of Mr. H.-D. Braune and Mr. P. Biemann from the GKSS is gratefully acknowledged. This work was supported by BMBF (research grant number 03ST5MP1/6).

References

- [1] Lekner, L.: Theory of reflection, Martinus Nijhoff Publishers: Amsterdam (1987)
- [2] Kunz, K.; Reiter, J.; Götzelmann, A.; Stamm, M.:
Model-free analysis of neutron reflectivity data from polymer thin films with the simulated annealing technique, *Macromolecules*, 26 (1993) 4316–4323
- [3] Kunz, K.: Interdiffusion von Polymeren an Grenzflächen, Diss., Univ. Mainz, FB Chemie und Pharmazie (1994)
- [4] Yang, X.; Pohlers, A.; Jehnichen, D.; Tietze, U.:
Determination of the interface quality between partial-digestible polymers by the interdiffusion with neutron reflectometry.
In: Schreyer, A.; Vollbrandt, J.; Willumeit, R. (Eds.):
GeNF-Experimental Report 2001, GKSS Research Centre, Geesthacht, 2002. Report No. GKSS 2002/4, pp. 113–115

	EXPERIMENTAL REPORT	GeNF TOREMA-2, PNR
Characterization of GaAlAs/GaAs superstructures		
Principal Proposer:	L. Koenders, V. Wagner PTB Braunschweig, Germany	
Experimental Team:	U. Tietze GKSS Research Centre	
Date(s) of Experiment:	October 2001 and December 2002	

Scientific Objective

The aim of the present investigation is to characterize 1-dimensional superstructures, which were produced by molecular beam epitaxy. When broken perpendicular to the layers these super structures could finally be used as lateral standards for scanning probe microscopy (SPM) on the scale ≤ 50 nm [1-4]. Such standards are urgently required by the needs arising in the study and metrology of nano sized systems for the characterization of their dimensions and roughness.

Experimental Techniques

Two samples were produced by molecular beam epitaxy of a series of $\text{Ga}_{1-x}\text{Al}_x\text{As}/\text{GaAs}$ layers on 2-inch GaAs wafers. The samples were characterized by specular neutron reflectometry with respect to the periods of the super structures. Hereby the penetration power of neutrons allows to probe rather thick structures, a well known favorable fact as compared to x-ray reflectometry.

Main Results

A first sample comprises three super structures with $\text{Ga}_{1-x}\text{Al}_x\text{As}/\text{GaAs}$ double layers with $x = 0.30$ and nominal periods of 30, 50 and 70 nm (see Fig.1). The second sample comprises two super structures of different composition x and nominal periods of 30 and 50 nm (see Fig.2).

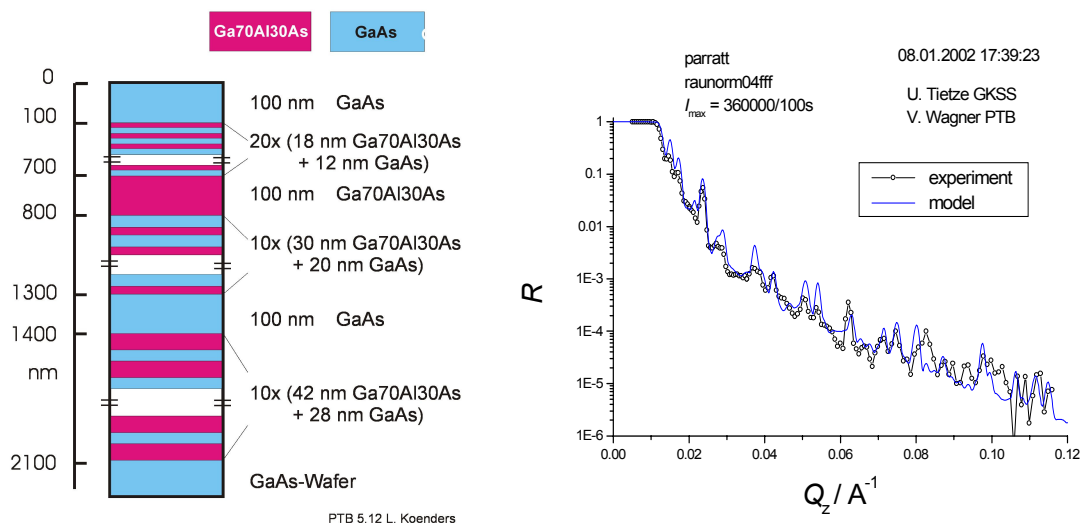


Figure 1: Structure of sample #1 and reflectivity R vs. scattering vector Q_z . Best fit was obtained with periods two percent larger than the nominal values. An overall parameter ($\sigma = 3$ nm) for the roughness/ interdiffusion of the layers was included in the model.

Fig. 1 shows the experimental results for sample #1. While for this sample the Bragg peaks of the layer structures are not much pronounced and for the buried structures only the first Bragg peaks are separated, the situation of sample #2 comprising only two super structures is much clearer. Fig. 2b showing the reflectivity $R(q)$ normalized by the Fresnel decay $\propto q^{-4}$ displays Bragg peaks up to the 10th order. In general in both samples the periods of the super structures are somewhat larger than expected from the MBE production process.

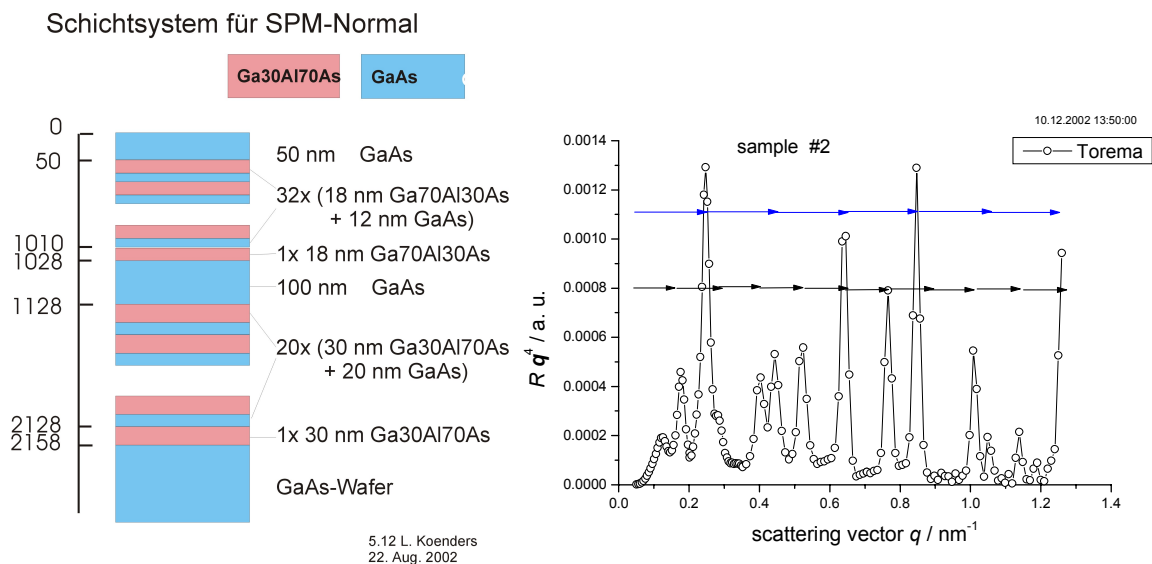


Figure 2a: The structure of sample #2 comprises one series of double layers with a nominal period of 50 nm and $x = 0.7$ and another one with a period of 30 nm and $x = 0.3$.

Figure 2b: Bragg peaks of the two super structures with period of $d_1 = 52.9$ nm and $d_2 = 31.0$ nm can be identified up to the 6th and 10th order respectively.

Relevance to other Applications or to other Techniques

Neutron reflectometry is used as an independent complementary method to characterize layer systems.

References

- [1] J. Garnaes et al., Proc. Quantitative Microscopy 1997, Lyngby, PTB-Bericht F-30 (1997) p. 149
- [2] D. Wüllner et al., Proc. Quantitative Microscopy 1997, Lyngby, PTB-Bericht F-30 (1997) p. 154
- [3] J. Garneas et al., in Precision Engineering – Nanotechnology: Proc. of the 1st Inte. EUPSEN Conf. vom 31.5.–4.6.1999 in Bremen, Ed. P. McKeown u.a., Verlag Shaker, Aachen, Vol. 2 (1999) 13
- [4] S. Nau, Entwicklung und Anwendung einer neuartigen Methode zur strukturellen Untersuchung GaAs-basierender epitaktischer Heterostrukturen, Diplomarbeit Uni. Marburg, Juni 1999

	EXPERIMENTAL REPORT	GeNF PNR
Reflectometer for polarised neutrons PNR		

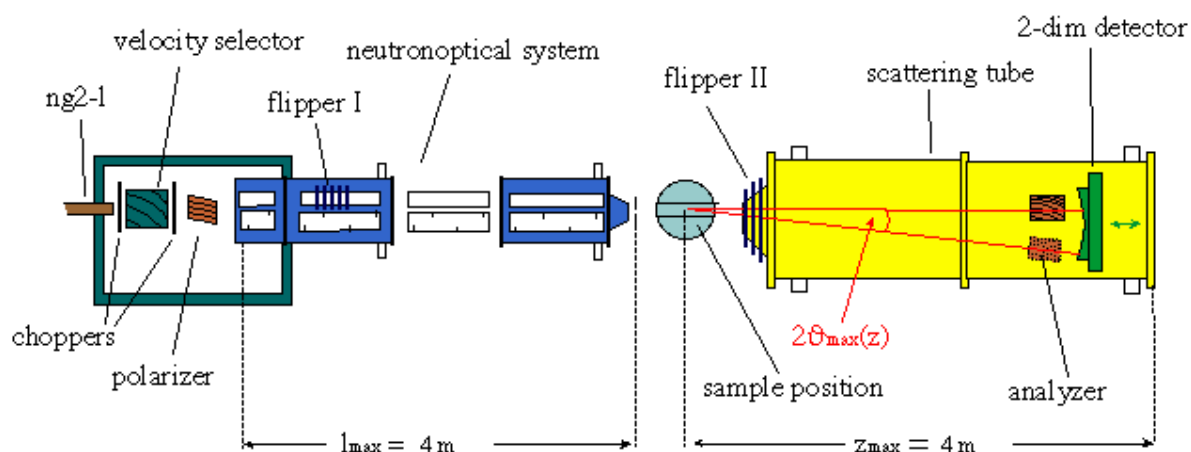
Short Instrument Description:

The polarised neutron reflectometer is used to study magnetic and other surfaces, layers, thin films and membranes applying cold non-polarised/polarised neutrons at high fluxes.

Local Contact:

Dr. Danica Solina
 Phone/Fax : +49 (0)4152 87–2806 / +49 (0)4152 87–2840
 e-mail: danica.solina@gkss.de

Schematic View of PNR:



Instrument Details:

Beamline:	beamline 8 (NG-2I), cross section 30 x 40 mm ²
Monochromator:	helical slot selector
Wavelength:	$\lambda \geq 0.635$ nm
Wavelength resolution:	$\Delta\lambda/\lambda = 0.05$
TOF equipment:	2 choppers, to be used if a resolution better than 0.05 is required
Polariser and analyser:	set of bent supermirrors
Spin flipper:	hf-flipper or Mezei-coil-flipper
Collimation lengths:	4 m
Flux at sample position: (beamsize: 0.5 x 40 mm ²)	$\Phi_{\text{nonpol}} = 1 \cdot 10^5 \text{ cm}^{-2} \text{ s}^{-1}$ (unpolarised) $\Phi_{\text{pol}} = 3 \cdot 10^4 \text{ cm}^{-2} \text{ s}^{-1}$ (polarised neutrons)
distance sample-detector:	3 m to 4 m
angular range:	$0^\circ \leq \theta \leq 4^\circ$
Detector:	2-dim position-sensitive ³ He-counter
Ancillary equipment:	perm.-magnets system, vertical field, 50 mT refrigerator cryostat – temp.-range: 12–475 K

	EXPERIMENTAL REPORT	GeNF PNR
Neutron Reflectivity from Black Foam Films¹		
Principal Proposer:	R. Krastev ¹ ¹ Hahn-Meitner Institute, Berlin, Germany	
Experimental Team:	R. Krastev ¹ , D. Lott ² , U. Tietze ² ² GKSS Research Centre	
Date(s) of Experiment:	10.12–13.12. 2002	

The aim

The foam films have been widely studied due to their well-defined geometry as model system to test theories on interaction forces which govern the stability of hydrophobic colloids^{2,3}. These films have thickness of only some nanometers but they can possess very extended areas. They have been utilized to study the structure of some macromolecules in confined volumes or the behaviour of the contacts between lipid bilayers which are the main structural component of the walls of the living cells. It is known that ordered structures like foam films also exist in *in vivo* systems, e.g., in animal and human lungs.

A foam film is formed by two monolayers of surfactant molecules with the hydrophobic parts facing the air and the hydrophilic head groups of the molecules in contact with a central water core. When the films are some tens nanometer thick the two surfactant-covered surfaces interact with each other and thus the chemical potential of the film is different than that of the bulk phase. Because of their very low reflectivity these films are called black foam films (BF). There are two types of BF – common black films (CBF) and Newton black films (NBF). The structure of NBF and CBF are essentially different: while the NBF is a bilayer film (i.e. two monolayers of amphiphilic surfactant molecules adsorbed onto each other) the CBF is described by the „sandwich model“ – a liquid layer containing solution between two adsorption monolayers of surfactant molecules. Changes in electrolyte concentration cause changes in the film thickness and in the interaction forces between two surfaces of the films. At higher electrolyte concentration the thinner NBF are stable while at lower concentrations the thicker CBF are the equilibrium state.

A general problem in the area of the proposed research is the investigation of the properties and the structure of the monolayers stabilizing the foam films and the correlation between this structure and the interaction forces in the film and the properties of the bulk solutions, for example surfactant concentration, electrolyte concentration, etc. The film thickness which is directly correlated to the interactions between the film interfaces have been measured by the microinterferometric method or X-ray reflectometry.^{4,5,6} Although the second method supplies more detailed information it still cannot answer the main questions in the foam film investigations: where is the border between the adsorbed surfactant layers and the water core and how much water is included in the swelled layers?

¹ These films are known as well as free-standing liquid films or soap film. Here the recommendations of IUPAC are followed and accordingly they are entitled as foam films.

² J. Israelaschvili *Intermolecular and surface forces*, Acad. Press, 1991.

³ D. Exerowa, P. Kruglyakov *Foam and Foam Films*, Elsevier, 1998.

⁴ J.S. Clunie, et al *Diss. Farad. Soc.* **42** (1966) 34

⁵ D. Platikanov, H.A. Graf, A. Weiss. *Coll. & Polym. Sci.* **268** (1990) 760.

⁶ J.J. Benattar, et al *Langmuir* **16** (2000) 5029

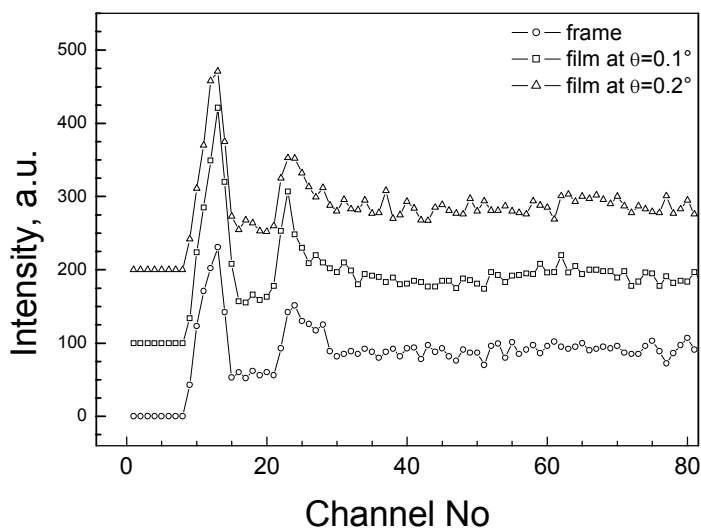
Experiment

Experiments were performed at the PNR reflectometer. A special aluminium experimental chamber was constructed. It allows formation of the foam films in saturated water vapours atmosphere which mainly governs the film stability. The chamber is equipped with two aluminium windows which allow the reflectivity measurements with neutrons to be carried. The vertical foam films were formed in a large rectangular hole in a glass plate. Formation of a vertical film allows the equilibrium film thickness to be reached fast because of the drainage under gravitational force. In the same time the film stays in contact with the solution from which it is prepared. The sample geometry makes the use of neutron reflectometer with horizontal scattering vector important. Because of this the PNR reflectometer is attractive for such studies.


The films were formed from commercially available concentrated surfactant solution dissolved in D_2O . Small amount of glycerol was added in order to increase the film stability.

Results and conclusions

A measurement was performed in the range of angle of incidence θ from 0.1° to 0.9° . The dependence of the intensity of the reflected neutron beam as a function of the channel number in the two-dimensional position sensitive detector at PNR is shown on the Figure. Two dependencies at different θ angles are presented. The curves are shifted along the Intensity axes with 100 a.u. for clarity. The first maximum corresponds to the position of the direct beam. A second maximum appears in channels 23–24 but its position does not change with the angle of incidence. Similar dependence is observed when the reflectivity was measured only from the glass frame without formed film. The position of the maximum is independent of the incident beam angle θ as well.



The observed behaviour shows that strong scattering from the frame in which the film is formed exists. One explanation for this behaviour could be the fact that the construction of the frame makes impossible to align the plane of the foam film with the neutron beam. This makes necessary the construction of a new film holding frame which is under preparation. Additional efforts have to be done to obtain films with higher stability. The film stability would be controlled via laser beam focused onto the film and a video camera. Further measurements are necessary to obtain more reliable results. The experiments done in this first trial were necessary to get preliminary data for the behaviour of the system.

	EXPERIMENTAL REPORT	GeNF PNR
Neutron reflectivity on Fe/Cr and Fe/Cr/Sn/Cr multilayers		
Principal Proposer:	D. Lott ¹ , D. Solina ¹ , M. Almokhtar ² , K. Mibu ³ , A. Schreyer ¹ ¹ GKSS Research Center; ² Physics Department, Assiut University, Assiut, Egypt; ³ Research Center for Low Temperature and Materials Sciences, Kyoto University, Uji, Kyoto 611-0011	
Experimental Team:	D. Lott ; U. Tietze; D. Solina GKSS Research Centre	
Date(s) of Experiment:	November 2002	

In Fe/Cr multilayer systems, the magnetic coupling of the Fe layers is mediated through the Cr layers. The Cr layers are antiferromagnetically ordered, showing commensurate (CSDW) and incommensurate spin density waves (ISDW) depending on temperature and the thickness of the separating Cr layers [1].

Recently, Fe/Cr/Sn/Cr multilayers were studied by Moessbauer spectroscopy [2]. The monolayer (ML) of Sn inserted into the Cr layers serves as a Moessbauer probe permitting the study of the local magnetic environment around Sn. In this way the details of the magnetic structures of Cr in these systems can be retrieved.

Here, neutron reflectivity was applied to a set of Fe(10Å)/Cr(t) and Fe(10Å)/Cr(t/2)/Sn(2Å)/Cr(t/2) multilayers with $t = 80 \text{ \AA}$ and $t = 160 \text{ \AA}$ in order to characterize their density profile and the magnetic coupling properties of the Fe-layers. All multilayers were grown on MgO (001) substrates. The systems with $t = 80 \text{ \AA}$ and $t = 160 \text{ \AA}$ have 60 and 50 repeats of the Fe/Cr and Fe/Cr/Sn/Cr unit cell, respectively. Measurements were made at the neutron reflectometer PNR at room temperature using a wavelength (λ) of 6.35 \AA with a relative wavelength resolution of $\Delta\lambda/\lambda = 0.05$.

The reflection spectra for the sample of $t=80\text{\AA}$ with and without Sn are shown in figure 1. The structural peaks are at $Q_z = 0.765 \text{ \AA}^{-1}$ and $Q_z = 0.745 \text{ \AA}^{-1}$ corresponding to period thicknesses of 84.5 \AA and 88 \AA for the Fe/Cr and Fe/Cr/Sn/Cr samples, respectively. Surprisingly, a small but clearly visible peak can be found in the spectra at half the Q_z position of the structural peak. This indicates the presence of an antiferromagnetic coupling component of adjacent Fe-layers. The effect is larger for the sample containing Sn, for which the 3/2 order peak can be also observed.

Figure 2 shows the same scans made with the sample of $t = 160 \text{ \AA}$. For both systems, three structural peaks are measured with corresponding period thicknesses of 162.5 \AA and 160.5 \AA with and without Sn, respectively. Again, additional peaks appear at the half positions of the structural peaks indicating the presence of antiferromagnetic coupling of adjacent Fe-layers. As observed in the spectra for the samples with $t = 80 \text{ \AA}$, the effect is much more pronounced for the sample with Sn insertion in the Cr-layers. It should be noted that in both sets of multilayers with $t = 80 \text{ \AA}$ and $t = 160 \text{ \AA}$, the insertion of Sn leads to a larger signal at the half order peaks.

First neutron diffraction measurements were carried out at ILL, Grenoble, to examine the SDW wave behavior in the Cr-layers of these films with respect to temperature. Here, drastic

changes could be observed in the spectra with and without Sn showing that the behavior of the SDW in the Cr-layer is altered by the additional Sn-layer.

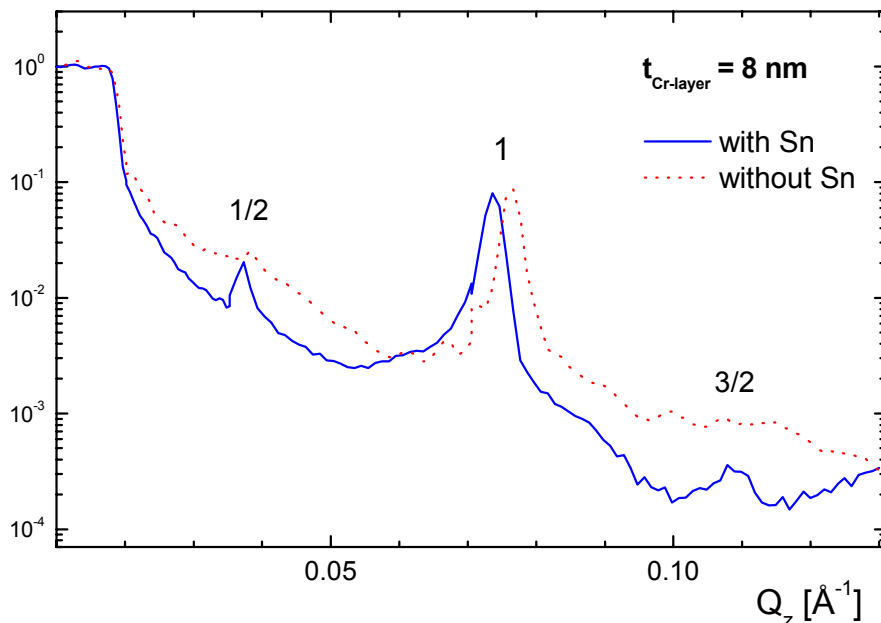


Figure 1: Neutron reflectivity of $[\text{Fe } 10\text{\AA}/\text{Cr } 80\text{\AA}]_{60}$ and $[\text{Fe } 10\text{\AA}/\text{Cr } 40\text{\AA}/\text{Sn } 2\text{\AA} /\text{Cr } 40\text{\AA}]_{60}$ multilayers (dashed and solid line, respectively). The order of the peaks are indicated in numbers referring to the structural Bragg reflection.

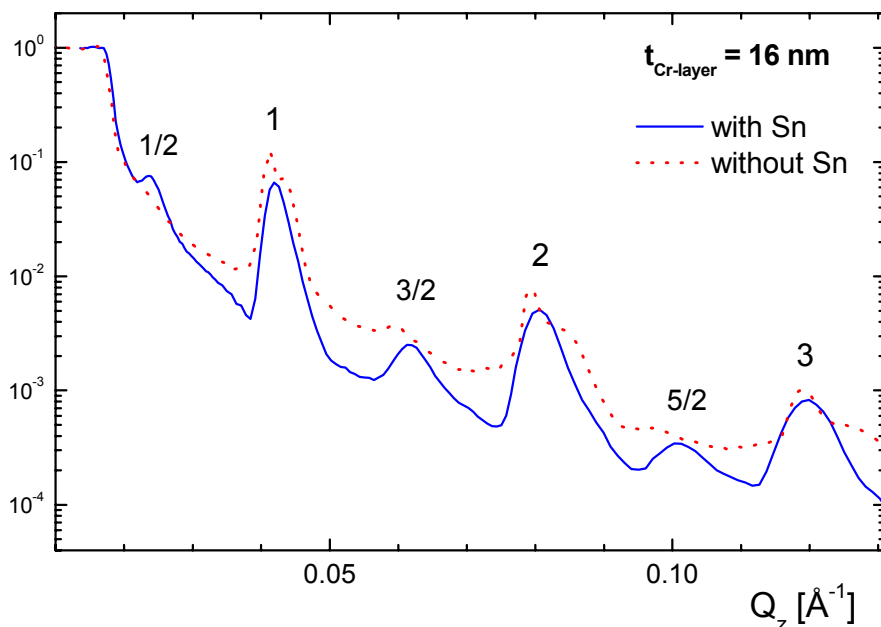



Figure 2: Neutron reflectivity of $[\text{Fe } 10\text{\AA}/\text{Cr } 160\text{\AA}]_{50}$ and $[\text{Fe } 10\text{\AA}/\text{Cr } 80\text{\AA}/\text{Sn } 2\text{\AA} /\text{Cr } 80\text{\AA}]_{50}$ multilayers (dashed and solid line, respectively). The order of the peaks are indicated in numbers referring to the structural Bragg reflection.

Reference

- [1] A.Schreyer et al., Phys. Rev. Lett, 79, 4914 (1997)
- [2] M. Almokhtar et al., Phys. Rev. B, 66, 134401 (2002)

	EXPERIMENTAL REPORT	GeNF ARES
Diffractometer for the analysis of residual stresses ARES		

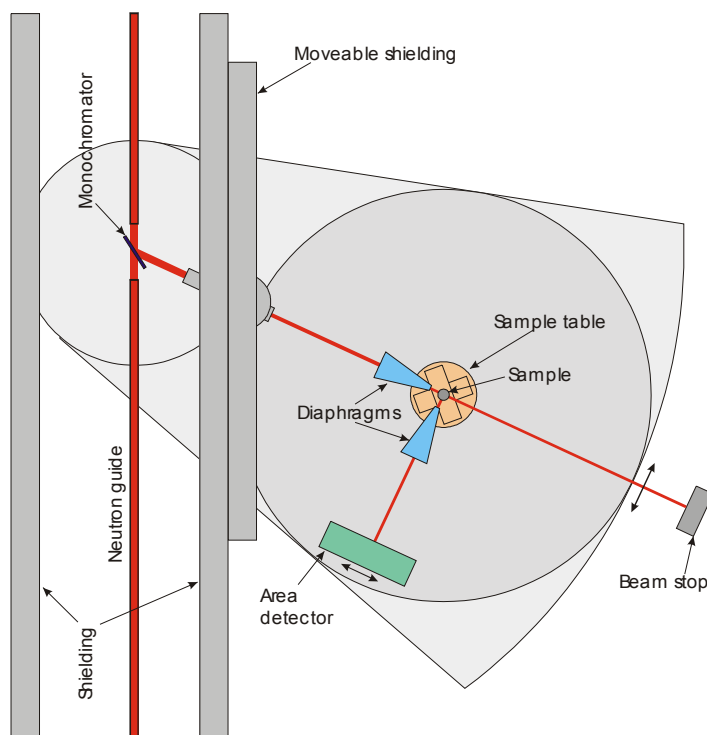
Short Instrument Description:

The diffractometer ARES is designed for the analysis of residual stresses ('strain scanner') in specimens with technical sizes (up to approx. 100 kg) using thermal neutrons.

Local Contact:


Dr. Peter Staron
 Phone/Fax : +49 (0)4152 87-1208 / +49 (0)4152 87-1356
 e-mail: peter.staron@gkss.de

Schematic View of ARES:



Instrument Details:

Location at FRG-1:	beamline 7; thermal neutron guide, cross section 42 × 90 mm ² , (supermirrors on top and bottom wall)
Monochromator:	elastically bent perfect Si monochromator, Si (311), Si (220), double focussing
Take-off angle:	57° to 120°, continuously selectable
Wavelength:	λ = 0.16–0.23 nm (with Si 311)
Flux at sample position:	Φ ≈ 5 · 10 ⁵ cm ⁻² s ⁻¹
Sample displacements:	x, y (range 200 mm), z (range 150 mm), Ω
Detector:	2-dim. position-sensitive ³ He-counter
Distance sample-detector:	100–150 cm
Sample environment:	load frame for in-situ tests planned

	EXPERIMENTAL REPORT	GeNF ARES
Residual stress in welded HY-80 steel		
Principal Proposer:	L. Grünitz Technical University of Hamburg-Harburg, Hamburg, Germany	
Experimental Team:	P. Staron GKSS Research Centre	
Date(s) of Experiment:	29.04.–13.05.02 and 03.09.–08.09.02	

The residual stress field in a thick HY-80 steel plate with a multi-pass weld was analyzed. This study is part of the investigation of the buckling behaviour of thick spherical shells for the ship building industry. Spherical shells form an important part of the pressure hull of submarines. The buckling strength of a spherical shell is greatly influenced by geometrical and structural imperfections (e.g. residual stress). Due to improvements in the manufacturing process geometrical imperfections become less important and the only imperfections left arise from the welding process. The finite element method (FEM) makes it possible to simulate the welding process and its effect on the buckling strength of the shell. The experiment carried out at GKSS will be used for the calibration and validation of the welding simulation. A more detailed knowledge of the influence of welding residual stress on the buckling behaviour of spherical shells will provide a more economic and/or safer construction.

Residual strains were measured in the weld region of a steel plate (300 mm × 400 mm) of 30 mm thickness with the diffractometer ARES using the (211) reflection at a diffracting angle of about 90°. A gauge volume of approximately 3×3×30 mm³ was used for scanning the transverse and normal strains, and a gauge volume of approximately 3×3×3 mm³ was used for the longitudinal strain. As the stress-free lattice distance d_0 can vary within the weld because of variations of solute content due to the heat treatment introduced by welding, a number of small cubes with 5 mm edge length were cut out of the weld by spark erosion. Macroscopic stresses are assumed to relax largely in these small pieces of material, thus they can serve as stress-free reference. Residual stresses were calculated using the diffraction elastic constants of $E_{211} = 222$ GPa and $\nu_{211} = 0.28$.

The first scan was carried out in the middle of the plate's thickness, 150 mm away from one edge. The results reveal tensile residual stresses in the longitudinal direction of 500 MPa in the center of the weld (Fig. 1). Transverse and normal stresses are close to zero in the weld center, while they are compressive up to -200 MPa near the heat affected zones on both sides of the weld. Far away from the weld, the stresses approach zero.

The second scan was done through the thickness of the plate, in the weld center. Oscillating longitudinal and transverse stresses were observed with amplitudes between +500 MPa and -500 MPa, while normal stresses are small (Fig. 2).

The results show that large tensile stresses are present in these welds whose influence on mechanical properties under service conditions still have to be assessed.

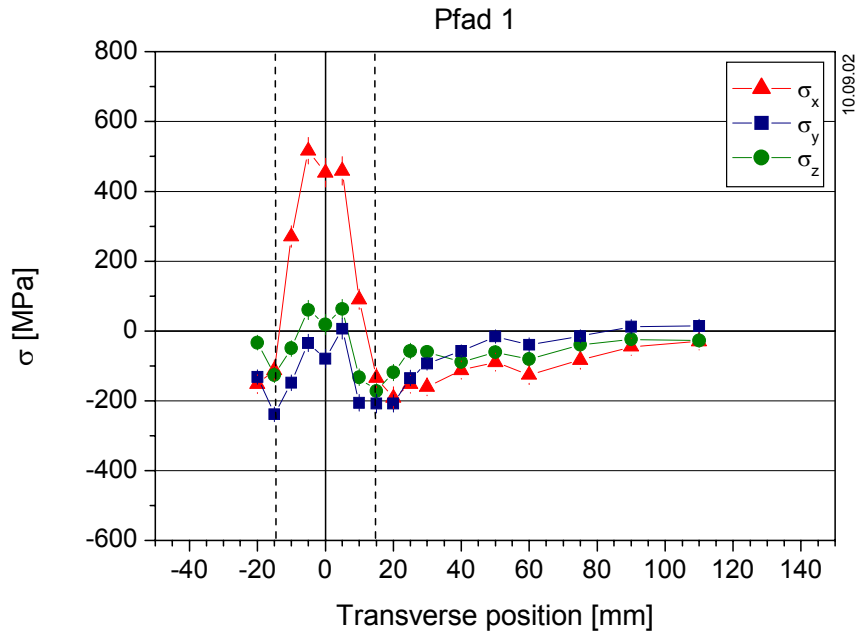


Figure 1: Residual stresses across the weld.

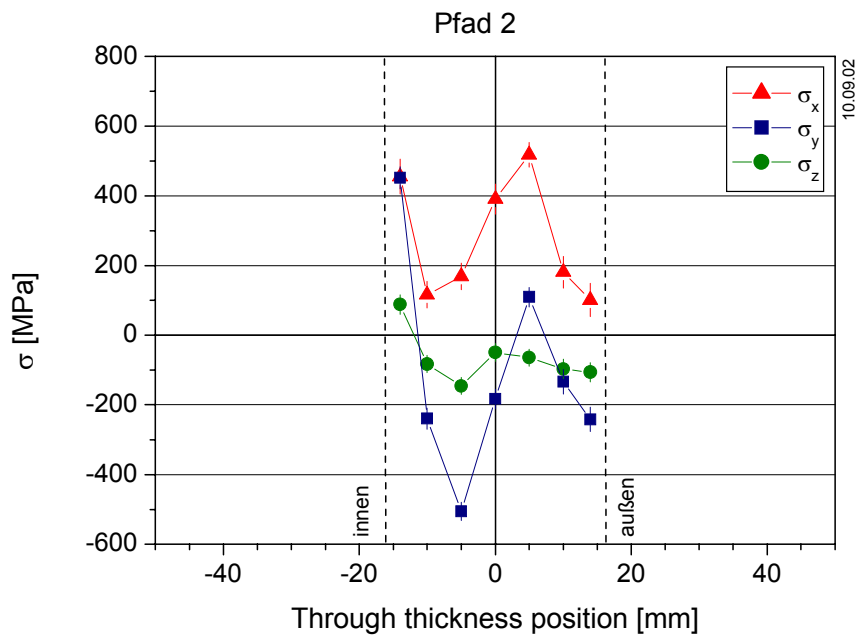



Figure 2: Residual stresses through the thickness of the plate.

	EXPERIMENTAL REPORT	GeNF ARES
Residual stress in IN718 turbine discs		
Principal Proposer:	W. Marketz Böhler Schmiedetechnik, Kapfenberg, Austria	
Experimental Team:	P. Staron GKSS Research Centre	
Date(s) of Experiment:	25.03.–12.04.02; 02.12.–14.12.02	

Residual stresses in forged turbine discs made of Ni-based superalloy IN718 were to be analyzed. Two different discs were looked at that were cooled under different conditions after forging. Disc 1 was slowly cooled in air while disc 2 was cooled in water. Due to results of finite element modelling, the choice of cooling should affect the residual stress state present in a disc after cooling. The level of residual stress that remains in the disc is crucial for additional work done on the disc like turning to a final shape.

Residual strains were measured in the two discs that had a diameter of 320 mm and a thickness of about 20 mm with the diffractometer ARES using the (311) reflection at a diffracting angle of about 100°. A gauge volume of approximately 3×3×30 mm³ was used for scanning the radial and axial strains, and a gauge volume of approximately 3×3×10 mm³ was used for the tangential strain. For determining the stress-free lattice distance d_0 , a small piece with size 4×5×6 mm³ was cut out of each disc by spark erosion. Macroscopic stresses are assumed to relax largely in these small pieces of material, thus they can serve as stress-free reference.

The scans were carried out approximately in the middle of a disc's thickness, where 5 points were measured along a radius of the discs. The results reveal a significant difference in the residual strains in both discs (Figures 1, 2). The strains in the disc that was slowly cooled in air are much smaller than those in the water-cooled disc. These results are in qualitative agreement with results of simulations; the next step will be a more quantitative comparison of residual stress results of experiment and simulation.

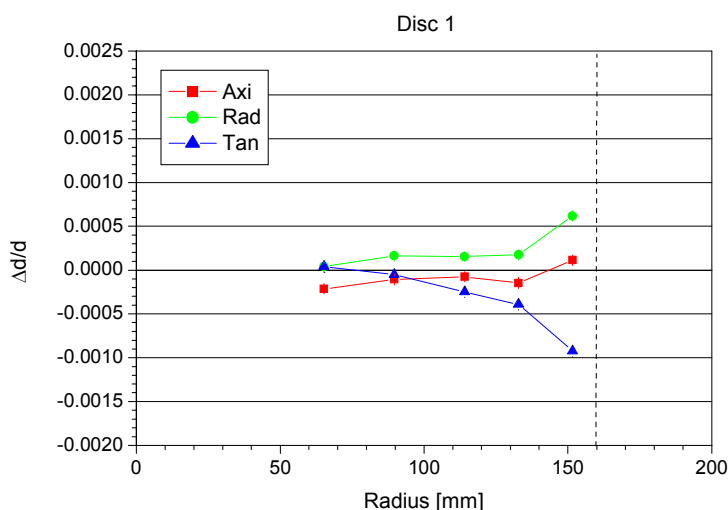


Figure 1: Measured strains along a radius of disc 1 (air cooled).

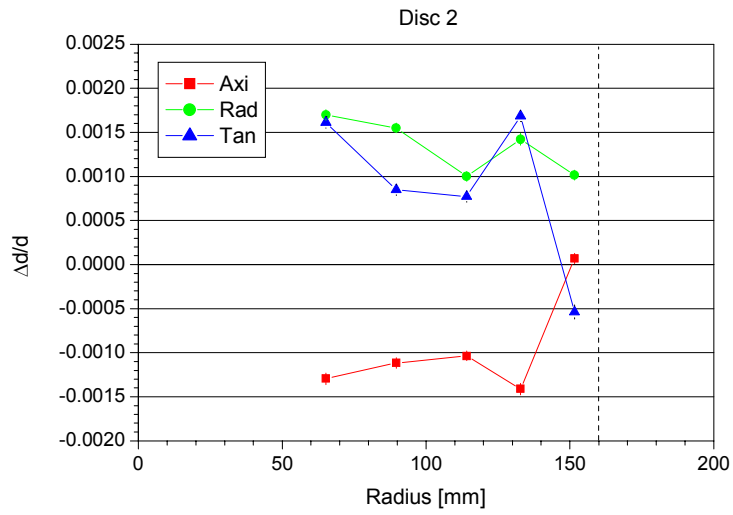



Figure 2: Measured strains along a radius of disc 2 (water cooled).

	EXPERIMENTAL REPORT	GeNF ARES
Residual stress in friction stir welded AA2024 sheets		
Principal Proposer:	P. Staron, M. Koçak GKSS Research Centre	
Experimental Team:	H.-U. Ruhnau, P. Staron GKSS Research Centre	
Date(s) of Experiment:	11.09.–06.10. and 11.11.–21.11.02	

Friction stir welding (FSW) is a solid state joining process that takes place below the melting point of the materials to be joined [1]. FSW uses a rotating cylindrical tool with a pin to frictionally heat the material. The tool pin stirs the plasticised material and therefore joins two pieces together when it is moved along the welding line. Advantages of this technique include e.g. weldability of materials that are difficult to fusion weld, low distortion, and excellent mechanical properties. FSW is currently under extensive investigation for joining aluminium alloys in the aerospace industry [2, 3].

The magnitude and distribution of residual stress in FSW welded Al alloys for aerospace applications should be known to assess their role in fatigue and corrosion behaviour of the welded joints. Attempts should be made to produce sound FSW joints with low residual stresses with industry-relevant approaches without causing any degradation in micro-structural and mechanical properties.

The aim of this study is to determine the residual stress state in FSW Al alloy sheets that have been subjected to mechanical tensioning during welding. Aluminium sheets (AA2024-T351) of size 250 mm × 380 mm with 6.3 mm and 3.2 mm thickness were produced by FSW at the BAE SYSTEMS, UK. Two sheets, one 6.3 mm thick and one 3.2 mm thick, were subjected to mechanical tensioning up to 70 % of the tensile yield strength in a special in-situ tensioning machine, then they were welded, and after welding they were released. Two other sheets were welded without being tensioned for reference purpose.

Residual strains were measured in the four sheets with the diffractometer ARES using the Al (311) reflection at a diffracting angle of about 84°. In the 6.3 mm thick sheets, a gauge volume of approximately 3×3×30 mm³ was used for scanning the transverse and normal strains to improve intensity. This choice of the gauge volume implies that the stresses are constant along x over the length of the volume element, which should be approximately true. A gauge volume of approximately 3×3×3 mm³ had to be used for the longitudinal strain, because larger stress gradients are present along the transverse (y) direction. The size of the gauge volume was reduced to approximately 2×2×30 mm³ or 2×2×2 mm³ for the 3.2 mm thick sheets. Since 2024 is a heat treatable alloy, the solute content in the matrix depends on the heat treatment the material has experienced [4]. Therefore, the lattice distance changes across the weld, which means that there is a local variation in the stress-free lattice distance in the weld region. Here, stress-free lattice distances d_0 were determined under the assumption of a plane stress condition [5].

The stress distribution in the untensioned reference sheet (Fig. 1a) is very similar to former results: there are stress peaks of about 130 MPa in the longitudinal direction in the heat affected zones on both sides of the weld with a minimum in the center of the weld, i.e. the weld nugget. The transverse stress is very small. This stress distribution seems to be typical for FSW aluminium sheets. Fig. 1b reveals a large effect of the mechanical tensioning on the residual stress state of the weld: a compressive longitudinal stress up to –150 MPa is achieved in the weld region. As a balance, the longitudinal stress farther away from the weld

is now tensile. The transverse stresses are still small, but compressive. The results in the 3.2 mm sheets (Fig. 2) are basically the same, even higher compressive stresses up to -200 MPa are achieved by tensioning.

Tensile residual stresses in general can have detrimental effects on mechanical properties, while compressive stresses can bring along beneficial effects. At least, the possibility of producing friction stir welds with very different residual stress states by the mechanical tensioning technique gives the chance to study the influence of the residual stress state on the mechanical performance of these welds.

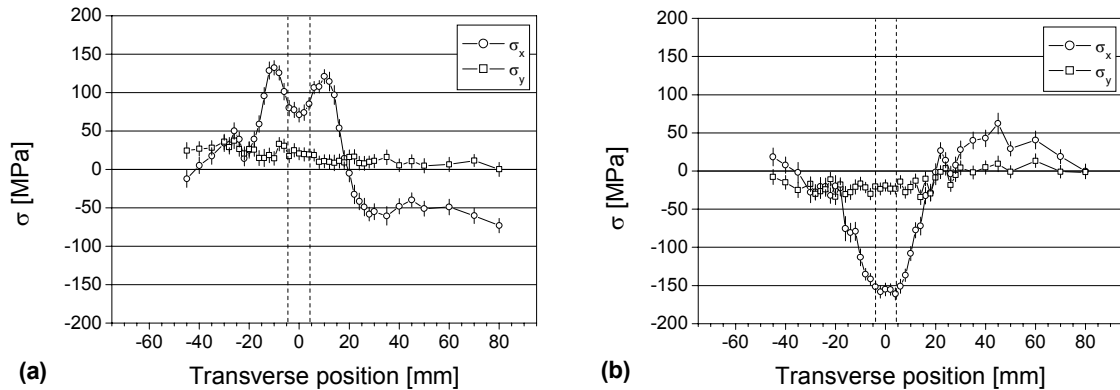


Figure 1: Residual stresses in friction stir welded 2024-T351 6.3 mm sheets: a) untensioned reference; b) tensioned to 70 % YTS prior to welding.

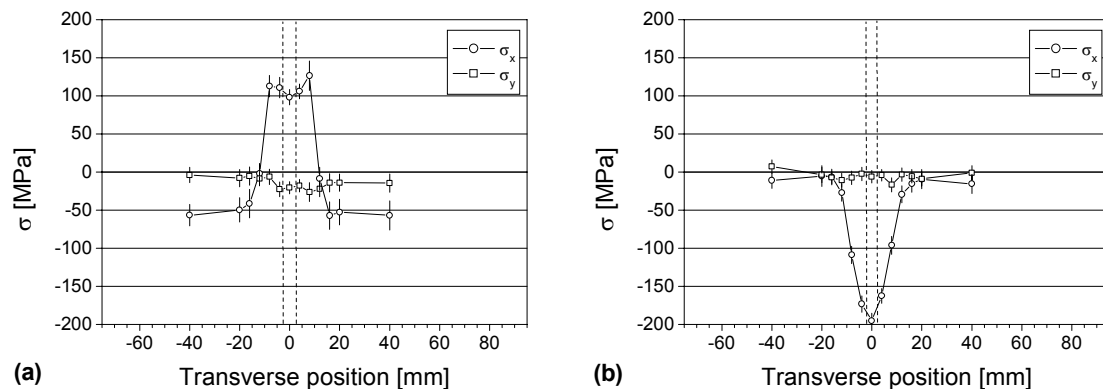



Figure 2: Residual stresses in friction stir welded 2024-T351 3.2 mm sheets: a) untensioned reference; b) tensioned to 70 % YTS prior to welding.

This work was carried out under the 5th Framework project WAFS (Project No. GRD1-1999-10271). Funding from the EU is gratefully acknowledged.

Reference

- [1] C.J. Dawes, W.M. Thomas: *Weld. Journal* 75, 1996, 41
- [2] S.W. Williams: "Welding of Airframes using Friction Stir", *Air and Space Europe*, Vol. 3 No. 3/4, 2001,
- [3] A. Heinz, A. Haszler, C. Keidel, S. Moldenhauer, R. Benedictus, W.S. Miller: *Mat. Sci. Eng. A* 280, 2000, 102-107
- [4] H.G. Priesmeyer: in 'Measurement of residual and applied stress using neutron diffraction', (eds. M.T.Hutchings, A.D. Krawitz), NATO ASI series E 216, 1992, 277-284
- [5] A.J. Allen, M.T. Hutchings, C.G. Windsor, C. Andreani: *Advances in Physics* 34, 1985, 445-473

	EXPERIMENTAL REPORT	GeNF ARES
Residual stress in friction stir welded AA7010 sheets		
Principal Proposer:	P. Staron, M. Koçak GKSS Research Centre	
Experimental Team:	H.-U. Ruhnau, P. Staron GKSS Research Centre	
Date(s) of Experiment:	07.10.–31.10.2002	

Friction stir welding (FSW) is a solid state joining process that takes place below the melting point of the materials to be joined. FSW uses a rotating cylindrical tool with a pin to frictionally heat the material. The tool pin stirs the plasticised material and therefore joins two pieces together when it is moved along the welding line. Advantages of this technique include e.g. weldability of materials that are difficult to fusion weld, low distortion, and excellent mechanical properties. FSW is currently under extensive investigation for joining aluminium alloys in the aerospace industry.

The magnitude and distribution of residual stress in FSW welded Al alloys for aerospace applications should be known to assess their role in fatigue and corrosion behaviour of the welded joints. Attempts should be made to produce sound FSW joints with low residual stresses with industry-relevant approaches without causing any degradation in microstructural and mechanical properties.

The aim of this study is to determine the residual stress state in FSW Al alloy sheets that have been subjected to mechanical tensioning during welding. Aluminium sheets (AA7010-T7651) of size 250 mm × 380 mm and 6.3 mm thickness were produced by FSW at the BAE SYSTEMS, UK. One sheet was subjected to mechanical tensioning up to 70 % of the tensile yield strength in a special in-situ tensioning machine, then it was welded, and after welding it was released. Another sheet was welded without being tensioned for reference purpose.

Residual strains were measured in the two sheets with the diffractometer ARES using the Al (311) reflection at a diffracting angle of about 84°. In the 6.3 mm thick sheets, a gauge volume of approximately 3×3×30 mm³ was used for scanning the transverse and normal strains to improve intensity. This choice of the gauge volume implies that the stresses are constant along x over the length of the volume element, which should be approximately true. A gauge volume of approximately 3×3×3 mm³ had to be used for the longitudinal strain, because larger stress gradients are present along the transverse (y) direction. In heat treatable Al alloys, the solute content depends on the heat treatment the material has experienced. Therefore, the lattice distance changes across the weld, which means that there is a local variation in the stress-free lattice distance in the weld region. Here, the stress-free lattice distances d_0 were determined under the assumption of a plane stress condition.

The stress distribution in the untensioned reference sheet (Fig. 1a) is very similar to former results found in 2024 alloys: there are stress peaks of about 130 MPa in the longitudinal direction in the heat affected zones on both sides of the weld with a minimum in the center of the weld, i.e. the weld nugget. The transverse stress is small. This stress distribution seems

to be typical for FSW aluminium sheets. Fig. 1b reveals a large effect of the mechanical tensioning on the residual stress state of the weld: a compressive longitudinal stress up to -150 MPa is achieved in the weld region. As a balance, the longitudinal stress farther away from the weld is now tensile. The transverse stresses are still small, but partly compressive. These results are basically the same as those obtained with mechanically tensioned 2024 sheets.

Tensile residual stresses in general can have detrimental effects on mechanical properties, while compressive stresses can bring along beneficial effects. At least, the possibility of producing friction stir welds with very different residual stress states by the mechanical tensioning technique gives the chance to study the influence of the residual stress state on the mechanical performance of these welds.

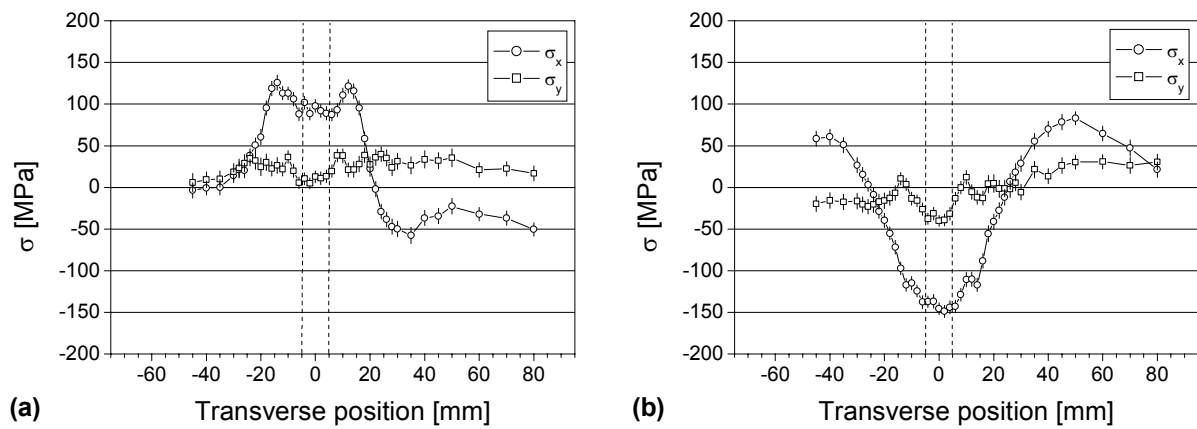


Figure 1: Residual stresses in friction stir welded 7010-T7651 6.3 mm sheets: a) untensioned reference; b) tensioned to 70 % YTS prior to welding.

	EXPERIMENTAL REPORT	GeNF ARES
Residual stress in a cold-stretched friction stir welded AA2024 sheet		
Principal Proposer:	P. Staron, M. Koçak GKSS Research Centre	
Experimental Team:	H.-U. Ruhnau, P. Staron GKSS Research Centre	
Date(s) of Experiment:	22.11.–30.1.2002	

Friction stir welding (FSW) is a solid state joining process that takes place below the melting point of the materials to be joined. FSW uses a rotating cylindrical tool with a pin to frictionally heat the material. The tool pin stirs the plasticised material and therefore joins two pieces together when it is moved along the welding line. Advantages of this technique include e.g. weldability of materials that are difficult to fusion weld, low distortion, and excellent mechanical properties. FSW is currently under extensive investigation for joining aluminium alloys in the aerospace industry.

The magnitude and distribution of residual stress in FSW welded Al alloys for aerospace applications should be known to assess their role in fatigue and corrosion behaviour of the welded joints. Attempts should be made to produce sound FSW joints with low residual stresses with industry-relevant approaches without causing any degradation in micro-structural and mechanical properties.

The aim of this study is to determine the residual stress state in an FSW Al alloy sheet that has been subjected to cold stretching up to 80 % of the tensile yield strength after welding. Two Al sheets (AA2024-T351) of size 250 mm × 380 mm and 3.2 mm thickness were produced by FSW at the BAE SYSTEMS, UK. One of the sheets was subjected to mechanical tensioning up to 80 % of the tensile yield strength in a special in-situ tensioning machine after it had been welded. Another sheet was welded without being additionally tensioned for reference purpose.

Residual strains were measured in the two sheets with the diffractometer ARES using the Al (311) reflection at a diffracting angle of about 84°. In the 3.2 mm thick sheets, a gauge volume of approximately 2×2×30 mm³ was used for scanning the transverse and normal strains to improve intensity. This choice of the gauge volume implies that the stresses are constant along x over the length of the volume element, which should be approximately true. A gauge volume of approximately 2×2×2 mm³ had to be used for the longitudinal strain, because larger stress gradients are present along the transverse (y) direction. Since 2024 is a heat treatable alloy, the solute content depends on the heat treatment the material has experienced. Therefore, the lattice distance changes across the weld, which means that there is a local variation in the stress-free lattice distance in the weld region. Here, the stress-free lattice distances d_0 were determined under the assumption of a plane stress condition.

The stress distribution in the untensioned reference sheet (Fig. 1a) is very similar to former results: there are stress peaks of about 130 MPa in the longitudinal direction in the heat affected zones on both sides of the weld with a minimum in the center of the weld, i.e. the weld nugget. The transverse stress is very small. This stress distribution seems to be typical

for FSW aluminium sheets. Fig. 1b reveals a large effect of the post weld cold stretch on the residual stress state of the weld: the tensile longitudinal stresses have been completely eliminated, instead there is compressive longitudinal stress in the weld region. The transverse stresses seem to be almost unaffected.

Tensile residual stresses in general can have detrimental effects on mechanical properties, while compressive stresses can bring along beneficial effects. At least, the possibility of producing friction stir welds with very different residual stress states by the mechanical tensioning technique gives the chance to study the influence of the residual stress state on the mechanical performance of these welds.

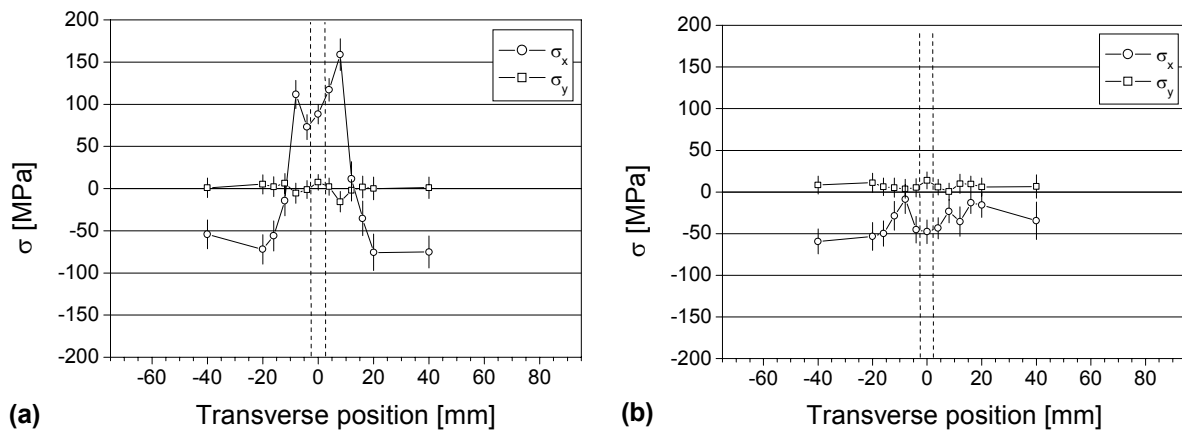



Figure 1: Residual stresses in friction stir welded 2024-T351 3.2 mm sheets: a) untensioned reference; b) tensioned to 80 % YTS after welding.

	EXPERIMENTAL REPORT	GeNF ARES
Residual stress in friction stir welded AA2024 thick plates		
Principal Proposer:	P. Staron, M. Koçak GKSS Research Centre	
Experimental Team:	H.-U. Ruhnau, P. Staron GKSS Research Centre	
Date(s) of Experiment:	26.06.–01.07.2002 and 29.07.–08.08.2002	

Friction stir welding (FSW) is a solid state joining process that takes place below the melting point of the materials to be joined. FSW uses a rotating cylindrical tool with a pin to frictionally heat the material. The tool pin stirs the plasticised material and therefore joins two pieces together when it is moved along the welding line. Advantages of this technique include e.g. weldability of materials that are difficult to fusion weld, low distortion, and excellent mechanical properties. FSW is currently under extensive investigation for joining aluminium alloys in the aerospace industry.

The magnitude and distribution of residual stress in FSW welded Al alloys for aerospace applications should be known to assess their role in fatigue and corrosion behaviour of the welded joints. Attempts should be made to produce sound FSW joints with low residual stresses with industry-relevant approaches without causing any degradation in microstructural and mechanical properties.

The aim of this study is to determine the residual stress state in FSW Al alloy thick plates. Two plates (AA2024-T351) with a size of 270 mm × 650 mm and 20 mm thickness were produced by FSW. Fig. 1 shows an optical macrograph of the weld cross section.

Residual strains were measured in the two plates with the diffractometer ARES using the Al (311) reflection at a diffracting angle of about 84°. The scan line was across the weld, 10 mm away from the surface of the plate, i.e. in the middle of the plate. A gauge volume of approximately 3×3×30 mm³ was used for scanning the transverse and normal strains to improve intensity. This choice of the gauge volume implies that the stresses are constant along x over the length of the volume element, which should be approximately true. A gauge volume of approximately 3×3×3 mm³ had to be used for the longitudinal strain, because larger stress gradients are present along the transverse (y) direction. Since 2024 is a heat treatable alloy, the solute content depends on the heat treatment the material has experienced. Therefore, the lattice distance changes across the weld, which means that there is a local variation in the stress-free lattice distance d_0 in the weld region. Here, d_0 was determined from a comb-like structure that was cut out of one plate by spark erosion. The cross section of the teeth of the comb was 2.5 × 2.5 mm², the length of the teeth was 40 mm.

The variations of d_0 across the weld are shown in Fig. 2. The maximum variation is 6·10⁻⁴ in the heat affected zones. The d_0 values shown in Fig. 2 were used to calculate residual stresses (Fig. 3). The stress distributions in both plates are very similar. The distribution of longitudinal stress (σ_x) in these thick plates is very similar to that observed in thin sheets up to 6.3 mm thickness: there are longitudinal stress peaks between 100 and 150 MPa in the heat affected zones on both sides of the weld with a minimum in the center of the weld, i.e.

the weld nugget. The transverse and normal stresses are very similar to each other in both plates. There appear to be also peaks in the transverse and normal stresses of about 50 MPa in the heat affected zones. Farther away from the weld the transverse and normal stresses are close to zero while the longitudinal stress is slightly compressive.

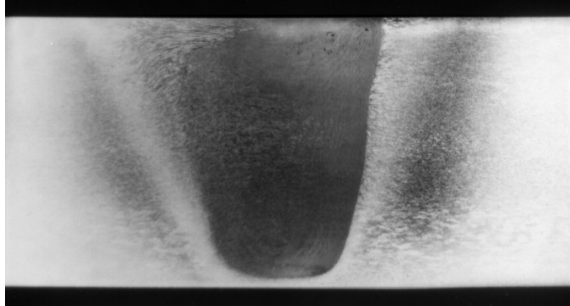


Figure 1:

Optical macrograph of a cross section of the friction stir weld of a 20 mm thick 2024 plate.

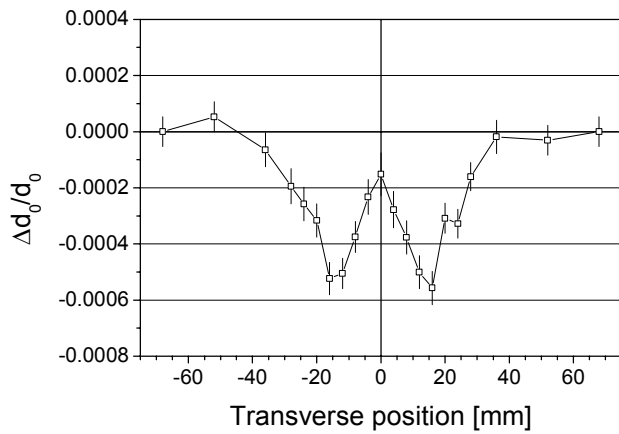


Figure 2:

Variation of d_0 across the weld as obtained from measurements of a 'comb' cut out of a 20 mm plate.

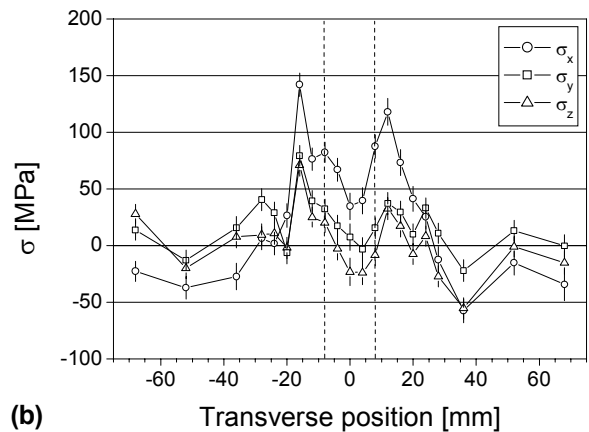
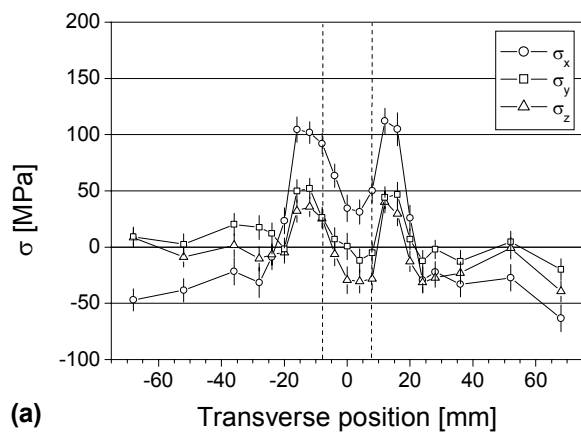



Figure 3: Residual stresses in two friction stir welded 2024-T351 20 mm plates: a) plate 1; b) plate 2.

This work was carried out under the 5th Framework project WAFS (Project No. GRD1-1999-10271). Funding from the EU is gratefully acknowledged.

	EXPERIMENTAL REPORT	GeNF FSS
Neutron time-of-flight spectrometer FSS		

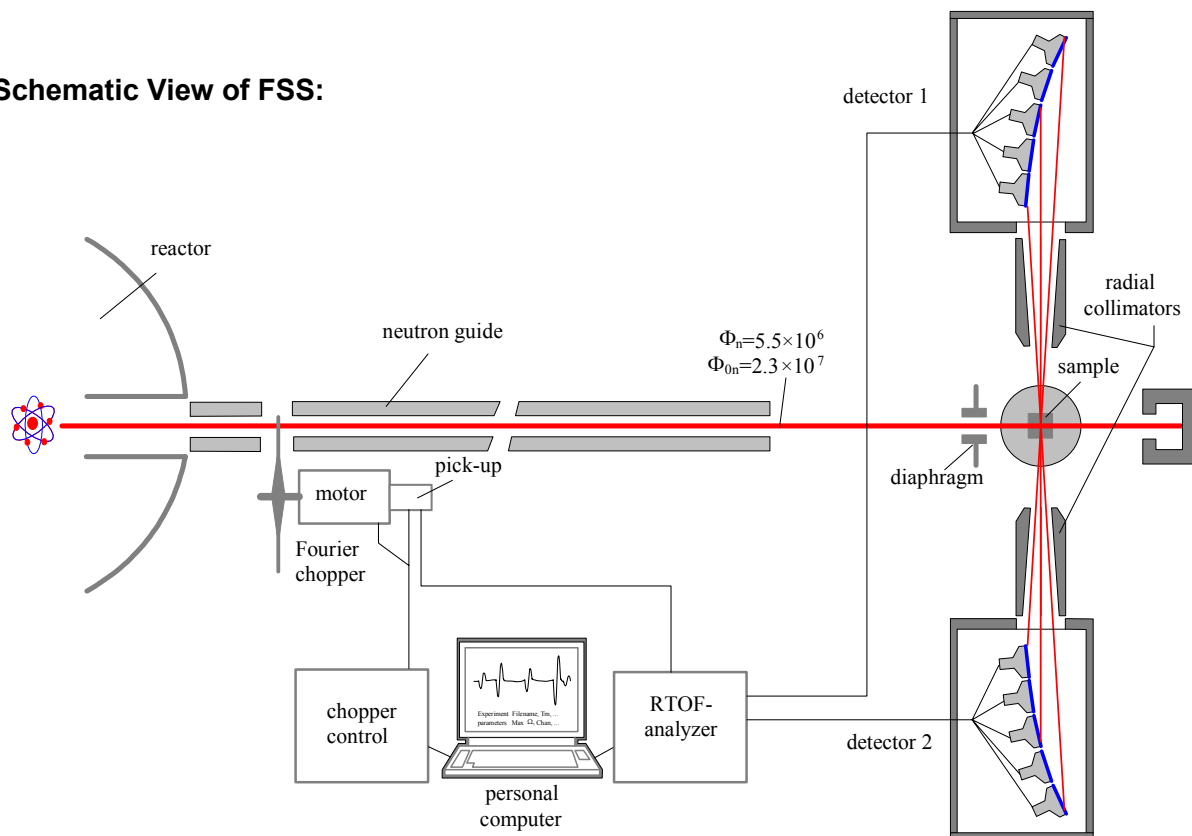
Short Instrument Description:

The spectrometer FSS is a Fourier reverse time-of-flight spectrometer (system Hiismäki) to investigate residual stresses in polycrystalline material specimens with technical sizes using thermal neutrons. Details can be found in P.Hiismäki, Modulation Spectrometry of Neutrons with Diffraction Applications, World Scientific, 1997.

Local Contact:

Prof. Dr. Hans Georg Priesmeyer
 Phone/Fax : +49 (0)4152 87-1315 / +49 (0)4152 87-1338
 e-mail: priesmeyer@gkss.de

Schematic View of FSS:




Instrument Details:

Location at FRG-1:	beam line 9, thermal neutrons
Flight path:	21.15 m Ni-coated curved neutron guide, radius of curvature: 3000 m characteristic wavelength: $\lambda_{char} = 0.183 \text{ nm}$ beam size: $2 \times 20 \text{ mm}^2$ to $15 \times 108 \text{ mm}^2$
Fourier chopper:	1024 slits, 1760 rpm max. operating speed
Flux at sample position:	$\Phi = 5.5 \cdot 10^6 \text{ cm}^{-2} \text{ s}^{-1}$
Wavelength range:	$\lambda = 0.1 \text{ nm}$ to 0.4 nm

Instrument Details (continued):

Timing resolution:	ca. $4 \cdot 10^{-3}$ ($\lambda = 0.1\text{--}0.4$ nm)
TOF analyser:	reverse time of flight correlator 2 x 3072 channels, 1 μ s minimum channel width
Detector:	2 Li-6 glass scintillation detector banks (90° & 270°) in time-focussing geometry
Ancillary equipment:	sample positioner for strain tensor determination – heater (up to 1000 °C) – stress rig: max. force: 30 t

	EXPERIMENTAL REPORT	GeNF FSS
Minimizing residual stresses and distortion of cast iron components		
Principal Proposer:	W. Stets ¹ ¹ Institut für Giessereitechnik (IfG), Düsseldorf, Germany	
Experimental Team:	H. G. Priesmeyer ² , V. Kudryashev ³ , U. Tietze ³ , G. Bokushava ³ ² Universität Kiel, Germany ³ GKSS Research Centre	
Date(s) of Experiment:	2002	

Scientific Objective

The technological objective of these investigations is the minimization of the residual stress fields induced into automotive structural components during the casting and subsequent cooling process. The work was performed in the context of a joint project between the Institut für Giessereitechnik (IfG), Düsseldorf – as coordinator –, GKSS Research Centre, MAGMA GmbH., Aachen, and a group of leading german casting companies on behalf of the car manufacturers AUDI and FORD Motor Company. The components under investigation were the following: brake discs (material: EN-GJL-150 lamellar graphite, 100 % perlitic); motor blocks (material: EN-GJV-500, vermicular graphite, 100 % perlitic); stress test lattices (material EN-GJV-500, see above); transverse control arms (material: EN-GJS-400-15, spheroidal graphite, 100 % ferritic). The perlitic microstructure consists of 88 % ferritic phase and 12 % cementite Fe₃C. Typical microstructures are shown in the next figure.

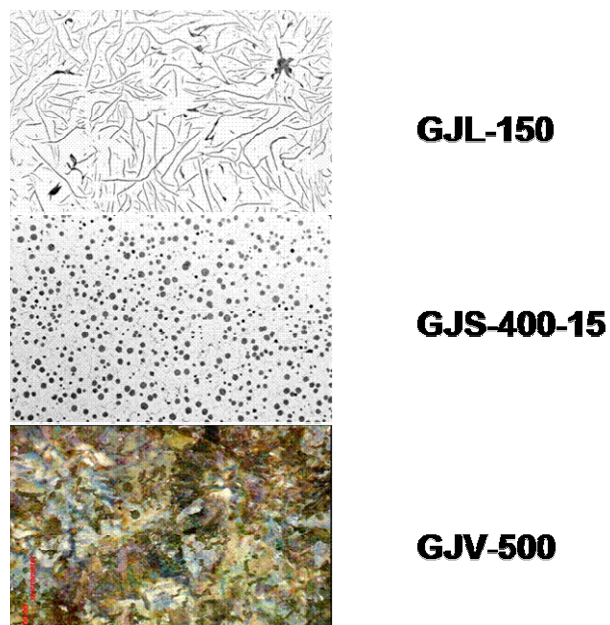


Figure 1:
Microstructure of the materials of the cast components.

Experimental Techniques

The measurements were made at the FSS neutron time-of-flight diffractometer at locations predetermined by finite element calculations. Figure 2a and 2b show a brake disk as a typical example.

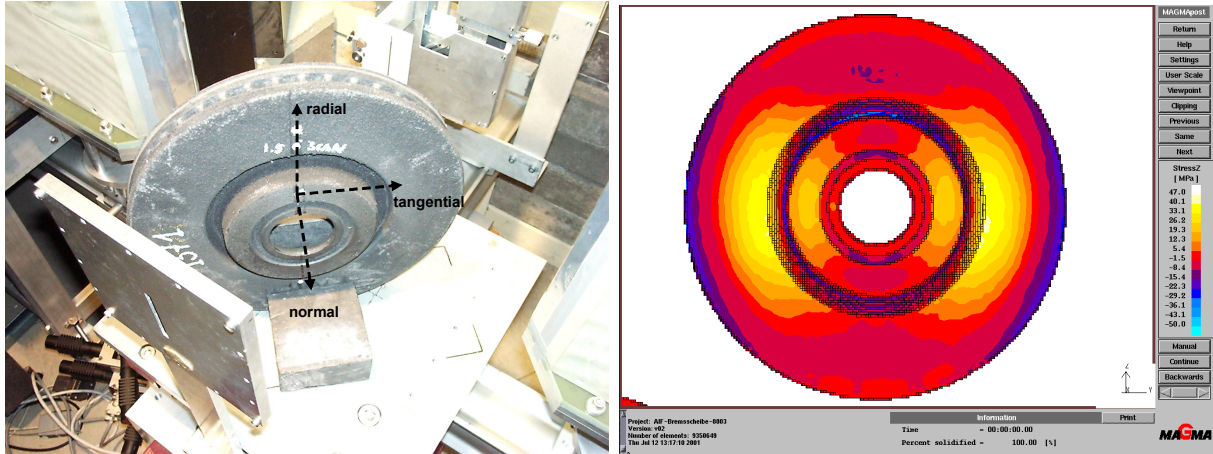


Figure 2a: Brake disk in measuring position. Figure 2b: Calculated stress field.

Similar measurements and calculations exist for the motor blocks and stress test lattices. The transverse suspensions have not yet been finished, partly due to their complicated geometry.

Main Results

The analysis of the data is still in progress, but discrepancies between the FE calculations and neutron measurements on an absolute scale have been observed. This may be caused by the relatively high content of cementite in the perlitic phase, which has an incompatible crystal size, not taken into account by the calculations. Another rather interesting result is shown in Figure 3, where two strain scans at the same location in a cast specimen are compared: the first measurement was made within three days after casting, while the second measurement was made about 4 weeks later. Whether the trend of relaxation is real, must be investigated in an experiment scheduled for early 2003. Relaxation would be a phenomenon of great economic concern.

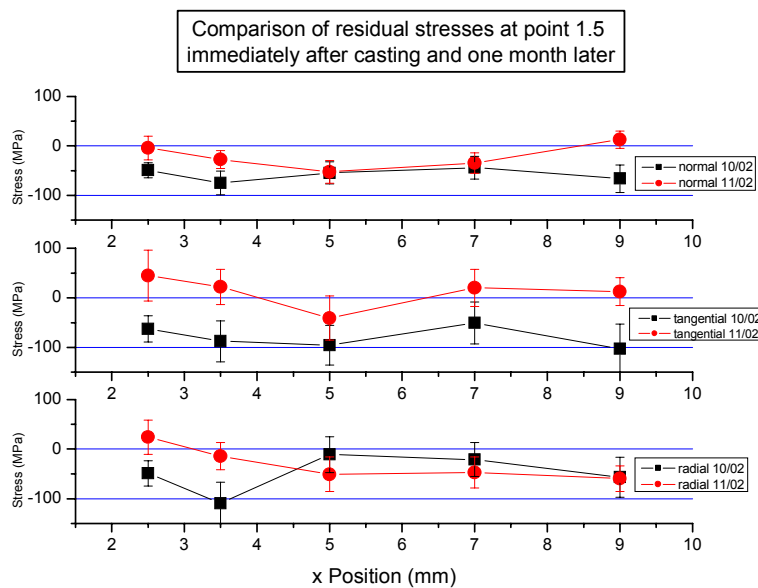



Figure 3: Stress scan through characteristic location within a break disk.

	EXPERIMENTAL REPORT	GeNF FSS
Neutron TOF diffraction from fiber-reinforced Al-MMC material		
Principal Proposer:	A. Wanner ¹ ¹ MPI Metallforschung Stuttgart, Germany	
Experimental Team:	H. G. Priesmeyer ² , V. Kudryashev ³ , U. Tietze ³ ² Universität Kiel, Germany ³ GKSS Research Centre	
Date(s) of Experiment:	April 2002	

Scientific Objective

Elastic strains in longitudinal and transverse directions relative to the axis of cylindrical specimens containing fiber reinforcements have been investigated by neutron time-of-flight diffractometry. The material consists of two phases (Al and Al₂O₃ fibers, the latter having a “two-dimensional random” orientation distribution). The experiments were feasibility studies at room temperature, to be extended in a future cooperation to temperatures up to 200 °C. By applying different load forces to the specimen, the diffraction elastic constants are to be measured at different temperatures.

Experimental Techniques

Measurements using a TOF spectrometer are able to produce Young’s moduli and Poisson’s ratios for as many crystal lattice planes as are covered by the neutron spectrum available. Therefore the GKSS Fourier Strain Scanner FSS was used to perform these investigations (cf. Fig.1).

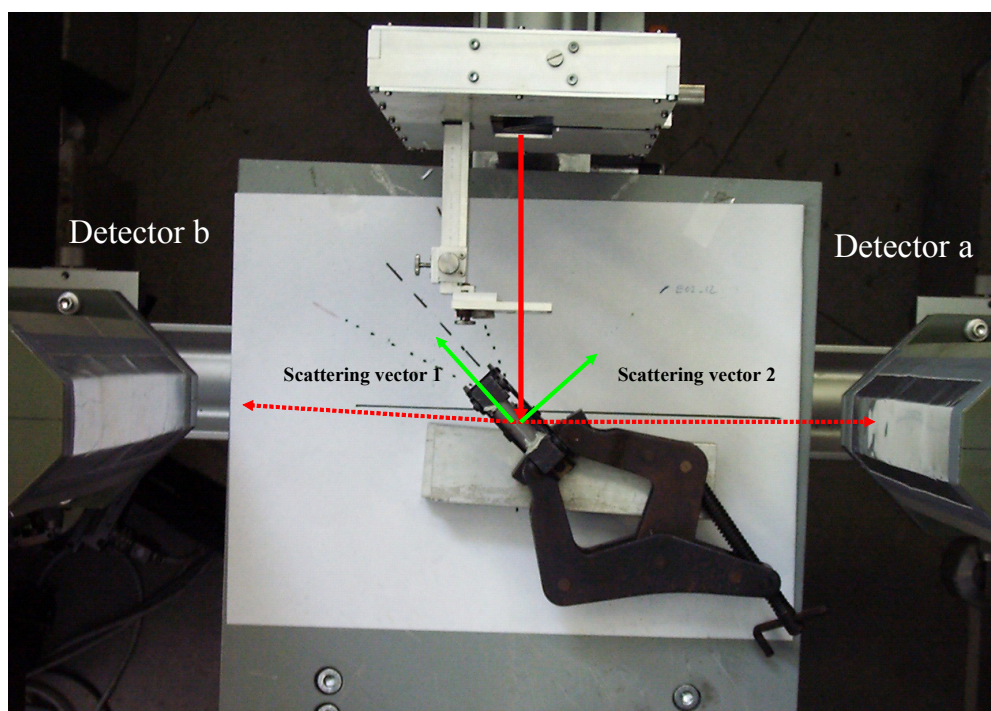


Figure 1: Specimen in measuring position at FSS.

The specimen geometry has to be maintained during the whole experiment, because of the extreme grades of texture inherent in the material (cf. Fig.2)

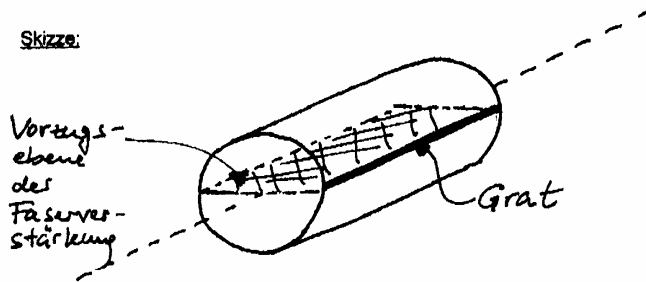


Figure 2:
Rough outline of specimen and fiber orientation.

Strains are calculated by comparison of the results of peak positions in the metal matrix composite and in pure cast aluminium. Typical spectra are shown in Fig. 3, where the upper row are the results from the a- and b- detector bank for the MMC, while the lower row shows the aluminium results. From these measurements it appears to be obvious, that due to the strong texture, only a limited number of lattice planes is accessible.

Neutron TOF spectra e02_20 (sample #2), e02_21(sample #1): delay 500 chn, Δt_c : 8 μ sec

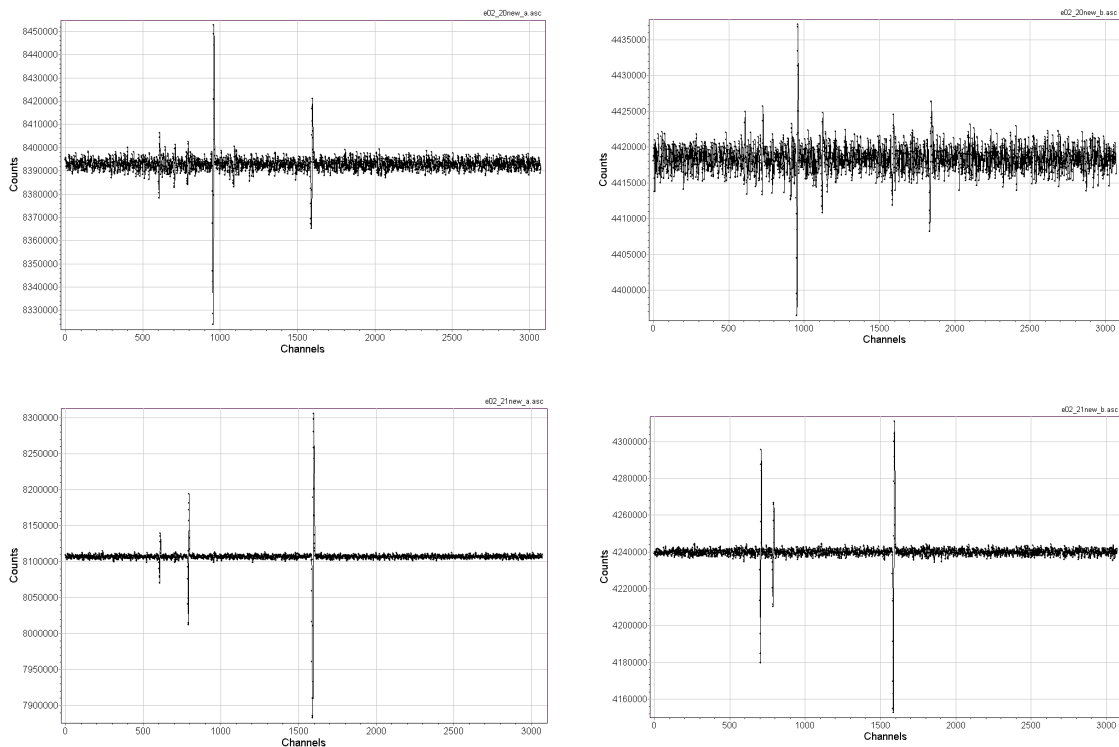



Figure 3: Neutron time-of-flight spectra for Al + Al₂O₃ fiber MMC and pure Al taken by FSS.

The preliminary experiments have shown that a more detailed investigation of the elastic properties at elevated temperatures will be feasible.

	EXPERIMENTAL REPORT	GeNF FSS
Stress investigations of Cu-Nb metal-matrix composites		
Principal Proposer:	Wen Hei Ye ¹ , H.-G. Brokmeier ¹ ¹ IWW, Technical University Clausthal, Germany	
Experimental Team:	H. G. Priesmeyer ² , V. Kudryashev ³ , U. Tietze ³ ² Universität Kiel, Germany ³ GKSS Research Centre	
Date(s) of Experiment:	June 2002	

Scientific Objective

The aim of this study is to determine both texture (at TEX II) and residual stresses (at FSS) of Cu/Nb composites treated at various temperatures between 4K to 1273 K. Through the heat treatment the microstructure of the Cu/Nb composite is changed, which leads to texture and strain changes. Because of their very good mechanical properties while keeping high electrical conductivity, Copper/Niobium metal matrix composites (MMC's), are of technological importance to potential use in long pulse high-field magnets and rotating electrical machinery. Copper and Niobium have basically no mutual solubility in the solid state. Therefore, the Cu/Nb fibre reinforced metal matrix composites are produced by mechanical processing (e.g. drawing, rolling or cold-extrusion) with very high strength and conductivity. It is claimed in the literature that Cu/Nb composites would have a tensile strength after deformation much greater than expected from the rule of mixtures.

Experimental Techniques

This Copper/Niobium composite consists of 50 Vol.% pure Cu and 50 Vol.% pure Nb. The size of the samples is 10*10*10 mm³ ; measurements were made in rolling direction and orthogonal to the rolling direction and repeated after turning the specimen by 90 degrees about the rolling direction.

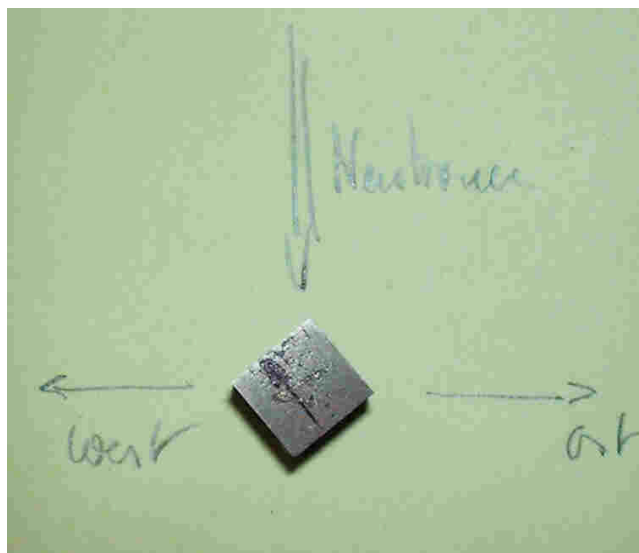


Figure 1:
 Top view of a typical Cu-Nb specimen,
 rolling direction indicated by arrow.

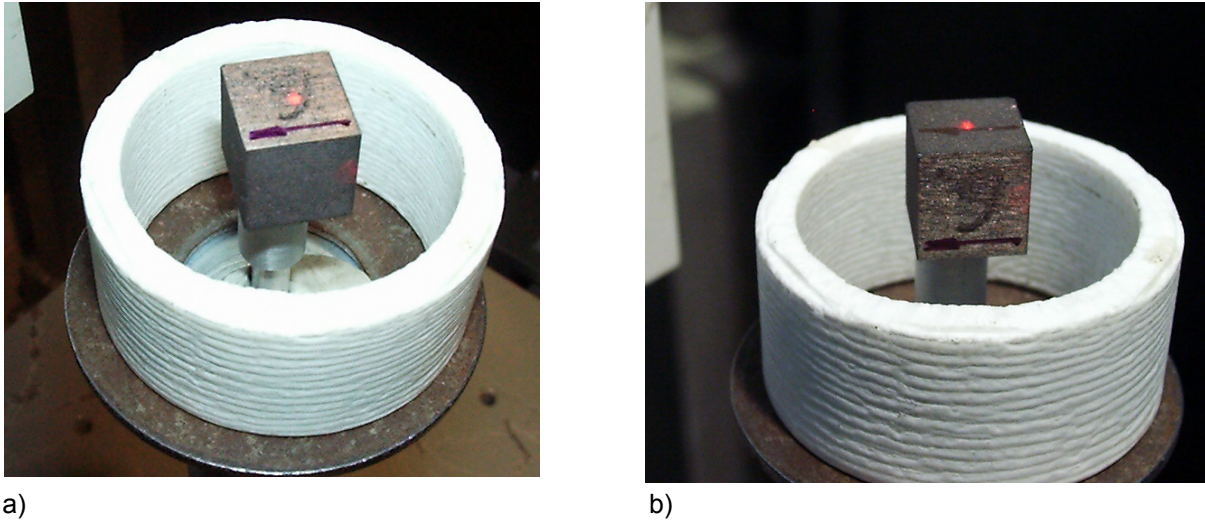


Figure 2 a/b: Specimen no. 6 in measuring position (neutron beam width $4 \times 10 \text{ mm}^2$, 2 mm radial collimation). Neutron background scattering is considerably reduced by a ${}^6\text{LiCO}_3$ ring (white).

Results

Eleven different specimens with different thermal treatment histories have been measured. Strains have been determined using the FSS niobium standard (annealed pure Nb powder) and annealed copper powder as references. The data analysis is still in progress and will be part of a PhD thesis. In addition, the results show that there are strong textures for the Cu- and Nb phases present in all samples.

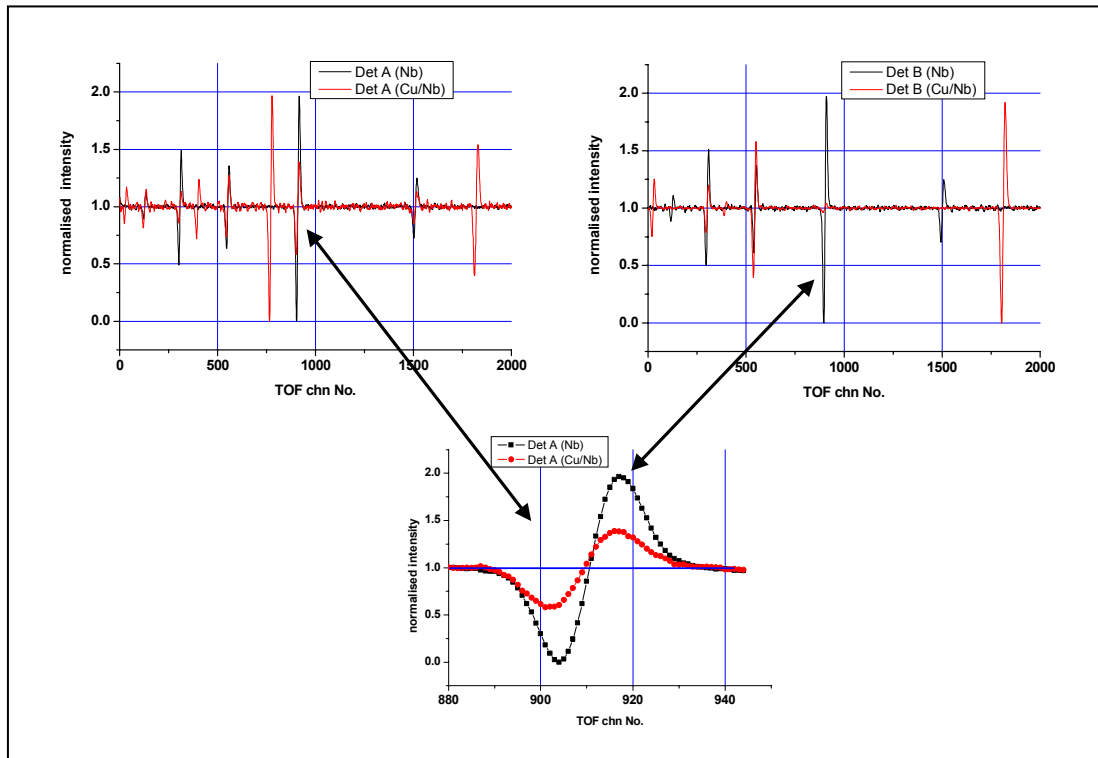



Figure 3: Typical neutron TOF spectra of Cu/Nb MMC and Nb powder collected at FSS, showing hkl-dependent strains and the influence of texture on reflection amplitudes.

	EXPERIMENTAL REPORT	GeNF TEX-2
Neutron texture diffractometer TEX-2		

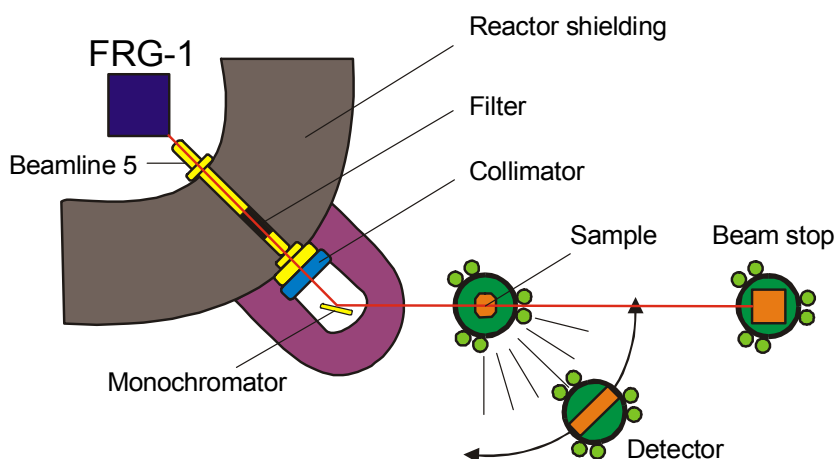
Short Instrument Description:

The four circle neutron texture diffractometer is used to characterise textures in metallic, ceramic and geologic materials applying thermal, non-polarised neutrons.

Local Contact:

Prof. Dr. Heinz-Günter Brokmeier
 Phone/Fax: +49 (0)4152 87-1207 / +49 (0)4152 87-1338
 e-mail: brokmeier@gkss.de

Schematic View of TEX-2:



Instrument Details:

Location at FRG-1:	beamline 5, thermal neutrons maximum beam cross section: 45 x 45 mm ²
Primary collimation:	30', 42', 51'
Monochromator:	Cu (111), Cu (200), PG (002), Ge (311)
Take-off angle:	17.2°, 27.2°, 37.2°, 47.2°, 57.2°
Wavelength range:	$\lambda = 0.0-0.27$ nm (in steps)
Flux at sample position:	$\Phi = 0.3-2 \cdot 10^6$ cm ⁻² s ⁻¹
Angular range	Φ : -360° to +360° X : -360° to +360° Ω : -46° to + 46° 2Φ : -75° to +120°
Detector:	³ He- single detector 38° JULIOS-PSD

Instrument Details (continued):

Sample geometries (standard): (various):	cube 10 mm edge, sphere 15–20 mm \varnothing cylinder 10–15 mm \varnothing , 10–15 mm high e.g. wires, tubes, tensile samples
Distances: sample– ^3He detector sample–JULIOS	40–200 cm 70–100 cm
Sample environment:	mirror furnace up to 2000 K loading device: tension up to 15 kN, compression up to 20 kN sophisticated set of sample holders

	EXPERIMENTAL REPORT	GeNF TEX-2
Modeling of Texture Evolution of Copper under Equal Channel Angular Pressing		
Principal Proposer:	Seung Chul Baik ¹ , Y. Estrin ² , R. J. Hellmig ² , Hyo-Tae Jeong ³ , Hyoung Seop Kim ⁴ ¹ Technical Research Labs., Pohang Iron & Steel Co. Ltd., Pohang, 790-785, Korea; ² Institut für Werkstoffkunde und Werkstofftechnik, TU Clausthal, Germany; ³ Dep't. Metall. Eng., Kangnung Natl. Uni., Gangneung 210-702, Korea; ⁴ Department of Metallurgical Engineering, Chungnam National University, Daejeon, 305-764, Korea	
Experimental Team:	B. Witassek, A. Günther, H.-G. Brokmeier Institut für Werkstoffkunde und Werkstofftechnik, TU Clausthal, Germany	
Date(s) of Experiment:	May 2002	

Abstract

Texture evolution was analysed with full-constraint Taylor model for an idealised perfectly plastic face centred cubic material as well as for real, strain-hardening, copper subjected to equal channel angular pressing (ECAP). For the idealised material, the stress in the plastically deformed part of the billet was shown to be uniform leading to complete filling of the die. FEM simulations showed that plastic deformation is localised in a narrow shear zone and that the plastic strain and texture in the billet become uniform after ECAP. A simplified recipe for texture calculation akin to that proposed by Gholinia *et al.* was suggested: it reduces the deformation under ECAP to a combination of two rotations separated by tension-compression. For the case of copper, a strain hardening model based on dislocation density evolution was used. It was shown that due to significant strain hardening during the first ECAP pass, the flowing material does not fill the outside die corner and a strain and texture non-uniformity develop. A gradual decrease of strain hardening in subsequent ECAP passes leads to a more uniform strain and texture across the billet. The simulated pole figures were shown to be in good agreement with the neutron diffraction data for copper deformed by ECAP (Routes A, C_r, B_c and B_c_r) suggesting that the model used provides a reliable modelling tool for simulating texture evolution under ECAP.

Experimental

ECAP experiments were conducted using samples of pure (99.95 %) copper. The details of the die and specimen geometry, shown schematically in Fig. 1, are given in Ref. 1. In what follows, a (Cartesian) laboratory coordinate system, (x,y,z), will be used. The x-axis is aligned with the extrusion direction (ED), the y-axis with the transverse direction (TD), and the z-axis with the normal direction (ND). Repetitive pressing was performed up to 4 passes. Complete pole figures for {111} reflections were measured by neutron diffraction at the GKSS Research Centre (Geesthacht, Germany). The samples with the length of 20 mm for measuring the pole figures were cut from the uniformly deformed middle portion of the workpieces that underwent ECAP. As neutron diffraction was measured over the entire transverse section of the workpiece, a measured pole figure represents the averaged texture of the workpiece.

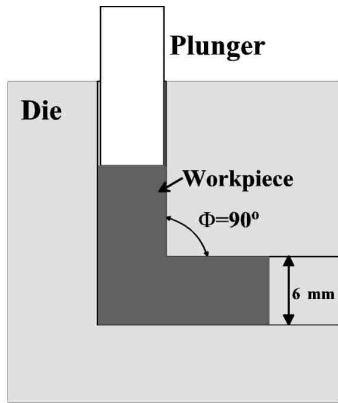
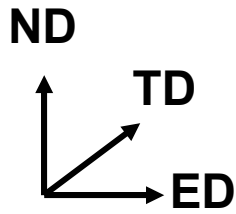


Figure 1:
Schematic diagram of the ECAP rig used.



Results

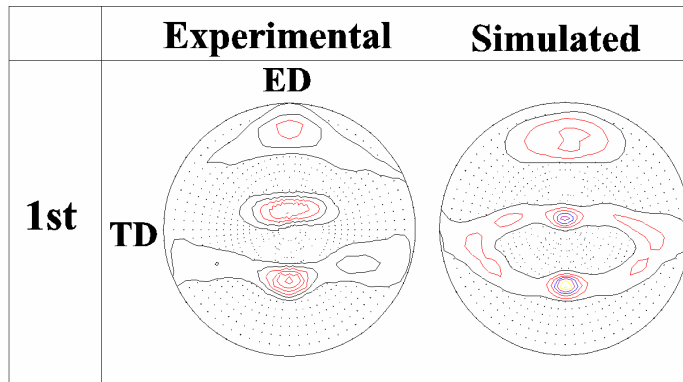


Figure 2: (111) pole figure (left) measured on copper after the first ECAP pass, along with a simulated one. (Contours in intervals of $0.5 \times$ random density.)

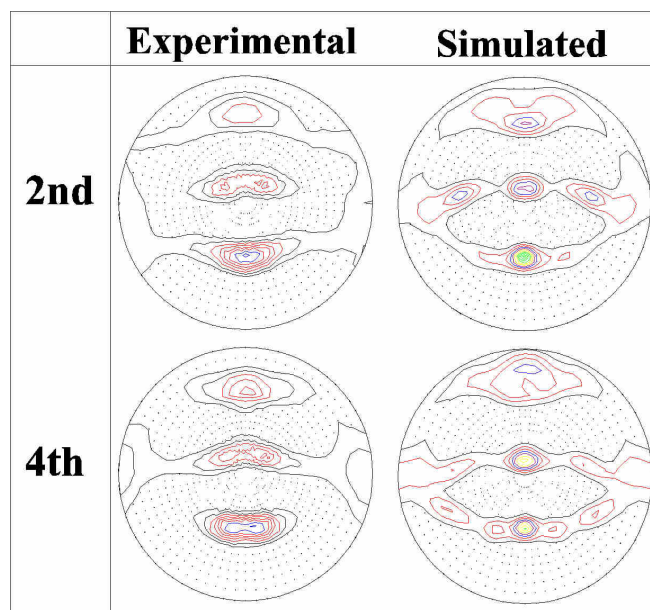



Figure 3: (111) pole figures measured on copper after the second and the fourth passes of ECAP, Route A, along with simulated ones. (Contours in intervals of $0.5 \times$ random density.)

	EXPERIMENTAL REPORT	GeNF TEX-2
Texture development during extrusion of Magnesium alloy AZ31		
Principal Proposer:	J. Bohlen, D. Letzig, K. U. Kainer GKSS Research Centre	
Experimental Team:	Yi, Sangbong, B. Witassek, H.-G. Brokmeier H.-G. Institut für Werkstoffkunde und Werkstofftechnik, TU Clausthal, Germany	
Date(s) of Experiment:	April – June, November, December 2002	

Magnesium alloys are interesting material perspective for reducing the structural weight of components due to their low density and good availability. However, mechanical properties occur to be moderate and have to be improved. The processing plays an important role for this improvement, especially for wrought alloys like sheets or extrusions. Generally, wrought materials offer a better quality of the microstructure and therefore offer the possibility to produce even very thin-walled structures from sheets or complex profiles from extrusions with homogeneous properties. Thus the understanding of the microstructural changes during the wrought process and its influence on the mechanical properties are the main objective for the improvement of the material properties.

The texture development during processing of magnesium wrought materials has to be understood in order to get improved more homogeneous mechanical properties. Especially, an anisotropic mechanical behaviour is caused by the shape and the strength of the texture based in the hexagonal lattice structure of magnesium alloys.

Several samples in a cube or cylinder shape have been taken from the remainder and the profile (rod) of an hydrostatic extrusion trial on magnesium alloy AZ31 in high purity quality. Hydrostatic extrusion gives a homogeneous pressure distribution on the billet from all directions and avoids friction between the container and the billet.

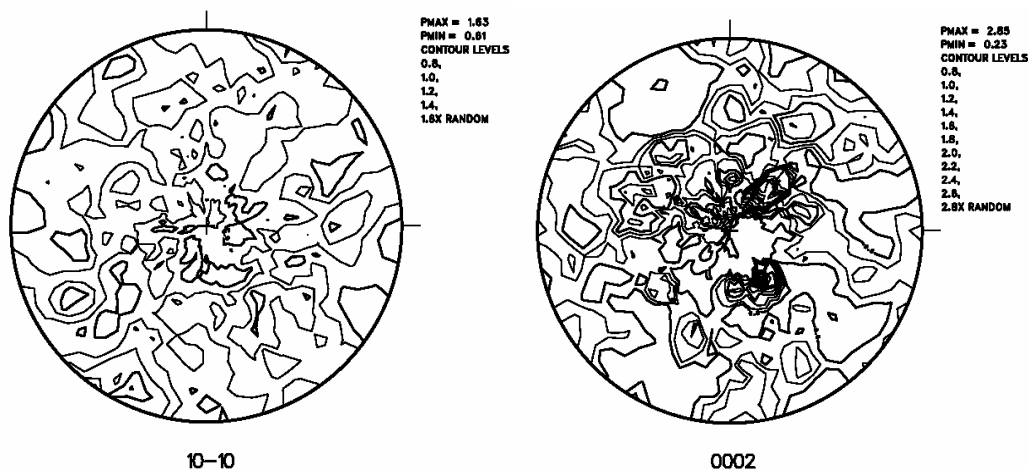


Figure 1: Pole figures of billet material.

The neutron beam at TEX-2 was used for texture measurements due to the high penetration depth of neutrons in order to receive an integrated information from the material at the related position.

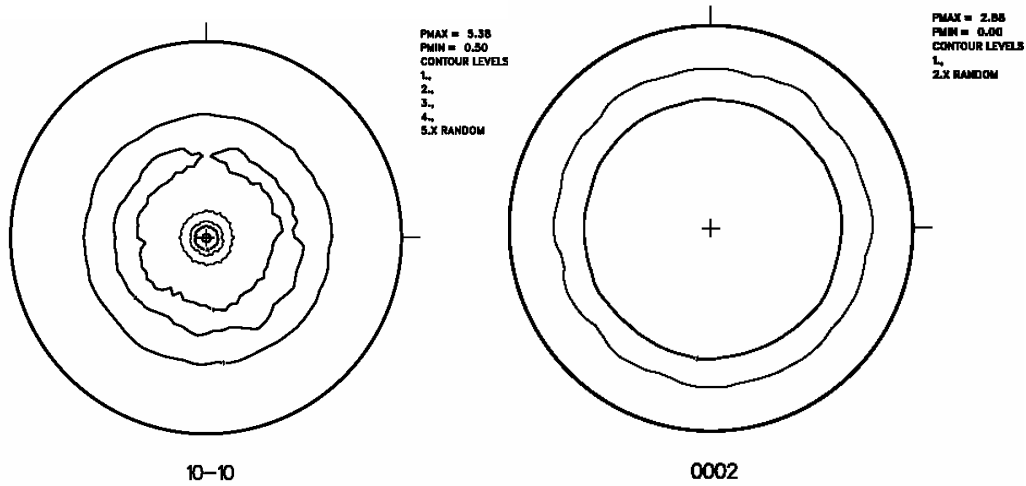


Figure 2: Pole figures of extruded profile at the begin of the extruded profile.

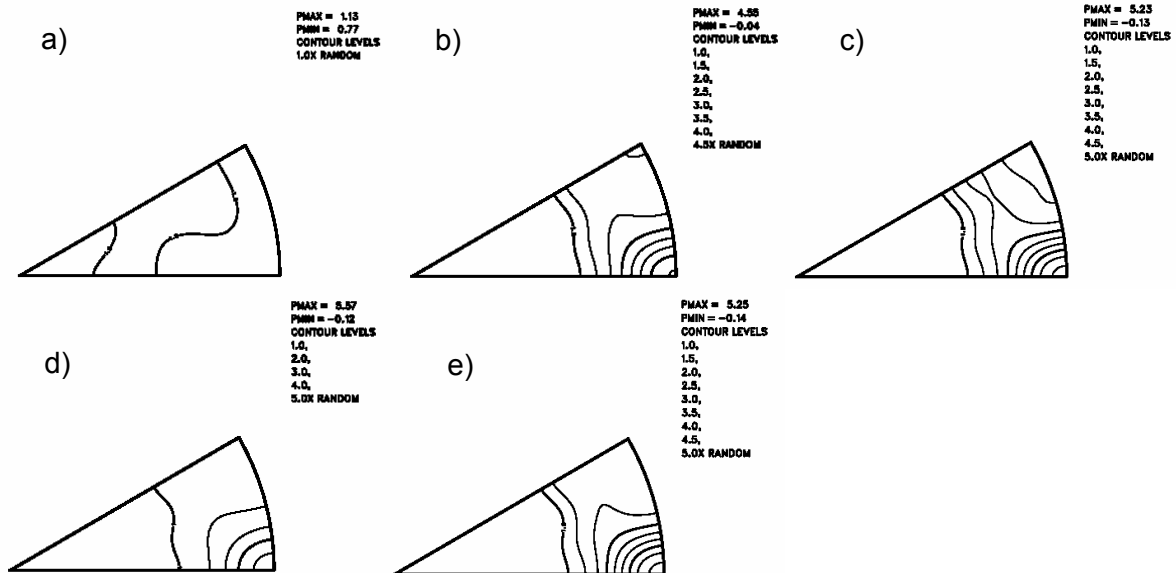



Figure 3: Inverse pole figures in extrusion direction from AZ31 after different steps of extrusion at 225°C. a) feedstock, b) after extrusion, c) centre sample near to the remainder, d) centre sample near to the begin of the profile, e) begin of extrusion profile.

In Figs. 1 and 2 the development of the texture from the cast billet to the extruded profile can be seen. A fibre texture with a random distribution of basal planes perpendicular to the extrusion direction results due to recrystallisation of the material and fundamental changes in the microstructure. However, Fig. 3 shows the changes in the texture from the cast billet (Fig. 3a) to the extruded profile (Fig. 3e) as well, but moreover a change in the texture over the extruded profile from the end near the remainder (Fig. 3b) to the begin (Fig. 3e) is found in terms of an increase in the peak intensity in the pole figures. Thus the properties are dependent on the position and also the microstructure is not homogeneous over the whole profile. It is supposed that an increase in the temperature of the billet due to friction between the billet and the die leads to a change in the deformation mechanisms and the recrystallisation behaviour. However, texture simulations are requested for a detailed analysis by showing the dependence of deformation mechanisms on the temperature.

	EXPERIMENTAL REPORT	GeNF TEX-2
Texture measurements in high Si content Fe alloys		
Principal Proposer:	R. E. Bolmaro, O. A. Lambri CONICET- Rosario national University. Argentina	
Experimental Team:	B. Witassek, H.-G. Brokmeier Institut für Werkstoffkunde und Werkstofftechnik, TU Clausthal, Germany	
Date(s) of Experiment:	October 2002	

Motivation

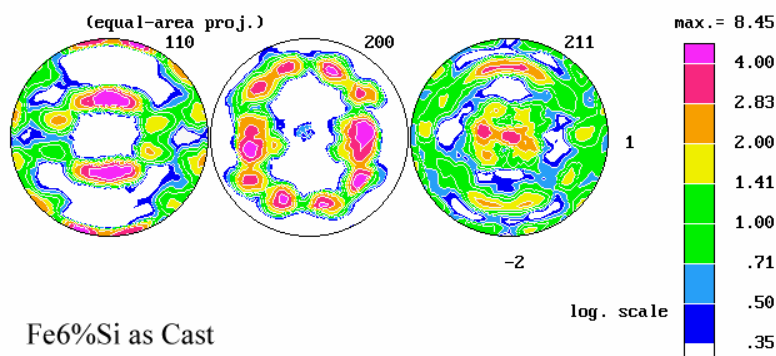
Fe based technological alloys like 6.5 % SiFe are of high interest because of their excellent magnetic properties [1, 2]. The incorporation of such a high Si content in commercial alloys is achieved by rapid quenching from fusion in a process called *single roller method*. After proper thermomechanical treatments, 1373 K during 1 hour, an adequate recrystallization texture is developed. Despite these alloys are already commercially produced [3, 4] it is still to be understood the relationship between micro-structure evolution and secondary-anomalous recrystallization. Thermomechanical treatments, annealing atmospheres and presence of alloying elements play a crucial role.

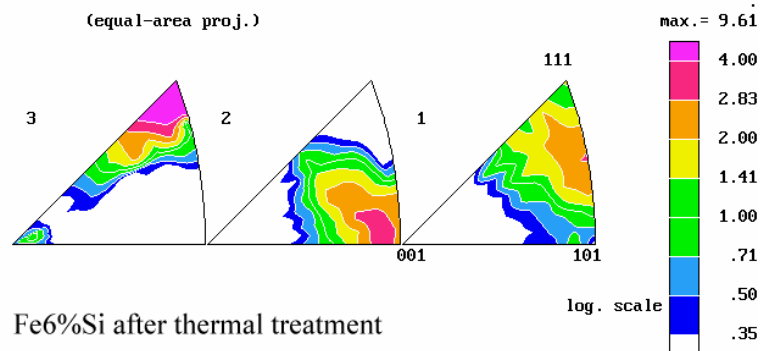
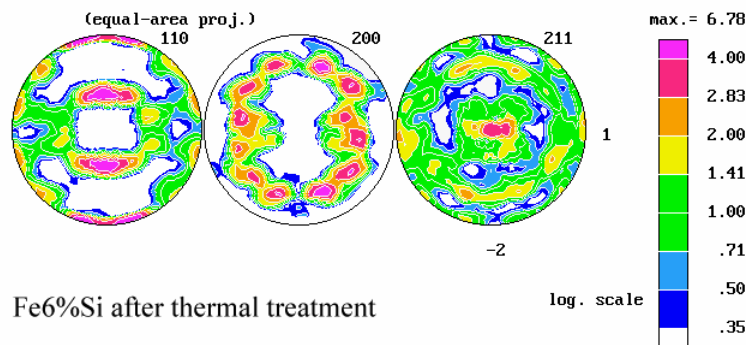
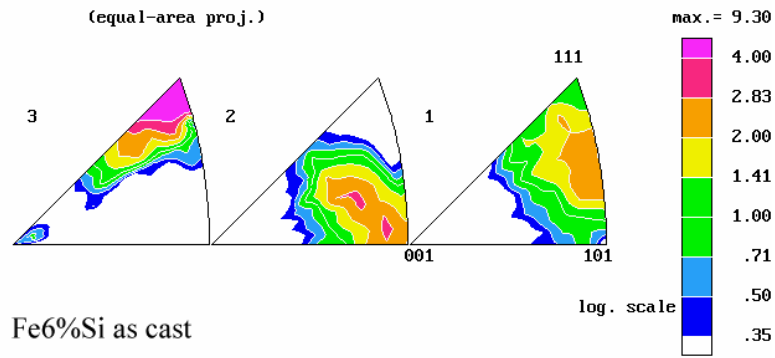
Recently we have studied dynamic behaviour, magnetic properties, recrystallization and its relationship with microstructure of traditional oriented grain Fe-Si alloys an high content Si alloys. Particularly for the high Si content alloys we have searched for the relationship between grain boundary relaxation and activation parameters [5, 6].

We are currently in search of the influence of thermomechanical treatment, annealing atmospheres and alloying elements over recrystallization texture development.

Results

Both textures are reducible to $\{111\} \langle 110 \rangle$ components which are not usually well behaving textures for transformer steels. Besides a slight texture severity decrement the inverse pole figures show a partial rotation of the $\langle 110 \rangle$ direction towards the rolling direction for the thermal treated sample.






Acknowledgements

This project was partially funded by the German-Argentine Intergovernmental Agreement # AL/A99-EXII/18 and CONICET-Argentina.

References

- [1] T. Watanabe, K.I. Arai, K. Yoshimi, H. Oikawa. *Phil. Mag. Lett.* 59(2), (1989), 47
- [2] K.I. Arai, K. Ohmori. *Metall. Trans. A* 17, 1295 (1986)
- [3] C. Appino, E. Ferrara, F. Fiorillo, I. Suberbielle, J. Degauque, C. Lebourg, M. Baricco. *J de Phys IV*, 8, (1998), 531
- [4] W. Cieurzyńska, J. Zbrozczyk, J. Frackowiak and K. Narita, *J. Mag. Mat.*, 133 (1994) 351.
- [5] O.A. Lambri, E.D. Bujales, P. Gorria, R.J. Tinivella. *J. of Mat. Sci.* 35 (2000), 79.
- [6] O. A. Lambri, J. I. Pérez-Landazábal, L. M. Salvatierra, L. M. Milani, C. Gómez-Polo and V. Recarte, *J. non Cryst. Solids.*, 287 (2001), 70.

	<h2>EXPERIMENTAL REPORT</h2>	<h2>GeNF TEX-2</h2>
<h3>Preferred orientation of phyllosilicates as a control of magnetic fabric, sedimentary rock samples from Rhenohercynian zone of Bohemian Massif</h3>		
Principal Proposer:	M. Chadima Masaryk University, Brno, Czech Republic	
Experimental Team:	A. Günther, B. Witassek, H.-G. Brokmeier Institut für Werkstoffkunde und Werkstofftechnik, TU Clausthal, Germany	
Date(s) of Experiment:	October – December 2002	

Regional setting and experimental objectives

The easternmost section of the Rhenohercynian Zone of the Bohemian Massif is characterized by the Lower Carboniferous flysch sediments, i.e. alteration of conglomerates, graywackes, siltstones and shales (fig.1). The sedimentary series were subsequently deformed by the Variscan fold and thrust deformation event. The ductile deformation, indicated by magnetic fabric (anisotropy of magnetic susceptibility, AMS measured by low-field Kappa bridge), gradually increases from the east to the west. The deformation occurred under the low-grade metamorphic condition and led to the origin of the N-S striking folds and cleavage.

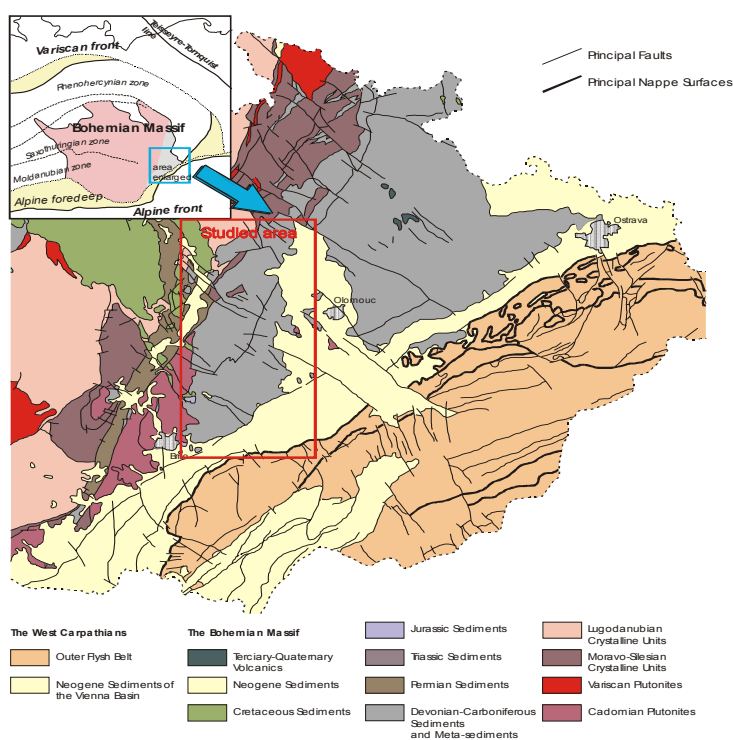


Figure 1: Geological map of the Easternmost margin of the Bohemian Massif with studied area outlined.

In the most deformed sediment the magnetic fabric progressively changes from primary to secondary one, from bedding parallel to cleavage parallel, respectively. The magnetic lineation is parallel to the bedding-cleavage intersection and the poles to magnetic foliation create a girdle between pole to bedding and pole to cleavage (fig. 2).

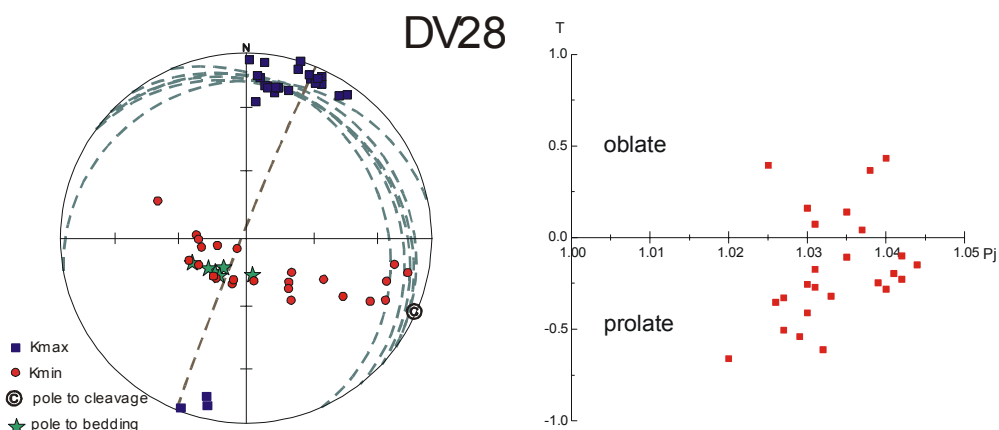


Figure 2: Example of the magnetic fabric – bedding – cleavage relationship of the most deformed samples.

The dominant carriers of magnetic properties of the sediments are paramagnetic phyllosilicates, chlorite and micas. Microscopic studies indicate that both the primary and secondary fabrics are due to phyllosilicate preferred orientation (fig. 3). Their strongly developed basal planes (001) dominate the grain shape and their measurement, therefore, determines the lattice and grain-shape preferred orientation.

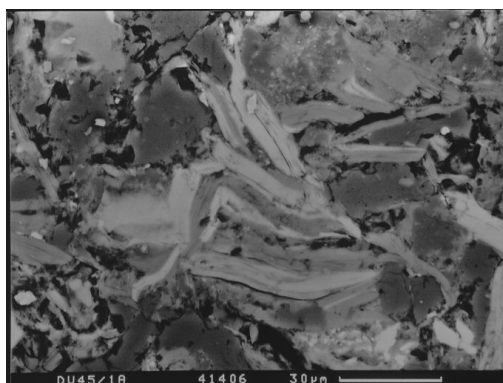


Figure 3: The SEM backscatter image showing the phyllosilicate.

The secondary fabric was formed by the different phyllosilicate reorientation mechanisms, e.g. micro-folding or preferential growth of new phyllosilicates under the anchi-metamorphic conditions. The neutron texture goniometry of phyllosilicate preferred orientation remarkably improved the understanding of the deformation processes. It showed the conventional technique of magnetic fabric measurement actually reflects the phyllosilicate preferred orientation (fig. 4). Combined with the high field torque measurement (anisotropy of paramagnetic minerals, carried it the ETH, Zürich) the texture goniometry will let us calculate the theoretic magnetic fabric necessary to evaluate the low field AMS – strain relationship.

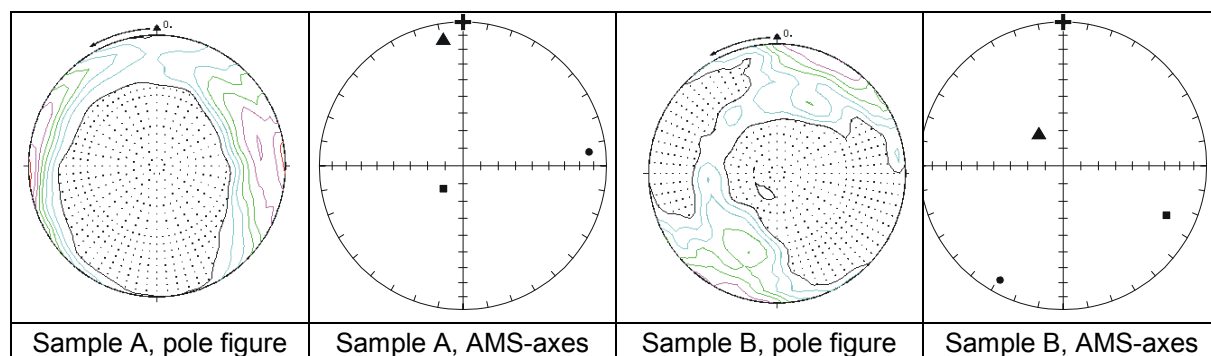



Figure 4: Maximum of chlorite (0002)-poles corresponds to the direction of minimum magnetic susceptibility (circle).

	EXPERIMENTAL REPORT	GeNF TEX-2
Reproduction of historical gypsum plaster		
Principal Proposer:	S. Follner ¹ , A. Wolter ² , H. Follner ¹ ¹ Institut für Mineralogie und Mineralische Rohstoffe, TU Clausthal, Germany ² Institut für Nichtmetallische Werkstoffe, TU Clausthal, Germany	
Experimental Team:	A. Günther, H.-G. Brokmeier Institut für Werkstoffkunde und Werkstofftechnik, TU Clausthal, Germany	
Date(s) of Experiment:	April – June 2002	

For centuries gypsum was used in external areas as mortar and also as masonry stones in several areas of Germany. The special property of the historical gypsum, still present in old buildings, is its exceptional strength which is comparable to concrete. These technically high-grade materials were largely supplanted with the introduction of Portland-Cement, and the knowledge of their mix formulations and production processes were lost. Localised leaching and delamination of gypsum mortar from walls exposed to the weather have resulted in a considerable need for external restoration. As part of the research project 18320 'Optimisation and Trials of Durable Gypsum Mortars by the Deutsche Bundesstiftung Umweltschutz it was aimed to produce a gypsum mortar with similar properties as the historical plaster.

Previous research showed that the property of strength of gypsum is connected to the order of the crystals [1–3]. In gypsum which is set from β -hemihydrate (produced by thermic dehydration of gypsum) a [010] fibre texture can be observed which continues from the surface into the sample. The formation of crystals in historical types of plaster can be summarised as four penetrating systems where the [010] fibre axis run approximately parallel to the diagonals of a cube. Due to the strong absorption of X-rays of sulphur and due to the small volume that can only be captured by X-ray diffraction, the pole figures were measured using neutron diffraction.

In the presented study a type of gypsum showing high strength and low capillary porosity was developed (C-gypsum). A submerged prism of this gypsum caused a maximum capillary rise of 2 mm after two weeks. Figure 1a shows the (020)-pole figure – measured by neutron diffraction – displaying four maxima as well. A slightly variation of the production process resulted in a second variety of gypsum (AS-gypsum) which didn't come near to the properties of C-gypsum. The fundamental advantage of this type of gypsum is its better processability. The (020)-pole figure shows only two but very broad maxima (fig.1b). A similar pole figure of a gypsum is obtained which was setted from a mixture of α -hemihydrate (processed by hydrothermal procedure) and newly developed hemihydrate (C+AS) at the ratio of 2:1 (Fig. 1c). The degradation for two maxima was also observed in (020)-pole figures of gypsum generated from several α -hemihydrates of different production processes. These compounds are characterised by a bigger hardness. The influence of the orientation distribution on the durability of gypsum is still not known.

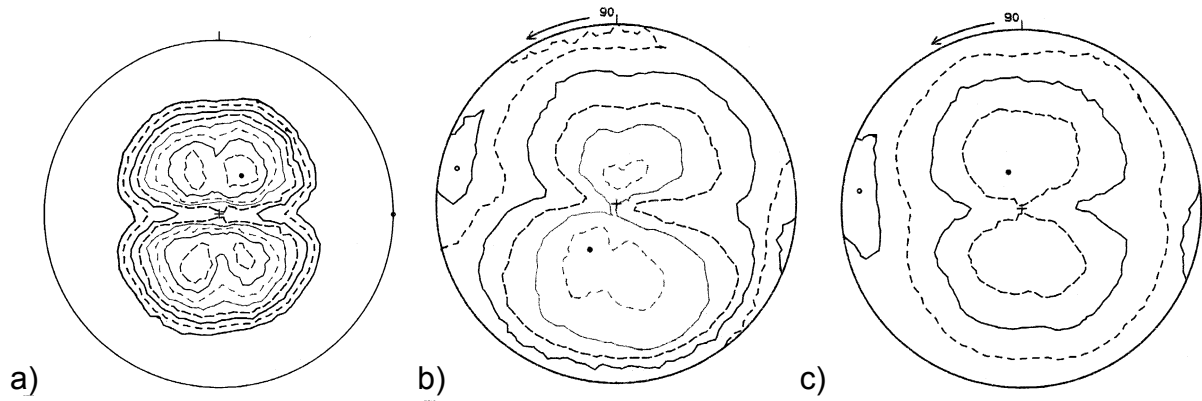


Figure 1: (020)-pole figures measured by neutron diffraction ($\lambda = 1.356 \text{ \AA}$) of
a) recently developed C-gypsum, b) AS-gypsum and
c) gypsum set from a mixture of α -hemihydrate and recently developed hemihydrates (C+AS).

References

- [1] Vogel, D., Follner, H., Jacobi, H., Kulke, H., Brokmeier, H.-G.: Characterization and reproduction of historical gypsum plasters and comparison with familiar modern preparations. *ZKG-International* 11 (1999) 640–648.
- [2] Follner, S., Wolter, A., Helming, K., Silber, C., Bartels, H., Follner, H.: On the real structure of gypsum crystals. *Cryst. Res. Technol.* 37 (2002) 207–218.
- [3] Follner, S., Wolter, A., Preusser, A., Indris, S., Silber, C., Follner, H.: The setting behaviour of α - and β - $\text{CaSO}_4 \cdot 0.5 \text{ H}_2\text{O}$ as a function of crystal structure and morphology. *Cryst. Res. Technol.* 37 (2002) 1075–1087.

	EXPERIMENTAL REPORT	GeNF TEX-2
Crystallographic preferred orientation of banded iron formations from Singhbhum Craton (Eastern India)		
Principal Proposer:	M. Mamtani, A. Mukherji, A. Chaudhuri Institute of Technology, Kharagpur-721302, India	
Experimental Team:	A. Günther, B. Witassek, H.-G. Brokmeier Institut für Werkstoffkunde und Werkstofftechnik, TU Clausthal, Germany	
Date(s) of Experiment:	April – June 2002	

There is a vast expanse of deformed iron ore bearing rocks, the Banded Iron Formations (BIF's) in the Singhbhum craton of eastern India. The structural geology of these BIF's is not properly understood till this day. Therefore, the Structural Geology Group at the Indian Institute of Technology (IIT), Kharagpur (India) has initiated structural studies on rocks from the Bonai Synclinorium, Orissa (India) that hosts BIF's.

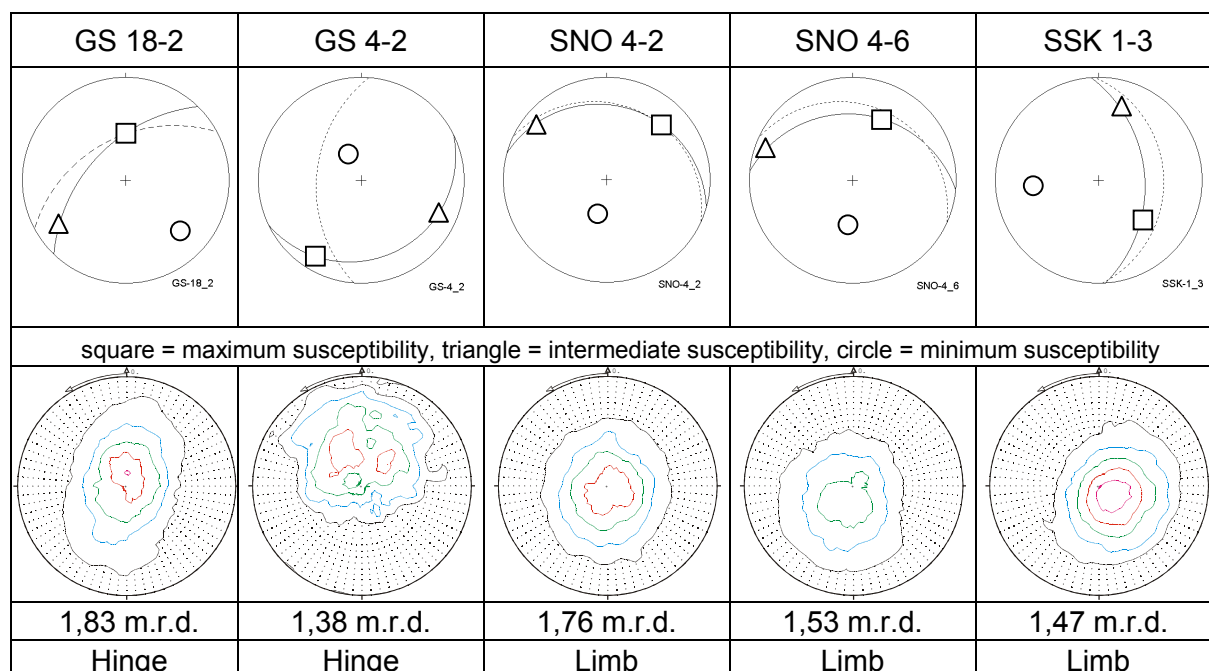
The study area is situated in the eastern part of India in the states of Orissa and Jharkhand. The Banded Iron Formations (BIF) occupy a unique position in Precambrian sedimentary history. Apart from being a marker horizon in the Iron Ore Group of rocks, they are the host rocks of the Iron ore deposits of this area. Stratigraphically the area consists of low-grade metasediments including phyllites, tuffaceous shales, banded hematite jasper (BHJ) and banded hematite quartzite (BHQ) with iron ore, ferruginous quartzite, local dolomite, mafic volcanics as well as mafic sill-like intrusives, all belonging to the Orissa Iron Ore Group (IOG), which constitutes the major supracrustal unit in the Singhbhum Orissa Iron Ore Craton (Saha, 1994). They are underlain by the Older Metamorphic Gneisses (the oldest rocks in the Singhbhum-Orissa Iron Ore Craton-early Archaean). Although emplacement of the Singhbhum Granite in the first phase preceded the formation of the Banded Iron Formations, a second phase of emplacement of these granites followed after the BIF's underwent orogeny.

AMS studies on the BHJ's and BHQ's of the Bonai Synclinorium were carried out at the Wadia Institute of Himalayan Geology (WIHG, Dehradun, India). The measurements were made with KLY-3S Kappabridge manufactured by Geofyzika Brno, Czech Republic. Cylindrical cores 22x26 mm size were drilled. A total of 24 numbers of samples from different parts (mines) of the study area were analysed. Generally 3 cores were drilled from each sample. Thus a total 90 number of cores were analyzed from mines at Gua, Bolani, Khandadhar, Sakradih, Joda and Noamundi. It was found that the values of Mean Susceptibility (K_m) vary between $1026 \cdot 10^{-6}$ SI and $236500 \cdot 10^{-6}$ SI. Flinn diagrams and Jelinek plots reveal that most of them fall in the oblate flattening field. However, a few samples fall in the prolate field indicating constriction. It is also found that some cores fall on the $k = 1$ line on diagrams implying plane strain. Under constant volume deformation, this would imply simple shear.

Lower hemisphere stereographic projections of the orientations of K1, K2 and K3 axis show that the magnetic foliation has good correlation with the S0 in most samples. Moreover, a few samples were collected from hinge and limb parts of mesoscopic folds. These have revealed that the orientations of magnetic foliation for samples from hinges lie at a high angle to the S0 while there is a parallelism between the two for samples from the limb parts. Mamtani *et al.* (2002a, b) have indicated that the deviation of the magnetic foliation and S0 at the hinge parts of folds implies the effect of strain and tectonics. The high values of K_m obtained from AMS studies imply that the major minerals that contribute to this susceptibility must be the ore-minerals, mainly hematite/magnetite. Moreover, the close similarity between the magnetic foliation and field structure indicates a relationship between deformation/strain and


magnetic data. Therefore, it has been concluded that subsequent to the deposition and formation of the iron ores as bands in the rocks, there must have been their re-orientation and recrystallization in the strain field under which the deformation/folding took place.

Recent studies on iron ore bearing rocks have revealed the importance of determining crystallographic preferred orientations (CPO's) of hematite (e.g. Siemes et al., 2000; Rosiere et al, 2001, Günther et al. 2002). These studies have demonstrated that the crystallographic preferred orientation of the c-axes of hematite ores is strongly related to the foliation and lineation of ores. The pole of the foliation is centered at the c-axis maximum. The lineation is oriented perpendicular to the long axis of the elliptical c-axis maximum or perpendicular to the c-axis great circle. The orientation of the c-axis of hematite with reference to the magnetic foliation and lineation is important for a complete application of magnetic data for structural interpretations. It has been demonstrated that there is a tendency of parallelism between the orientation of crystallographic c-axes of hematite, the pole of the foliation plane and the direction of minimum magnetic susceptibility. Therefore, it is proposed that the CPO of hematite in the oriented rock samples from the Bonai Synclinorium, Orissa (India) be carried out with the help of neutron diffraction technique (table below showing first results).



References

- Günther, A., Brokmeier, H.-G., Petrovsky, E., Siemes, H. and Hellming, K. 2002. Mineral preferred orientation and magnetic properties as indicators of varying strain conditions in naturally deformed iron ore. *Appl. Physics A* 75 1–3.
- Mamtani, M.A., Mukherji, A. and Chaudhuri, A.K. 2002a. Application of Anisotropy of Magnetic Susceptibility (AMS) studies in structural geology. Abstract Volume: DST Sponsored National Interactive Workshop on Palaeomagnetism and Rock Magnetic Research in India, Cochin, pp.11–13.
- Mamtani, M.A., Mukherji, A. and Chaudhuri, A.K. 2002b. Application of anisotropy of magnetic susceptibility studies in structural geology. *Deep Continental Studies In India-DST Newsletter*; 12(1), pp.10–12.
- Rosiere, C.A., Siemes, H., Quade, H., Brokmeier, H.G. and Jansen, E.M. 2001. Microstructures, textures and deformation mechanisms in hematite; *Jour. Struc. Geol.*, 23, pp.1429–1440.
- Saha, A. K., 1994. Crustal Evolution of Singhbhum-North Orissa Eastern India; *Geol. Soc. Ind. Mem.* 27, 341p.
- Siemes, H., Schaeben, H., Rosiere, C.A. and Quade, H. 2000. Crystallographic and magnetic preferred orientation of hematite in banded iron ores; *Jour. Struc. Geol.*, 22, pp.1747–1759.

	EXPERIMENTAL REPORT	GeNF TEX-2
Quartz rich tectonites from Pie de Palo Sierra-Córdoba-Argentina		
Principal Proposer:	R. Martino ¹ , R. E. Bolmaro ² ¹ CONICET- Córdoba National University; Argentina ² CONICET- Rosario National University; Argentina	
Experimental Team:	A. Günther, B. Witassek, H.-G. Brokmeier Institut für Werkstoffkunde und Werkstofftechnik, TU Clausthal, Germany	
Date(s) of Experiment:	August – October 2002	

Introduction

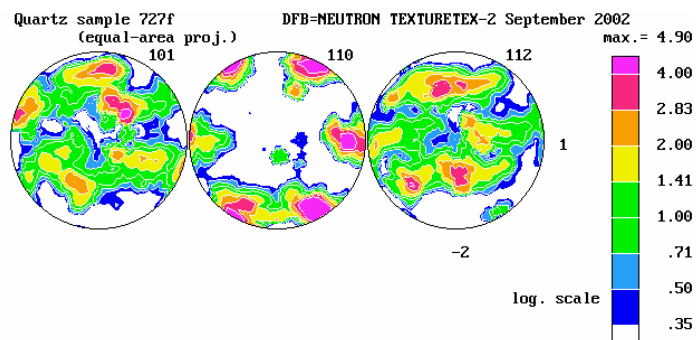
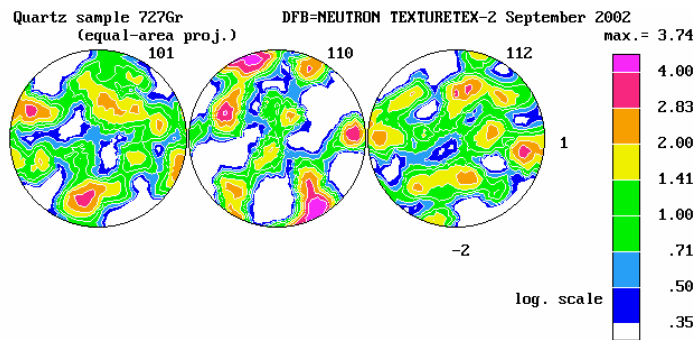
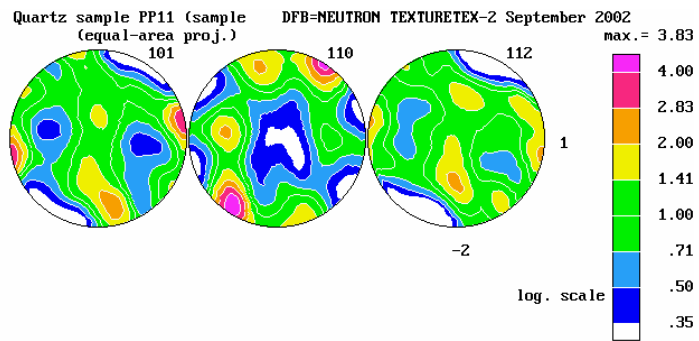
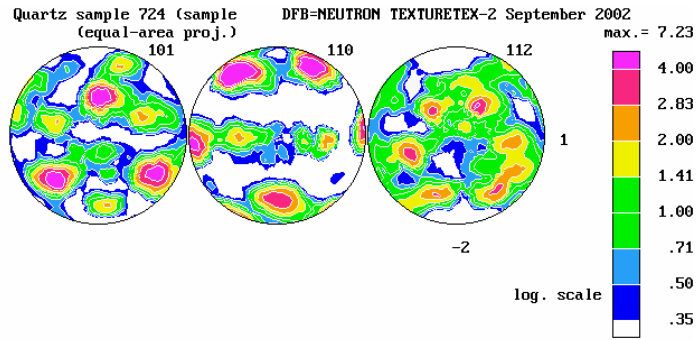
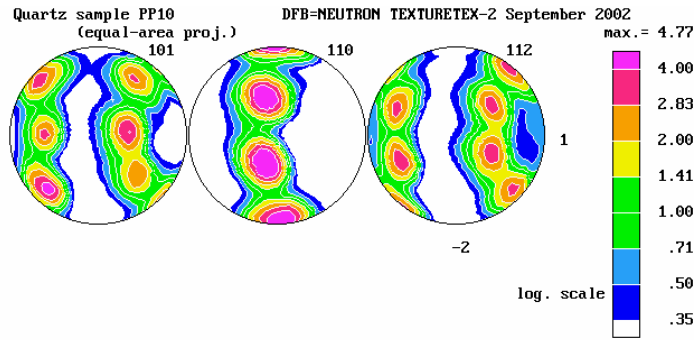
Pié de Palo is a “sierra” (hill) consisting of ductile entangled shearing systems of crystalline rocks, alongside of the Argentine Precordillera. It is divided from west to east in three metamorphic units: Cauce Group (CG), Ophiolitic Unit (OU) and the Higher Units (HU), separated the last ones from the first ones by the Pirquitas Landslide. The CG is formed by marble, meta-quartzites, quartz schists and low degree metamorphic schists (green schists facies) during non-coaxial local deformation in a contraction regime produced by the activity of the Angaco Deformation Fringe (ADF) circa 395.7±0.2 Ma (Inferior Devonian) generating a milonitic foliation oriented N 320°/20°E with an associated stretching lineation oriented 90°/20-25. The OU is formed by an association of ophiolitic rocks with micaceous and graphitic schists. The HU are formed by a set of migmatites, schists and quartzites over a Grenvillian basement upon which is lying a metasedimentary crust formed by marbles, calcolithic schists and metaquartzites. The metamorphic process undergone by the bedrock is a low pressure/low temperature (LP/LT) process with some migmatized portions (M2, P = 686±40 MPa, T = 790 °C±17) meanwhile on the overlying crust the conditions were of high pressure/high temperature (P = 1300±100 Mpa – T = 600±50 °C). The age of this last one is approximately 460 Ma (medium Ordovician). Associated to this metamorphic event, a strong non-coaxial penetrative deformation, in a contraction regime, has been developed. It is represented by a foliation plane oriented N 35°/40°E to which a stretching lineation is associated oriented N 125°/35-40°. This deformation would have produced a strong imbrication of the HU. The main question we are trying to answer is: Which are the kinematic, deformation mechanisms and textures developed by the quartz in the already described conditions of metamorphic LP/LT non-coaxial deformation regime?

Experimental Work

Two veins (named PP10-PP11) coming from ADF and three quartz veins from the metasedimentary crust of Quebrada de Las Flores (724, 727 f, 727 gr) have been exploratory studied. These samples are representative of the internal deformation in ADF and the penetrative strain in the HU. Results are currently under evaluation.

Acknowledgements

This project was partially funded by the German-Argentine Intergovernmental Agreement # AL/A99-EXII/18 and CONICET-Argentina.



	EXPERIMENTAL REPORT	GeNF TEX-2
Texture of bone mineral in sauropod dinosaur bones		
Principal Proposer:	A. Pyzalla, M. Stempniewicz Institute for Materials Science and Technology, TU Berlin, Germany	
Experimental Team:	A. Günther, H.-G. Brokmeier Institut für Werkstoffkunde und Werkstofftechnik, TU Clausthal, Germany	
Date(s) of Experiment:	July – September 2002	

Scientific Objective

The motivation of this experiment is substantiated by the growing interest in bio-structures, that is structures optimised by nature in the process of functional adaptation to fulfil their roles. It should be noted that bone fulfils two major roles: a metabolic (reservoir for calcium and phosphates) and a mechanical one. The mechanical function becomes dominant especially when the skeleton is heavily loaded like it surely was in the case of giant terrestrial animals – sauropod dinosaurs. On the other hand, the skeletons of dinosaurs are the only material remains, and thus, the only way to extend the knowledge about the extinct creatures. Thus, here we investigate bones of individuals belonging to the same species yet buried in different stages of ontogenetical development in order to see how the process of mechanical adaptation proceeded.

The whole structural stiffness (resistance to deformation under applied loads) and strength (load required to fail a whole bone) are influenced by both the material and geometrical features. From a mechanical perspective, the composition and organisation of the material influences directly the ability to bear loads. Obviously, the composition of the sauropod bone has been altered in the process of fossilisation, thus, no direct characterisation of mechanical properties is possible. It has already been shown that the mineral present in the fossil bone is the native bone apatite that experienced ion exchange (-OH groups exchanged with -F) and crystallinity increase. The current work is dedicated to the determination of the bone structure at the lowest hierarchical level, that is texture of the bone mineral.

Experimental Techniques

Since bone mineral is known to be a highly organised three-dimensional mesh of apatite crystals, neutrons were chosen for the texture characterisation as they enable measurements on bulk and coarse-grained samples. For samples collected from middle shaft of femora of *Barosaurus africanus* (died presumably as a still growing individual) and *Brachiosaurus brancai* (died as an adult) (0002) pole figures were measured. This (0002) is a well resolved reflex, relatively easy to interpret, as it is known to be the main direction prone to show preferred orientation in modern bone.

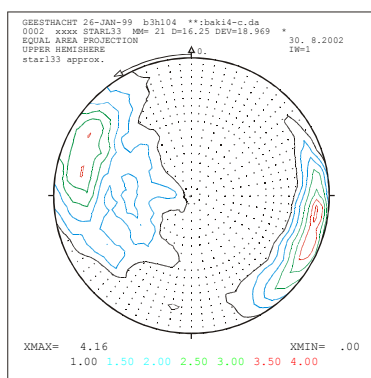
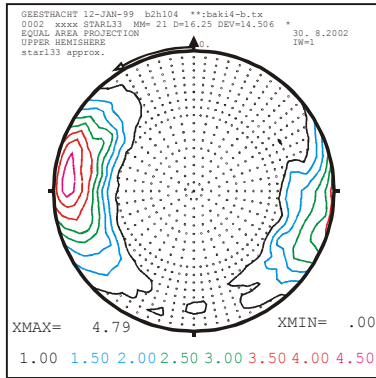
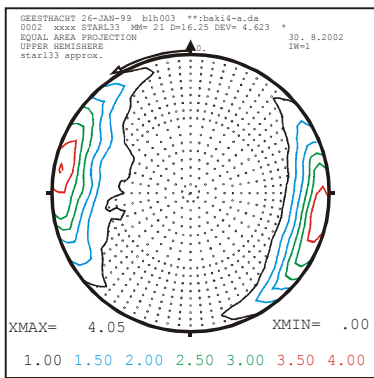
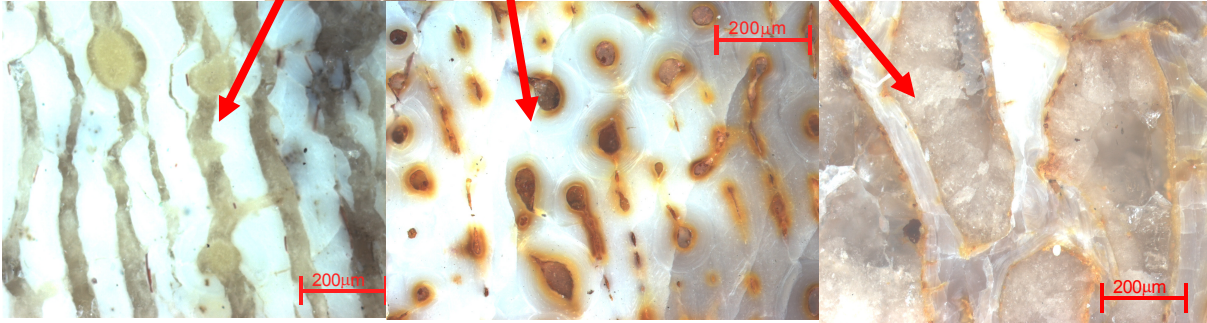
Main Results

As expected, the c-axis of the bone mineral appears to be oriented along the length of the long bone axis, which is interpreted as adaptability of the apatite distribution to the mechanical load (long bones carry mostly axial loads). This orientation is present in both lamellar and osteonal bone structures, associated with young and mature bone respectively, at the same degree. The chief difference is observed in trabecular bone. In the case of still growing individual the axial orientation of the mineral shows that the trabeculae are in fact dissolved osteonal bone, while in the case of mature individual the orientation is lost due to the process of bone remodelling. The mineral is re-oriented to meet the direction of single trabecula.

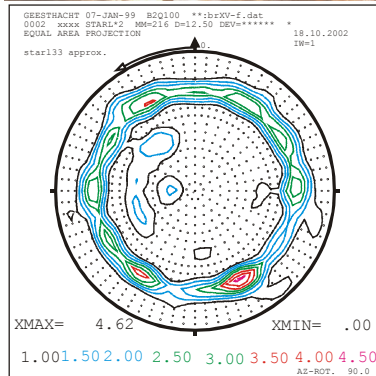
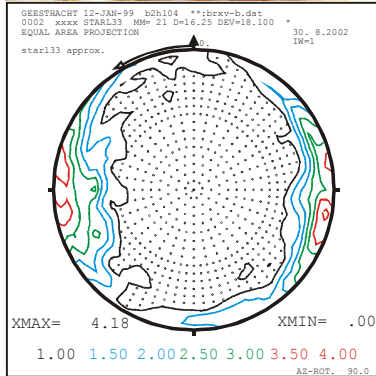
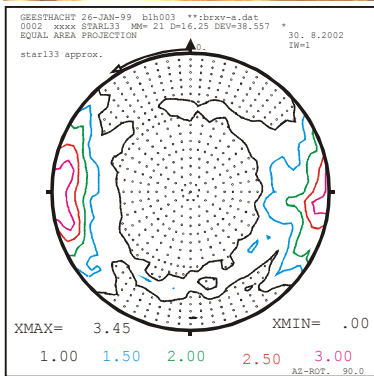
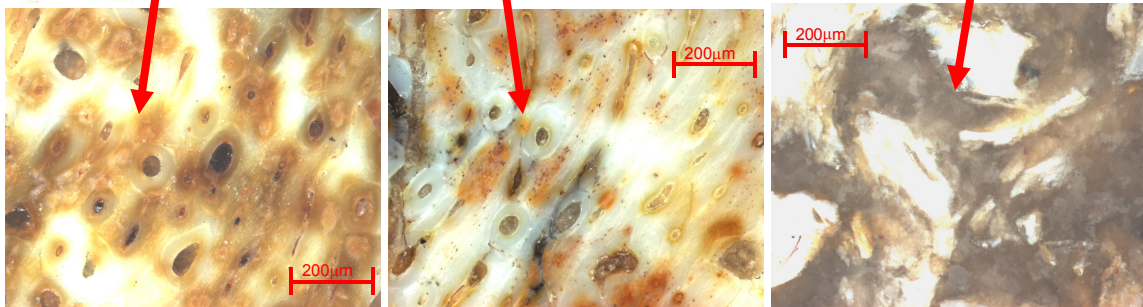
References

- [1] Thomas R.D.K., Olson E.C. *A Cold Look at the Warm-Blooded Dinosaurs* Westview Press 1980;
- [2] Turner C.H., Burr D.B. *Bone* 14: 595–608, 1993;
- [3] Heinrich W-D. *Mitt. Mus. Nat. kd. Berl. Geowiss.* 2:25–61, 1999;
- [4] Bacon G.E. *et al. Journal of Applied Crystallography* 12, 1979;
- [5] Weiner *et al. Journal of Structural Biology* 126, 1999, pp. 241–255

Barosaurus africanus



Brachiosaurus brancai



	EXPERIMENTAL REPORT	GeNF TEX-2
Texture investigations of Cu-Nb-rings		
Principal Proposer: Experimental Team: Date(s) of Experiment:	W. Singer ¹ , H.-G. Brokmeier ² , Wenhai Ye ² ¹ DESY-MPL, Germany ² Institut für Werkstoffkunde und Werkstofftechnik, TU Clausthal, Germany Wenhai Ye ² , B. Witassek ² , H.-G. Brokmeier ² July – September 2002	

One of the candidate for producing accelerator units is made of copper/niobium. Compared to pure niobium a cost reduction on one hand by the fabrication and on the other hand by material costs itself are obtained by copper/niobium cavities. The present work deals with two fabrication techniques to get Cu/Nb (explosive bonding and co-extrusion) the pre-product for cavities. Our test samples are Cu/Nb rings cut from the two types of tubes.

In both techniques a Nb tube was put into a Cu tube and thereafter connected by explosive bonding or by co-extrusion. The manufacturing processes cause residual stresses and textures. In addition to a characterisation of the processed tubes, the aim of this set of experiments was to test the influence of the different thermal expansion (annealing up to 1273 K and cooling down to 77 K) on the residual stresses and on the texture. In particular the stress can lead to damages and a limitation of the life time during application.

The present Cu/Nb ring samples are co-extruded (a) and co-extruded plus annealed (b) at 1073 K for two hours. Neutron diffraction is able to measure non-destructively the texture at different position of the ring for both phases, in spite of the small volume fraction of the 1 mm Nb. The set up used for the texture measurements is shown in figure 1. A detector slit system of 6 mm for the incoming beam and 6 mm for the scattered beam led to low volume fractions. Consequently the total counting time for one ring position was about 50 h.

The ODFs are shown in figure 2 (co-extruded) and figure 3 (co-extruded plus annealed). It may be seen that Cu has a recrystallization texture, which increases strongly by annealing. The Nb part shows a deformation texture in both states. It is open if the slight texture change after annealing is true or if it is in the texture variation along the perimeter of the co-extruded tube.

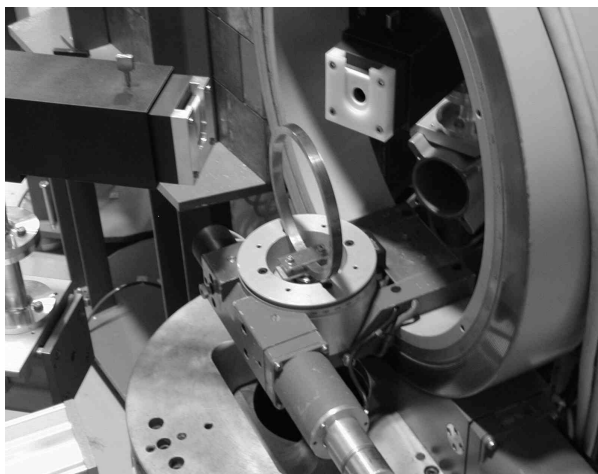


Figure 1:
Cu/Nb-ring mounted in the Eulerian cradle at TEX-2.

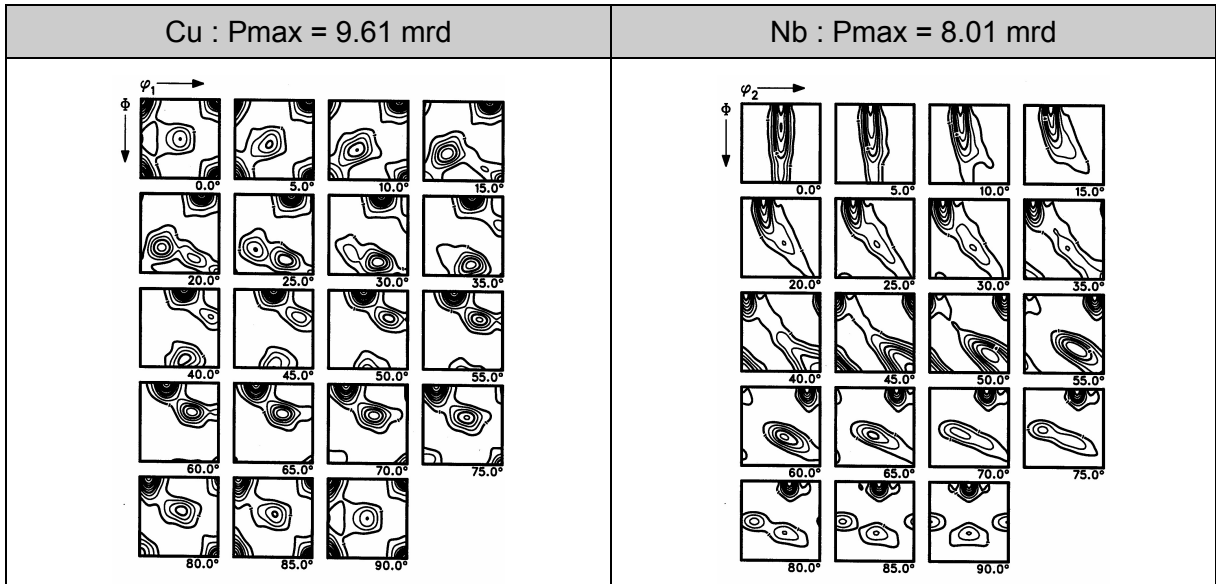


Figure 2: ODFs of a co-extruded Cu/Nb-ring.

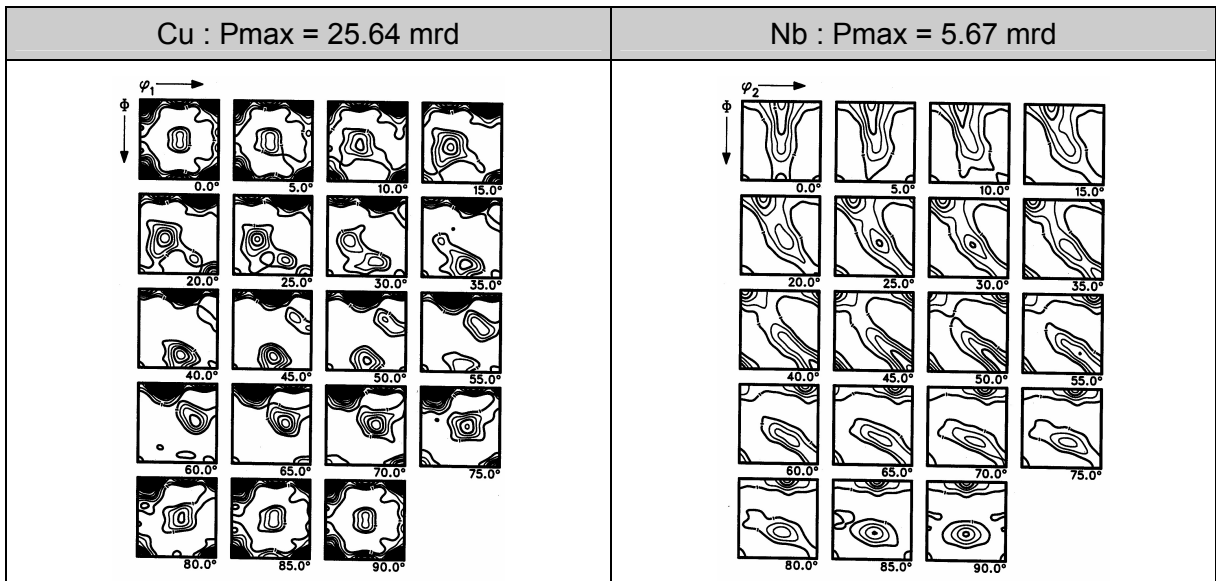



Figure 3: ODFs of a co-extruded Cu/Nb-ring after annealing 1073 K/2 h.

	EXPERIMENTAL REPORT	GeNF TEX-2
Quantitative texture analysis of R-phase in aged Ni-rich Ti-50.7at.%Ni shape memory alloy using neutron diffraction		
Principal Proposer:	H. Sitepu FaME38 at ILL-ESRF, BP 156, F-38042 Grenoble Cedex 9, France	
Experimental Team:	H.-G. Brokmeier Institut für Werkstoffkunde und Werkstofftechnik, TU Clausthal, Germany	
Date(s) of Experiment:	July – September 2002	

Sitepu *et al.* (2002) has recently investigated the transformation of a Ni-rich NiTi shape memory alloy of nominal composition 50.7 atomic percent nickel using differential scanning calorimetry, transmission electron microscopy and neutron diffraction. The sample was solution annealed, water quenched and aged at 400 °C for 20 hours. The material shows a two-step transition on cooling with differential scanning calorimetry peaks at 18 °C and 7 °C, while on heating a single differential scanning calorimetry peak occurs at 43 °C, see Fig.1. The results derived from Rietveld refinement with generalized spherical harmonic description (Sitepu, 2002, and references therein) for neutron diffraction data showed that the aging leads to the formation of Ni₄Ti₃ precipitates in the microstructure. In the presence of the precipitates the martensitic transformation occurs from the cubic B2-phase via the R-phase to B19' martensite. However, the first peak on cooling is not due to the formation of R-phase alone. Below the peak temperature, R-phase is present along with B19' (25.9 % volume fraction) and with residual B2 (3.7 % volume fraction) and the precipitates (7.2 % volume fraction). The second peak is related to the transformation of R-phase and B2 to B19'.

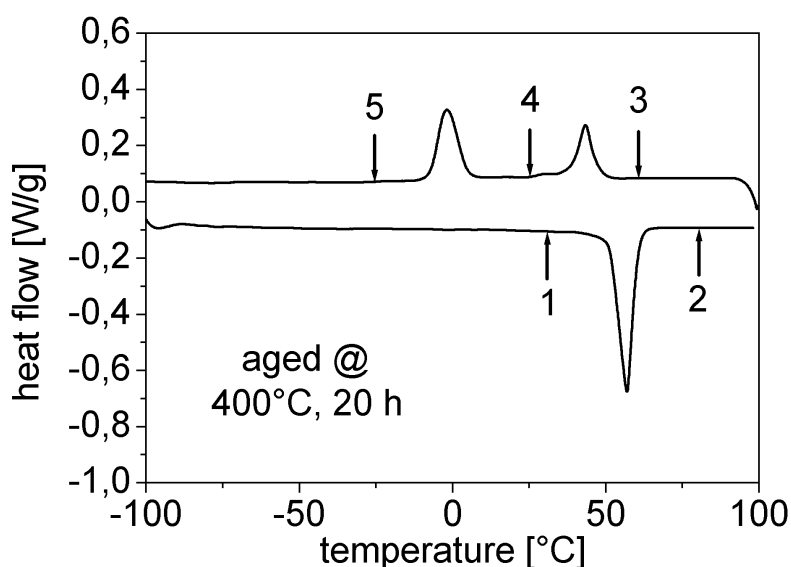


Figure 1: The differential scanning calorimetry curve for the aged Ni-rich NiTi shape memory alloy of nominal composition 50.7 atomic percent nickel which shows a two step transformation on cooling from B2→R→B19', and a one step transformations on heating B19'→ B2. On cooling, the R-phase and B19' phase are present after the first release of latent heat. This is due to a heterogeneous microstructure after solution annealing and ageing (Sitepu *et al.*, 2002).

The objective of the present paper is to investigate the texture of the R-phase (at arrow 4 in Figure 1) using the TEX-2, the neutron texture diffractometer at FRG-1, GKSS Research Centre Geesthacht, Germany. The texture index (Bunge, 1982) of the R-phase (63 % in volume fraction) derived from Rietveld refinement with the generalized spherical harmonic for whole neutron diffraction data at arrow 4 in Figure 1, on cooling, is 1.6 multiples of the random density. The present study is a continuation of the previous work carried out by Sitepu and Brokmeier (2003a) on the austenitic phase NiTi alloys with nominal compositions of 50.1 (sample M), 50.7 (sample F) and 50.8 (sample G) atomic percent nickel (see Fig. 2). Sitepu and Brokmeier (2003a) showed that neutron diffraction is an excellent tool to investigate the minor variation in the texture of NiTi alloys which is very sensitive to the variation of the content of nickel in the materials. For this reason, neutron diffraction was used to measure the pole figures of the R-phase (at arrow 4 in Figure 1). The results are being submitted to Materials Science and Engineering A (Sitepu and Brokmeier, 2003b).

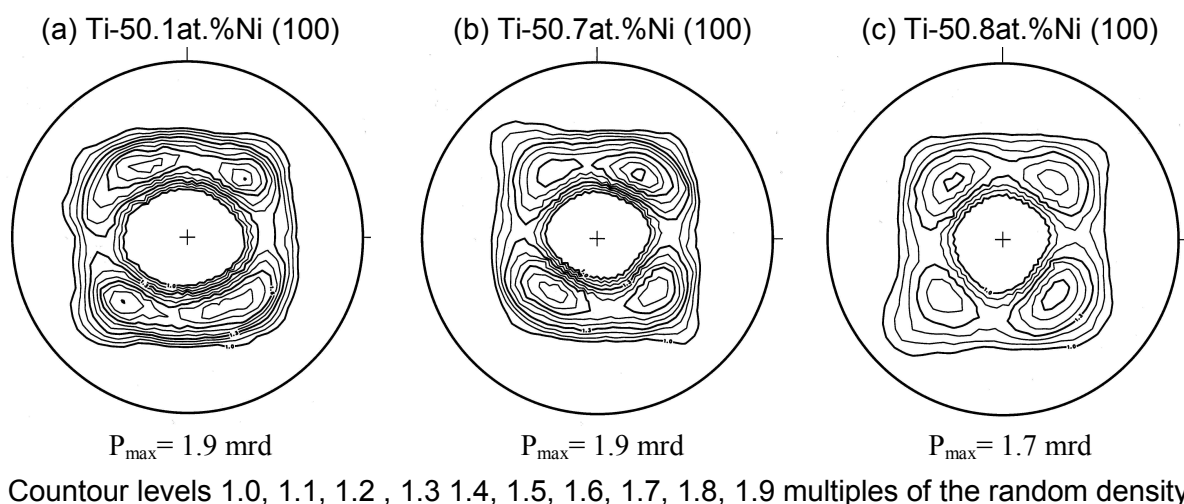


Figure 2: Measured pole-figures for the austenitic phase of the fresh solution annealed NiTi alloys with nominal compositions of (a) 50.1 (b) 50.7 and (c) 50.8 atomic percent nickel. The maximum values of pole figures (P_{\max}) for the three samples are 1.9, 1.9 and 1.7 multiples of the random density, respectively (Sitepu and Brokmeier, 2003a).

References

- [1] Bunge, H.-J. (1982). *Texture Analysis in Materials Science: Mathematical Methods*, translated by P.R. Morris. Butterworths, London.
- [2] Sitepu, H. (2002). *J. Appl. Cryst.* 35, 274–277.
- [3] Sitepu, H. and Brokmeier, H.-G. (2003a). *Materials Science Forum*. Accepted
- [4] Sitepu, H. and Brokmeier, H.-G. (2003b). *Materials Science and Engineering A* (2003b). To be submitted
- [5] Sitepu H., Schmahl, W. W., Khalil Allafi J., Eggeler G., Dlouhy A., Többers D. M., Tovar, M., *Scripta Materialia* 46(7) (2002) 543–548.

	EXPERIMENTAL REPORT	GeNF TEX-2
Annealing texture of a Cu-Nb composite		
Principal Proposer:	Wenhai Ye, H.-G. Brokmeier Institut für Werkstoffkunde und Werkstofftechnik, TU Clausthal, Germany	
Experimental Team:	Wenhai Ye, B. Witassek, H.-G. Brokmeier Institut für Werkstoffkunde und Werkstofftechnik, TU Clausthal, Germany	
Date(s) of Experiment:	April, June, September 2002	

Copper/niobium metal matrix composites (MMC's) play an important role in the area of long pulse high-field magnets and in rotating electrical machinery. This is due to their excellent mechanical properties while keeping high electrical conductivity. It is known that Cu and Nb have basically no mutual solid state solubility. Moreover, the constitution of Cu-Nb intermetallic compounds is unknown. Therefore, by mechanical processing (e.g. drawing, rolling or co-extrusion) one can manufacture Cu/Nb fibre reinforcements without any precipitation having very high strength and conductivity. In Cu/Nb composites a remarkable behaviour occurs which is called "its tensile strength after deformation is much greater than expected from the rule of mixtures [1, 2]".

The investigated copper/niobium composite consists of pure Cu and pure Nb in the mixture 1:1. Cold extruded material was prepared to cubic samples of 10*10*10 mm³. The aim of this work is to study the texture of Cu/Nb composites at thermal processing between 4 K to 1273 K. Heat treatment will change the microstructure of the Cu/Nb composite, which lead to the texture changes.

The samples present here are the as-extruded material and a 1073 K/2 h heat treated cube. The texture change is documented by pole figures (Fig.1) and by the orientation distribution functions (ODF's) (Fig.2) for Cu as well as for Nb.

The as-extruded material shows typical deformation textures in Cu as well as in Nb, which can be explained by the rectangular extrusion process and by the co-extrusion of Cu and Nb. Due to recrystallization texture changes can be observed. In the case of Cu the cube component becomes dominant. Niobium which has a much higher recrystallization temperature compared to copper shows only a slight texture change (see α -fibre).

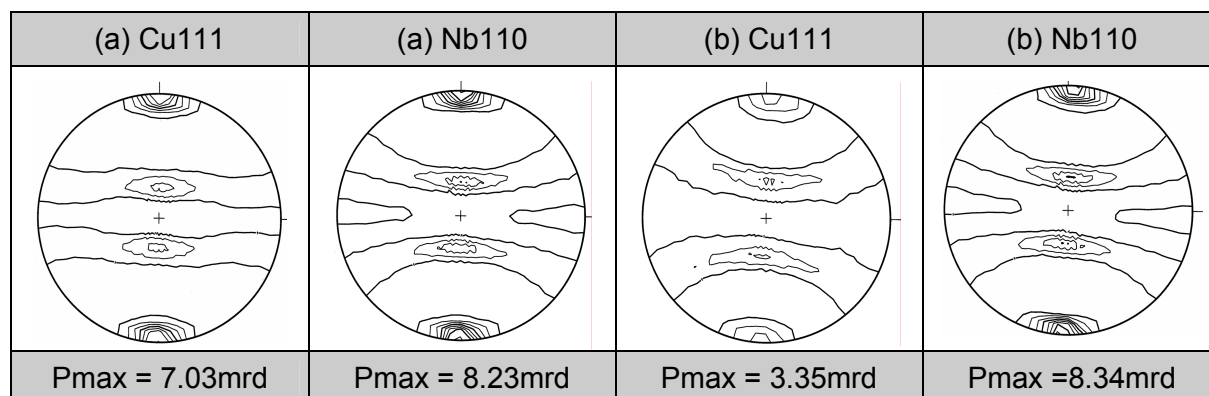


Figure 1: Pole figures of Cu and Nb (a) as-extruded and (b) heat treated at 1073 K/2 h.

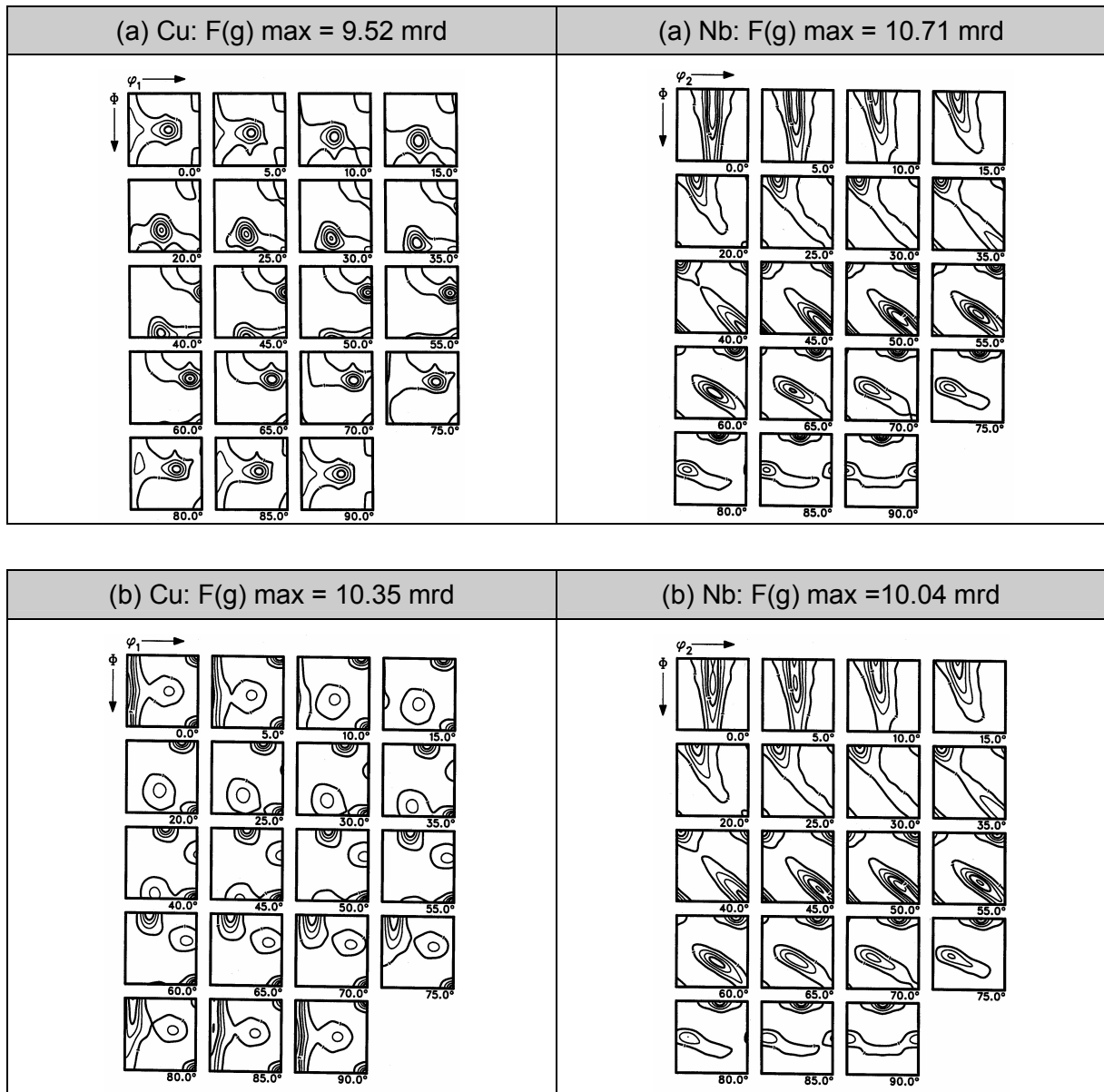



Figure 2: ODFs of Cu and Nb (a) as-extruded and (b) heat treated at 1073 K/2 h.

References

- [1] Spitzig, W. A.; Pelton, A. R.; Laabs, F. C.: Acta metall. 35 (1987), 2472.
- [2] Raab, D.; Heringhaus, F.; Hangen, U.; Gottstein, G.: Z. Metallkd. 86 (1995), 6.

	EXPERIMENTAL REPORT	GeNF TEX-2
The variation of texture during tensile test of Mg alloy AM20		
Principal Proposer:	Sangbong Yi, H.-G. Brokmeier Institut für Werkstoffkunde und Werkstofftechnik, TU Clausthal, Germany	
Experimental Team:	Sangbong Yi, B. Witassek, H.-G. Brokmeier Institut für Werkstoffkunde und Werkstofftechnik, TU Clausthal, Germany	
Date(s) of Experiment:	November 2002	

For reducing weight and exhaust gases of transport vehicles the study on magnesium alloys is rapidly increasing in recent years. Among others, this is based on the higher specific strength of magnesium compared to aluminium. An extensive understanding on the texture of hexagonal magnesium is by all means needed to get better mechanical properties. Important is also the anisotropy, which is more significant in hexagonal materials than in cubic materials. The goal of this study is to show the influence of the initial texture on the activation of different deformation systems and on the mechanical behavior. In order to measure the texture of tensile samples, initial and broken, the neutron beam at TEX-2 was used. This is due to the high penetration depth of neutron radiation. Figure 1 shows one of the samples mounted in the Eulerian cradle.

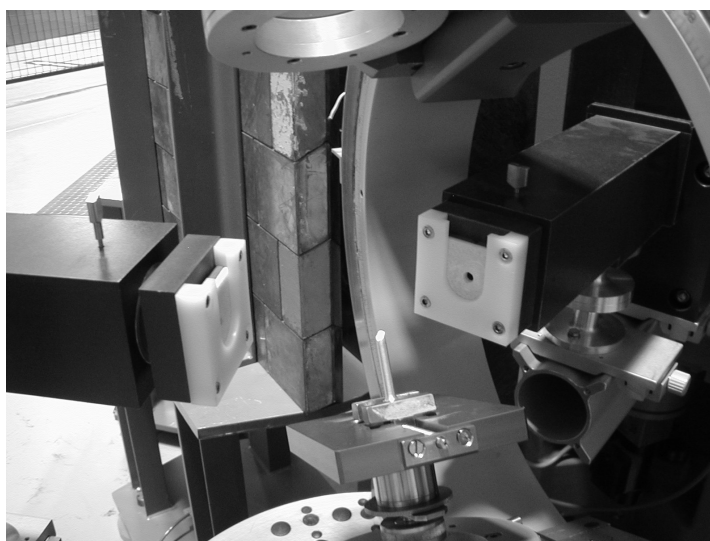


Figure 1:
The broken tensile specimen mounted on the Euler cradle in TEX-2.

The tensile specimen was cut from a rectangular extruded billet oriented 90° to the extrusion direction. The uniaxial tension test was carried out at room temperature with an initial strain rate of $6 \times 10^{-4} \text{ sec}^{-1}$. In figure 2 the stress-strain curve is shown. One can see clearly that this sample has a rapid strain hardening after yielding, which can be explained by the activation of $\{10\bar{1}2\} \langle 10\bar{1}1 \rangle$ tensile twins. The twin boundaries act as a barrier against the movements of further slip systems so that the strain hardening is appeared. The critical resolved shear stress (CRSS) of tensile twinning and of $\{0002\} \langle 1\bar{1}20 \rangle$ basal slip is much lower than the CRSS for other slip systems. This material has a relatively low yield strength of 135.6 MPa. The relatively easy activation of twinning is related directly to the initial texture of this sample.

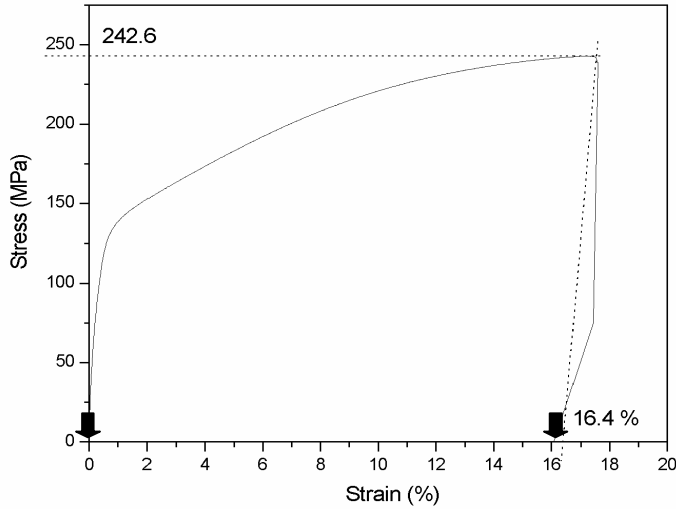


Figure 2: The stress-strain curve of magnesium alloy AM20 which was cut perpendicular to the extrusion direction. The arrows indicate the texture measuring points.

The texture of the initial tensile sample is composed of four components, (a) $\{0\ 0\ 0\ 1\}\langle 1\ -1\ 0\ 0\rangle$ (Euler angle = $\varphi_1, \Phi, \varphi_2 = 30, 0, 0$), (b) $\{1\ 0\ -1\ 0\}\langle 0\ 0\ 0\ 1\rangle$ ($90, 90, 0$), (c) $\{0\ 0\ 0\ 1\}\langle -1\ -1\ 2\ 0\rangle$ ($60, 0, 30$) and (d) a fibre between $\{1\ 0\ -1\ 0\}\langle 0\ 0\ 0\ 1\rangle$ and $\{0\ 0\ 0\ 1\}\langle -1\ -1\ 2\ 0\rangle$. These texture components mean that the most of the basal planes lay parallel (b) and normal (a)(c) to tensile direction. $\{0\ 0\ 0\ 2\}$ tensile direction is very favorable for activating the tensile twin, and this component becomes rapidly weak after twinning and disappears completely at the end of the deformation stage (Fig. 3). The fibre component become also weak and this fibre has a trend of changing to a $\{1\ 0\ -1\ 2\}\langle -1\ -2\ 3\ 0\rangle$ (Euler angle = $90, 45, 0$) with increasing deformation. However, the $\{1\ 1\ -2\ 0\}\langle 1\ -1\ 0\ 0\rangle$ (Euler angle = $0, 90, 30$) component is formed new and becomes stronger with increasing deformation, which is related to the activation of basal slip. For a more detailed explanation about the relationship between initial textures, texture developments and active deformation modes, texture simulations and in-situ texture measurements during uniaxial tension are requested.

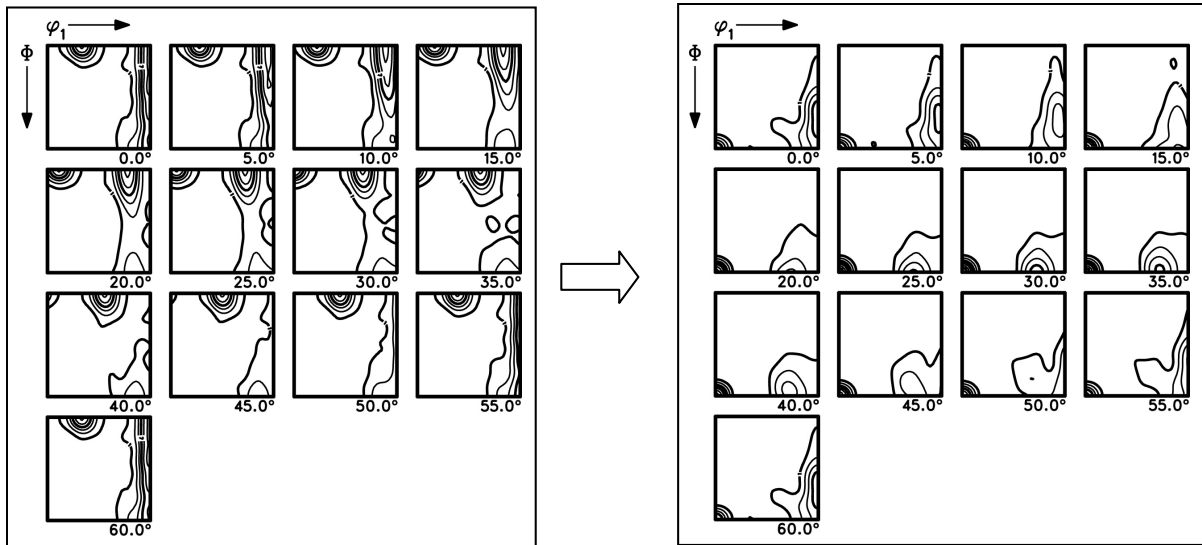



Figure 3: The full ODF of tensile specimen, before tension (left, $F_{max} = 12.05$) and after breaking (right, $F_{max} = 15.10$); φ_2 section, Intensity levels = 1, 3, 5, 7, 9, 11, 13, 15.

	EXPERIMENTAL REPORT	GeNF POLDI
Polarised diffractometer POLDI		

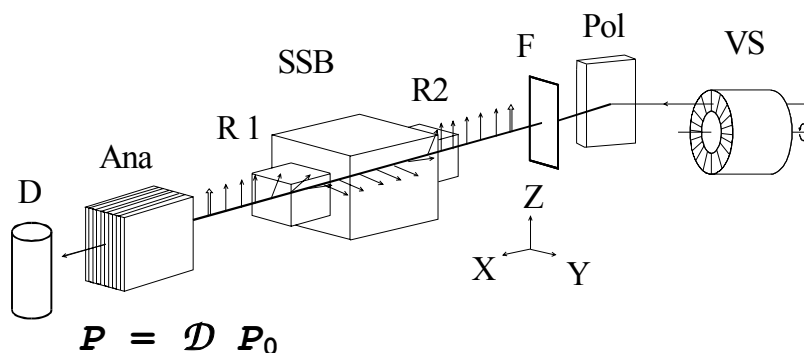
Short Instrument Description:

With the polarised diffractometer 3-D depolarisation analysis is used to investigate magnetic properties and correlations in magnetic materials. With minor modifications a time of flight option in non-polarised mode is additionally available for the purpose of dosimeter calibration.

Local Contact:

Dr. Volker Wagner, PTB – Physikalisch Technische Bundesanstalt, Braunschweig
 Phone/Fax : +49 (0)531 592–7400 / +49 (0) 531 592–7505
 e-mail: volker.wagner@ptb.de


Schematic View of POLDI:



Set-up for full 3-dimensional neutron depolarisation analysis in the transmitted beam.

Instrument Details:

Location at FRG-1:	beamline 7, thermal neutrons cross section 10 x 4 cm ² ,
Polariser / monochromator (Pol)	Cu ₂ MnA (111), PG(002), Si (311) doubly focussing; helical slot selector (VS)
Take-off-angle:	10° < 2 Θ _M < 65°
Wavelength:	λ = 0.1 to 0.36 nm, 2 nd order suppression by velocity selector (VS)
Flux at sample position:	Φ _{max} = 0.8 · 10 ⁵ cm ⁻² s ⁻¹ (polarised)
Analyser (Ana):	Co/Ti-supermirror
Overall polarisation:	0.94
3D depolarisation analysis in transmitted beam:	accuracy < 1% for any component of D
Sample environment fitting in the magnetically shielded sample box (SSB) for 3D depolarisation analysis:	– refrigerator T > 12 K, Orange cryostat T > 1.5 K – DC magnetic field < 160 A/cm – pulsed field < 8.0 kA/cm
Detector (D):	³ He-counter
Instrument control / data acquisition:	remote internet PC control IEEE bus, serial bus and special interfaces

	EXPERIMENTAL REPORT	GeNF POLDI
Magnetic mesostructure of dilute alloy (Pd_{0.984}Fe_{0.016})_{0.95}Mn_{0.05} – test of simple models of depolarizing inhomogeneities		
Principal Proposer:	G. Gordeev, L. Axelrod, V. Zabenkin (PNPI, Gatchina, Russia) V. Wagner (PTB, Braunschweig, Germany)	
Experimental Team:	V. Wagner, S. Braun (PTB, Braunschweig, Germany) G. Gordeev, L. Axelrod (PNPI, Gatchina, Russia)	
Date(s) of Experiment:	3 weeks in October 2002	

Scientific Objective

There are two simple models for description of magnetic inhomogeneities that produce a neutron depolarization in magnetic materials [1]. These models deal with the inhomogeneities having random magnetization orientation and an anisotropic shape. As well known, in the disordered dilute alloys there are two types of fluctuations whose spin correlation function is usually described as a sum of Lorentzian and squared Lorentzian. The first item describes thermodynamic fluctuations that do not produce any visible depolarization. The second function describes the configuration fluctuations of the induction. Practically depolarization is produced by these fluctuations. Therefore we have selected a squared Lorentzian as *the model 1*, which results in exponential decay of the correlation of the magnetic inhomogeneities. We supposed that the inhomogeneities have the sizes R_{\parallel} and R_{\perp} along and perpendicular to the anisotropy axis, respectively, and an isotropic distribution of magnetization orientations, i.e. an isotropic magnetic susceptibility χ . The second *model 2* differs from model 1 only in the law of decay of the spin correlation function inside inhomogeneities. So the second model have also two parameters that are the same as in the first model. For the both models we assumed the magnetic anisotropy was produced by applied external magnetic field, i.e. we considered uniaxial anisotropy with its axis along the field direction. The indexes of parameters R_{\parallel} and R_{\perp} refer to the field direction.

Experimental Techniques

In the experiment the all components of the depolarization matrix $\hat{\mathbf{D}}$ defined by the equation $\mathbf{P} = \hat{\mathbf{D}} \cdot \mathbf{P}_0$ were determined. From $\hat{\mathbf{D}}$, the depolarization $\Delta P = -\ln(\det(\hat{\mathbf{D}}))$ and the angle of polarization rotation $\Phi \sim \langle B \rangle_{\text{mac}}$ around the macroscopic induction were obtained. The depolarization ΔP is produced by the fluctuating part ΔB of local induction $B_{\text{loc}} = \langle B \rangle_{\text{mac}} + \Delta B$, here $\langle B \rangle_{\text{mac}}$ is a mean macroscopic induction. Using the theoretical conception of depolarization [1], we have obtained from matrix $\hat{\mathbf{D}}$ such parameters of the shape anisotropy as $R_{\perp} / R_{\parallel}$ and of the scattering power $\chi \cdot R_{\perp}$ for each of both models.

The depolarization measurements were carried out on the instrument Poldi of FRG-I reactor. The neutron wavelength was chosen 0,15 nm.

We measured the depolarization of the neutron beam transmitted the sample. The sample was a parallelepiped of (Pd_{0.984}Fe_{0.016})_{0.95}Mn_{0.05} alloy magnetized along different directions, namely along each of its three geometrical sizes ($d_z = 25$ mm $d_y = 11$ mm and $d_x = 1.2$ mm). The coordinate axis X coincided with the neutron beam direction. In two cases (H \parallel Y and H \parallel Z) the sample was mounted in a yoke of soft material in order to avoid a stray field.

Main Results

The sample was magnetizing even in the absence of external magnetic field (during zero field cooling, ZFC). Probably the reason for that is a small magnetic field at the sample

position and a very high susceptibility of the sample. For *model 1* the ratio R_{\perp}/R_{\parallel} is close to unity and practically does not depend on temperature. For *model 2* the parameters were found the same as for *model 1*.

However, in field cooling (FC) these parameters behave differently than they do in ZFC. For example see Figs.1 and 2, where these parameters are presented for the two directions of anisotropy axis (Fig.1 for Z-axis and Fig.2 for Y-axis). The parameters of *both models* are quite alike qualitatively and numerically for each anisotropy direction, but they slightly depend upon the sample magnetization direction.

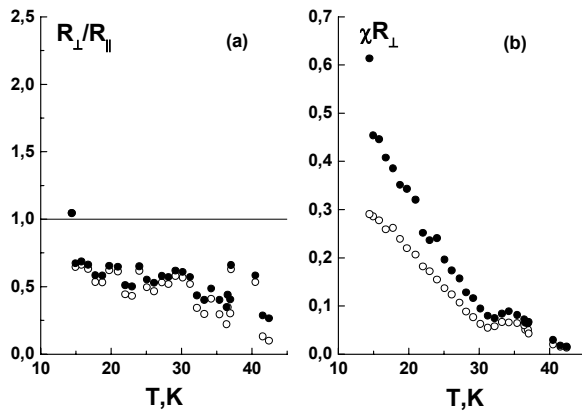


Fig. 1: Parameters for FC at $H = 8$ A/cm $H||Z$.

● *model 1*; ○ *model 2*.

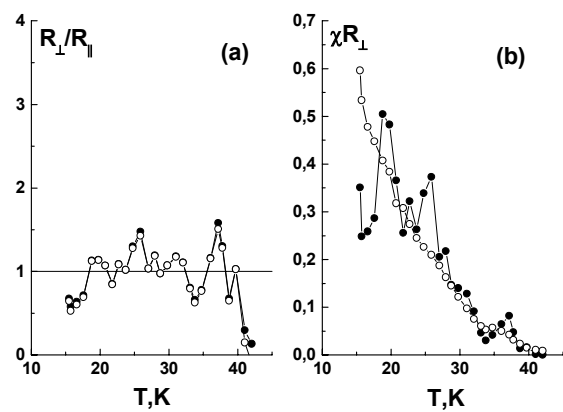


Fig. 2: Parameters for FC at $H = 6.5$ A/cm $H||Y$.

● *model 1*; ○ *model 2*.

In the case of $H || Z$ for both models (Fig.1) the ratio R_{\perp}/R_{\parallel} increased sharply near $T = 40$ K and then increased again below $T = 15$ K. The size R_{\perp} is larger than R_{\parallel} at $15 < T(K) < 40$, i.e. the inhomogeneities have an elongated form. Only at $T < 20$ K the ratio tends to 1, i.e. their form became spherical. However, for $H || Y$ the ratio saturated to 1 in the range 20 K $< T = 38$ K.

It should be noted that dependences of parameter $\chi \cdot R_{\perp}$ in both models are similar to dependence of the depolarization for both cases $H || Z$ and $H || Y$. But they differ one from the other in the numerical values. It seems strange that this parameter for $H || Y$ is larger for $H || Z$, although the external field is less for the latter case. Perhaps this results due to nonmonotonic depolarization dependence on the field value observes previously in the FC regimes [2]. Depolarization in case $H || X$ is very small and therefore it is not possible to compare the models in this case.

The qualitative agreement of the parameters of the two models is not too surprising. In fact, for large inhomogeneities with sharp edges the type of magnetization correlation function is not important at the distance more than the size of inhomogeneity.

Relevance to others Applications or to others Techniques

The obtained results demonstrate possibility to make use of 3D-neutron depolarization analysis for getting information about parameters of magnetic mesostructure. It is useful for a study of very large magnetic inhomogeneities when SANS experiment is invalid.

References

- [1] S.V. Maleyev, Polarized Neutrons and Magnetism, PNPI, Gatchina, 2002, p.43
- [2] G. Gordeev, L. Axelrod, V. Zabenkin, I. Lazebnik, S. Grigoriev, V. Wagner, H. Eckerlebe: What are the mesoscopic magnetic inhomogeneities in the dilute PdFeMn alloy? Polarized neutron study. (to be published in Physica B, 2003)

	EXPERIMENTAL REPORT	GeNF POLDI
Developments of electronic mixed field personal dosimeters		
Principal Proposer:	M. Luszik-Bhadra PTB, Braunschweig, Germany	
Experimental Team:	R. Böttger, H. Friedrich, M. Luszik-Bhadra, S. Löb, A. Reiske PTB, Braunschweig, Germany	
Date(s) of Experiment:	April 2001, March 2002, September 2002	

The thermal beam facility installed by the PTB at the GKSS (behind the POLDI device) has been used for the characterisation of electronic mixed field personal dosimeters.

For radiation protection of individuals, a good direct-reading electronic dosimeter working in mixed neutron/photon fields is still lacking. The problems are chiefly related to the energy-dependent personal dose equivalent response to neutrons.

In Figure 1 the response (ratio of measured personal dose equivalent $H_{p,m}(10)$ to conventionally true value $H_{p,c}(10)$) is shown for some devices [1]. The calibration measurements were performed using the quasi-monoenergetic reference fields produced at the PTB accelerator in the energy range between 24 keV and 14.8 MeV and the thermal calibration beam at the GKSS. The dose equivalent response of the personal dosimeters should ideally be unity at all energies, but it deviates drastically from this value, even in a energy region, in which neutrons contribute considerably to the dose at workplaces at nuclear facilities, i.e. between 100 keV and 300 keV. The dose equivalent response of the SIEMENS EPD-N and the FUJI ELECTRIC EPD(NRN) is about a factor of ten too low in the most important energy region around 200 keV, while the ALOKA PDM-313 shows a response too high in the intermediate neutron energy region. A new development, the RADOS-DIS-N shows a drastical overresponse to thermal neutrons. In cooperation with the Paul Scherrer Institute (PSI), optimised shieldings and wall materials for the small ionisation chambers are being tested to improve the response of the RADOS-DIS-N device in the thermal region.

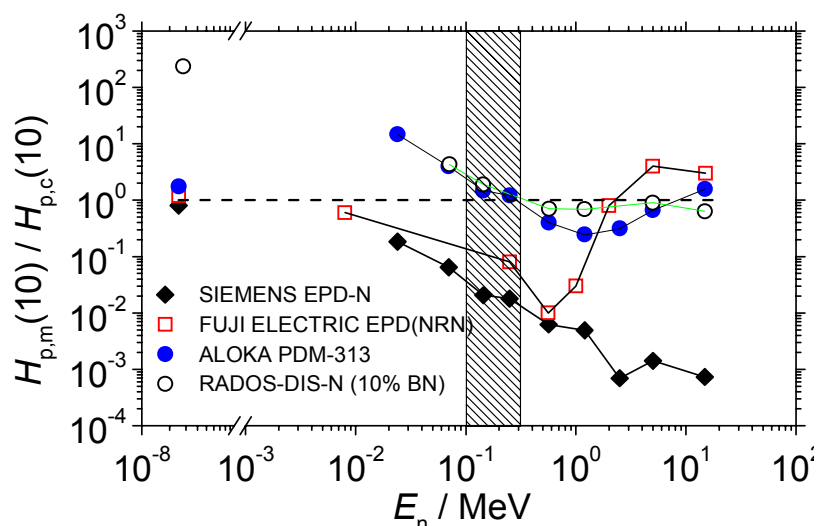


Figure 1:
Neutron response
of electronic personal
dosimeters for normally
incident radiation (see text).

Extended investigations were also performed with the PTB DOS-2002, a personal dosimeter for mixed fields which is under development at the PTB. It uses only a single silicon detector with optimised converters and absorbers, and its pulse height information. Despite its simplified set-up, a dose equivalent response to neutrons better than that of other devices is achieved. New response functions with respect to personal dose equivalent $H_p(10)$ have been determined by measurements in the quasi-monoenergetic reference fields at the PTB in the energy range from 24 keV to 14.8 MeV and in fields with broad spectral distributions using the radionuclide sources ^{252}Cf (bare), $^{252}\text{Cf}(\text{D}_2\text{O}, \text{mod})$ – with and without cadmium shielding – $^{241}\text{Am-Be}$ as well as the thermal neutron beam at the GKSS [2]. The spectral distributions of all fields and the readings of the dosimeters in these fields were taken as inputs for an unfolding procedure to determine the dosimeter response in the overall energy region from thermal to 15 MeV. The measurements and the results of the unfolding procedure are shown in Figure 2.

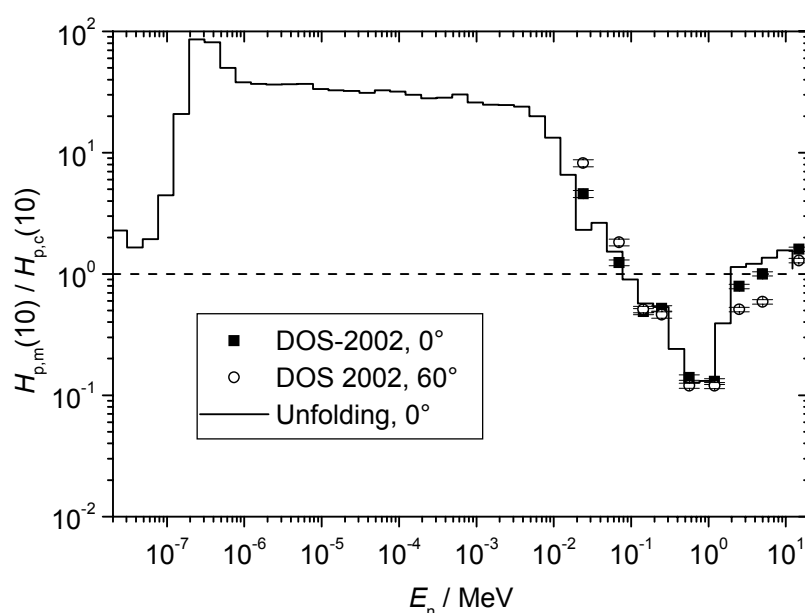



Figure 2: Ratio of measured personal dose equivalent $H_{p,m}(10)$ to conventionally true value $H_{p,c}(10)$ for normally incident neutrons (■) and neutrons 60° to normal incidence (○) as a function of neutron energy for the DOS-2002. The uncertainties correspond to one standard uncertainty. The solid line is a result of an unfolding procedure for normal incidence (see text).

Since dosimeter responses can vary drastically in the thermal and epithermal energy region (see Figures 1 and 2), the well known spectral distribution of the thermal neutron beam at the GKSS, measured by the time-of-flight method (see GeNF, experimental report 2001), is absolutely necessary for studying the response of these dosimeters.

References

- [1] Luszik-Bhadra, M. and Rimpler, A.: Stand und Perspektiven elektronischer Personendosimeter für Neutronen/Photonenstrahlungsfelder. Contribution to FS Jahrestagung, Kloster Seon, Germany, 21–25 April 2002 (TÜV-Verlag).
- [2] Luszik-Bhadra, M.; Coleman, J.; Schlegel, D. and Zimbal, A.: Active neutron / photon dosimeters. Contribution to European IRPA Congress 2002, Florence, Italy, 8–11 October 2002, CD-ROM.

	EXPERIMENTAL REPORT	GeNF POLDI
Neutron Diffraction Test of the <i>Umweganregung</i> Monochromator based on an Elastically Bent Perfect Crystal		
Principal Proposer:	P. Mikula Nuclear Physics Institute, 250 68 Rez, Czech Rep.	
Experimental Team:	P. Mikula, M. Vrana, V. Wagner Nuclear Physics Institute, Rez, Czech. Rep.; PTB, Braunschweig, Germany	
Date(s) of Experiment:	December 2002	

Scientific Objective

In July 2001 we carried out an original experiment three cylindrically bent Si single crystal slabs of different cuts with the goal to identify the umweg-effects on in a large range of the neutron wavelength from about 0.7 nm to 0.25 nm. The aim was to find the strongest effects for their possible use (as monochromators) in powder diffractometry. In course of this experiment we have found many strong umweganregung effects which potentially could be good candidates for ultra high resolution neutron monochromators [1, 2]. The purpose of this experiment is to prove that umweganregung monochromator really could be effectively used at high flux neutron sources.

Experimental Technique and Main Results

As can be seen from Fig. 1, the $\theta-2\theta_D$ scan (carried out in the former experiment on a cylindrically bent Si-crystal slab with the main face parallel to the planes (110)) provided several strong umweg reflections [1, 2]). For θ -angle smaller than 15° , umweg effects simulate the allowed reflection (111). On the other hand for the θ -angle larger than 25° umweg effects simulate the forbidden reflection (222) [2]. For this latter experiment we chose the umweg reflection simulated the forbidden reflection (222) which appeared at $\theta = 30^\circ$. In this case it has been found that forbidden 222 primary reflection is simulated through a cooperative action of $153/131$ and $311/513$ (secondary/tertiary) reflections at $\lambda = 0.156$ nm.

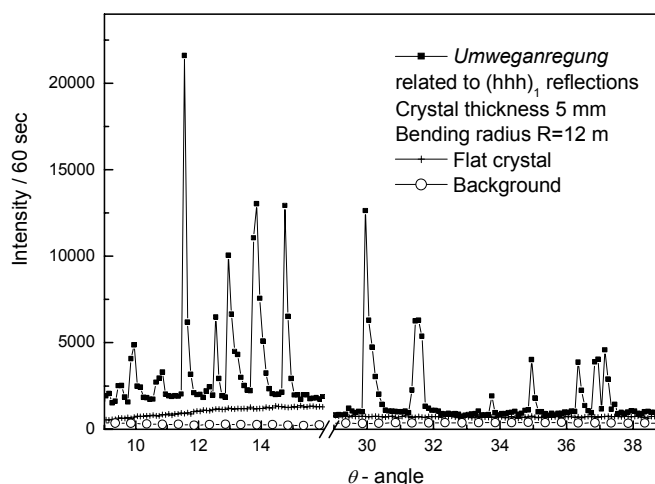


Figure 1:
 $\theta-2\theta_D$ scan for cylindrically bent perfect crystal slab of the thickness 5 mm and radius of curvature of 12 m.

The experiment was carried out on POLDI diffractometer installed at the end of the thermal neutron guide tube. Bent Si slab with the bending radius of 10 m was adjusted in the monochromator drum for the forbidden reflection (222) at $\theta = 30^\circ$. As a sample we used a well annealed solid polycrystalline α -Fe of 8 mm diameter. In order to minimize the influence of the sample dimension on the instrument resolution we used two 2 mm Cd slits for the beams entering and outgoing from the sample and a rather large sample-detector distance of 142 cm. For imaging of the diffracted beam profile we used a linear position sensitive detector with the spatial resolution of about 1.5 mm and the width of the detector cell of 0.3 mm. Fig. 2 displays the diffraction profile of the Fe(211) reflection taken at $2\theta = 83.5^\circ$.

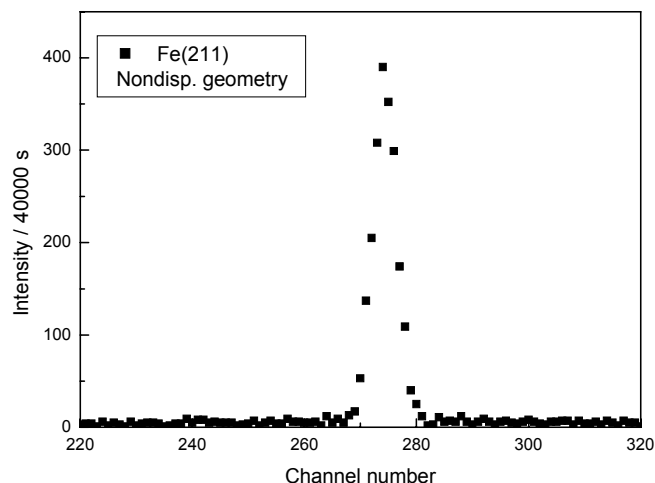



Figure 2:
Fe(211) powder diffraction profile as imaged by the linear position sensitive detector.

It can be seen from Fig. 2 that this experiment fully confirmed the predictions that the umweg effect can be used for high resolution neutron monochromatization. Calculation of the instrument resolution from *FWHM* of the Fe(211) diffraction profile provides the value 5×10^{-4} on the $\Delta d/d$ scale which is practically determined by the spatial resolution of the detector and the width of the slits. Therefore, this mentioned value of the instrumental resolution can be considered as a maximum estimation value. On the basis of these preliminary results we can state that when taking into account that at the high flux neutron sources the neutron current can be about by two orders magnitude higher, a reasonable measurement time in a real experiment can be expected with such an *umweganregung* monochromator.

References

- [1] P. Mikula, M. Vrána and V. Wagner, *Neutron Diffraction Studies of Umweganregung Effects in Elastically Bent Perfect Crystals*, GKSS Experimental Report, GENF-POLDI, p. 151–152 (in this Report references to other earlier related papers can be found).
- [2] P. Mikula, M. Vrána and V. Wagner, *On a possible use of multiple Bragg reflections for high resolution monochromatization of neutrons*, Submitted for the conference ECNS 2003.

	EXPERIMENTAL REPORT	GeNF POLDI
Domain structure of Ba-ferrit glass ceramics		
Principal Proposer:	V. Wagner ¹ , Th. Klupsch ² , ¹ Physik. Tech. Bundesanstalt, 38116 Braunschweig, Germany ² Institute for Physic. High Technology, Jena, Germany	
Experimental Team:	V. Wagner, F. Kaufmann, W. Berne. K. Kahnt Physik. Tech. Bundesanstalt, 38116 Braunschweig, Germany	
Date(s) of Experiment:	50 days in 10/2001, 4/2002, 7/2002	

Scientific Objective

Ba-ferrit glass ceramics consist of single-domain Ba-ferrite particles (platelets of diameter in the range from 50 to 500 nm with increasing aspect ratio from 6 to 9) imbedded in a SiO₂ matrix and produced by the glass crystallization method [1]. This ferromagnetic ceramic is a new hard magnetic material which is magnetically isotropic and thereby any 3-dimensional pattern of the magnetization may be stored. Furthermore it is chemically inert.

The coercive field H_c attains values as high as 340 kA/m compared to 430 kA/m expected on the basis of Stoner-Wohlfarth particles. In order to get insight of the magnetization reversal on a mesoscopic length scale we investigated the magnetic domain structure – domain size and magnetic texture – by neutron depolarization technique.

Experimental Techniques

The the bulk magnetization and its domain structure were observed by neutron depolarization technique in the remanent and the demagnetized state in several samples of Ba-ferrite glass ceramics. The samples were supplied by *R. Müller*, IPHT Jena. They were mounted in a solenoid closed by a soft magnetic yoke and were magnetized by a series of magnetic field pulses of increasing strength ($0 < H_{app} < 800$ kA/m). After each pulse both the depolarization of a beam of thermal neutrons transmitted through the sample and the rotation of the beam polarization were observed. The domain structure was deduced from the depolarization and the remanent magnetization from the rotation of the polarization of the transmitted beam [2].

Main Results

The measurements were taken along the initial branch of remanent magnetization M_{rem} and after reversal of the magnetic field pulses, along the demagnetized branch $M_{dem}^{(1,2)}$ until the complete magnetization reversal (see Fig. 1). Several samples with volume fraction of Ba-ferrite of about 30 % were studied [3]. Typically the mean domain size (as measured by the correlation length ζ of the magnetic fluctuations) was about 240 nm in the virgin state produced by annealing at 800 K for 1 h. The anisotropy of the depolarization indicated no or only little magnetic texture. The mean domain size in the remanent state increased up to 580 nm at saturation remanence. At same time texture continually developed with preferred orientation of the domain magnetization along the magnetizing field. Upon magnetization reversal the mean domain size decreased slowly and then attained a maximum ($\zeta \cong 1 \mu\text{m}$) during magnetization reversal (see Fig.2). In general the behaviour was similar to what has been reported for powders of micro-crystalline Ba-ferrite particles produced by the glass crystallization method [4]. The mean domain size exceeds the mean size of the Ba-ferrite particles. The magnetic behaviour seems to be dominated by strong magnetic correlations

between neighbouring particles on a length scale exceeding the particle size, although the dipolar coupling is weak compared with the magnetocrystalline anisotropy [5].

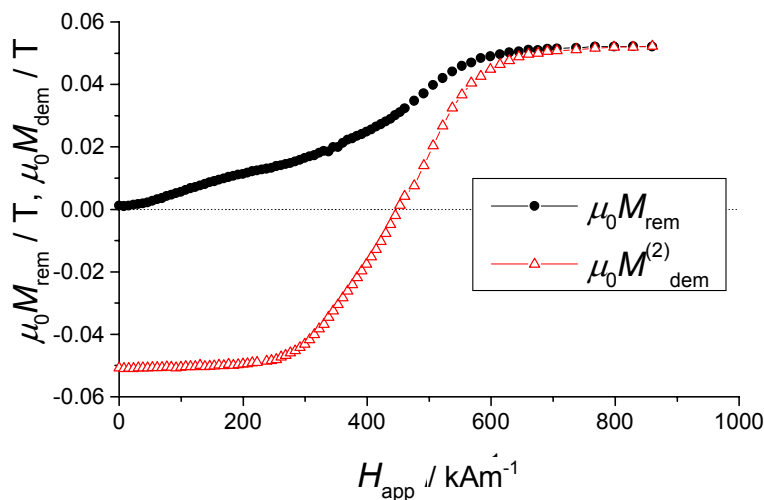


Figure 1:
Remanent magnetization M_{rem} and $M_{dem}^{(2)}$ vs. applied field H_{app} for magnetization starting from the virgin state and after magnetization reversal.

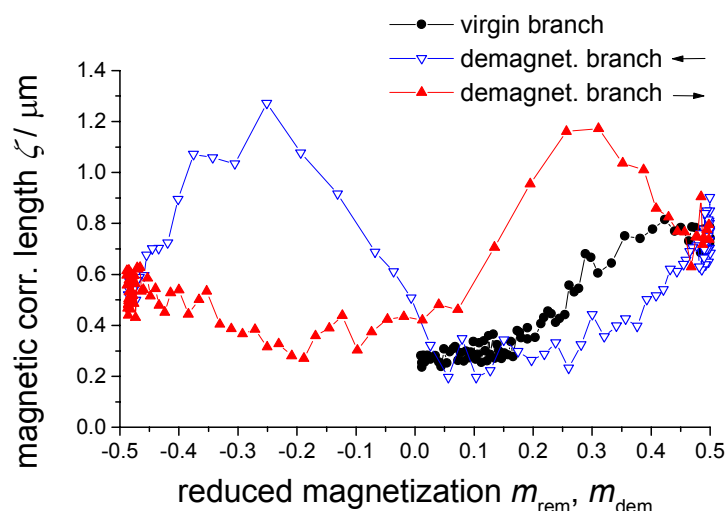



Figure 2:
Magnetic correlation length ζ vs. reduced magnetization $m_{rem,dem} = M_{rem,dem} / M_{saturation}$ for the initial branch starting from the virgin state (full circles) and during magnetization reversal (triangles).

Relevance to others Applications or to others Techniques

3D-neutron depolarization analysis is a technique complementary to small angle neutron scattering for the investigation of the magnetic mesostructure. It is very useful for studying large magnetic inhomogeneities in the case where USANS experiments are not possible.

References

- [1] R. Mueller, C. Ulbrich, W. Schueppel, H. Steinmetz, and E. Steinbeiss, J. Europ. Cer. Soc. 19 (1999) 1547
- [2] R. Rosman and M. Th. Rekveldt, Phys. Rev. B:Condens. Matter 43 (1991) 8437
- [3] Preliminary results were reported by V. Wagner et al., 47th Annual Conference on Magnetism and Magnetic, Tampa, Florida, November 2002, abstracts booklet p. 226
- [4] P. T. Por et al., J. Magnetism & Magn. Materials, 161 (1996) 367
- [5] Th. Klupsch et al., J. Magnetism & Magn. Materials 236 (2001) 209

	EXPERIMENTAL REPORT	GeNF RÖDI & TOREMA
Internship: x-ray and neutron scattering methods applied to thin films		
Co-ordinators:	D. M. Solina, D. Lott, M. Störmer, U. Tietze, A. Schreyer GKSS Research Centre	
Date(s) of Experiment:	October 2002	

2002 has seen the revival of the internship program between GKSS and Hamburg University. The program supplies an overview of thin film fabrication as well as x-ray and neutron thin film analysis techniques. With the advent of magnetic films in the computer, as well as other recording industries, special emphasis is placed on the use of neutrons in the investigation of exchange coupling by illustrating the versatility of the method in the study of these films.

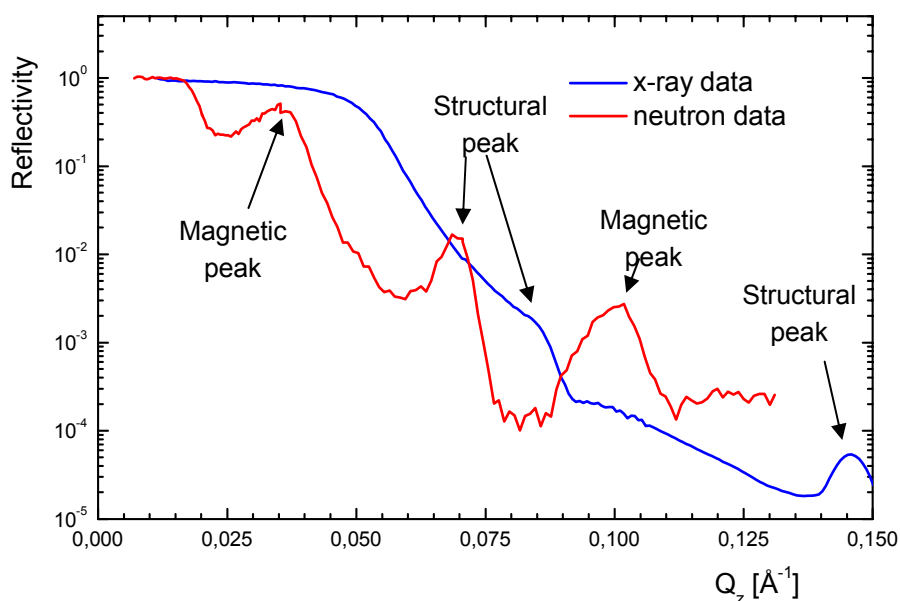



Figure 1: X-ray and neutron reflectivity spectra taken for a FeCr/Cr multilayer illustrating the additional information available with neutrons.

Prior to their arrival at GKSS the students are given a compilation of notes with activities to prepare themselves for their time at GKSS. During the four day internship the students indulge their curiosity by making, measuring and analysing their own films. Throughout the internship the students have access to thin film scientists to assist in the learning process and guide them where necessary. At the end of their internship the culmination of the student's experiences are presented to their university as agreed.

It is hoped that by participating in the program the student will take away with them not only knowledge about the various techniques but also open doors to the career choices available in thin film and neutron science.

	EXPERIMENTAL REPORT	GeNF RÖDI INCOATC- Bruker AXS
Characterisation of FeMn-FeNi exchange bias films using X-ray reflection and diffraction		
Principal Proposer:	J. Fassbender Universität Kaiserslautern, Germany	
Experimental Team:	D. M. Solina; D. Lott; A. Schreyer GKSS Research Centre	
Date(s) of Experiment:	July–August 2002	

Scientific Objective

FeMn is a promising antiferromagnetic (AFM) material owing to its large exchange bias field (H_E) and low coercivity (H_C). When coupled with FeNi, a good system is established for the unravelling of the mechanics of exchange biasing. With the final objective being the study of the bias exchange between FeMn and FeNi layers with neutrons, the Universität Kaiserslautern has prepared a number of FeMn/FeNi films which were first tested by the thin films group at GeNF and INCOATEC for their quality with X-rays.

Experimental Technique

The supplied films were prepared using Molecular Beam Epitaxy (MBE). The layer structure was MgO/Fe(0.5nm)/Pt(5nm)/Cu(100nm)/FeMn(10nm)/FeNi(5nm)/Cu(2nm)/Cr(2nm), where the MgO substrate was either [001] or [110] orientated crystal. The films were characterised using x-ray diffraction and reflection on RÖDI and verified using INCOATEC's BRUKER AXS D8 machine. Both machines have been fitted with a parallel beam set-up with resolution better than $0.03^\circ\theta$ FWHM.

Results and Conclusions

X-ray diffraction showed that the copper layer has been deposited with good crystalline quality with orientation that of the associated substrate. Peaks other than those for the substrate and copper layer peaks have not been identified. This may be a result of the small thicknesses of the FeMn and FeNi layers providing not enough reflected intensity. However, the expected peak for FeMn is situated very near to the substrate peak position such that the peak might be covered by the substrate peak. Still, the strong copper reflection confirms that the MBE process has the potential to produce good quality films.

Modelling of the reflectivity data however, suggests that the interfaces adjoining the FeNi layer are quite rough (see Fig. 1) which would normally indicate poor deposition technique however the strong crystallinity of the copper layer contradicts this statement. This roughness however, is not a fallacy of the MBE technique rather it seems to be related to the choice of the capping layer. Recent studies [1, 2] using X-ray Photoelectron Spectroscopy (XPS) to investigate the FeMn-FeNi interface have shown the segregation of copper at the FeMn-FeNi interface when the adjoining layer to the NiFe is copper. In the

samples examined in this study the capping layer was comprised of a first layer of copper and then chromium. The reflectivity data was modelled with a single Cr-Cu layer where diffusion was assumed and it is probable that copper also diffused through the adjoining FeNi layer.

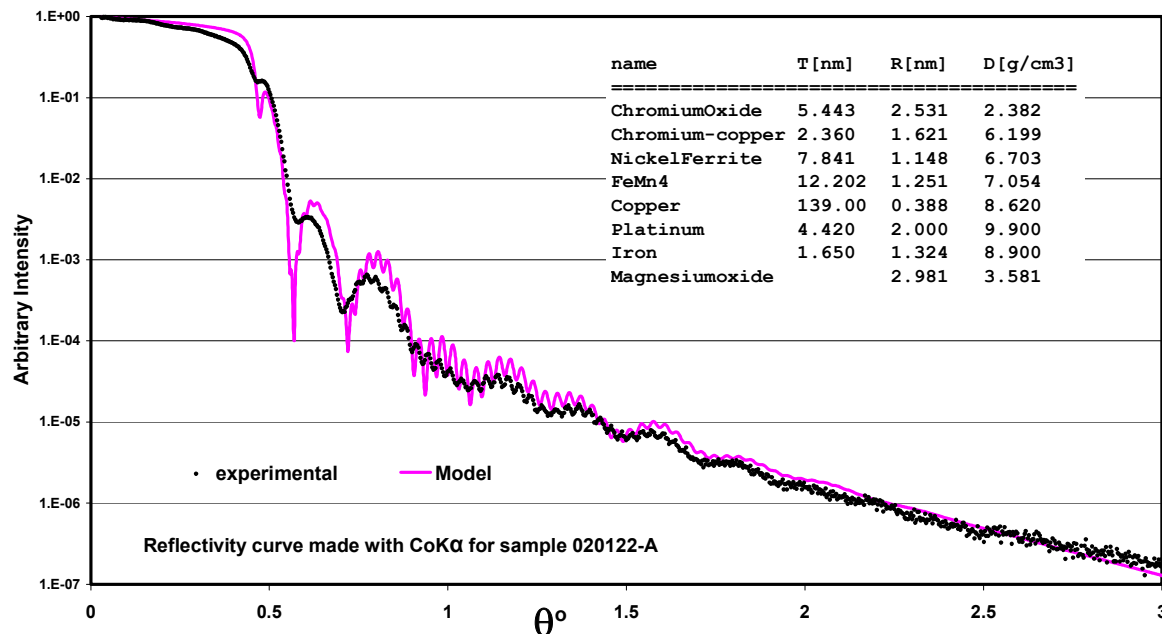


Figure 1: X-ray reflection data taken using CoKα source on sample 020122-A and modelled using REFSIM [3] where T, R and D are the thickness, roughness and density respectively.

Consequently, an alternative capping layer would be needed in order to improve the quality of the interface.

References

- [1] J. Appl. Phys. 92 (5), 2620 (2002)
- [2] Mat. Sci. Eng. B90, 296, (2002)
- [3] Grassl, S., Fuchs. D., Reflectivity Software WIN-REFSIM, Version 1.1d Copyright SIEMENS AG (1992-1995), BRUKER ANALYTICAL X-RAY SYSTEMS Inc., Karlsruhe, Germany

Institut für Werkstoffforschung

Geesthacht Neutron Facility (GeNF)



Max-Planck-Strasse, Telephone +49 4152 87-1268
 D-21502 Geesthacht Telefax +49 4152 87-1336

Application for the use of Neutron Scattering Facilities at FRG-1

Experiment title:		
Description of the proposed experiment: (Outline of the scientific background and relevant features of the envisaged experiment; aims of the experiment and results to be achieved; preliminary work carried out)		
This is <input type="checkbox"/> a new proposal <input type="checkbox"/> a continuation proposal; then please attach a report on previous results		
Category <input type="checkbox"/> Material Science <input type="checkbox"/> Chemistry <input type="checkbox"/> Biology <input type="checkbox"/> Physics <input type="checkbox"/> Engineering <input type="checkbox"/> Geoscience <input type="checkbox"/> Medicine <input type="checkbox"/> Other		
Proposer: <i>(title, surname, initials)</i>	Address:	Phone: Fax: E-mail:
Co-Proposer:		
Instrument required:	Days required:	Requested starting date:
Experiment details:		
<input type="checkbox"/> Polarized neutrons	Wavelength (nm):	
<input type="checkbox"/> Non-polarized neutrons	Approx. range of momentum transfer:	

Sample environment

To be provided by GKSS:

- Magnet, horizontal Cryostat, horizontal Closed cycle refrigerator
 Magnet, vertical Cryomagnet, vertical

Temperature range:

Magnetic field strength:

Others:

If sample environment equipment will be provided by user, please give details:

Description of sample

Substance formula:

- solid liquid powder
 single crystal polycrystal gas
 other

Size:

Weight:

Container required:

Safety aspects

Is the sample	yes	no
toxic?	<input type="checkbox"/>	<input type="checkbox"/>
explosive?	<input type="checkbox"/>	<input type="checkbox"/>
flammable?	<input type="checkbox"/>	<input type="checkbox"/>
radioactive?	<input type="checkbox"/>	<input type="checkbox"/>
contaminant?	<input type="checkbox"/>	<input type="checkbox"/>
corrosive?	<input type="checkbox"/>	<input type="checkbox"/>

Is there any other danger associated with the proposed sample or sample environment?
If yes, what are the risks?:

Estimated sample activation during experiment (Bq):

After the experiment the sample will be

- removed by user stored at GKSS given to GKSS-disposal

Are the experimentalists licensed to handle radioactive materials?

(§ 3 Strahlenschutzverordnung) yes no

Are the experimentalists security screened?

(§ 12b Atomgesetz) yes no

– Access is limited to persons whose trustworthiness is predetermined –

The proposer is obliged to send a report on the experimental results to GKSS not later than 3 months after finishing the experiment.

The proposer certifies that the above details are complete and correct.

Date:

Signature of proposer: